

Semiconductor Nanomaterials for Energy Conversion and Storage

Guest Editors: Xiang Wu, Xijin Xu, Chuanfei Guo,
and Chee Kiang Ivan Tan





Semiconductor Nanomaterials for Energy Conversion and Storage

Journal of Nanomaterials

Semiconductor Nanomaterials for Energy Conversion and Storage

Guest Editors: Xiang Wu, Xijin Xu, Chuanfei Guo,
and Chee Kiang Ivan Tan



Copyright © 2015 Hindawi Publishing Corporation. All rights reserved.

This is a special issue published in "Journal of Nanomaterials." All articles are open access articles distributed under the Creative Commons Attribution License, which permits unrestricted use, distribution, and reproduction in any medium, provided the original work is properly cited.

Editorial Board

Domenico Acierno, Italy
Katerina Aifantis, USA
Sheikh Akbar, USA
Nageh K. Allam, USA
Margarida Amaral, Portugal
Jordi Arbiol, Spain
Raul Arenal, Spain
Ilaria Armentano, Italy
Lavinia Balan, France
Thierry Baron, France
Andrew R. Barron, USA
Hongbin Bei, USA
Stefano Bellucci, Italy
Enrico Bergamaschi, Italy
D. Bhattacharyya, New Zealand
Giovanni Bongiovanni, Italy
Theodorian Borca-Tasciuc, USA
Mohamed Bououdina, Bahrain
Torsten Brezesinski, Germany
C. Jeffrey Brinker, USA
Christian Brosseau, France
Yibing Cai, China
Chuanbao Cao, China
Victor M. Castao, Mexico
Albano Cavaleiro, Portugal
Bhanu P. S. Chauhan, USA
Wei Chen, China
Yuan Chen, Singapore
Tupei Chen, Singapore
Shafiul Chowdhury, USA
Kwang-Leong Choy, UK
Jin-Ho Choy, Korea
Yu-Lun Chueh, Taiwan
Elisabetta Comini, Italy
Giuseppe Compagnini, Italy
David Cornu, France
Miguel A. Correa-Duarte, Spain
P. Davide Cozzoli, Italy
Majid Darroudi, Iran
Shadi A. Dayeh, USA
Luca Deseri, USA
Yong Ding, USA
Bin Dong, China
Zehra Durmus, Turkey
Joydeep Dutta, Oman

Ali Eftekhari, USA
Samy El-Shall, USA
Farid El-Tantawy, Egypt
Ovidiu Ersen, France
Claude Estournès, France
Andrea Falqui, Saudi Arabia
Xiaosheng Fang, China
Bo Feng, China
Matteo Ferroni, Italy
Wolfgang Fritzsche, Germany
Alan Fuchs, USA
Peng Gao, China
Miguel A. Garcia, Spain
Siddhartha Ghosh, Singapore
P. K. Giri, India
Russell E. Gorga, USA
Jihua Gou, USA
Alexander Govorov, USA
Jean M. Greneche, France
Changzhi Gu, China
Lin Guo, China
John Zhanhu Guo, USA
Smrati Gupta, Germany
K. Hamad-Schifferli, USA
Michael Harris, USA
Jr-Hau He, Taiwan
Nguyen D. Hoa, Vietnam
Michael Z. Hu, USA
Nay Ming Huang, Malaysia
Qing Huang, China
Shaoming Huang, China
David Hui, USA
Zafar Iqbal, USA
B. Jeyadevan, Japan
Xin Jiang, Germany
Rakesh Joshi, Australia
Myung-Hwa Jung, Korea
Jeong-won Kang, Korea
Hassan Karimi-Maleh, Iran
Antonios Kelarakis, UK
Alireza Khataee, Iran
Ali Khorsand Zak, Iran
Wonbaek Kim, Korea
Dojin Kim, Korea
Philippe Knauth, France

Ralph Krupke, Germany
Christian Kübel, Germany
Prashant Kumar, UK
Sushil Kumar, India
Sanjeev Kumar, India
Subrata Kundu, India
Michele Laus, Italy
Eric Le Bourhis, France
Burtrand Lee, USA
Jun Li, Singapore
Meiyong Liao, Japan
Silvia Licoccia, Italy
Wei Lin, USA
Jun Liu, USA
Zainovia Lockman, Malaysia
Songwei Lu, USA
Jue Lu, USA
Ed Ma, USA
Malik Maaza, South Africa
Lutz Mädler, Germany
Gaurav Mago, USA
Morteza Mahmoudi, Iran
Mohammad A. Malik, UK
Devanesan Mangalaraj, India
Sanjay R. Mathur, Germany
Paulo Cesar Morais, Brazil
Mahendra A. More, India
Paul Munroe, Australia
Jae-Min Myoung, Korea
Rajesh R. Naik, USA
Albert Nasibulin, Russia
Toshiaki Natsuki, Japan
Koichi Niihara, Japan
Sherine Obare, USA
W.-Chun Oh, Republic of Korea
Atsuto Okamoto, Japan
Abdelwahab Omri, Canada
Ungyu Paik, Republic of Korea
Edward A. Payzant, USA
Ton Peijs, UK
O. Perales-Pérez, Puerto Rico
Wenxiu Que, China
Peter Reiss, France
Orlando Rojas, USA
Marco Rossi, Italy



Cengiz S. Ozkan, USA
Vladimir Šepelák, Germany
Huaiyu Shao, Japan
Prashant Sharma, USA
Donglu Shi, USA
Bhanu P. Singh, India
Surinder Singh, USA
Vladimir Sivakov, Germany
Yanlin Song, China
Ashok Sood, USA
Marinella Striccoli, Italy
Jing Sun, China
Xuping Sun, Saudi Arabia
Ashok K. Sundramoorthy, USA

Sabine Szunerits, France
Nyan-Hwa Tai, Taiwan
Bo Tan, Canada
Ion Tiginyanu, Moldova
Valeri P. Tolstoy, Russia
Muhammet S. Toprak, Sweden
Ramon Torrecillas, Spain
Takuya Tsuzuki, Australia
Tamer Uyar, Turkey
Bala Vaidhyanathan, UK
Luca Valentini, Italy
Rajender S. Varma, USA
Antonio Villaverde, Spain
Ajayan Vinu, Australia

Shiren Wang, USA
Yong Wang, USA
Ruibing Wang, Macau
Magnus Willander, Sweden
Ping Xiao, UK
Zhi Li Xiao, USA
Yangchuan Xing, USA
Doron Yadlovker, Israel
Piaoping Yang, China
Yoke K. Yap, USA
Ramin Yousefi, Iran
William W. Yu, USA
Kui Yu, Canada
Renyun Zhang, Sweden

Contents

Semiconductor Nanomaterials for Energy Conversion and Storage, Xiang Wu, Xijin Xu, Chuanfei Guo, and Chee Kiang Ivan Tan

Volume 2015, Article ID 624146, 2 pages

The Electronic Structures and Optical Properties of Electron Tuned Fe-Doped SnO₂ Materials, Zhe Wang, Bao-Jun Huang, Chang-Wen Zhang, Xi-Jin Xu, and Pei-Ji Wang

Volume 2015, Article ID 534831, 6 pages

SnO₂-Based Nanomaterials: Synthesis and Application in Lithium-Ion Batteries and Supercapacitors, Qinqin Zhao, Lisha Ma, Qiang Zhang, Chenggang Wang, and Xijin Xu

Volume 2015, Article ID 850147, 15 pages

A Facile Low-Temperature Hydrothermal Method to Prepare Anatase Titania/Cellulose Aerogels with Strong Photocatalytic Activities for Rhodamine B and Methyl Orange Degradations, Caichao Wan, Yun Lu, Chunde Jin, Qingfeng Sun, and Jian Li

Volume 2015, Article ID 717016, 8 pages

Fabrication of Robust Superhydrophobic Bamboo Based on ZnO Nanosheet Networks with Improved Water-, UV-, and Fire-Resistant Properties, Jingpeng Li, Qingfeng Sun, Qiufang Yao, Jin Wang, Shenjie Han, and Chunde Jin

Volume 2015, Article ID 431426, 9 pages

Synthesis, Characterization, and Photocatalytic Activity of g-C₃N₄/K₂TaO₆ Composites under Visible Light Irradiation, Zhiqing Yong, Jian Ren, Huilin Hu, Peng Li, Shuxin Ouyang, Hua Xu, and Defa Wang

Volume 2015, Article ID 821986, 7 pages

Enhanced Light Output of Dipole Source in GaN-Based Nanorod Light-Emitting Diodes by Silver Localized Surface Plasmon, Huamao Huang, Haiying Hu, Hong Wang, and Kuiwei Geng

Volume 2014, Article ID 180765, 8 pages

Synthesis of Hierarchical CoO Nano/Microstructures as Anode Materials for Lithium-Ion Batteries, Dan Qin, Peng Yan, Guangzhong Li, Yunchuang Wang, Yukuan An, and Juan Xing

Volume 2014, Article ID 489862, 5 pages

Cross-Linked ZnO Nanowalls Immobilized onto Bamboo Surface and Their Use as Recyclable Photocatalysts, Chunde Jin, Jingpeng Li, Jin Wang, Shenjie Han, Zhe Wang, and Qingfeng Sun

Volume 2014, Article ID 687350, 7 pages

Facile Synthesis of Carbon-Coated Zn₂SnO₄ Nanomaterials as Anode Materials for Lithium-Ion Batteries, Xiaoxu Ji, Xintang Huang, Qinghuai Zhao, Aihua Wang, and Xuyan Liu

Volume 2014, Article ID 169373, 6 pages

Optical and Magnetic Properties of Fe Doped ZnO Nanoparticles Obtained by Hydrothermal Synthesis, Xiaojuan Wu, Zhiqiang Wei, Lingling Zhang, Xuan Wang, Hua Yang, and Jinlong Jiang

Volume 2014, Article ID 792102, 6 pages

Direct Growth of Copper Oxide Films on Ti Substrate for Nonenzymatic Glucose Sensors, Xiaoxu Ji, Aihua Wang, and Qinghuai Zhao

Volume 2014, Article ID 287303, 5 pages

Editorial

Semiconductor Nanomaterials for Energy Conversion and Storage

Xiang Wu,¹ Xijin Xu,² Chuanfei Guo,³ and Chee Kiang Ivan Tan⁴

¹College of Chemistry and Chemical Engineering, Harbin Normal University, Harbin 150025, China

²School of Physics and Technology, University of Jinan, Jinan 250022, China

³Department of Physics, University of Houston, Houston, TX 77004, USA

⁴Institute of Materials Research and Engineering (IMRE), A*STAR, Singapore 117602

Correspondence should be addressed to Xiang Wu; wuxiang05@163.com

Received 14 December 2014; Accepted 14 December 2014

Copyright © 2015 Xiang Wu et al. This is an open access article distributed under the Creative Commons Attribution License, which permits unrestricted use, distribution, and reproduction in any medium, provided the original work is properly cited.

Energy and environmental problems have raised great concerns in recent decades. On one hand, people have an increasing demand on energy for which the consumption causes many environmental problems. On the other hand, clean energy is significantly increasing, but the consumption of fossil energy is still abundant. To date, beside conventional energy including fossil energy, hydroelectric power, and wind energy, scientists have developed several technologies to generate energy by converting solar energy into electricity or heat, by converting heat energy to electricity, or by converting mechanical energy to electricity. Indeed, generation of energy is only one of many issues for energy engineering. Now we have three big challenges in the area of new energy: generation, transport, and storage of energy. A demonstration that energy can be generated, transported, and stored by applying new materials and nanostructures is of great importance in both scientific research and practical applications.

As Guest Editors, we have successfully organized two special issues titled *Self-Assembly of 1D Semiconductor Nanostructures* and *Metal Oxide Heterostructures for Water Purification* in the past two years. Now it is our pleasure to finish the third special issue which is presented herein. This special issue covers all topics related to semiconductor materials and nanostructures for the generation, transport, and storage of energy, such as solar cells, supercapacitors, and lithium ion batteries. This special issue consists of one review paper and ten research papers that are contributed from Chinese scientists.

The review article by Xu et al. summarized the syntheses of phase-pure SnO₂ hierarchical structures with different morphologies such as nanorods, nanosheets, and nanospheres, as well as their modifications by doping and compositing with other materials. They reviewed the design of SnO₂-based nanostructures with improved performance in the areas of lithium-ion batteries and supercapacitors. The article by X. Ji et al. reported the growth of carbon-coated Zn₂SnO₄ materials by a facile hydrothermal method using the Zn₂SnO₄ octahedron as the precursor and glucose as carbon source and studied their electrochemical properties, revealing that carbon-coated Zn₂SnO₄ exhibits high rate capability and long cycle life compared with bare Zn₂SnO₄, indicating its promising application as anode for lithium-ion batteries. Q. Sun and his coworkers reported a portable cross-linked ZnO nanowalls/bamboo composites catalyst. Compared with those powder photocatalysts, the as-prepared photocatalyst was very easily separated from the dye aqueous solution and cyclically used.

The work from X. Wu studied the optical and magnetic properties of diluted magnetic semiconductors Zn_{1-x}Fe_xO nanoparticles with different doping consistency. Photoluminescence spectra exhibited a slight blue shift and the UV emission is annihilated with the increase of Fe³⁺ concentration. The obvious ferromagnetic properties are found for all doped samples at room temperature, and the saturation magnetization is enhanced with the increase of iron doping content. X. Ji et al. designed a new CuO film on Ti substrate

(CuO/Ti) electrode by effectively taking advantage of the conductivity and biocompatibility of the substrate. Then they investigated the application of this new electrode for glucose determination, demonstrating that the fabricated glucose biosensor exhibited a high sensitivity, fast response, an appropriate linear range, and good stability. The good analytical performance, low cost, and one-step preparation method make this electrode material promising for the development of a nonenzymatic glucose sensor. Wang et al. studied the nanorod based LEDs, and the light output of dipole power in the planar LED, the nanorod LED, and the LSP assisted LED were also studied by two-dimensional finite difference time domain method.

P. Yan et al. reported the synthesis of hierarchical CoO nano/microstructures via a hydrothermal method followed by a subsequent thermal annealing process. They studied electrochemical properties of as-synthesized hierarchical CoO nano/microstructures, revealing a high initial capacity of about 1370 mAh/g and superior cycle stability. Good rate capability is also obtained in CoO nano/microstructures as anode materials for LIBs.

The paper by Wang studied the electronic structures and optical properties of $\text{Sn}_{15}\text{FeO}_{32}$ with electron-injection by means of the full-potential linearized augmented plane-wave method (FP-LAPW). Their results showed that Fe-doped SnO_2 materials are all direct transition semiconductors. The Fermi level goes into conduction band gradually and the band gap decreases with the increase of electron injection. The peaks of optical properties, such as the imaginary part of dielectric function and absorption spectra, change greatly at low energy. The absorption spectra exhibit blue shift, and the optical absorption edge increases, which are consistent with the change of the band gaps. C. Jin et al. reported the bamboo with multifunction of superhydrophobicity, UV-resistance, and fire-resistance fabricated by coating with ZnO nanosheet networks via a hydrothermal method and subsequent modification with FAS-17.

Li and Lu's work studied in situ preparation of anatase titania (TiO_2) homogeneously dispersed in cellulose aerogels substrates. The obtained anatase titania/cellulose (ATC) aerogels showed interconnected three-dimensional architecture surrounded by numerous anatase TiO_2 particles aggregates. Compared with commercially available Degussa P_{25} , ATC aerogels displayed more excellent photocatalytic activities for Rhodamine B and methyl orange degradations under UV radiation. Finally, Yong et al. synthesized novel graphitic carbon nitride/ KTaO_3 ($g\text{-C}_3\text{N}_4/\text{KTaO}_3$) nanocomposite photocatalysts by a facile and simple ultrasonic dispersion method. Compared to either $g\text{-C}_3\text{N}_4$ or KTaO_3 , the composite photocatalysts show significantly increased photocatalytic activity for degradation of Rhodamine B (RhB) under visible light irradiation. They thought the increased photocatalytic performance of the composite could be attributed to the enhanced photogenerated charge carrier separation capacity.

We sincerely hope that the special issue can provide a valuable reference to the current development and future research of energy storage and conversion. Finally, we also hope that the collection of these articles will inspire researchers and stimulate new ideas in relative research field.

Acknowledgment

As Guest Editors, we would like to give many thanks to all of the above authors for their contributions to this special issue. At the same time, we are also grateful to the selfless referees for their hard work in reviewing these manuscripts.

*Xiang Wu
Xijin Xu
Chuanfei Guo
Chee Kiang Ivan Tan*

Research Article

The Electronic Structures and Optical Properties of Electron Tuned Fe-Doped SnO₂ Materials

Zhe Wang, Bao-Jun Huang, Chang-Wen Zhang, Xi-Jin Xu, and Pei-Ji Wang

School of Physics, University of Jinan, Jinan 250022, China

Correspondence should be addressed to Pei-Ji Wang; ss_wangpj@ujn.edu.cn

Received 21 July 2014; Accepted 14 August 2014

Academic Editor: Xiang Wu

Copyright © 2015 Zhe Wang et al. This is an open access article distributed under the Creative Commons Attribution License, which permits unrestricted use, distribution, and reproduction in any medium, provided the original work is properly cited.

By means of the full-potential linearized augmented plane-wave method (FP-LAPW), the electronic structures and optical properties of Sn₁₅FeO₃₂ with electron-injection are studied. The results show that Fe-doped SnO₂ materials are all direct transition semiconductors. The Fermi level goes into conduction band gradually and the band gap decreases with the increase of electron injection. The peaks of optical properties, such as the imaginary part of dielectric function and absorption spectra, change greatly at low energy. The absorption spectra exhibit blue shift, and the optical absorption edge increases, which are consistent with the change of the band gaps.

1. Introduction

The diluted magnetic semiconductors (DMS) have attracted a lot of experimental and theoretical attention [1–4] because their spin and charges can be manipulated, which will hereby induce many interestingly magnetic and magneto-optic characteristics. Though the magnetic and electronic properties in some typical DMS systems, such as SnO₂, ZnO, and GaN, have been investigated extensively, many challenges to realize DMS materials for practical applications [5–7] still exist.

As a wide band-gap semiconductor, doped SnO₂ play a promising role in short-wavelength LED, gas sensor, and laser diode due to its large band gap (3.6 eV) and high exciton binding energy (130 meV) at the room temperature [8–10]. The electronic structures, magnetic, and optical properties of transition metal (Co, Cr, Mo, Eu, etc.) doped SnO₂ bulk semiconductors materials have been researched in theory and experiment [11–13]. As the important one of the family, the structures and optical properties of Fe-doped SnO₂ have also caused much attention [14–16]. Adhikari et al. [17] fabricated Fe-doped SnO₂ nanoparticles with a chemical coprecipitation method and studied their structures and magnetism. Kim et al. [18] studied the structure, magnetic and optical properties, and Hall effects of Co- and Fe-doped SnO₂. When Fe doped SnO₂, for charge balance, Fe ions must have the ionic

valence of Fe⁴⁺ without introducing any defects [19]. But Fe ions do not have 4+ oxidation state; hence, the holes are created. So the electronic injection is necessary to obtain the better performance of SnO₂. It is well known that the injection of electrons into semiconductors is indispensable to realize spin-related devices, such as spin transistors [20]. The bleach in the absorption spectra by using size-dependent electron injection from excited CdSe quantum dots into TiO₂ nanoparticles is observed. It can be theoretically predicted using the first principles calculation, even if there are many difficulties such as the room temperature and external magnetic field in experiment [21, 22]. In this work, first-principles spin polarized calculations were used to explore the electron injection into Fe-doped SnO₂, and its optical and magnetic properties were studied in order to understand the transition mechanism.

2. Computational Details

The first-principle calculations are performed using FP-LAPW as implemented in WIEN2k code [23, 24]. The exchange and correlation effects are treated with the generalized gradient approximations (GGA) [25, 26]. The parameter of $R_{\text{mt}}K_{\text{max}}$ is chosen to be seven (R_{mt} is the smallest muffin-tin radius in the unit cell and K_{max} is the cut-off for the plane

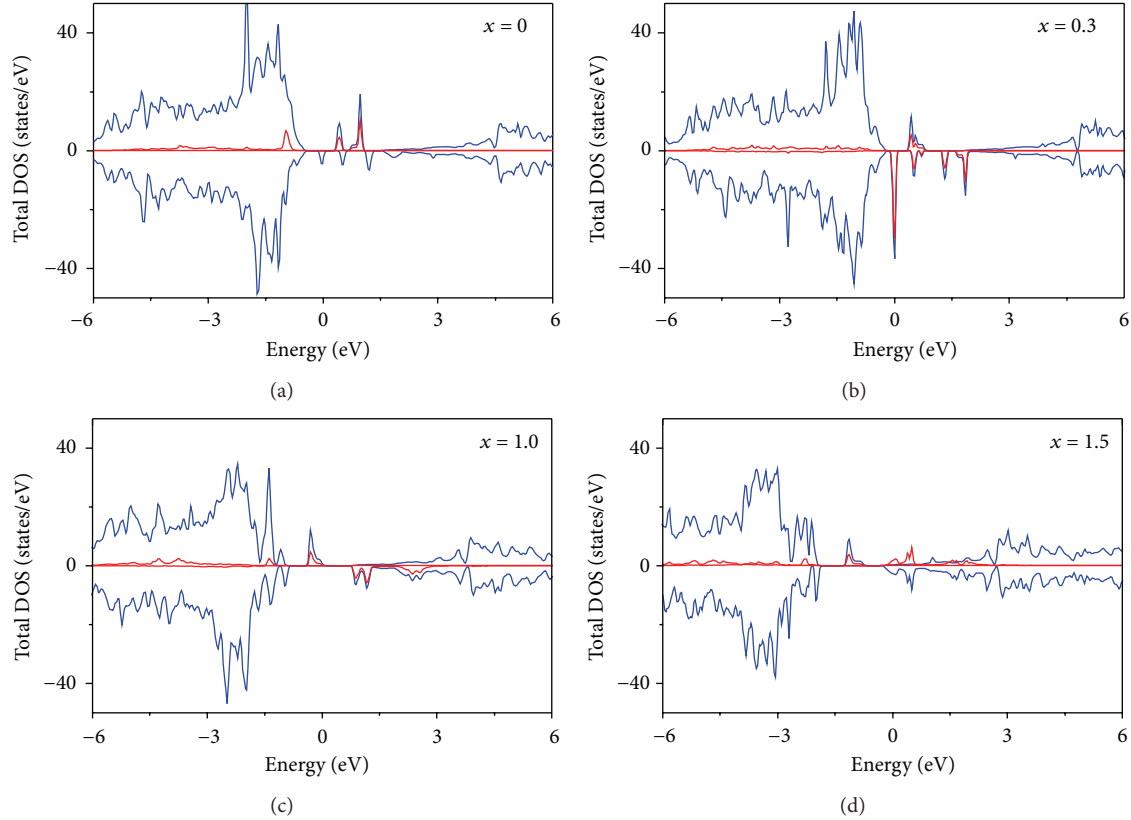


FIGURE 1: (Color online) The total DOS of the $\text{Sn}_{15}\text{FeO}_{32}$ supercell. The blue lines represent total DOS and the red lines represent Fe total DOS, respectively. (a) $x = 0$, (b) $x = 0.3$, (c) $x = 1.0$, and (d) $x = 1.5$.

wave). The cut-off energy required in the calculations of the solid state is 0.0001Ry. For k -space integration, a grid of $4 \times 3 \times 3k$ points in the first Brillouin zone is used. Atomic sphere radii of Sn, O, and Fe atoms are set to be 2.0, 1.8, and 2.0 a.u., respectively. The lattice parameters of SnO_2 crystals are consistent with the experimental values, which are $a = b = 0.4737$ nm, $c = 0.3186$ nm, and $\alpha = \beta = \gamma = 90^\circ$ [27].

All calculation models are constructed with $2 \times 2 \times 2$ supercell of SnO_2 , which contains 16 Sn atoms and 32 O atoms. In current work, only substitutional doping of Fe with Sn atoms is considered. Then, electron injection into $\text{Sn}_{15}\text{FeO}_{32}$ is taken with electron concentrations of $x = 0, 0.3, 0.5, 1.0, 1.2, \text{ and } 1.5$, respectively, and x is electron injection concentrations. The valence states for Sn, O, are Fe are $5s^25p^2$, $2s^22p^4$, and $3d^64s^2$, respectively.

3. Results and Discussion

3.1. Electronic Structure

3.1.1. Density of States (DOS). The calculated total DOS of the $\text{Sn}_{15}\text{FeO}_{32}$ supercell is shown in Figure 1. It can be seen that Fe substitutions into SnO_2 DMS induce exchange-split impurity states in the band gap, and the size of impurity states increases with the increase of injected electrons. When the concentration of injected electrons is less than 1.0, the material shows a half-metallic behavior with the majority

spin being semiconducting and the minority spin being metallic with sufficient unfilled states above the Fermi level. The 100% spin polarization carriers suggest that electron-injected Fe-doped SnO_2 can be used for spin injection where highly polarized spin current is desired. With the increase of the injected electrons, the conduction band moves to valence band gradually. Besides that, the DOS near the Fermi level reverses when the injected electron is 1.0. When the concentration of injected electrons is large than 1.0, the material shows a metallic behavior with both the majority spin and minority spin across the Fermi level.

The total and partial DOS of $\text{Sn}_{15}\text{FeO}_{32}$ supercell with electron-injection concentration $x = 0$ and 1.0 are presented in Figure 2, respectively. The coupling effect of Fe d, O p, and Sn p states can be found after Fe doping from Figure 2. The impurity states in the band gap are mostly composed of Fe 3d state hybridized with the O 2p states. The DOS (Figure 2(b)) indicates that the exchange-split Fe 3d states strongly hybridize with the O 2p states at the top of the valence band, which is partly spin-polarized. When electron-injection concentration is 1.0, the partial DOS of Fe atom is greatly changed, especially in the Fermi level. The lowermost valence bands largely derive from Fe 3d, O 2p, and Sn 5p state when the band ranges from -6.0 to -3.5 eV. The O 2p state and Fe 3d state are formed when the bands are between -3.5 and -0.7 eV. The states derive from Fe 3d when the bands are between -0.7 and 0.3 eV. However, the states derive from Fe

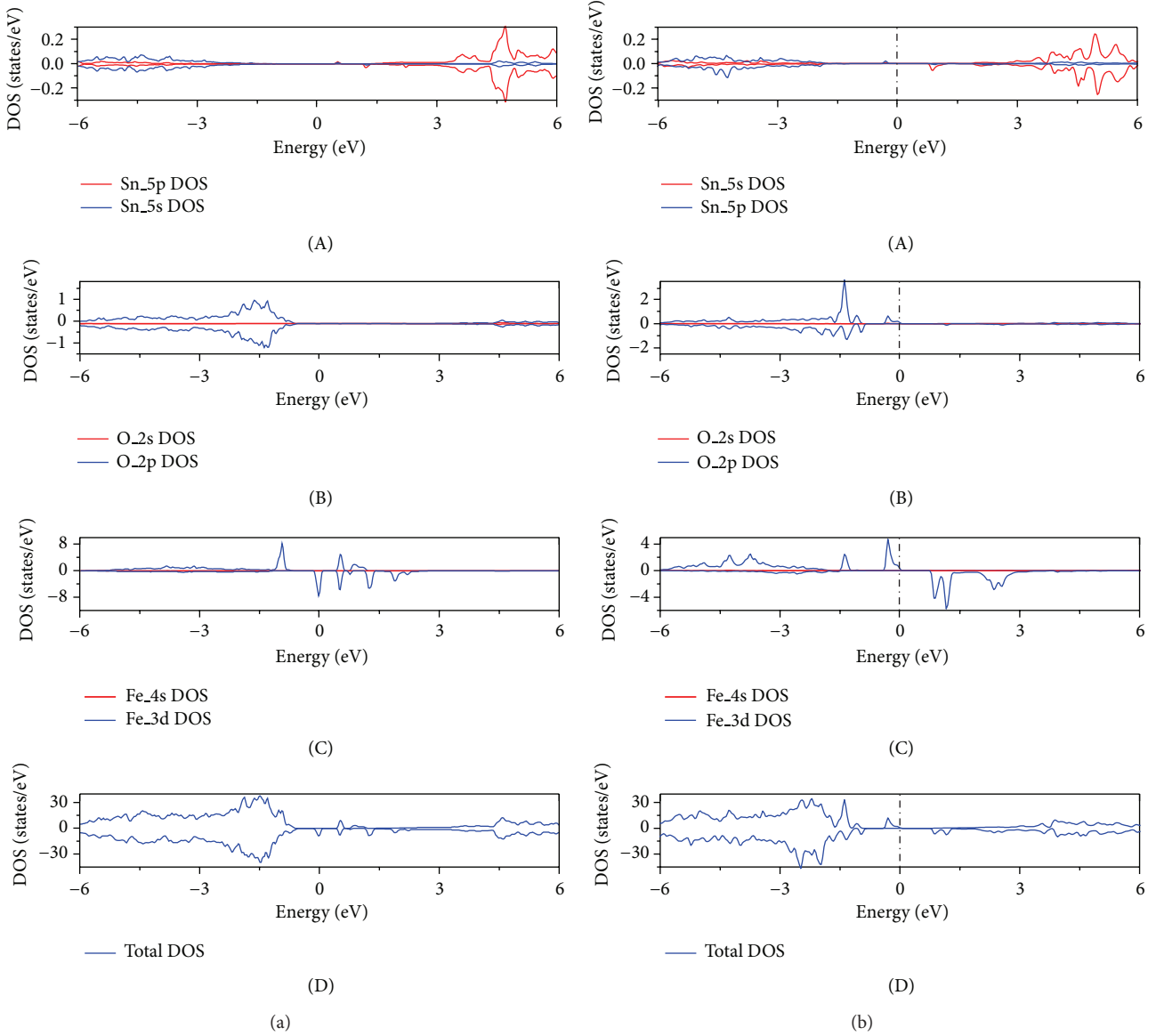


FIGURE 2: (Color online) Total DOS plots and partial DOS plots of the $\text{Sn}_{15}\text{FeO}_{32}$ supercell with electron-injection (1) $x = 0$ and (2) $x = 1.0$.

3d and O 2p when electron-injection concentration is 1.0, and Fe 3d turns to down from spin up, indicating that particles reverse has happened. When the bands are in the range from 0.3 to 2.6 eV, the states mainly derive from Fe 3d. When the bands locate in the range from 2.6 to 6.0 eV, the states mainly derive from Sn 5p.

3.1.2. Band Structure. The band structure of $\text{Sn}_{15}\text{FeO}_{32}$ supercell is shown in Figure 3, when $x = 0.5$. At the Fermi level, occupied and not occupied electrons exist when spin down and up, respectively. Figure 4 shows the band structures of spin-up $\text{Sn}_{15}\text{FeO}_{32}$ with the concentration of inject electrons to be 1.0 and 1.5. Furthermore the band gaps become narrower and narrower until zero with the increase of the injected electrons, indicating the excellent conductivity. Each band

structure displays a direct band gap at the highly symmetric G point as well as in pure SnO_2 , as shown in [28].

3.2. Optical Properties. It is well known that the interaction of a photon with the electrons can be described according to time-dependent perturbations of the ground-state electronic states, and the optical transitions between occupied and unoccupied states are caused by the electric field of the photon. More importantly, solid dielectric function reflects the information between energy band structure and optical spectral lines and can characterize the physical properties of materials. The formula of dielectric function is defined by

$$\varepsilon(\omega) = \varepsilon_1(\omega) + i\varepsilon_2(\omega), \quad (1)$$

where $\varepsilon_1(\omega)$ is the real part of the function, while $\varepsilon_2(\omega)$ is the imaginary part.

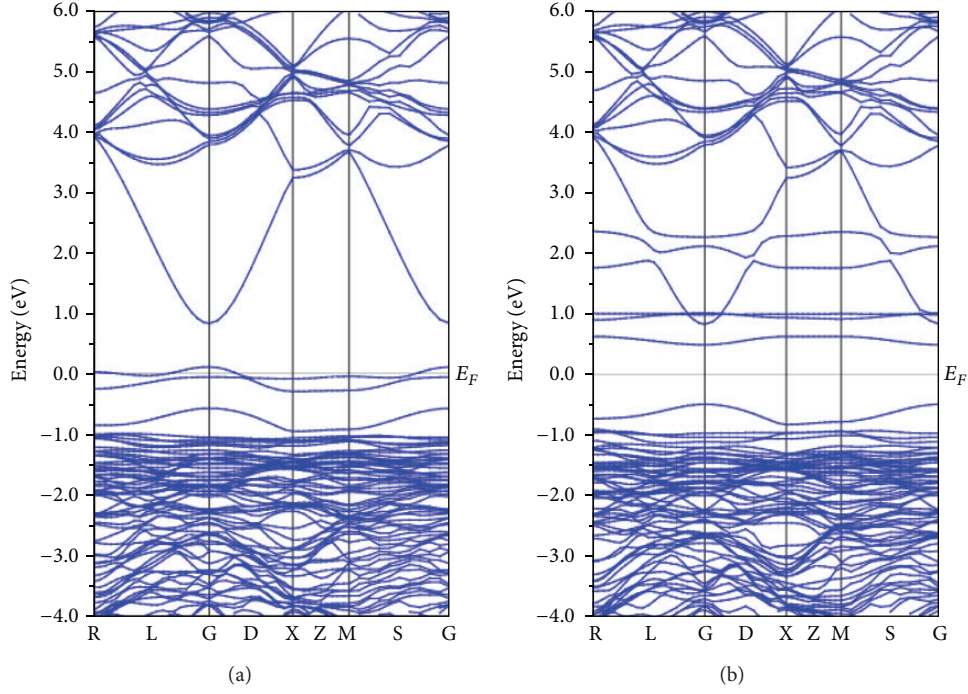


FIGURE 3: Band structures for supercell: $\text{Sn}_{15}\text{FeO}_{32}$. (a) $x = 0.5$ when spin up and (b) $x = 0.5$ when spin down.

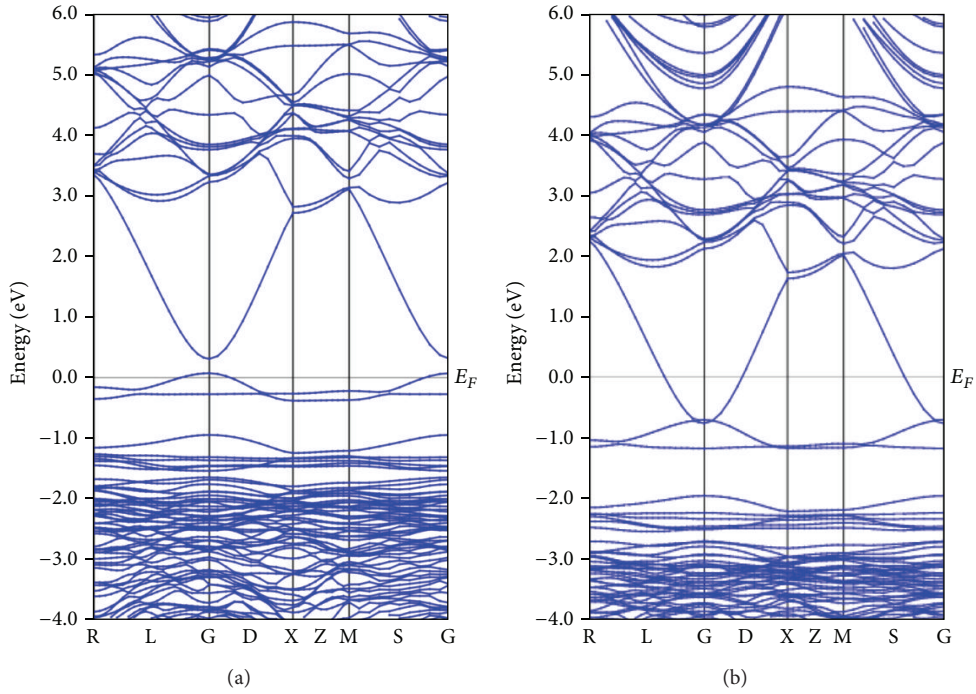


FIGURE 4: Band structures for supercell: $\text{Sn}_{15}\text{FeO}_{32}$. (a) $x = 1.0$ and (b) $x = 1.5$.

The real part $\varepsilon_1(\omega)$ of the dielectric function can be evaluated from the imaginary part $\varepsilon_2(\omega)$ by the Kramer-Kronig relationship, while the imaginary part $\varepsilon_2(\omega)$ has the following expression [29]:

$$\varepsilon_2(\omega) = \frac{4\pi^2}{m^2\omega^2} \sum_{V,C} \int_{BZ} d^3k \frac{2}{2\pi} |e \cdot M_{cv}(K)|^2 \times \delta[E_C(k) - E_V(k) - \hbar\omega]. \quad (2)$$

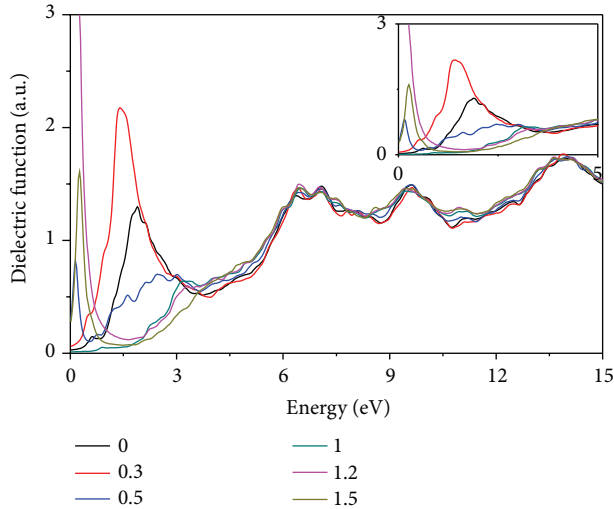


FIGURE 5: The imaginary part of dielectric function $\epsilon_2(\omega)$ of $\text{Sn}_{15}\text{FeO}_{32}$ with electron-injection.

Among this, $\hbar = h/2\pi$, m is the mass of free electrons, e is the charge of free electrons, ω is the frequency of incident photons, C represents the conduction band, V represents valence band, BZ represents the first Brillouin Zone, and K is the reciprocal vector.

Figure 5 shows the imaginary spectra of optical dielectric function $\epsilon_2(\omega)$, with the number of ions of 0, 0.3, 0.5, 1.0, 1.2, and 1.5. There are three main dielectric peaks ranging from 7.0 to 14.0 eV. The first peak at about 7.1 eV should mainly be caused by the transition between O 2p state in the highest valence band and Sn 5s in the lowest conduction band. The second peak located at about 9.8 eV mainly derives from the transition from O 2p to Sn 5p state, which is reflected by the DOS. The peak at 14.0 eV can be attributed to the combination of the transition between O 2s and Sn 5s and that between Fe 3d and Sn 5p. At the same time, there are some unapparent folded peaks, and they could be attributed to multilevels direct or indirect transition. From 0 to 5.0 eV, the peaks changed greatly, which are in consistency with the DOS in Figure 1.

Figure 6 shows the absorption spectra with the number of ions of 0, 0.3, 0.5, 1, 1.2, and 1.5. In the imaginary spectra of optical dielectric function, three main dielectric peaks exist ranging from 7.2 to 12.0 eV, which have no significant differences between various electron-injections, and are in consistency with the dielectric function in Figure 6. As the electron concentrations increase, the overall curves move to the high energy, that is the blue-shift. From 0 to 5.0 eV, the peaks changed greatly, the results are consistent with the Ref 30 of Fe-doped TiO_2 . The spectra become smooth gradually, and the float/drift of the intensities is not apparent, indicating that such optical and electronic devices can work relatively stable.

4. Conclusions

In summary, the band structure, the total and partial DOS, and the optical properties of $\text{Sn}_{15}\text{FeO}_{32}$ with electron

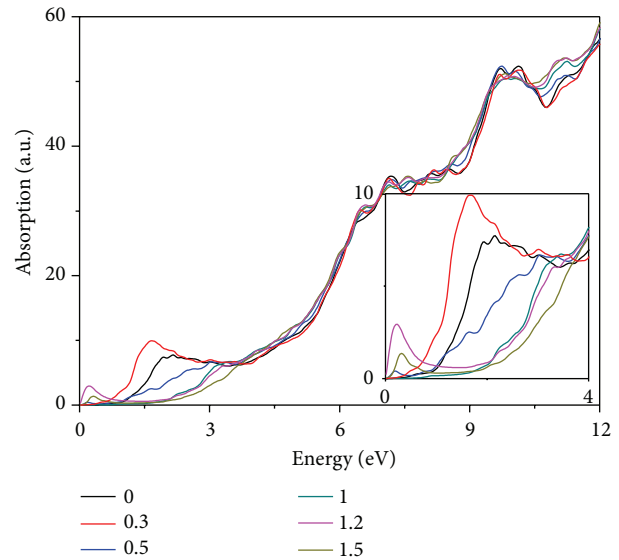


FIGURE 6: Absorption spectra of $\text{Sn}_{15}\text{FeO}_{32}$ with electron-injection.

injection have been investigated by the FP-LAPW method. With the increase of the injected electrons, the conduction band moves to valence band gradually. The SnO_2 material shows half-metallic properties when the injected electron is less than 1.0. There exists strong coupling interaction between Fe atom and O atom. For the optical properties (the imaginary part of dielectric function, absorption, and reflection), we found that the peaks changed greatly at low energy, the blue shift occurred, and the optical absorption edge increased.

Conflict of Interests

The authors declare that there is no conflict of interests regarding the publication of this paper.

Acknowledgments

This work was supported by the National Natural Science Foundation of China (Grant nos. 61172028 and 61076088) and the Natural Science Foundation of Shandong Province (Grant no. ZR2010EL017).

References

- [1] D. Awschalom and M. E. Flatté, "Challenges for semiconductor spintronics," *Nature Physics*, vol. 3, pp. 153–159, 2007.
- [2] S. A. Wolf, D. D. Awschalom, R. A. Buhrman et al., "Spintronics: a spin-based electronics vision for the future," *Science*, vol. 294, no. 5546, pp. 1488–1495, 2001.
- [3] Y.-W. Son, M. L. Cohen, and S. G. Louie, "Half-metallic graphene nanoribbons," *Nature*, vol. 446, no. 7133, pp. 347–349, 2007.
- [4] E. Kan, L. Yuan, and J. L. Yang, "Electron-induced ferromagnetic ordering of Co-doped ZnO," *Journal of Applied Physics*, vol. 102, no. 3, Article ID 033915, 2007.

- [5] S. Dhar, O. Brandt, A. Trampert et al., "Origin of high-temperature ferromagnetism in (Ga,Mn)N layers grown on 4H-SiC(0001) by reactive molecular-beam epitaxy," *Applied Physics Letters*, vol. 82, no. 13, pp. 2077–2079, 2003.
- [6] J. Schliemann and A. H. MacDonald, "Noncollinear ferromagnetism in (III,Mn)V semiconductors," *Physical Review Letters*, vol. 88, Article ID 137201, 2002.
- [7] Q. Wang, Q. Sun, P. Jena, and Y. Kawazoe, "Ferromagnetic GaN-Cr nanowires," *Nano Letters*, vol. 5, no. 8, pp. 1587–1590, 2005.
- [8] K. L. Chopra, S. Major, and D. K. Pandya, "Transparent conductors—a status review," *Thin Solid Films*, vol. 102, no. 1, pp. 1–46, 1983.
- [9] A. L. Dawar and J. C. Joshi, "Semiconducting transparent thin films: their properties and applications," *Journal of Materials Science*, vol. 19, no. 1, pp. 1–23, 1984.
- [10] L. Kaplan, A. Ben-Shalom, R. L. Boxman, S. Goldsmith, U. Rosenberg, and M. Nathan, "Annealing and Sb-doping of SnO films produced by filtered vacuum arc deposition: structure and electro-optical properties," *Thin Solid Films*, vol. 253, no. 1–2, pp. 1–8, 1994.
- [11] H. Wang, Y. Yan, Y. S. Mohammed, X. Du, K. Li, and H. Jin, "First-principle study of magnetism in Co-doped SnO₂," *Journal of Magnetism and Magnetic Materials*, vol. 321, no. 5, pp. 337–342, 2009.
- [12] A. Kar and A. Patra, "Optical and electrical properties of Eu³⁺-Doped SnO₂ nanocrystals," *Journal of Physical Chemistry C*, vol. 113, no. 11, pp. 4375–4380, 2009.
- [13] E. Zampiceni, E. Bontempi, G. Sberveglieri, and L. E. Depero, "Mo influence on SnO₂ thin films properties," *Thin Solid Films*, vol. 418, no. 1, pp. 16–20, 2002.
- [14] R. H. R. Castro, P. Hidalgo, R. Muccillo, and D. Gouvea, "Microstructure and structure of NiO-SnO₂ and Fe₂O₃-SnO₂ systems," *Applied Surface Science*, vol. 214, pp. 172–177, 2003.
- [15] E. Comini, A. Vomiero, G. Faglia, G. D. Mea, and G. Sberveglieri, "Influence of iron addition on ethanol and CO sensing properties of tin oxide prepared with the RGTO technique," *Sensors and Actuators B: Chemical*, vol. 115, no. 2, pp. 561–566, 2006.
- [16] D. Kotsikau, M. Ivanovskaya, D. Orlik, and M. Falasconi, "Gas-sensitive properties of thin and thick film sensors based on Fe₂O₃-SnO₂ nanocomposites," *Sensors and Actuators B: Chemical*, vol. 101, no. 1–2, pp. 199–206, 2004.
- [17] R. Adhikari, A. K. Das, D. Karmakar, T. V. C. Rao, and J. Ghatak, "Structure and magnetism of Fe-doped SnO₂ nanoparticles," *Physical Review B—Condensed Matter and Materials Physics*, vol. 78, no. 2, Article ID 024404, 2008.
- [18] H. S. Kim, L. Bi, G. F. Dionne, C. A. Ross, and H. J. Paik, "Structure, magnetic and optical properties, and Hall effect of Co- and Fe-doped SnO₂ films," *Physical Review B*, vol. 77, Article ID 214436, 2008.
- [19] X. L. Wang, Z. X. Dai, and Z. Zeng, "Search for ferromagnetism in SnO₂ doped with transition metals (V, Mn, Fe, and Co)," *Journal of Physics: Condensed Matter*, vol. 20, no. 4, Article ID 045214, 2008.
- [20] S. Datta and B. Das, "Electronic analog of the electro-optic modulator," *Applied Physics Letters*, vol. 56, p. 665, 1990.
- [21] I. Robel, M. Kuno, and P. V. Kamat, "Size-dependent electron injection from excited CdSe quantum dots into TiO₂ nanoparticles," *Journal of the American Chemical Society*, vol. 129, no. 14, pp. 4136–4137, 2007.
- [22] M. Kohda, Y. Ohno, K. Takamura, F. Matsukura, and H. Ohno, "A spin Esaki diode," *Japanese Journal of Applied Physics 2: Letters*, vol. 40, no. 12, pp. L1274–L1276, 2001.
- [23] K. Schwarz, "DFT calculations of solids with LAPW and WIEN2k," *Journal of Solid State Chemistry*, vol. 176, no. 2, pp. 319–328, 2003.
- [24] K. Schwarz, P. Blaha, and G. K. H. Madsen, "Electronic structure calculations of solids using the WIEN2k package for material sciences," *Computer Physics Communications*, vol. 147, no. 1–2, pp. 71–76, 2002.
- [25] H. J. Monkhorst and J. D. Pack, "Special points for Brillouin-zone integrations," *Physical Review B: Solid State*, vol. 13, no. 12, pp. 5188–5192, 1976.
- [26] J. P. Perdew, K. Burke, and M. Ernzerhof, "Generalized gradient approximation made simple," *Physical Review Letters*, vol. 77, no. 18, pp. 3865–3868, 1996.
- [27] W. H. Baur and A. A. Khan, "Rutile-type compounds—IV. SiO₂, GeO₂ and a comparison with other rutile-type structures," *Acta Crystallographica Section B*, vol. 27, pp. 2133–2139, 1971.
- [28] Z. G. Zhu, R. C. Deka, A. Chutia et al., "Enhanced gas-sensing behaviour of Ru-doped SnO₂ surface: a periodic density functional approach," *Journal of Physics and Chemistry of Solids*, vol. 70, no. 9, pp. 1248–1255, 2009.
- [29] X. D. Zhang, M. L. Guo, C. L. Liu et al., "First-principles investigation of electronic and optical properties in wurtzite Zn_{1-x}Mg_xO," *European Physical Journal B*, vol. 62, pp. 417–421, 2008.

Review Article

SnO₂-Based Nanomaterials: Synthesis and Application in Lithium-Ion Batteries and Supercapacitors

Qinqin Zhao, Lisha Ma, Qiang Zhang, Chenggang Wang, and Xijin Xu

School of Physics and Technology, University of Jinan, 336 Nanxin Zhuang West Road, Jinan, Shandong 250022, China

Correspondence should be addressed to Xijin Xu; sps_xuxj@ujn.edu.cn

Received 8 August 2014; Accepted 24 September 2014

Academic Editor: Chuanfei Guo

Copyright © 2015 Qinqin Zhao et al. This is an open access article distributed under the Creative Commons Attribution License, which permits unrestricted use, distribution, and reproduction in any medium, provided the original work is properly cited.

Tin dioxide (SnO₂) is an important n-type wide-bandgap semiconductor, and SnO₂-based nanostructures are presenting themselves as one of the most important classes due to their various tunable physicochemical properties. In this paper, we firstly outline the syntheses of phase-pure SnO₂ hierarchical structures with different morphologies such as nanorods, nanosheets, and nanospheres, as well as their modifications by doping and compositing with other materials. Then, we reviewed the design of SnO₂-based nanostructures with improved performance in the areas of lithium-ion batteries (LIBs) and supercapacitors.

1. Introduction

As one of the most important classes of materials, metal oxide semiconductor nanomaterials present themselves in various areas of science and technology, due to their shape- and size-dependent physical and chemical properties [1, 2]. Among various metal oxide nanomaterials, SnO₂ has become the foremost one, because of its wide applications in lithium batteries [3–6], supercapacitors [7–10], gas sensors [11, 12], and catalysis [13, 14]. Recently, reports on the applications of SnO₂ nanostructures mainly depend on their morphologies and structural features. Thus, considerable efforts have been devoted to synthesizing SnO₂ nanostructures with different morphologies, such as nanorods [15–17], nanowires [18–20], nanotubes [11], nanosheets [2, 21], and 3D nanospheres self-assembled from these low-dimensional nanostructures via interactions such as van der Waals forces, hydrogen, and covalent bonding [3, 22–24].

Various methods have been adopted for the preparation of nanoscaled SnO₂ nanostructures, such as hydrothermal route and template method. However, because the performance enhancement to meet the increasing requirements is still to be a challenge, then many researchers have established various ways to improve the performance of SnO₂-based materials, including doping [25, 26], synthesis of stannate nanomaterials [27], and constructing the heterojunctions

[28]. In this respect, development of suitable synthetic strategies has become crucial to achieve the desired properties.

In this review, we outline the synthetic strategies of phase-pure SnO₂ hierarchical structures and the approaches to enhance the performance. The applications of hierarchical SnO₂-based nanostructures in lithium-ion batteries and supercapacitors are also reviewed. By focusing on the hierarchical SnO₂-based nanostructures, we hope to provide a better understanding on their physicochemical properties and the design principles when used in energy conversion and energy storage and further explore the new possibilities to advance the future research.

2. SnO₂-Based Nanomaterials

2.1. Phase-Pure SnO₂ Nanostructures. Many researchers have devoted their efforts to manipulate the structures and morphologies of SnO₂ in order to improve the performances and widen their applications. Two kinds of synthesis strategies have generally been explored as follows.

(1) Hydrothermal Method. Hydrothermal method has been paid much attention, due to its simplicity, low cost, high efficiency, and convenient manipulation combined with flexible control over the sizes and morphologies of the resulting nanostructures [9, 11, 17, 23, 24], in which aqueous solution

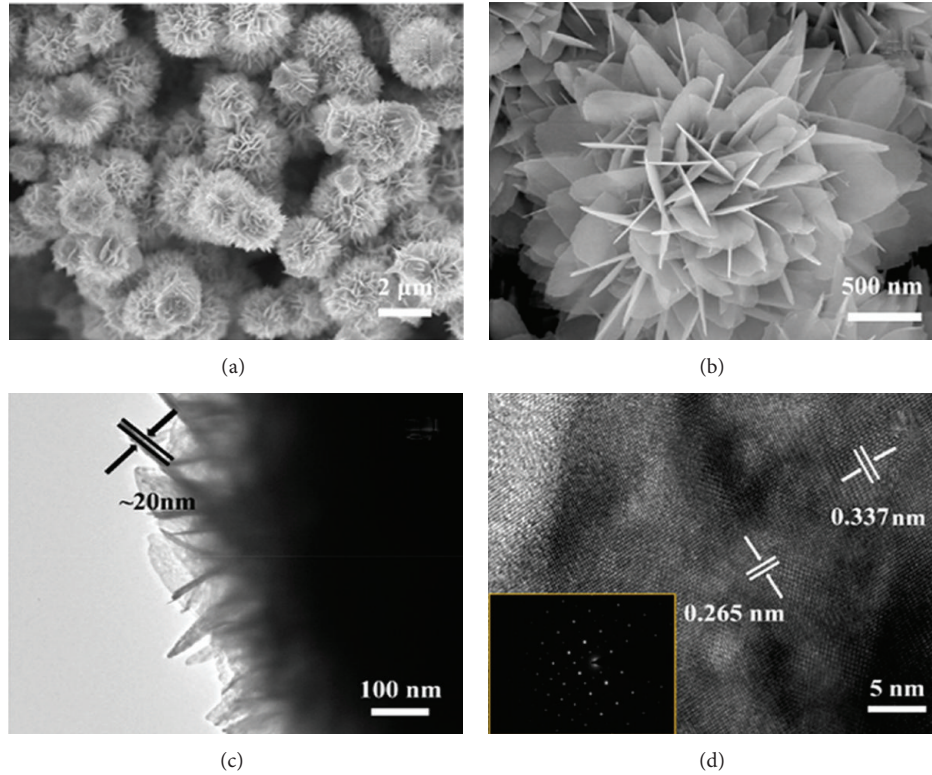
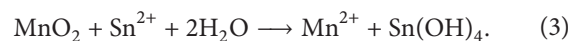
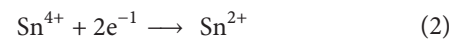
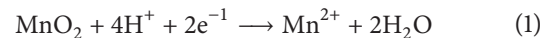


FIGURE 1: (a)-(b) FESEM images, (c) low-magnification TEM image, and (d) high-resolution TEM (HRTEM) image of the prepared hierarchical SnO₂ nanostructures. Inset in d exhibits the typical corresponding SAED pattern adapted from [2] with permission.

is used as the reaction medium, to create a high temperature and high pressure reaction environment by heating the reaction vessel to a certain temperature. In 2004, Cheng et al. [16] synthesized single-crystalline SnO₂ nanorods with diameter of about 5 nm and length of about 20 nm. Furthermore, many researchers developed the method and synthesized different SnO₂ architectures by adjusting the precursors and experimental conditions [2, 11, 17]. For example, SnO₂ hollow microspheres composed of SnO₂ nanoparticles have been synthesized [29]. Recently, Liu et al. [2] developed a facile approach to fabricate hierarchical SnO₂ nanosheets, using SnCl₂·2H₂O as tin source and sodium citrate as controlling agents. The ultrathin nanosheets with a thickness of about 20 nm are shown in Figures 1(a) and 1(b), which corresponds to the TEM image of Figure 1(c). The HRTEM image (Figure 1(d)) exhibits the well-defined lattice fringes combined with the SAED pattern. Their growth mechanism is generally summarized in Figure 2 [2, 30]. First of all, SnO₂ nanocrystals were formed due to the hydrolysis of SnCl₂, whereas in the second step, the grown small SnO₂ nanoparticles are further assembled with each other to form nanosheets because of the “oriented attachment” growth process. Subsequently, the fast oriental attachment of the SnO₂ nanoparticles results in the formation of SnO₂ nanosheets. Moreover, the new formed particles would spontaneously “land” on the as-formed sheets and further grow to another sheet, which led to the formation of flower-like SnO₂ architectures.

(2) *Template Method.* Template-based methods offer many advantages, including simplicity, low cost, and narrow size

distribution [11]. However, there are some limitations. For example, the post treatment process of the templates always damages the nanoarchitectures, and it is difficult to remove the template and limit the ability to produce large-scaled nanomaterials. Generally, templates such as silica nanorods [31], MoO₃ nanorods [32], and carbon nanotubes [33] can be removed through calcination at high temperature (e.g., to remove carbon or polystyrene spheres), or chemical dissolution (e.g., use of hydrofluoric acid to remove silica templates), which may result in collapse of some fraction of the hollow structures [34, 35]. Therefore, it is highly desirable to develop new strategies for synthesizing hollow SnO₂ nanostructures. Zhang et al. [11] developed a reactive-template method to fabricate porous SnO₂ nanotubes using MnO₂ nanorods as the sacrificial template. The overall synthesis procedure is illustrated in Figure 3, which is based on the redox chemistry between reductive Sn²⁺ and oxidative MnO₂ in an acidic environment. Chemical reactions for the formation of SnO₂ nanotubes included in a basic aqueous solution are shown in (1)–(3):



When the MnO₂ nanorods are completely dissolved because of reduction, then the Sn(OH)₄ nanotubes with a hollow interior are eventually formed. Finally, porous SnO₂

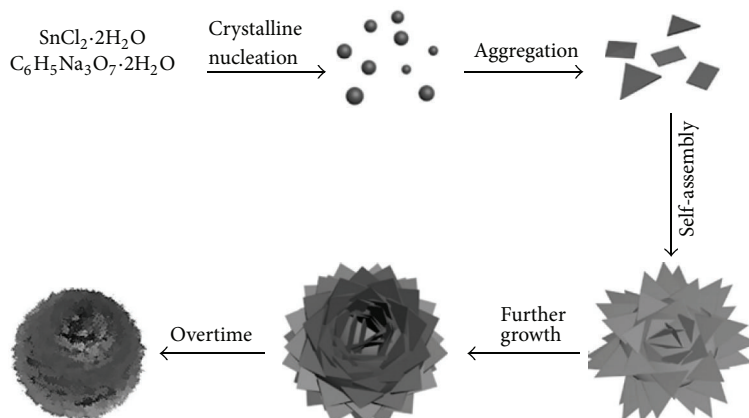


FIGURE 2: Schematic for the possible growth of the as-synthesized hierarchical SnO_2 nanostructures adapted from [2] with permission.

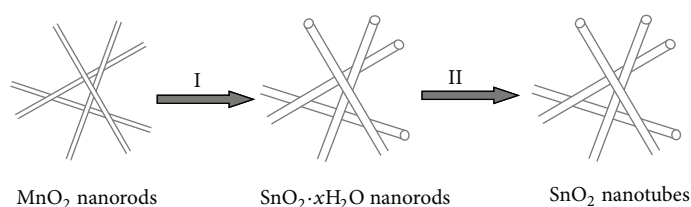
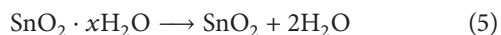


FIGURE 3: Synthesis process for SnO_2 nanotubes via a reactive-template strategy adapted from [11] with permission.

nanotubes were obtained by annealing the product at 500°C for 2 h ((4)-(5)):



The morphologies of the MnO_2 nanorods and the as-prepared SnO_2 nanotubes (Figures 4(a), 4(b), and 4(c)) exhibit their 1D structure. The SnO_2 nanotubes show a rough surface because the tube walls are composed of many nanoparticles with a size in the range of 5–15 nm (Figures 4(d) and 4(e)). The hollow porous structure of the nanotubes is also visible, as indicated by the dashed lines in Figures 4(d) and 4(e). The pore-size distribution (inset of Figure 4(f)) calculated using the Barrett-Joyner-Halenda (BJH) method for both the adsorption and desorption branches of the isotherm indicates that most of the pores have a diameter in the range of 2–6 nm. Such porous structure leads to a Brunauer-Emmett-Teller (BET) specific surface area of $66.1 \text{ m}^2/\text{g}$.

Wang et al. [36] fabricated SnO_2 nanorods that consisted of SnO_2 hollow microspheres via the soft template relying on the use of $(\text{CH}_2)_6\text{N}_4$ and demonstrated that it is a nontoxic, water-soluble method to prepare the hollow structure under the hydrothermal treatment.

(3) *Other Synthesis Methods.* Besides the above-mentioned methods, there are many other approaches for the fabrication of SnO_2 -based nanostructures. Spray pyrolysis is a process for preparing particles or films by forming droplets from a precursor solution and then evaporating and decomposing

them in a reactor. This process has proven to be quite useful for the preparation of various nanostructure and composite particles, as is shown in Figure 5, with many reports onto the effect of the main variables on particle formation [37]. Hong et al. [38] prepared Pd-loaded double-shelled SnO_2 yolk-shell spheres by one-step spray pyrolysis. Patil et al. [39] synthesized high-purity nanostructured SnO_2 powders through spray pyrolysis. Ju et al. [40] reported the use of spray pyrolysis to produce SnO_2 powders with uniform morphology and narrow size distribution. In addition, others method are also used to synthesize SnO_2 -based nanostructures. Yan et al. [41] synthesized the hierarchical SnO_2 hollow spheres by two layers of tetragonal prism nanorod arrays, formed on the surface of self-generated NO bubbles in the aqueous solution. This method is promising in the design of the hollow structures without further heat treatment. Dai et al. [18] synthesized SnO_2 nanowires, sandwiched nanoribbons, and nanotubes by high temperature thermal oxide method. Chen et al. [15] reported that SnO_2 nanorod arrays were synthesized in a ternary solvent system comprising acetic acid, ethanol, and water using SnCl_4 as the Sn source and NaBr as the additive. The growth of SnO_2 crystals was carefully controlled in the mixed solvents, leading to the exclusively heterogeneous nucleation on a substrate and finally the mesocrystalline nanorod arrays were obtained. Most of the above methods are illustrated in Table 1.

2.2. *Doped Hierarchical SnO_2 Nanostructures.* Doping of oxide nanomaterials is a general approach to tailor their electrical and optical properties. Thus, many efforts have been carried out to improve the performance of the materials

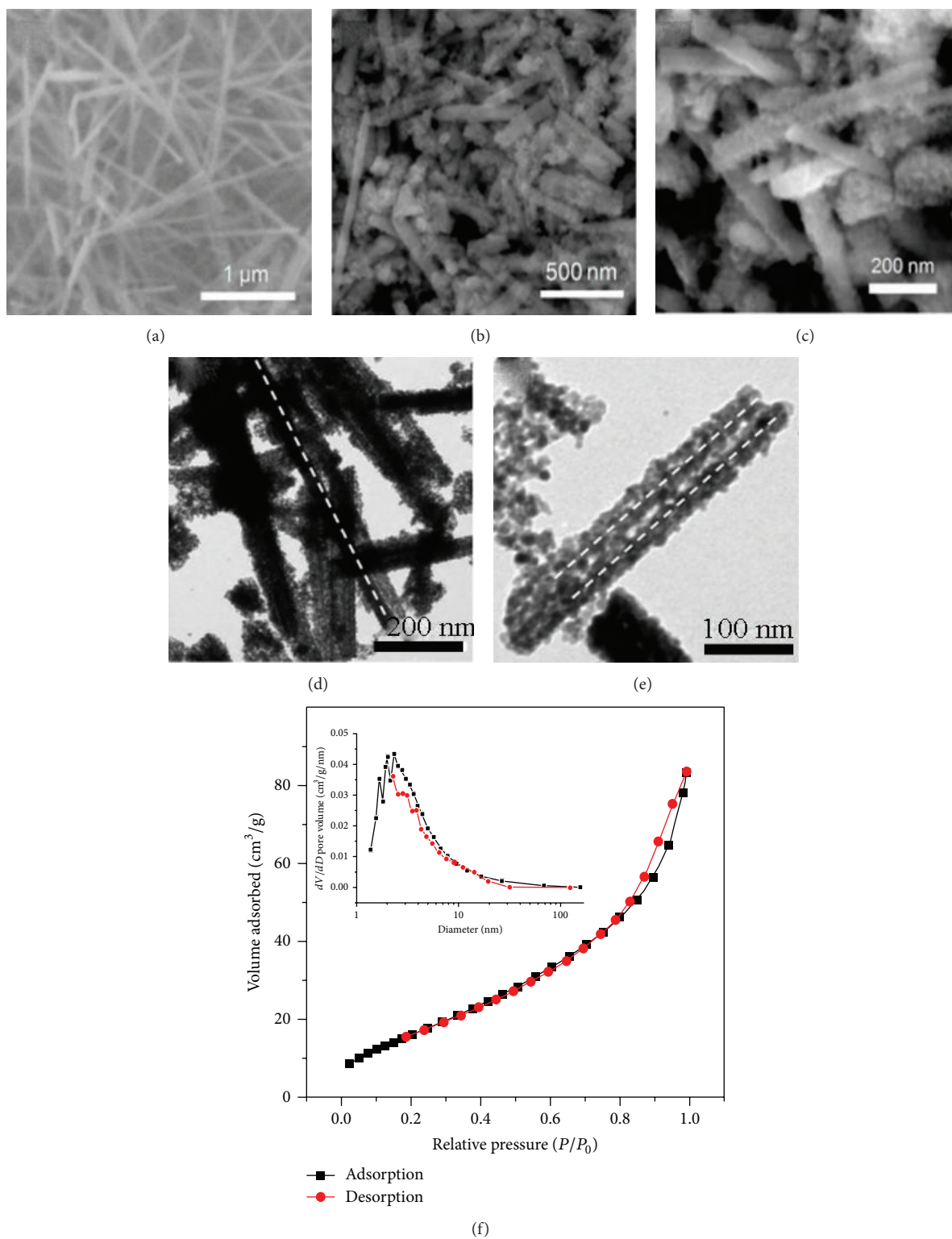


FIGURE 4: SEM images of (a) MnO₂ nanorods and ((b), (c)) SnO₂ nanotubes. ((d), (e)) TEM images of SnO₂ nanotubes. (f) N₂ adsorption-desorption isotherm with the BJH pore-size distribution in the inset, adapted from [11] with permission.

TABLE 1: Summary of various methods for SnO₂-based nanostructure synthesis.

Structure type	Method	Matrix	Growth reagent	Growth condition	Reference
SnO ₂ nanosheets	Hydrothermal method	In solution	SnCl ₄ ·2H ₂ O, C ₆ H ₅ Na ₃ O·2H ₂ O ethanol, water	Autoclave 180°C, 8 h	[2]
3D SnO ₂ nanoflowers	Hydrothermal method	Ti foil	SnCl ₄ ·5H ₂ O, NaOH, water	Autoclave 200°C (2, 4, 8, 16 h)	[9]
Zn-doped SnO ₂ nanorods	Hydrothermal method	In solution	SnCl ₄ ·5H ₂ O, ZnCl ₂ , NaOH, ethanol, water	Autoclave 200°C, 24 h	[14]
Single-crystalline SnO ₂ nanorods	Hydrothermal method	In solution	SnCl ₄ ·5H ₂ O, alcohol, water	Autoclave 150°C, 24 h	[16]
SnO ₂ hollow microspheres	Hydrothermal method	In solution	SnCl ₄ ·5H ₂ O, carbamide, water	Autoclave 160°C, 16 h	[29]
Porous SnO ₂ nanotubes	Template method	In solution	MnSO ₄ ·H ₂ O, SnCl ₄ ·2H ₂ O, HCL	Autoclave 160°C, 12 h	[11]
SnO ₂ hollow microspheres	Template method	In solution	SnCl ₂ , H ₂ O ₂ , NaOH, (CH ₂) ₆ N ₄	Autoclave 200°C, 30 h	[36]
Pd-Loaded SnO ₂ Yolk-Shell nanostructures	Spray pyrolysis	Spray solution	C ₂ O ₄ Sn, Pd(NO ₃) ₂ ·xH ₂ O, C ₁₂ H ₂₂ O ₁₁ , HNO ₃	Air flow rate 10 Lmin ⁻¹ , 1000°C	[38]
SnO ₂ nanoparticles	Spray pyrolysis	Spray solution	SnCl ₄ ·5H ₂ O	Air flow rate 17 kg/m ² , 673 K and 1073 K	[39]
SnO ₂ powders	Spray pyrolysis	Spray solution	SnCl ₄ ·5H ₂ O, citric acid, ethylene glycols	Gas flow rate 40 L/min, 900°C	[40]
Tin Oxide nanowires, nanoribbons, and nanotubes	High temperature thermal oxide method	Gas	Sn foil + SnO-layered N ₂ flow gas	Lindberg blue tube furnace configuration 1050–1150°C	[18]

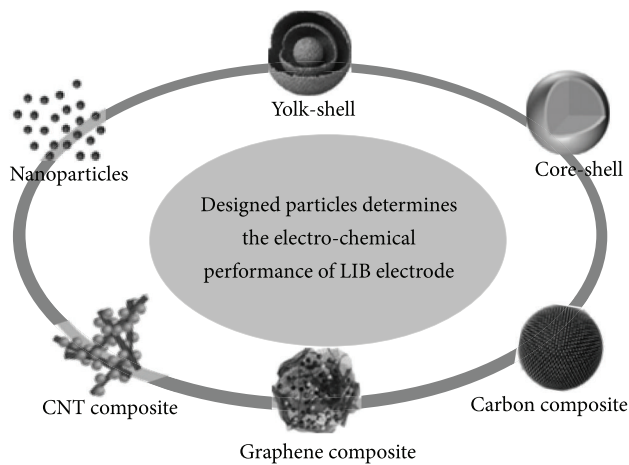


FIGURE 5: Various nanostructure and composite particles prepared by spray pyrolysis adapted from [37] with permission.

by doping other elements. For example, Yin and Guo [42] prepared Fe-doped SnO₂ gas sensor for CO detection, and the response value of the composite material to 2000 ppm CO was raised 13 times than that of pure SnO₂. Turgut et al. [43] synthesized Mo/F double doped SnO₂ films and obtained the best electrical and optical properties. In relation to SnO₂ nanostructures, doping with element Zn has been paid more attention by several groups [14, 44–46]. As previous reports

[2, 44], Sn(IV) would form Sn(OH)₆²⁻ ions in highly alkaline solution and then undergo decomposition to obtain SnO₂ nuclei. After introduction of Zn²⁺ into the reaction mixture, different morphologies of Zn-doped SnO₂ nanostructures can be formed. Jia et al. [44] synthesized Zn-doped SnO₂ hierarchical architectures assembled by nanocones via a solvothermal approach. Li et al. [47] reported that Zn-doped SnO₂ nanostructures are composed of dense SnO₂ nanowires with growth orientation along the (101) direction. Huang et al. [14] modified the morphologies and properties of the flower-like single-crystalline SnO₂ nanorods by Zn doping in a facile hydrothermal synthesis route without any complex or toxic organic reagents. After Zn doping, the morphology changed from nanorods with a constant diameter (Figures 6(a) and 6(b)) to needle-like nanorods (Figures 6(c) and 6(d)). The needle-like nanorods are of smooth surfaces and rectangular cross section with a diameter of 30–50 nm and a length up to several hundred nanometers. The lattice spacing of crystallographic planes marked in the image (Figure 6(f)) has been measured to be 0.35 nm and 0.27 nm, respectively, corresponding to the (110) and (101) planes of rutile SnO₂. In addition, doping of other elements, such as Co and Fe, was also synthesized by a chemical route using polyvinyl alcohol as surfactant [23]. Moreover, Wang et al. [48] have reported the synthesis of hierarchical SnO₂ nanoflowers using NaF as the morphology-controlling agent and SnCl₄·2H₂O as the tin source. This resulted in the simultaneous Sn²⁺ self-doping of SnO₂ nanostructures and led to the formation of tunable

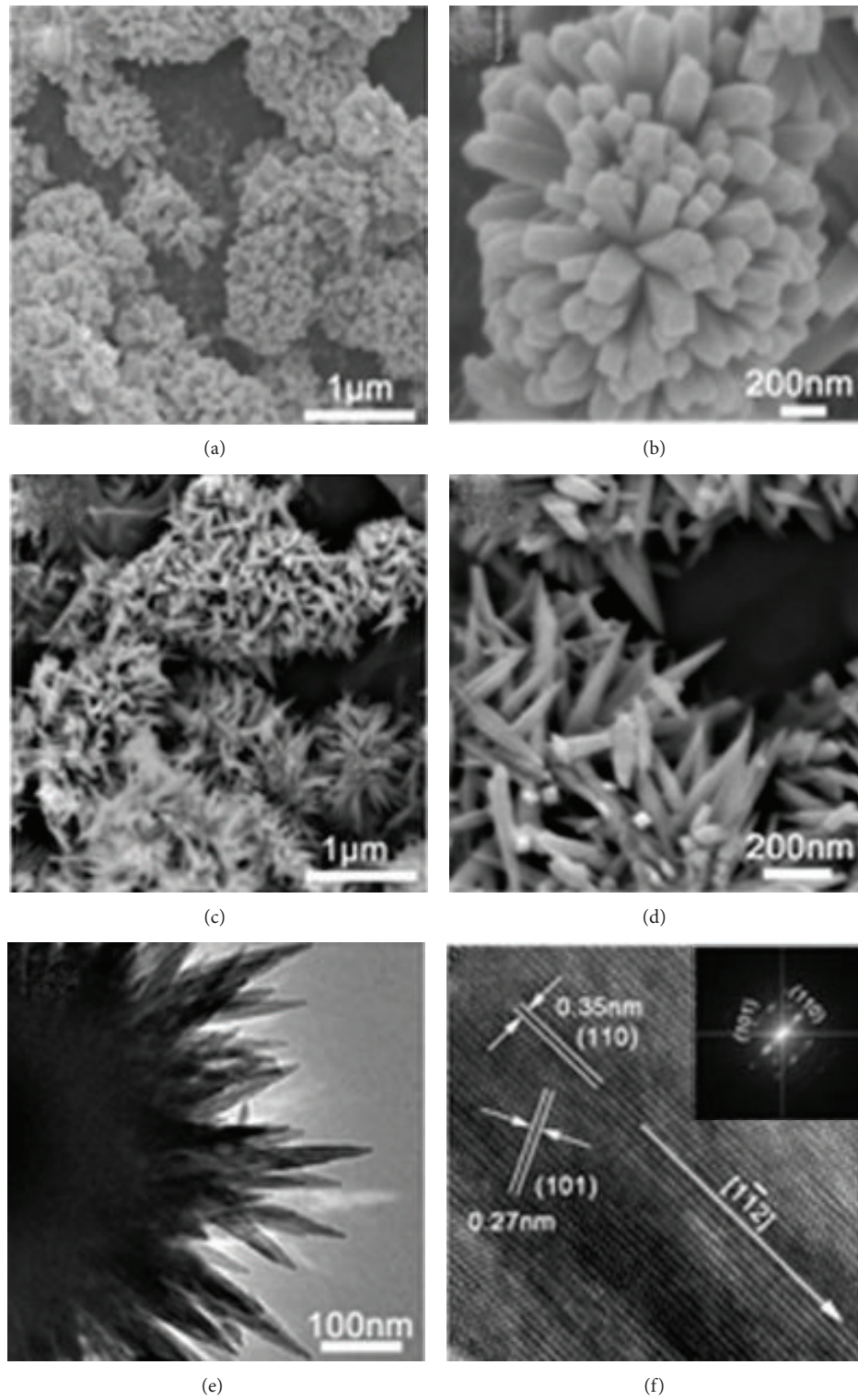


FIGURE 6: SEM and TEM images of pure SnO₂ nanorods and Zn-doped SnO₂ nanorods. ((a), (b)) SEM image of pure SnO₂ nanorods, ((c), (d)) SEM image of Zn-doped SnO₂ nanorods, (e) TEM image, and (f) HRTEM image of a typical nanorod. Inset in (f) is the fast Fourier transform (FFT) of the HRTEM image adapted from [14] with permission.

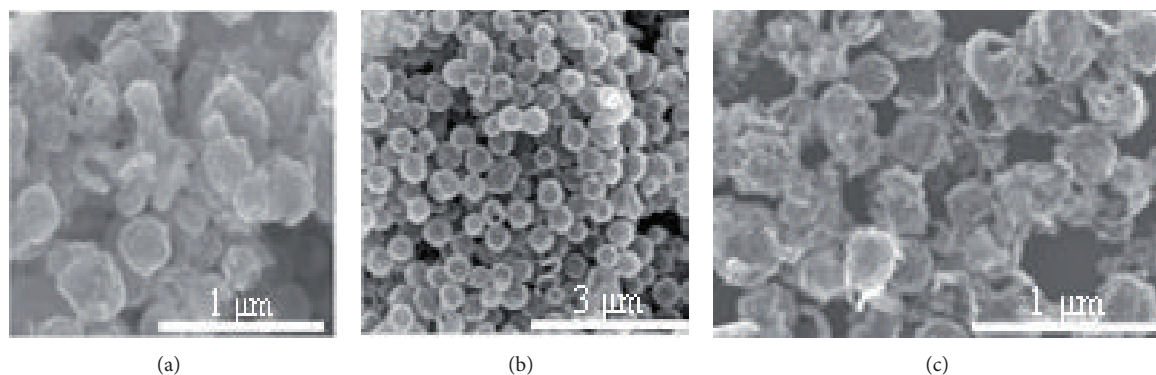


FIGURE 7: SEM images of $\text{WO}_3\text{-SnO}_2$ HNS nanocomposites with different added amounts of Na_2SnO_3 , (a) 0.2 mmol, (b) 0.5 mmol, and (c) 1 mmol adapted from [52] with permission.

oxygen vacancies bandgap states and the corresponding shifting in the semiconductor Fermi levels and further extended absorption in the visible spectral range.

2.3. SnO_2 -Based Nanocomposites. Recently, many researchers have reported the fabrication of sensitized semiconductor by noble metal particles or the formation of semiconductor heterojunction, in which the performance can be greatly improved. Chung et al. [49] synthesized Au@ZnO core-shell structure for gaseous formaldehyde sensing at room temperature. The sensor response of the Au@ZnO core-shell structure was enhanced to 10.57 from 1.91 of the pure ZnO. Ju et al. [28] prepared NiO/ZnO PN heterojunction TEA gas sensor and the response is much higher than that of pure ZnO nanosheet sensor and other reported oxide chemiresistive gas sensors. Herein, SnO_2 -based nanocomposites have been actively pursued in order to improve their performance in gas sensors [50, 51], dye-sensitized solar cells [47], and so on. Li et al. [51] prepared the composites of SnO_2 nanocrystal/graphene-nanosheets on the basis of the reduction of graphene oxide (GO) by Sn^{2+} ion. The morphologies of SnO_2 /graphene-nanosheets composites were changed with different ratios of Sn^{2+} and GO. Li et al. [52] synthesized $\text{WO}_3\text{-SnO}_2$ hollow nanospheres by hydrothermal process with a diameter and thickness of about 550 nm and 30 nm, respectively. The influence of the Na_2SnO_3 concentrations on the morphologies of nanocomposites was investigated due to its alkaline nature Na_2SnO_3 which may control the hydrolysis degree of Na_2WO_4 , as shown in Figure 7. When the reaction was carried out with 0.2 mmol Na_2SnO_3 , a small number of nanospheres coexisted with irregular aggregates of nanoparticles (Figure 7(a)). As the amount of Na_2SnO_3 was increased to 0.5 mmol, the obtained product consisted of large nanospheres (Figure 7(b)). However, particles aggregated without an orderly shape were collected when the amount of Na_2SnO_3 increased to 1 mmol, as shown in Figure 7(c).

Besides, the composites of SnO_2 nanostructures with other materials such as Fe_2O_3 , CuO , and ZnO have also been reported. Liu et al. [53] demonstrated the growth of $\text{Fe}_2\text{O}_3@\text{SnO}_2$ nanoparticle decorated graphene flexible films. Choi et al. [54] prepared CuO -loaded SnO_2 hollow spheres by

ultrasonic spray pyrolysis. Moreover, ZnO-SnO_2 nanocomposites have been also investigated in some reports [55, 56].

2.4. Stannate Nanomaterials. Stannate nanomaterials like ZnSnO_3 [57, 58], Zn_2SnO_4 [59, 60], and CdSnO_3 [61] have also attracted much more attention for higher reversible capacities, low cost, easy preparation, and especially various morphologies [58–61]. Wang et al. [61] synthesized highly porous CdSnO_3 nanoparticles using citric acid (Figure 8) and applied it as an anode material for rechargeable LIBs. It can be seen that there was a sharp contrast between the bright cavities and dark edges, which further confirmed the formation of the porous structure (Figures 8(a), 8(b), and 8(c)). For the CdSnO_3 nanoparticles, the HRTEM images showed lattice fringes spacing of *ca.* 0.1996 nm, corresponding to the (024) planes of rhombohedral-phase CdSnO_3 (Figure 8(d)).

Zn_2SnO_4 have also drawn much attention as anode materials [27]. Zhao et al. [62] fabricated monodispersed hollow Zn_2SnO_4 boxes by the simple coprecipitation and alkali etching way. The hollow boxes exhibit an electrochemical performance with high capacity and good cycling stability than the solid cubes and those reported. Wang et al. [60] prepared flower-like Zn_2SnO_4 composites through a green hydrothermal synthesis, in which the flower-like Zn_2SnO_4 structures are composed of several 1D Zn_2SnO_4 nanorods. These structures generally consist of several sharp tips branching out in three dimensions with large surface area. Duan et al. [58] fabricated amorphous ZnSnO_3 hollow nanoboxes for the first time in a large scale by a facile alkaline solution etching method.

3. Applications of SnO_2 -Based Nanomaterials

3.1. Lithium-Ion Batteries. In order to address both energy and power demands, there is an urgent need to develop clean energy sources systems. Herein, LIBs have attracted widespread attention because of their high energy density, high power, smooth discharge, and light weight as well as being environment friendly [63]. The electrode's material is one of the key components for perfecting LIBs. It plays a crucial role in establishing the overall properties of the

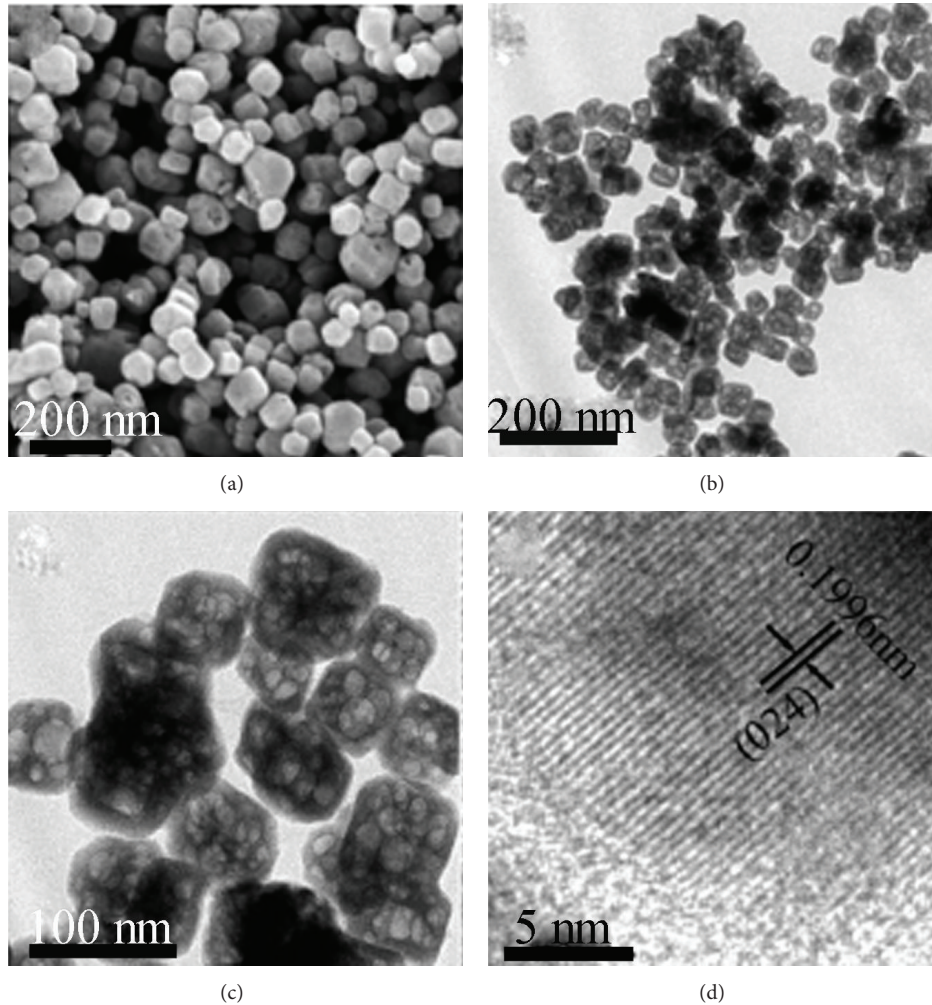


FIGURE 8: SEM and TEM images of CdSnO_3 : (a) an SEM image, (b) low-magnification and (c) high-magnification TEM images, and (d) HRTEM image, adapted from [61] with permission.

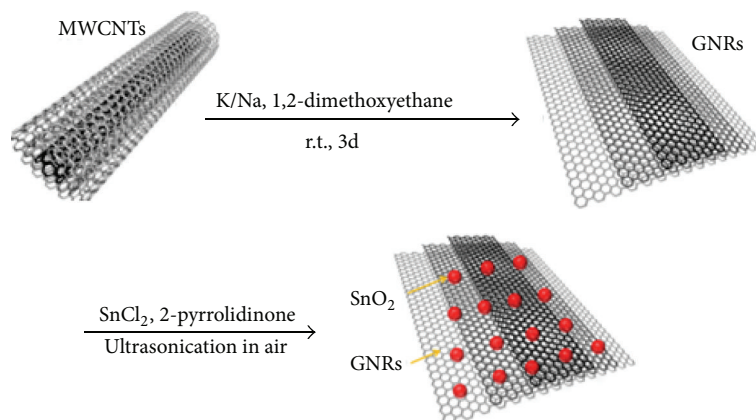


FIGURE 9: Scheme for the synthesis of the GNRs/ SnO_2 composite, adapted from [78] with permission.

battery. SnO_2 has been demonstrated to be one of the most promising anode materials for high performance LIBs [33, 64–66], due to its high theoretical specific storage capacity

(782 mAh/g), compared with the commercially used graphite (372 mAh/g) [67, 68]. The mechanism of LIBs for SnO_2 is based on the alloying/dealloying processes, which are the

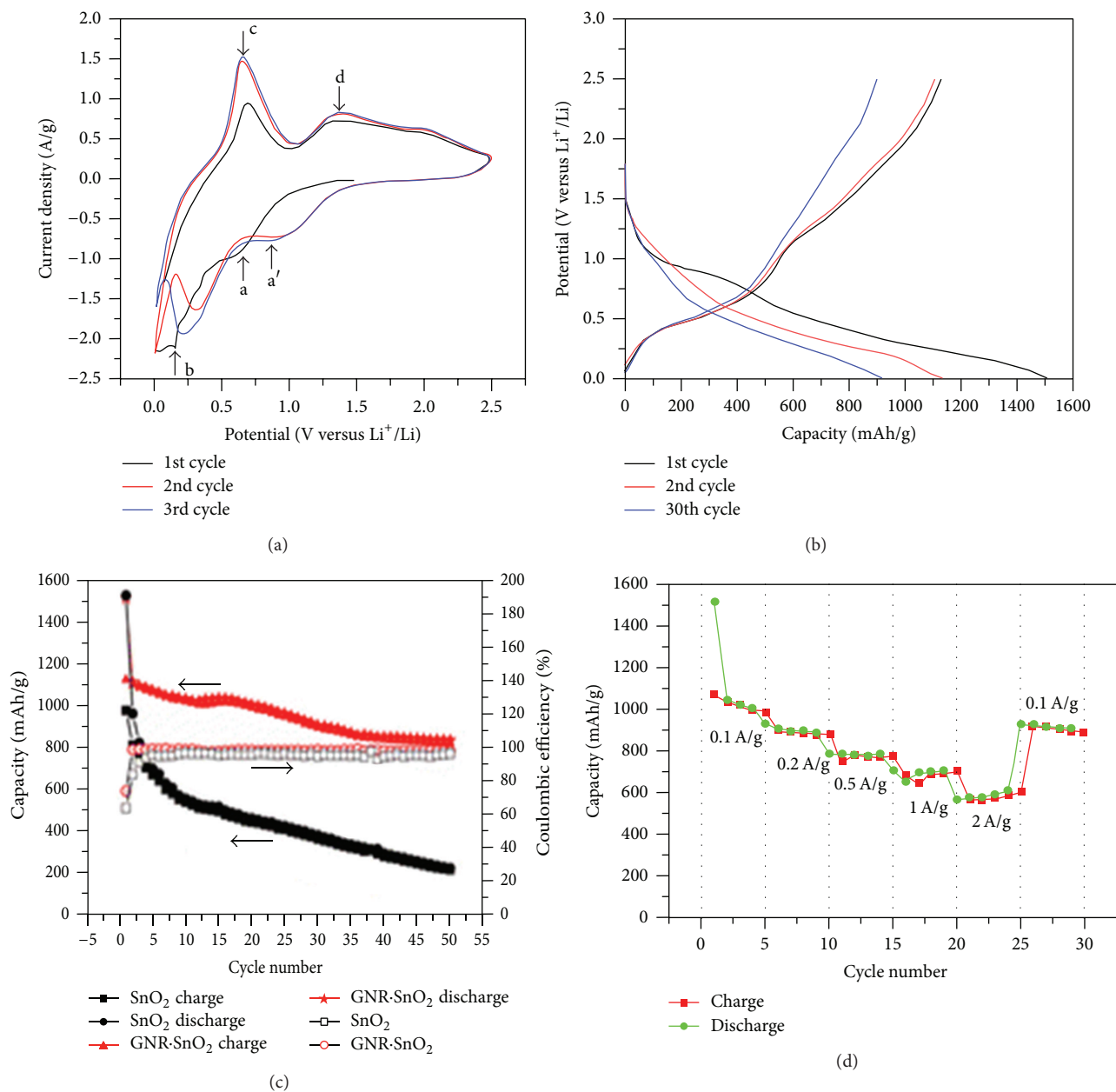
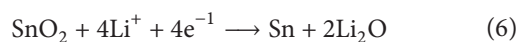


FIGURE 10: The electrochemical performance of the GNRs/SnO₂ composite electrodes. The specific capacities are calculated based on the total mass of the GNRs/SnO₂ composite in the anode electrodes: (a) CV curves of the first, second, and third cycles of the composite electrodes at a scan rate of 0.5 mV/s over the voltage range of 0.01~2.5 V. (b) The first, second, and 30th charge/discharge curves of the composite electrode at a rate of 100 mA/g. (c) Comparison of capacity retention and Coulombic efficiency of GNRs and the GNRs/SnO₂ composite at a rate of 100 mA/g. (d) Rate capability of the composite electrodes with various current densities adapted from [78] with permission.

intrinsic driving force for the electrochemical activity [68, 69]:



However, the lithiation/delithiation process often induces the large volume expansion and further causes pulverization. This will lead to severe internal strain, cracking, and blocking of the electrical contact pathways in the electrodes, which

result in their rapid deterioration and low retention of the electrical capacity [70, 71]. To overcome the above problems, many efforts have been carried out to optimize the structures, compositions, and morphologies of SnO₂-based materials, such as 0D nanoparticles [64, 72], 1D nanowires [73], 2D nanosheets [35], and the doping [74, 75] or composition [76] with other materials.

Wu et al. [22] reported that hierarchical SnO₂ nanostructures that consist of SnO₂ nanosheets exhibit superior reversible capacities (discharge capacity of 516 mAh/g) and

cyclic capacity retention (80%) after 50 cycles at a current rate of 400 mA/g, which is much higher than that of commercial SnO₂ nanoparticles (286 mA/g, 48% retention). This can be ascribed to its stable porous structure. The high porosity, short transport paths of SnO₂ nanosheets, and the interconnections between the individual building blocks of such hierarchical structures endow those promising candidates as anode materials for LIBs. Wang et al. [77] fabricated N-doped G-SnO₂ sandwich papers. The sandwich structure not only assures solid contact between the SnO₂ particle and the graphene layer, but also facilitates high electrode conductivity and renders the elastomeric space needed to accommodate the volume changes of SnO₂. When this material is used in LIBs, it exhibits a very large capacity, high rate capability, and excellent cycling stability. All the excellent electrochemical performances of this material with respect to commercial SnO₂ nanoparticles can be attributed to the structural features that provide a large number of surface defects induced onto the graphene by N-doping, excellent electronic conductivity, short transportation length for both lithium ions and electrons, and enough elastomeric space to accommodate volume changes upon Li insertion/extraction. Lin et al. [78] synthesized a composite made from graphene nanoribbons (GNRs) and SnO₂ nanoparticles used as the anode material for LIBs. The synthesis route of the GNRs/SnO₂ composite is illustrated in Figure 9. First, the GNRs were obtained using K/Na alloy to unzip the MWCNTs. Then, SnCl₂ and 2-pyrrolidinone were added into the GNRs with ultrasonication for reducing Sn²⁺ to Sn⁰. Lastly, the Sn NPs were oxidized overnight using ultrasonication in air. The CV curves of the initial three cycles show the reversibility of the composite electrode charge/discharge process, as shown in Figure 10(a). The composite, as an anode material for LIBs, exhibits reversible capacities of over 1520 and 1130 mAh/g for the first discharge and charge, respectively, which is more than the theoretical capacity of SnO₂ (Figure 10(b)). The reversible capacity retains ~825 mAh/g at a current density of 100 mA/g with a Coulombic efficiency of 98% after 50 cycles (Figure 10(c)). Furthermore, the composite shows good power performance with a reversible capacity of ~580 mAh/g at the current density of 2 A/g, as shown in Figure 10(d). The high capacity and good power performance and retention can be attributed to uniformly distributed SnO₂ NPs along the high-aspect-ratio GNRs. The GNRs act as conductive additives that buffer the volume changes of SnO₂ during cycling. This work provides a starting point for exploring the composites made from GNRs and other transition metal oxides for lithium storage applications.

Besides, Yang et al. [79] synthesized SnO₂/graphene nanosheet nanocomposite as an anode material for LIBs. The SnO₂-In₂O₃/GNS nanocomposite exhibits obvious enhancement electrochemical performance in terms of lithium storage capacity (962 mAh/g at 60 mA/g rate), initial Coulombic efficiency (57.2%), cycling stability (60.8% capacity retention after 50 cycles), and rate capability (393.25 mAh/g at 600 mA/g rate after 25 cycles) compared to SnO₂/GNS and pure SnO₂-In₂O₃ electrode.

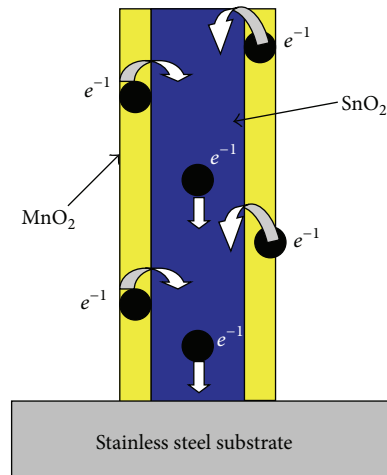


FIGURE 11: Schematic image of the amorphous MnO₂ loaded on the SnO₂ nanowires grown on the stainless steel substrate. The SnO₂ nanowire provides a direct path for the electrons adapted from [90] with permission.

3.2. *Supercapacitors.* Supercapacitors, also called electrochemical capacitors, have been known for over than fifty years and considered as one of the most promising energy storage devices for a wide range of uninterruptible power supplies and civilian and military applications in electric vehicles [80–82]. In contrast to conventional capacitors and LIBs, supercapacitors possess much higher energy density and also exhibit higher specific power. Up to now, there are mainly three kinds of electrode materials for supercapacitors which are as follow: metal oxides, carbon, and conducting polymers [83–86]. Due to low cost and environmental compatibility consideration, metal oxide candidates with good capacitive values have attracted much attention [87].

SnO₂-based supercapacitors have been paid significant attention due to their high electrochemical capacitor (EC) and chemical stability [88, 89]. Yan et al. [90] synthesized SnO₂/MnO₂ composite for the application of supercapacitor electrodes. The prepared process was shown in Figure 11. This nanostructure has several advantages: (1) a thin layer of MnO₂ would enable a fast, reversible faradic reaction and would provide a short ion diffusion path; (2) SnO₂ nanowires, with high conductivity, would provide a direct path for the electrons transport; and (3) SnO₂ nanowires would create channels for the effective transport of electrolyte. Based on the above, it exhibited a specific capacitance (based on MnO₂) as high as 637 F g⁻¹ at a scan rate of 2 mVs⁻¹ (800 F g⁻¹ at a current density of 1 A g⁻¹) in 1M Na₂SO₄ aqueous solution (Figure 12(a)). Temperature is an important influence factor on supercapacitor cells. It is valuable to evaluate the capacitive behavior of SnO₂/MnO₂ composites at various temperatures. Figure 12(b) shows the specific capacitance obtained at different temperatures and scan rates. It can be seen obviously that the specific capacitance and rate capability increase with the increase of temperature. This is attributed to the decrease of effective internal resistance with increasing temperature. The energy density

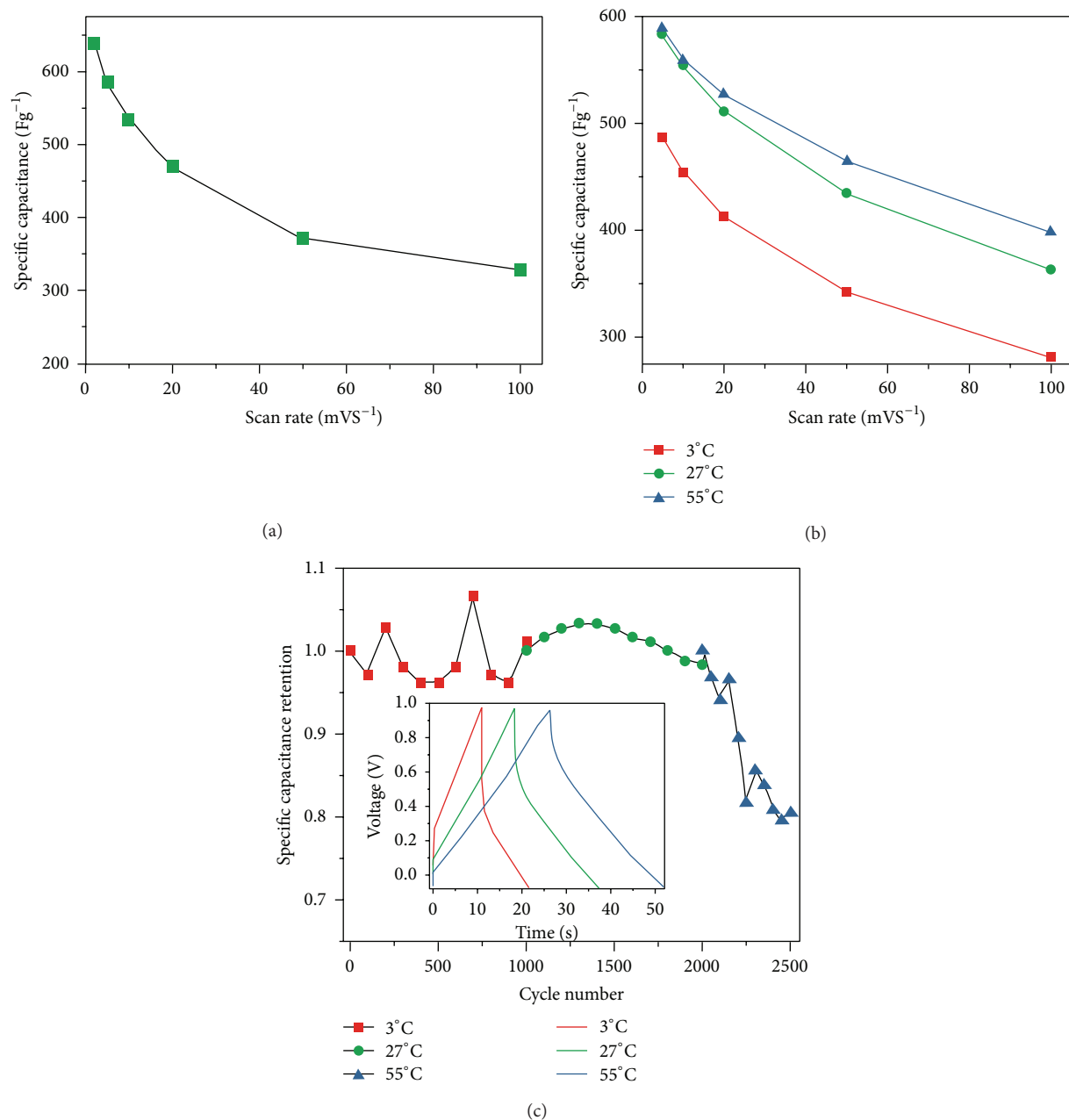


FIGURE 12: (a) Plotted curve of the variation in the specific capacitance of the SnO₂/MnO₂ composites as a function of the scan rate. (b) Specific capacitance obtained at different scan rates at 3, 27, and 55°C. (c) Curve showing long-term stability as a function of the cycle number tested by constant current charge/discharge method (current density of 20 A g⁻¹), which was carried out continuously at 3 ± 1°C (ice water bath) and then at 27°C (room temperature) and finally at 55 ± 2°C (water bath). The inset shows the first cycle of charge/discharge curves at different temperatures at a high current density of 20 A g⁻¹ adapted from [90] with permission.

and power density measured at 50 A g⁻¹ are 35.4 Wh kg⁻¹ and 25 kW kg⁻¹, respectively, demonstrating a good rate capability. After that, the SnO₂/MnO₂ composite electrode shows an excellent long-term cyclic stability (less than 1.2% decrease of the specific capacitance is observed after 2000 CV cycles), as shown in Figure 12(c). Li et al. [89] fabricated Fe₃O₄@SnO₂ core-shell nanorods. The hybrid nanorod film displayed well-defined electrochemical features in Na₂SO₄ aqueous electrolyte, charging/discharging within seconds

and with much higher areal capacitance (7.013 mF cm⁻² at 0.20 mA cm⁻²) than pristine Fe₃O₄ nanorod film. In addition, the PANI/SnO₂ composite electrode exhibited specific capacitance of 173 F g⁻¹ at a scan rate of 25 mV s⁻¹ [8, 91]. Bao et al. [92] designed Zn₂SnO₄/MnO₂ core/shell nanocarbon microfiber hybrid composites for high-performance supercapacitor electrodes. The hybrid composite exhibited excellent rate capability with specific energy of 36.8 Wh/kg and specific power of 32 kW/kg at current density of 40 A/g,

respectively, as well as good long-term cycling stability (only 1.2% loss of its initial specific capacitance after 1000 cycles).

Moreover, compared with other materials, graphene has been used as the electrode of electrochemical supercapacitors (ESCs), due to its good capacitive performance, superior conductivity, large surface-to-volume ratio, and suitable pore size distribution [93]. As we know, carbon and metal oxide materials are two hotspots as electrode materials for electrochemical supercapacitors (ESCs), in which energy can be stored due to the formation of an electrical double layer at the interface of the electrode. If integrating the above two kinds of materials into the electrodes of ESCs, their capacitive performance will be greatly enhanced because most of the metal oxide can contribute pseudo-capacitance to the total capacitance apart from the double-layer capacitance from carbon materials [94–96]. Thus, combined SnO₂ with graphene for the supercapacitors can obviously enhance the performance of capacitance. Li et al. [51] synthesized SnO₂/graphene (SnO₂/G) nanocomposites by a facile solvent-based synthesis route based on the oxidation-reduction reaction. The electrochemical performance of SnO₂/graphene showed an excellent specific capacitance of 363.3 F g⁻¹, which was five-fold higher than that of the as-synthesized graphene (68.4 F g⁻¹). El-Deen et al. [97] fabricated graphene/SnO₂ nanocomposite which exhibited high specific capacitance (323 F g⁻¹), excellent cycling stability, very good salt removal efficiency (83%), and distinct electrosorptive capacity of 1.49 mg g⁻¹.

4. Conclusion

In this paper, we discussed the synthesis of phase-pure SnO₂ hierarchical structures with different morphologies including nanoparticles, nanorods, nanosheets, nanosphere, and the porous and hollow structures. We also reviewed their modifications by doping and compositing with other materials and synthesis of stannate nanomaterials. Reaction parameters such as the chemical state of the tin precursors (Sn(IV) versus Sn(II) salts), concentration, additives, and solvents play an important role in adjusting their morphologies. SnO₂-based nanostructures, such as anode materials, demonstrate superior cycle performance of lithium storage by doping. In the supercapacitors, the prepared SnO₂-based nanostructures provide fast ion and electron transfer, which led to a prominent supercapacitor performance. Therefore, SnO₂-based nanostructures with a proper design can possess advanced physical and chemical properties, which are vital for a variety of energy and environment applications.

Although significant progress has been made in the synthesis of SnO₂-based nanostructures, further efforts are still required to understand the mechanism of doping and nanocomposites better, which are still unclear but crucial for the design of SnO₂-based nanostructures in enhancement of their lithium storage, supercapacitors, and energy conversion performance. After the introduction of components with different chemical compositions, SnO₂-based nanomaterials got wide applications. However, it is still a challenge in the large-scale synthesis of SnO₂ nanocrystals with more specific facets exposed. We hope that the present paper will further

expand the applications of SnO₂-based nanostructures to meet the environment- and energy-related demands.

Conflict of Interests

The authors declare that there is no conflict of interests regarding the publication of this paper.

Acknowledgments

The authors thank the University of Jinan (UJN) for the support on new staff, and the project was supported by the Taishan Scholar (no. TSHW20120210), the National Natural Science Foundation of China (Grant no. 11304120), and the Encouragement Foundation for Excellent Middle-aged and Young Scientist of Shandong Province (Grant no. BS2012CL005).

References

- [1] J. S. Chen and X. W. Lou, "SnO₂-based nanomaterials: synthesis and application in lithium-ion batteries," *Small*, vol. 9, no. 11, pp. 1877–1893, 2013.
- [2] Y. Liu, Y. Jiao, Z. Zhang, F. Qu, A. Umar, and X. Wu, "Hierarchical SnO₂ nanostructures made of intermingled ultrathin nanosheets for environmental remediation, smart gas sensor, and supercapacitor applications," *ACS Applied Materials and Interfaces*, vol. 6, no. 3, pp. 2174–2184, 2014.
- [3] X. W. Lou, C. M. Li, and L. A. Archer, "Designed synthesis of coaxial SnO₂@carbon hollow nanospheres for highly reversible lithium storage," *Advanced Materials*, vol. 21, no. 24, pp. 2536–2539, 2009.
- [4] S.-L. Chou, J.-Z. Wang, H.-K. Liu, and S.-X. Dou, "SnO₂ meso-scale tubes: one-step, room temperature electrodeposition synthesis and kinetic investigation for lithium storage," *Electrochemistry Communications*, vol. 11, no. 2, pp. 242–246, 2009.
- [5] Y. Han, X. Wu, Y. Ma, L. Gong, F. Qu, and H. Fan, "Porous SnO₂ nanowire bundles for photocatalyst and Li ion battery applications," *CrystEngComm*, vol. 13, no. 10, pp. 3506–3510, 2011.
- [6] P. Meduri, C. Pendyala, V. Kumar, G. U. Sumanasekera, and M. K. Sunkara, "Hybrid tin oxide nanowires as stable and high capacity anodes for li-ion batteries," *Nano Letters*, vol. 9, no. 2, pp. 612–616, 2009.
- [7] S. N. Pusawale, P. R. Deshmukh, and C. D. Lokhande, "Chemical synthesis of nanocrystalline SnO₂ thin films for supercapacitor application," *Applied Surface Science*, vol. 257, no. 22, pp. 9498–9502, 2011.
- [8] Y. L. Gao, J. X. Wu, W. Zhang et al., "SO₄²⁺/SnO₂ as a new electrode for electrochemical supercapacitors," *Ceramics International*, vol. 40, no. 6, pp. 8925–8929, 2014.
- [9] X. Meng, M. Zhou, X. Li et al., "Synthesis of SnO₂ nanoflowers and electrochemical properties of Ni/SnO₂ nanoflowers in supercapacitor," *Electrochimica Acta*, vol. 109, no. 30, pp. 20–26, 2013.
- [10] S. Faraji and F. N. Ani, "Microwave-assisted synthesis of metal oxide/hydroxide composite electrodes for high power supercapacitors—a review," *Journal of Power Sources*, vol. 263, pp. 338–360, 2014.

- [11] J. Zhang, J. Guo, H. Xu, and B. Cao, "Reactive-template fabrication of porous SnO₂ nanotubes and their remarkable gas-sensing performance," *ACS Applied Materials & Interfaces*, vol. 5, no. 16, pp. 7893–7898, 2013.
- [12] Y. Jia, L. He, Z. Guo et al., "Preparation of porous tin oxide nanotubes using carbon nanotubes as templates and their gas-sensing properties," *Journal of Physical Chemistry C*, vol. 113, no. 22, pp. 9581–9587, 2009.
- [13] X. Wang, H. Fan, and P. Ren, "Self-assemble flower-like SnO₂/Ag heterostructures: correlation among composition, structure and photocatalytic activity," *Colloids and Surfaces A: Physicochemical and Engineering Aspects*, vol. 419, no. 20, pp. 140–146, 2013.
- [14] H. Huang, S. Tian, J. Xu et al., "Needle-like Zn-doped SnO₂ nanorods with enhanced photocatalytic and gas sensing properties," *Nanotechnology*, vol. 23, no. 10, Article ID 105502, 2012.
- [15] S. Chen, M. Wang, J. Ye et al., "Kinetics-controlled growth of aligned mesocrystalline SnO₂ nanorod arrays for lithium-ion batteries with superior rate performance," *Nano Research*, vol. 6, no. 4, pp. 243–252, 2013.
- [16] B. Cheng, J. M. Russell, W. Shi, L. Zhang, and E. T. Samulski, "Large-Scale, Solution-Phase Growth of Single-Crystalline SnO₂ Nanorods," *Journal of the American Chemical Society*, vol. 126, no. 19, pp. 5972–5973, 2004.
- [17] N. Talebian and F. Jafarinezhad, "Morphology-controlled synthesis of SnO₂ nanostructures using hydrothermal method and their photocatalytic applications," *Ceramics International*, vol. 39, no. 7, pp. 8311–8317, 2013.
- [18] Z. R. Dai, J. L. Gole, J. D. Stout, and Z. L. Wang, "Tin oxide nanowires, nanoribbons, and nanotubes," *Journal of Physical Chemistry B*, vol. 106, no. 6, pp. 1274–1279, 2002.
- [19] X. L. Wang, N. Aroonyadet, Y. Z. Zhang et al., "Aligned epitaxial SnO₂ nanowires on sapphire: growth and device applications," *Nano Letters*, vol. 14, no. 6, pp. 3014–3022, 2014.
- [20] Z. Yang, G. Du, Q. Meng et al., "Dispersion of SnO₂ nanocrystals on TiO₂(B) nanowires as anode material for lithium ion battery applications," *RSC Advances*, vol. 1, no. 9, pp. 1834–1840, 2011.
- [21] X. Li, X. Meng, J. Liu et al., "Tin oxide with controlled morphology and crystallinity by atomic layer deposition onto graphene nanosheets for enhanced lithium storage," *Advanced Functional Materials*, vol. 22, no. 8, pp. 1647–1654, 2012.
- [22] H. B. Wu, J. S. Chen, X. W. Lou, and H. H. Hng, "Synthesis of SnO₂ hierarchical structures assembled from nanosheets and their lithium storage properties," *Journal of Physical Chemistry C*, vol. 115, no. 50, pp. 24605–24610, 2011.
- [23] Y. Gao and Z. Tang, "Design and application of inorganic nanoparticle superstructures: current status and future challenges," *Small*, vol. 7, no. 15, pp. 2133–2146, 2011.
- [24] W. Shi, S. Song, and H. Zhang, "Hydrothermal synthetic strategies of inorganic semiconducting nanostructures," *Chemical Society Reviews*, vol. 42, no. 13, pp. 5714–5743, 2013.
- [25] J. Kaur, J. Shah, R. K. Kotnala, and K. C. Verma, "Raman spectra, photoluminescence and ferromagnetism of pure, Co and Fe doped SnO₂ nanoparticles," *Ceramics International*, vol. 38, no. 7, pp. 5563–5570, 2012.
- [26] J. M. D. Coey, A. P. Douvalis, C. B. Fitzgerald, and M. Venkatesan, "Ferromagnetism in Fe-doped SnO₂ thin films," *Applied Physics Letters*, vol. 84, no. 8, pp. 1332–1334, 2004.
- [27] Y. Zhao, Y. Huang, Q. Wang et al., "Hollow Zn₂SnO₄ boxes coated with N-doped carbon for advanced lithium-ion batteries," *Ceramics International*, vol. 40, no. 1, pp. 2275–2280, 2014.
- [28] D. Ju, H. Xu, Z. Qiu, J. Guo, J. Zhang, and B. Cao, "Highly sensitive and selective triethylamine-sensing properties of nanosheets directly grown on ceramic tube by forming NiO/ZnO PN heterojunction," *Sensors and Actuators, B: Chemical*, vol. 200, pp. 288–296, 2014.
- [29] F. Du, Z. Guo, and G. Li, "Hydrothermal synthesis of SnO₂ hollow microspheres," *Materials Letters*, vol. 59, no. 19–20, pp. 2563–2565, 2005.
- [30] G. Xi and J. Ye, "Ultrathin SnO₂ nanorods: template- and surfactant-free solution phase synthesis, growth mechanism, optical, gas-sensing, and surface adsorption properties," *Inorganic Chemistry*, vol. 49, no. 5, pp. 2302–2309, 2010.
- [31] J. Ye, H. Zhang, R. Yang, X. Li, and L. Qi, "Morphology-controlled synthesis of SnO₂ nanotubes by using 1D silica mesostructures as sacrificial templates and their applications in lithium-ion batteries," *Small*, vol. 6, no. 2, pp. 296–306, 2010.
- [32] B. Liu and H. C. Zeng, "Salt-assisted deposition of SnO₂ on α -moO₃ nanorods and fabrication of polycrystalline SnO₂ nanotubes," *Journal of Physical Chemistry B*, vol. 108, no. 19, pp. 5867–5874, 2004.
- [33] Y. Wang, H. C. Zeng, and J. Y. Lee, "Highly reversible lithium storage in porous SnO₂ nanotubes with coaxially grown carbon nanotube overlayers," *Advanced Materials*, vol. 18, no. 5, pp. 645–649, 2006.
- [34] N. Du, H. Zhang, J. Chen, J. Sun, B. Chen, and D. Yang, "Metal oxide and sulfide hollow spheres: layer-by-layer synthesis and their application in lithium-ion battery," *Journal of Physical Chemistry B*, vol. 112, no. 47, pp. 14836–14842, 2008.
- [35] X. M. Yin, C. C. Li, M. Zhang et al., "One-step synthesis of hierarchical SnO₂ hollow nanostructures via self-assembly for high power lithium ion batteries," *Journal of Physical Chemistry C*, vol. 114, no. 17, pp. 8084–8088, 2010.
- [36] H. Wang, J. Liang, H. Fan et al., "Synthesis and gas sensitivities of SnO₂ nanorods and hollow microspheres," *Journal of Solid State Chemistry*, vol. 181, no. 1, pp. 122–129, 2008.
- [37] D. S. Jung, Y. N. Ko, Y. C. Kang, and S. B. Park, "Recent progress in electrode materials produced by spray pyrolysis for next-generation lithium ion batteries," *Advanced Powder Technology*, vol. 25, no. 1, pp. 18–31, 2014.
- [38] Y. J. Hong, J.-W. Yoon, J.-H. Lee, and Y. C. Kang, "One-pot synthesis of Pd-loaded SnO₂ yolk-shell nanostructures for ultrasensitive methyl benzene sensors," *Chemistry*, vol. 20, no. 10, pp. 2737–2741, 2014.
- [39] L. A. Patil, M. D. Shinde, A. R. Bari, and V. V. Deo, "Novel trapping system for size wise sorting of SnO₂ nanoparticles synthesized from pyrolysis of ultrasonically atomized spray for gas sensing," *Sensors and Actuators, B: Chemical*, vol. 143, no. 1, pp. 316–324, 2009.
- [40] S. H. Ju, H. C. Jang, and Y. C. Kang, "Characteristics of nano-sized tin dioxide powders prepared by spray pyrolysis," *Journal of the Ceramic Society of Japan*, vol. 117, no. 1368, pp. 922–925, 2009.
- [41] W. Yan, M. Fang, X. Tan et al., "Template-free fabrication of SnO₂ hollow spheres with photoluminescence from Sni," *Materials Letters*, vol. 64, no. 19, pp. 2033–2035, 2010.
- [42] X.-T. Yin and X.-M. Guo, "Selectivity and sensitivity of Pd-loaded and Fe-doped SnO₂ sensor for CO detection," *Sensors and Actuators, B: Chemical*, vol. 200, pp. 213–218, 2014.
- [43] G. Turgut, E. Sonmez, S. Aydin, R. Dilber, and U. Turgut, "The effect of Mo and F double doping on structural, morphological, electrical and optical properties of spray deposited SnO₂ thin

- films," *Ceramics International*, vol. 40, no. 8, pp. 12891–12898, 2014.
- [44] T. Jia, W. Wang, F. Long, Z. Fu, H. Wang, and Q. Zhang, "Synthesis, characterization, and photocatalytic activity of Zn-doped SnO₂ hierarchical architectures assembled by nanocones," *Journal of Physical Chemistry C*, vol. 113, no. 21, pp. 9071–9077, 2009.
- [45] M. Torabi and S. K. Sadrnezhaad, "Electrochemical evaluation of nanocrystalline Zn-doped tin oxides as anodes for lithium ion microbatteries," *Journal of Power Sources*, vol. 196, no. 1, pp. 399–404, 2011.
- [46] X. Liu, J. Iqbal, Z. Wu, B. He, and R. Yu, "Structure and room-temperature ferromagnetism of Zn-doped SnO₂ nanorods prepared by solvothermal method," *The Journal of Physical Chemistry C*, vol. 114, no. 11, pp. 4790–4796, 2010.
- [47] Z. Li, Y. Zhou, T. Yu, J. Liu, and Z. Zou, "Unique Zn-doped SnO₂ nano-echinus with excellent electron transport and light harvesting properties as photoanode materials for high performance dye-sensitized solar cell," *CrystEngComm*, vol. 14, no. 20, pp. 6462–6468, 2012.
- [48] H. Wang, K. Dou, W. Y. Teoh et al., "Engineering of facets, band structure, and gas-sensing properties of hierarchical Sn²⁺-Doped SnO₂ nanostructures," *Advanced Functional Materials*, vol. 23, no. 38, pp. 4847–4853, 2013.
- [49] F.-C. Chung, Z. Zhu, P.-Y. Luo, R.-J. Wu, and W. Li, "Au@ZnO core-shell structure for gaseous formaldehyde sensing at room temperature," *Sensors and Actuators B: Chemical*, vol. 199, pp. 314–319, 2014.
- [50] B. Mondal, B. Basumatari, J. Das, C. Roychaudhury, H. Saha, and N. Mukherjee, "ZnO-SnO₂ based composite type gas sensor for selective hydrogen sensing," *Sensors and Actuators B: Chemical*, vol. 194, pp. 389–396, 2014.
- [51] Y. Li, X. Lv, J. Lu, and J. Li, "Preparation of SnO₂-nanocrystal/graphene-nanosheets composites and their lithium storage ability," *The Journal of Physical Chemistry C*, vol. 114, no. 49, pp. 21770–21774, 2010.
- [52] H. Li, B. Liu, D. Cai et al., "High-temperature humidity sensors based on WO₃-SnO₂ composite hollow nanospheres," *Journal of Materials Chemistry A*, vol. 2, no. 19, pp. 6854–6862, 2014.
- [53] S. Liu, R. Wang, M. Liu et al., "Fe₂O₃@SnO₂ nanoparticle decorated graphene flexible films as high-performance anode materials for lithium-ion batteries," *Journal of Materials Chemistry A*, vol. 2, no. 13, pp. 4598–4604, 2014.
- [54] K.-I. Choi, H.-J. Kim, Y. C. Kang, and J.-H. Lee, "Ultrasensitive and ultrasensitive detection of H₂S in highly humid atmosphere using CuO-loaded SnO₂ hollow spheres for real-time diagnosis of halitosis," *Sensors and Actuators B: Chemical*, vol. 194, pp. 371–376, 2014.
- [55] A. Hamrouni, H. Lachheb, and A. Houas, "Synthesis, characterization and photocatalytic activity of ZnO-SnO₂ nanocomposites," *Materials Science and Engineering B*, vol. 178, no. 20, pp. 1371–1379, 2013.
- [56] W. W. Wang, Y. J. Zhu, and L. X. Yang, "ZnO-SnO₂ hollow spheres and hierarchical nanosheets: hydrothermal preparation, formation mechanism, and photocatalytic properties," *Advanced Functional Materials*, vol. 17, no. 1, pp. 59–64, 2007.
- [57] B. Geng, C. Fang, F. Zhan, and N. Yu, "Synthesis of polyhedral ZnSnO₃ microcrystals with controlled exposed facets and their selective gas-sensing properties," *Small*, vol. 4, no. 9, pp. 1337–1343, 2008.
- [58] J.-F. Duan, S.-C. Hou, S.-G. Chen, and H.-G. Duan, "Synthesis of amorphous ZnSnO₃ hollow nanoboxes and their lithium storage properties," *Materials Letters*, vol. 122, pp. 261–264, 2014.
- [59] W. Cun, W. Xinming, Z. Jincai et al., "Synthesis, characterization and photocatalytic property of nano-sized Zn₂SnO₄," *Journal of Materials Science*, vol. 37, no. 14, pp. 2989–2996, 2002.
- [60] K. Wang, Y. Huang, H. Huang et al., "Hydrothermal synthesis of flower-like Zn₂SnO₄ composites and their performance as anode materials for lithium-ion batteries," *Ceramics International*, vol. 40, no. 6, pp. 8021–8025, 2014.
- [61] L. Wang, W. Zhang, C. Wang et al., "A facile synthesis of highly porous CdSnO₃ nanoparticles and their enhanced performance in lithium-ion batteries," *Journal of Materials Chemistry A*, vol. 2, no. 14, pp. 4970–4974, 2014.
- [62] Y. Zhao, Y. Huang, Q. Wang et al., "Preparation of hollow Zn₂SnO₄ boxes for advanced lithium-ion batteries," *RSC Advances*, vol. 3, no. 34, pp. 14480–14485, 2013.
- [63] Y. N. Zhou, M. Z. Xue, and Z. W. Fu, "Nanostructured thin film electrodes for lithium storage and all-solid-state thin-film lithium batteries," *Journal of Power Sources*, vol. 234, pp. 310–332, 2013.
- [64] D. Deng and J. Y. Lee, "Hollow core-shell mesospheres of crystalline SnO₂ nanoparticle aggregates for high capacity Li⁺ ion storage," *Chemistry of Materials*, vol. 20, no. 5, pp. 1841–1846, 2008.
- [65] C. Wang, Y. Zhou, M. Ge, X. Xu, Z. Zhang, and J. Z. Jiang, "Large-scale synthesis of SnO₂ nanosheets with high lithium storage capacity," *Journal of the American Chemical Society*, vol. 132, no. 1, pp. 46–47, 2010.
- [66] Z. Wang, D. Luan, F. Y. C. Boey, and X. W. Lou, "Fast formation of SnO₂ nanoboxes with enhanced lithium storage capability," *Journal of the American Chemical Society*, vol. 133, no. 13, pp. 4738–4741, 2011.
- [67] X. W. Lou, Y. Wang, C. Yuan, J. Y. Lee, and L. A. Archer, "Template-free synthesis of SnO₂ hollow nanostructures with high lithium storage capacity," *Advanced Materials*, vol. 18, no. 17, pp. 2325–2329, 2006.
- [68] H. Wang and A. L. Rogach, "Hierarchical SnO₂ nanostructures: recent advances in design, synthesis, and applications," *Chemistry of Materials*, vol. 26, no. 1, pp. 123–133, 2014.
- [69] Y. H. Jin, K. M. Min, S. D. Seo, H. W. Shim, and D. W. Kim, "Enhanced Li storage capacity in 3 nm diameter SnO₂ nanocrystals firmly anchored on multiwalled carbon nanotubes," *Journal of Physical Chemistry C*, vol. 115, no. 44, pp. 22062–22067, 2011.
- [70] S. Ding, D. Luan, F. Y. C. Boey, J. S. Chen, and X. W. Lou, "SnO₂ nanosheets grown on graphene sheets with enhanced lithium storage properties," *Chemical Communications*, vol. 47, no. 25, pp. 7155–7157, 2011.
- [71] J.-M. Tarascon and M. Armand, "Issues and challenges facing rechargeable lithium batteries," *Nature*, vol. 414, no. 6861, pp. 359–367, 2001.
- [72] H.-X. Zhang, C. Feng, Y.-C. Zhai, K.-L. Jiang, Q.-Q. Li, and S.-S. Fan, "Cross-stacked carbon nanotube sheets uniformly loaded with SnO₂ nanoparticles: a novel binder-free and high-capacity anode material for lithium-ion batteries," *Advanced Materials*, vol. 21, no. 22, pp. 2299–2304, 2009.
- [73] L.-Y. Jiang, X.-L. Wu, Y.-G. Guo, and L.-J. Wan, "SnO₂-based hierarchical nanomicrostructures: facile synthesis and their applications in gas sensors and lithium-ion batteries," *The Journal of Physical Chemistry C*, vol. 113, no. 32, pp. 14213–14219, 2009.

- [74] Y. Wang, I. Djerdj, B. Smarsly, and M. Antonietti, "Antimony-doped SnO₂ nanopowders with high crystallinity for lithium-ion battery electrode," *Chemistry of Materials*, vol. 21, no. 14, pp. 3202–3209, 2009.
- [75] X. Wang, X. Cao, L. Bourgeois et al., "N-doped graphene-SnO₂ sandwich paper for high-performance lithium-ion batteries," *Advanced Functional Materials*, vol. 22, no. 13, pp. 2682–2690, 2012.
- [76] P. Wu, N. Du, H. Zhang, J. Yu, and D. Yang, "CNTs@SnO₂@C coaxial nanocables with highly reversible lithium storage," *The Journal of Physical Chemistry C*, vol. 114, no. 51, pp. 22535–22538, 2010.
- [77] X. Wang, X. Cao, L. Bourgeois et al., "N-doped graphene-SnO₂ sandwich paper for high-performance lithium-ion batteries," *Advanced Functional Materials*, vol. 22, no. 13, pp. 2682–2690, 2012.
- [78] J. Lin, Z. Peng, C. Xiang et al., "Graphene nanoribbon and nanostructured SnO₂ composite anodes for lithium ion batteries," *ACS Nano*, vol. 7, no. 7, pp. 6001–6006, 2013.
- [79] H. Yang, T. Song, S. Lee et al., "Tin indium oxide/graphene nanosheet nanocomposite as an anode material for lithium ion batteries with enhanced lithium storage capacity and rate capability," *Electrochimica Acta*, vol. 91, pp. 275–281, 2013.
- [80] X. Lu, W. Zhang, C. Wang, T.-C. Wen, and Y. Wei, "One-dimensional conducting polymer nanocomposites: synthesis, properties and applications," *Progress in Polymer Science (Oxford)*, vol. 36, no. 5, pp. 671–712, 2011.
- [81] S. Sarangapani, B. V. Tilak, and C. P. Chen, "Materials for electrochemical capacitors theoretical and experimental constraints," *Journal of the Electrochemical Society*, vol. 143, no. 11, pp. 3791–3799, 1996.
- [82] E. Faggioli, P. Rena, V. Danel, X. Andrieu, R. Mallant, and H. Kahlen, "Supercapacitors for the energy management of electric vehicles," *Journal of Power Sources*, vol. 84, no. 2, pp. 261–269, 1999.
- [83] K. W. Nam, W. S. Yoon, and K. B. Kim, "X-ray absorption spectroscopy studies of nickel oxide thin film electrodes for supercapacitors," *Electrochimica Acta*, vol. 47, no. 19, pp. 3201–3209, 2002.
- [84] J.-H. Sung, S.-J. Kim, and K.-H. Lee, "Fabrication of microcapacitors using conducting polymer microelectrodes," *Journal of Power Sources*, vol. 124, no. 1, pp. 343–350, 2003.
- [85] C. G. Liu, H. T. Fang, F. Li, M. Liu, and H. M. Cheng, "Single-walled carbon nanotubes modified by electrochemical treatment for application in electrochemical capacitors," *Journal of Power Sources*, vol. 160, no. 1, pp. 758–761, 2006.
- [86] H. Mi, X. Zhang, X. Ye, and S. Yang, "Preparation and enhanced capacitance of core-shell polypyrrole/polyaniline composite electrode for supercapacitors," *Journal of Power Sources*, vol. 176, no. 1, pp. 403–409, 2008.
- [87] C. D. Lokhande, D. P. Dubal, and O. S. Joo, "Metal oxide thin film based supercapacitors," *Current Applied Physics*, vol. 11, no. 3, pp. 255–270, 2011.
- [88] Y. M. Dai, S. C. Tang, J. Q. Peng et al., "MnO₂@SnO₂ coreshell heterostructured nanorods for supercapacitors," *Materials Letters*, vol. 130, pp. 107–110, 2014.
- [89] R. Li, X. Ren, F. Zhang, C. Du, and J. Liu, "Synthesis of Fe₃O₄@SnO₂ core-shell nanorod film and its application as a thin-film supercapacitor electrode," *Chemical Communications*, vol. 48, no. 41, pp. 5010–5012, 2012.
- [90] J. Yan, E. Khoo, A. Sumboja, and P. S. Lee, "Facile coating of manganese oxide on tin oxide nanowires with high-performance capacitive behavior," *ACS Nano*, vol. 4, no. 7, pp. 4247–4255, 2010.
- [91] P. Manivel, S. Ramakrishnan, N. K. Kothurkar et al., "Optical and electrochemical studies of polyaniline/SnO₂ fibrous nanocomposites," *Materials Research Bulletin*, vol. 48, no. 2, pp. 640–645, 2013.
- [92] L. H. Bao, J. F. Zang, and X. D. Li, "Flexible Zn₂SnO₄/MnO₂ core/shell nanocable-carbon microfiber hybrid composites for high-performance supercapacitor electrodes," *Nano Letters*, vol. 11, no. 3, pp. 1215–1220, 2011.
- [93] T. Lu, Y. Zhang, H. Li, L. Pan, Y. Li, and Z. Sun, "Electrochemical behaviors of graphene-ZnO and graphene-SnO₂ composite films for supercapacitors," *Electrochimica Acta*, vol. 55, no. 13, pp. 4170–4173, 2010.
- [94] G. Arabale, D. Wagh, M. Kulkarni et al., "Enhanced supercapacitance of multiwalled carbon nanotubes functionalized with ruthenium oxide," *Chemical Physics Letters*, vol. 376, no. 1-2, pp. 207–213, 2003.
- [95] B. J. Lee, S. R. Sivakkumar, J. M. Ko, J. H. Kim, S. M. Jo, and D. Y. Kim, "Carbon nanofibre/hydrous RuO₂ nanocomposite electrodes for supercapacitors," *Journal of Power Sources*, vol. 168, no. 2, pp. 546–552, 2007.
- [96] D. Kalpana, K. S. Omkumar, S. S. Kumar, and N. G. Renganathan, "A novel high power symmetric ZnO/carbon aerogel composite electrode for electrochemical supercapacitor," *Electrochimica Acta*, vol. 52, no. 3, pp. 1309–1315, 2006.
- [97] A. G. El-Deen, N. A. M. Barakat, K. A. Khalil, M. Motlak, and H. Y. Kim, "Graphene/SnO₂ nanocomposite as an effective electrode material for saline water desalination using capacitive deionization," *Ceramics International*, vol. 40, no. 9, pp. 14627–14634, 2014.

Research Article

A Facile Low-Temperature Hydrothermal Method to Prepare Anatase Titania/Cellulose Aerogels with Strong Photocatalytic Activities for Rhodamine B and Methyl Orange Degradations

Caichao Wan,¹ Yun Lu,² Chunde Jin,³ Qingfeng Sun,³ and Jian Li¹

¹ Material Science and Engineering College, Northeast Forestry University, Harbin 150040, China

² Research Institute of Wood Industry, Chinese Academy of Forestry, Beijing 100091, China

³ School of Engineering, Zhejiang Agricultural and Forestry University, Lin'an 311300, China

Correspondence should be addressed to Yun Lu; luyun@criwi.org.cn, Qingfeng Sun; qfsun@nefu.edu.cn and Jian Li; nefulijian@163.com

Received 12 August 2014; Revised 8 October 2014; Accepted 8 October 2014

Academic Editor: Chuanfei Guo

Copyright © 2015 Caichao Wan et al. This is an open access article distributed under the Creative Commons Attribution License, which permits unrestricted use, distribution, and reproduction in any medium, provided the original work is properly cited.

A facile low-temperature hydrothermal method for in situ preparation of anatase titania (TiO₂) homogeneously dispersed in cellulose aerogels substrates was described. The formed anatase TiO₂ aggregations composed of a mass of evenly dispersed TiO₂ nanoparticles with sizes of 2–5 nm were embedded in the interconnected three-dimensional (3D) architecture of the cellulose aerogels matrixes without large-scale reunion phenomenon; meanwhile, the obtained anatase titania/cellulose (ATC) aerogels also had a high loading amount of TiO₂ (ca. 35.7%). Furthermore, compared with commercially available Degussa P25, ATC aerogels displayed comparable photocatalytic activities for Rhodamine B and methyl orange degradations under UV radiation, which might be useful in the fields of catalysts, wastewater treatment, and organic pollutant degradation. Meanwhile, the photocatalytic reaction behaviors of ATC aerogels under UV irradiation were also illuminated.

1. Introduction

Titanium dioxide (TiO₂), one of the most important semiconductor materials, has been extensively applied as photocatalyst for decontamination of water polluted with organic pollutants due to its high optical reactivity, chemical and physical inertness, nontoxicity, and low cost [1–3]. TiO₂ crystals mainly exist in two stable polymorphic forms: anatase (tetragonal, space group *I4₁/amd*) and rutile (tetragonal, space group *P4₂/mnm*) [4]. Generally, it is accepted that anatase TiO₂ is more efficient as photocatalyst, and rutile TiO₂ is preferable for blocking UV irradiation, notwithstanding that some catalysts with mixed phases exhibit significantly higher catalytic activities like Degussa P25 [5, 6].

In fact, nanoscale particles with large specific surface area and high surface energy are very easy to reunite leading to conspicuous performance degradation. The confinement of nanoparticles can be achieved by using some

special matrixes with unique structures as hosts like multiwalled carbon nanotubes [7–9], graphene [10], fibers [11], and some traditional inorganic or synthetic polymer-based aerogels [12, 13], which could provide a means of particle dispersion and act as protection of metallic nanoparticles against air oxidation. In particular, owing to large specific surface area, high porosity, multiscale micronanostructure, stable chemical property, renewability, and biodegradability, cellulose aerogels are widely considered as good supports for nanomaterials, such as TiO₂, ZnO, Ag, and ZrO₂ [14–17]. In particular, TiO₂/cellulose aerogels hybrids are useful for photocatalysts, UV shields, antibacterial materials, and synthesis of transition-metal carbide materials [18–21]. Furthermore, synthesis of anatase TiO₂/cellulose (ATC) composites generally depends on high-temperature calcination treatment using cellulose or cellulose derivatives as templates at 400–700°C [22–24], so as to get anatase TiO₂ crystals and

avoid excessive crystal transformation from anatase to rutile while exceeding the critical temperature.

Herein, a facile low-temperature hydrothermal method was employed to prepare ATC aerogels instead of the common calcination process. Moreover, distinguishing from some previous literatures about TiO₂/cellulose composites with improved activity, in this study, a green NaOH/polyethylene glycol (PEG) aqueous solution was used to fabricate the cellulose aerogels, and the resulting environmentally friendly nanoporous aerogels were selected as hosts to support the nano-TiO₂. The obtained ATC aerogels were characterized by scanning electron microscopy (SEM), transmission electron microscopy (TEM), energy dispersive X-ray spectroscopy (EDX), X-ray photoelectron spectroscopy (XPS), X-ray diffraction (XRD), and thermogravimetry (TG). Meanwhile, the photocatalytic activities of ATC aerogels for two typical organic pollutants including Rhodamine B (RhB) and methyl orange (MO) degradations were also investigated and compared with those of P25. Based on which, the photocatalytic reaction behaviors of ATC aerogels under UV irradiation were illuminated.

2. Materials and methods

2.1. Materials. Sixty-mesh powder of wheat straw after grinding and sieving was collected and dried in a vacuum at 60°C for 24 h before being used. All chemicals were supplied by Tianjin Kemiou Chemical Reagent Co., Ltd., and used as received.

2.2. Cellulose Hydrogel Preparation. A mild effective chemical pretreatment process was employed to extract and purify cellulose from the wheat straw powder, which could refer to our previous report [25]. The obtained dried cellulose was mixed with an aqueous solution of NaOH/PEG-4000 (9:1 by weight) with magnetic stirring at room temperature for about 6 h to form a 2 wt% homogenous cellulose solution. Then, the cellulose solution underwent a freeze-thaw process by freezing the solution at -15°C for 12 h and subsequently thawing it out at room temperature for 0.5 h under vigorous stirring. After being frozen again for 3 h at -15°C, the solution was regenerated by placing it into a coagulation bath of 1 v% hydrochloric acid for 6 h, repeating this process until the formation of the amber-like hydrogel. Afterwards, the obtained hydrogel was rinsed repeatedly with distilled water and anhydrous ethyl alcohol (EtOH) to remove superfluous hydrogen ions and chlorine anions.

2.3. ATC Aerogel Preparation. The low-temperature hydrothermal preparation of ATC aerogel was described in Scheme 1. Tetrabutyl orthotita (TBOT) (5 mL) and EtOH (200 mL) were mixed with magnetic stirring for 30 min and then transferred into a Teflon-lined stainless-steel autoclave. The cellulose hydrogel was subsequently placed into the above reaction solution. After the autoclave was sealed and heated to 110°C for 4 h, 100 mL deionized water (pH = 6.5) was added, and the solution was reheated to 70°C for 4 h. After reaction, the prepared sample was removed from the

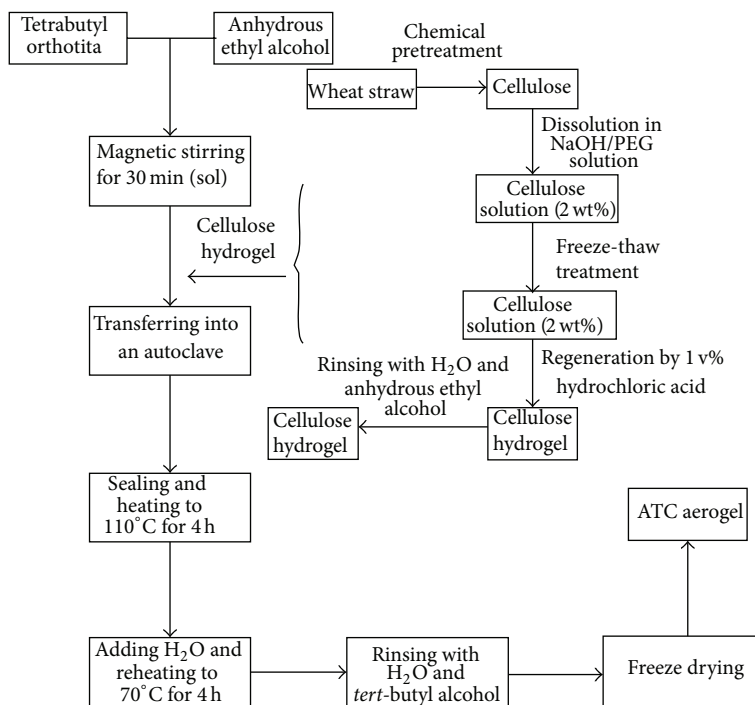
solution and ultrasonically rinsed with deionized water and *tert*-butyl alcohol in sequence for 30 min. Finally, the sample was subjected to a freeze-drying process at -35°C for 48 h, and the following ATC aerogel was successfully fabricated. Moreover, the pure TiO₂ particles powders were prepared following the above hydrothermal process without adding the cellulose hydrogel, and the mixed solution after reaction was filtered, washed by distilled water, and dried at 60°C for 24 h to get dried TiO₂ particles powders. The pure cellulose aerogel was obtained by the direct *tert*-butyl alcohol freeze-drying process of the cellulose hydrogel.

2.4. Characterizations. Microstructures and surface chemical compositions were evaluated by SEM (FEI, Quanta 200) equipped with EDX spectrometer operating at 15–20 kV on gold-sputtered samples. TEM observation was carried out on a FEI, Tecnai G2 F20 TEM. Crystalline structures were identified by XRD instrument (Rigaku, D/MAX 2200) operating with Cu K α radiation ($\lambda = 1.5418 \text{ \AA}$) at a scan rate (2θ) of $4^\circ \cdot \text{min}^{-1}$, accelerating voltage of 40 kV, and applied current of 30 mA ranging from 10° to 80°. XPS spectra were recorded using a Thermo Escalab 250Xi XPS spectrometer (Germany). Deconvolution of the overlapping peaks was performed using a mixed Gaussian-Lorentzian fit program. Thermal stabilities were determined using a TG analyzer (TA Q600) with a heating rate of $10^\circ \text{C} \cdot \text{min}^{-1}$ in a N₂ environment.

2.5. Photocatalytic Activities Measurements. The photocatalytic activities of ATC aerogels were evaluated by measuring the decomposition of RhB and MO, while pure TiO₂ nanoparticles (commercial Degussa P25) were used for comparison, and the amount of P25 and the amount of ATC aerogels were controlled by the same titania loading determined by the following TG tests. A 100 W mercury lamp with main wavelength of 365 nm was purchased from Beijing BrightStars Science and Technology Corp. and selected as UV light source. For typical photocatalytic experiments of the hybrid aerogels, ATC aerogels samples with sizes of about 20 mm (diameter) \times 10 mm (height) were immersed into the circular disks with 30 mL RhB or MO aqueous solutions ($50 \text{ mg} \cdot \text{L}^{-1}$), respectively. Before irradiation, the solutions with ATC aerogels were magnetically stirred in the dark for 30 min to achieve adsorption equilibrium. Then, the dishes were exposed to the mercury lamp for about 1 h, and the distances between the lamps and the dishes were approximately 10 cm. Samples were taken at every time interval (20 min) and centrifuged for removing photocatalysts. Concentration of the filtrate was analyzed by a TU-1901 UV-vis spectrophotometer (Beijing Purkinje, China) at 554 nm for RhB or 464 nm for MO. The efficiency was calculated by

$$Y = 100 \times \left(\frac{C - C_0}{C_0} \right), \quad (1)$$

where C_0 and C are the initial dye concentration and the concentration at time t , respectively. Similarly, the photocatalytic experiments of P25 for RhB and MO were following the above procedures.



SCHEME 1: Diagram of the low-temperature hydrothermal preparation of ATC aerogel.

3. Results and Discussion

Figure 1(a) showed the SEM image of ATC aerogels. As shown, porous and interconnected three-dimensional (3D) architecture with pore sizes of a few hundred nanometers to several micrometers, originated from the original cellulose hydrogels architecture, could be clearly identified. In addition, it was observed that numerous white ellipsoidal substances surrounding the porous skeleton structure were generated, which might be derived from titanium compounds. To further investigate the chemical components of the newly generated white ellipsoidal substances, the area in the green box with some evident aggregations of particles (Figure 1(a)) was tested by EDX, and the results demonstrated that apart from C and O elements from the cellulose substrates as well as Au element from the coating layer used for SEM observation, new strong peaks corresponding to Ti element were detected (inset in Figure 1(a)), confirming that the white ellipsoidal substances primarily consisted of titanium compounds. Moreover, from the higher magnification SEM image (Figure 1(b)), it was clear that the ellipsoidal substances containing Ti element tightly adhered to the cellulose matrixes, indicating potential good interface bonding.

In order to further explore the composition and structure of the ellipsoidal substances as well as the interaction between the ellipsoidal substances and the cellulose aerogels matrixes, the samples were observed by TEM. The TEM images of different magnifications of ATC aerogels were represented in Figure 2. Apparently, the cellulose aerogels matrixes were loaded with a mass of evenly dispersed nanoparticles as indicated by the dark spots in the TEM image with lower magnification (Figure 2(a)). These abundant particles might

be responsible for the formation of the ellipsoidal substances. The higher magnification TEM image (Figure 2(b)) showed that the size of nanoparticles was found to range between 2 and 5 nm and no large-scale aggregation was observed, indicating that the combination of nanoparticles and cellulose aerogels effectively hindered the reunion phenomenon.

XPS measurements were performed to elucidate the surface chemical composition and the oxidation state of ATC aerogels. In the high-resolution XPS spectra of Ti 2p (Figure 3(a)), the binding energies of Ti 2p_{3/2} and 2p_{1/2} were centered at 457.2 and 462.5 eV, respectively, which revealed that the titanium elements were in the oxidation state IV, corresponding to Ti⁴⁺ (TiO₂) [26, 27]. Meanwhile, the result also suggested that the ellipsoidal substances observed by SEM were composed of TiO₂ particles; besides, the nanoparticles in the TEM images might be exactly the generated TiO₂ particles. The O 1s spectra of ATC aerogels displayed the contributions of three components (Figure 3(b)) including TiO₂ (529.8 eV), adsorbed water (531.2 eV), and hydroxyl groups (O–H) (532.1 eV) [28]. Moreover, in the C 1s spectra (Figure 3(c)), major peak at 284.7 eV was related to C–C, C=C, and C–H bonds and the peak at around 287.7 eV suggested the presence of Ti–O–C bond [29].

The XRD patterns of the TiO₂ particles and ATC aerogels were shown in Figure 3(d). For the TiO₂ particles, a series of characteristic peaks, corresponding to the (103), (004), (112), (200), (105), (211), (213), (204), (116), (220), (107), (215), and (301) planes, were observed, which were regarded as an attributive indicator of anatase phase TiO₂ crystallites (JCPDS file number 21-1272) [30]. Similarly, ATC aerogels also exhibited typical strong peaks assigned to anatase phase as well as cellulose characteristic peaks at 11.9°, 19.8°, and 22.0°

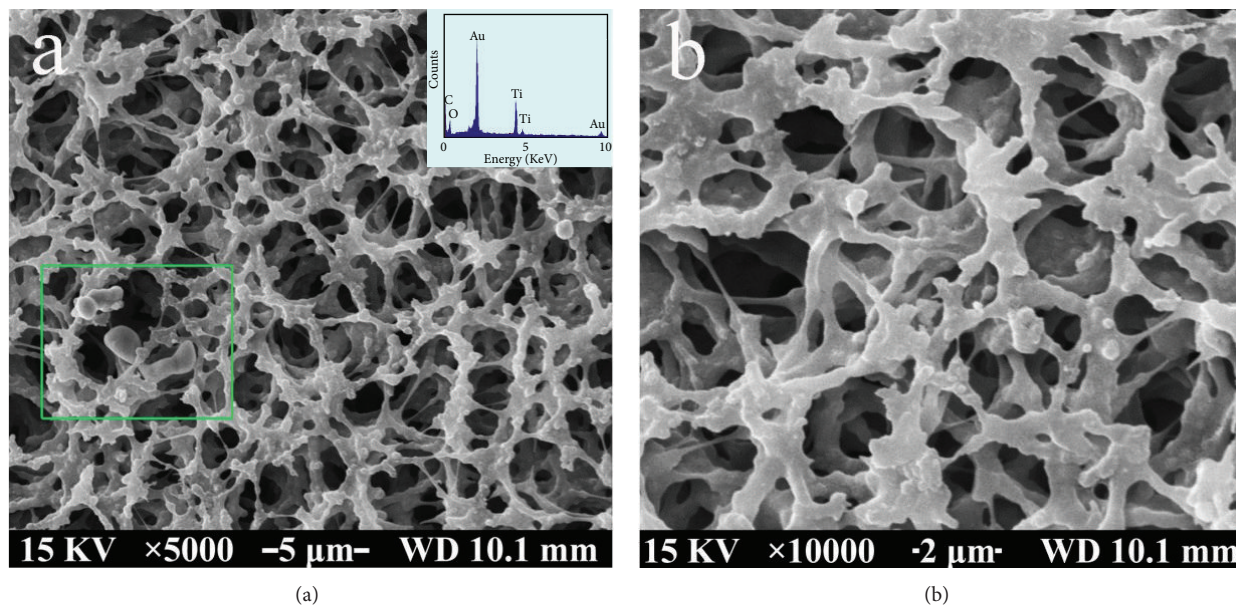


FIGURE 1: (a) Low-magnification and (b) high-magnification SEM images of ATC aerogels, respectively. The green box was the area of EDX analysis, and the corresponding EDX spectrum was shown in Figure 1 as an inset.

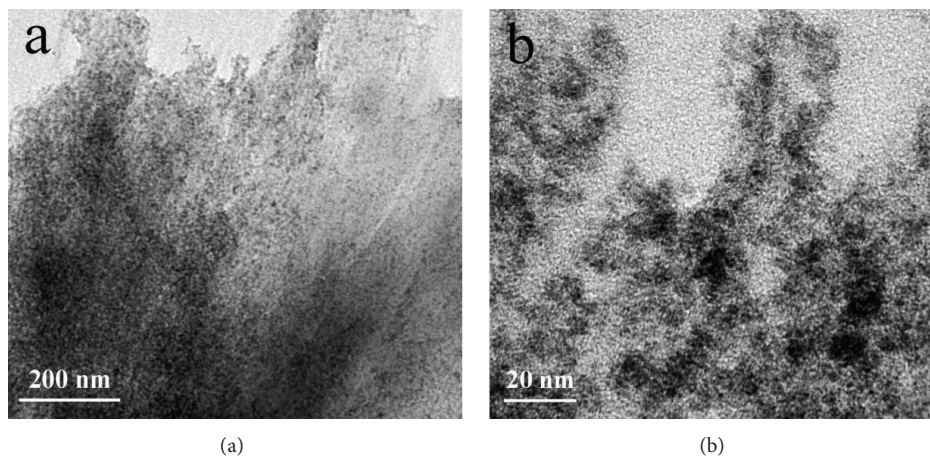


FIGURE 2: TEM images of different magnifications of ATC aerogels, respectively.

belonging to (101), (10 $\bar{1}$), and (002) planes [31]. In particular, no peaks of rutile TiO₂ phase (JCPDS file number 21-1276) were detected, indicating the high anatase phase purity of ATC aerogels. Meanwhile, the result also revealed that the anatase TiO₂ was successfully fabricated and combined with cellulose aerogels by the facile low-temperature hydrothermal method. Moreover, it was obvious that the characteristic peaks of the anatase TiO₂ were broad, which was an indication of the small size of the TiO₂ particles formed in the ATC aerogels. The crystallite size as calculated by the Debye-Scherrer equation [32] was 4.3 nm, which was consistent with the TEM results from Figure 2(b).

Figure 4 showed the TG and DTG curves of ATC aerogels and the pure cellulose aerogels, respectively. The DTG curve for pure cellulose aerogels showed one major exothermic peak at around 362°C, which represented a typical thermal

decomposition behavior of cellulose in an inert atmosphere, as previously reported [33]. In comparison, the maximum loss of weight of ATC aerogels shifted to a temperature of ~323°C, 39°C lower than that of the pure cellulose aerogels according to the DTG curves. The potential reasons for the shift might be the catalytic character of TiO₂ [34, 35], and the loosening of molecular chains in crystalline regions of cellulose as the result of infusion of TiO₂ particles [36]. Moreover, ATC aerogels had high residual ash (ca. 44.1%), far higher than that of the pure cellulose aerogels samples (ca. 8.4%), which indicated high loading amount of TiO₂ in the hybrid ATC aerogels samples (ca. 35.7%).

RhB and MO, the two kinds of common organic pollutants, were employed to evaluate the photocatalytic activities of ATC aerogels. For the sake of comprehending the photocatalytic property, the commercially available TiO₂ P25

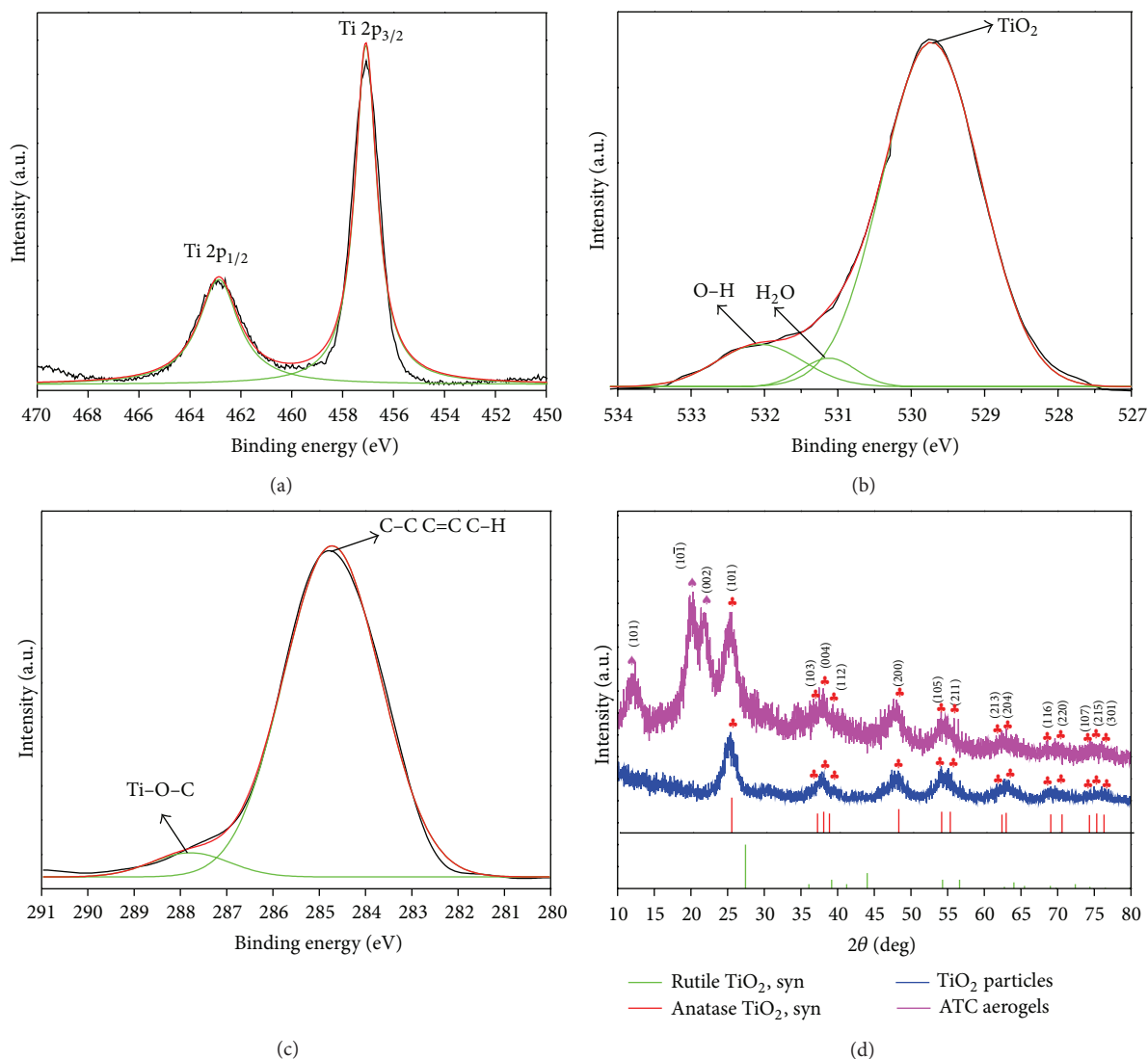


FIGURE 3: High-resolution XPS spectra of ATC aerogels in (a) Ti 2p, (b) O 1s, and (c) C 1s regions. (d) XRD patterns of the TiO₂ particles and ATC aerogels.

(Degussa, Germany) was used as a photocatalytic reference. As shown in Figure 5(a), the concentrations of the RhB and the MO solutions changed a little for the wheat straw, indicating an inferior photocatalytic performance under UV irradiation. On the contrary, both of P25 and ATC aerogels showed strong photodegradation abilities for RhB and MO due to the drastic changes of concentration before and after the experiments. Compared with P25, ATC aerogels exhibited similar concentration change tendency for RhB and slightly faster rate of photocatalytic degradation for MO, respectively, which proved that the photocatalytic activities of ATC aerogels were comparable with those of P25 only taking account of these two kinds of organic pollutants. Moreover, the strong photocatalytic activities of ATC aerogels might be due to good dispersion, potential higher surface area, and smaller crystallite size of the formed anatase TiO₂ [37, 38]. Furthermore, Figure 5(b) showed the macrographs of RhB and MO

degradations by ATC aerogels, and the significant color differences before and after the UV radiation further indicated the superior photocatalytic activities of ATC aerogels.

Based on the results mentioned above, photocatalytic reaction behaviors of ATC aerogels under UV irradiation for RhB and MO degradations were illuminated in Figure 6. When the surface of ATC aerogels was illuminated by UV light with energy equal to or larger than the band gap energy of anatase TiO₂ nanocrystals, the electrons were excited in the valance band (VB) to the conduction band (CB), leading to the formation of a positive hole (h⁺) in the VB and an electron (e⁻) in the CB [39–41]. The generated electron-hole pairs immediately interacted with surface adsorbed molecular oxygen to yield superoxide radical anions ([•]O₂⁻) and with water to produce the highly reactive HO[•] radicals, respectively. These radicals groups repeatedly attacked RhB and MO molecules, eventually resulting in their degradations

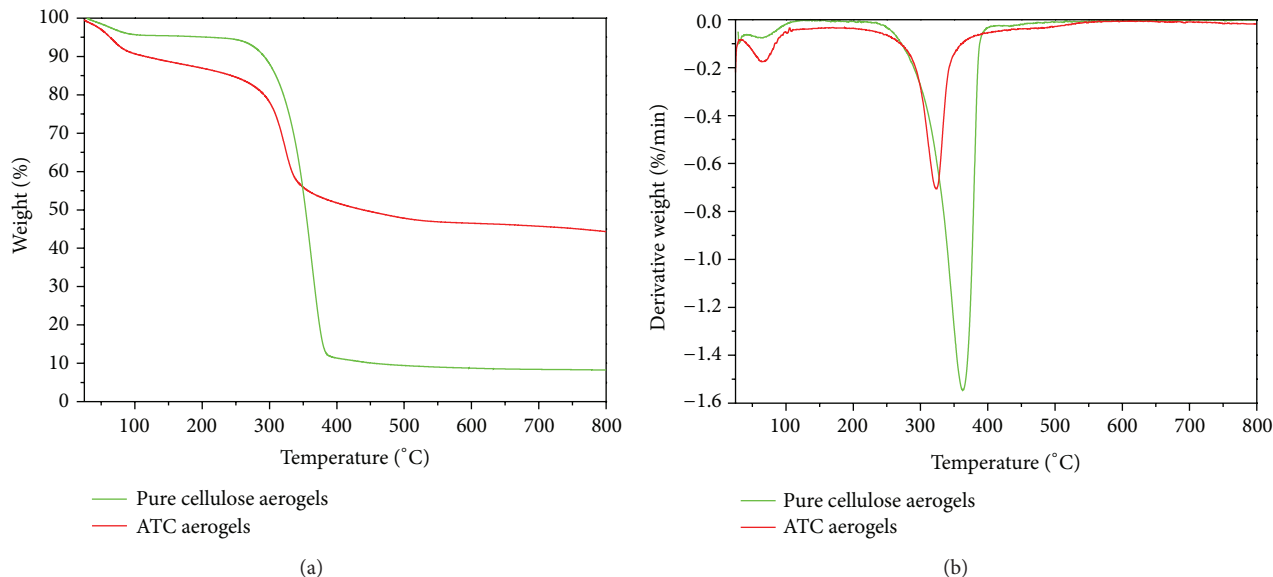


FIGURE 4: TG and DTG curves of ATC aerogels and the pure cellulose aerogels, respectively.

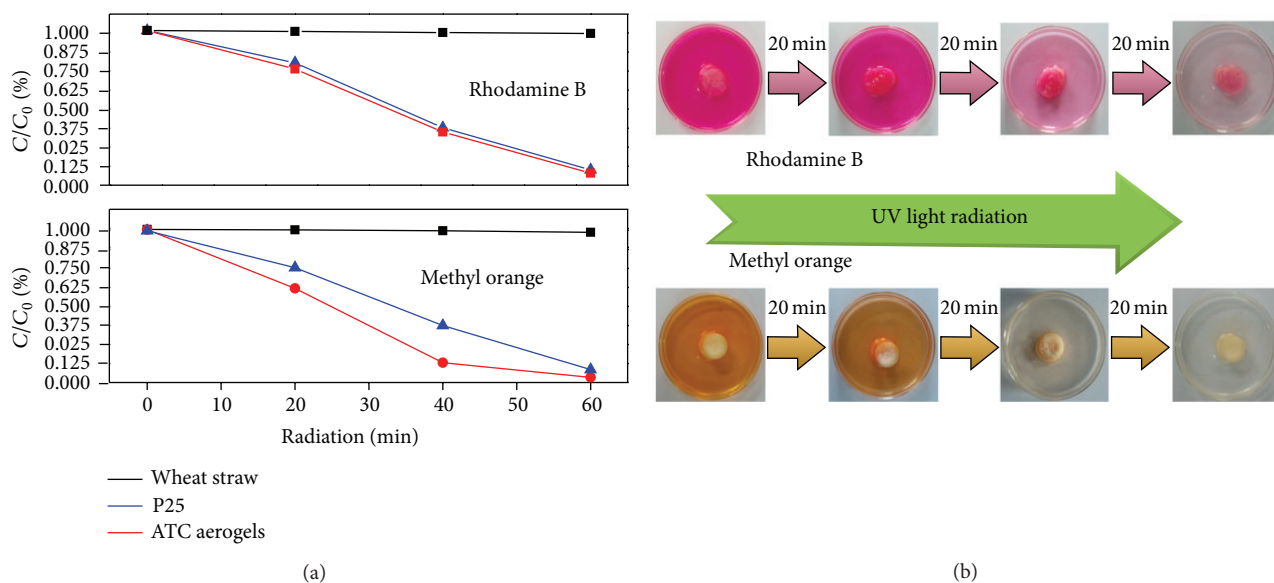


FIGURE 5: (a) Photocatalytic activities of the wheat straw, P25, and ATC aerogels for RhB and MO degradations. (b) Macrographs of RhB and MO degradations by ATC aerogels under UV radiation.

into CO_2 and H_2O [42, 43], which were responsible for the photocatalytic activity.

4. Conclusions

In conclusion, ATC aerogels were successfully fabricated via a mild simple low-temperature hydrothermal method. The as-prepared ATC aerogels were composed of cross-linked 3D architecture originated from the original cellulose hydrogels, and the 3D architecture was surrounded by plentiful ellipsoidal aggregations formed by a mass of evenly dispersed anatase TiO_2 nanoparticles with sizes of 2–5 nm. Meanwhile,

a high loading amount of TiO_2 in the hybrid ATC aerogels samples (ca. 35.7%) was also obtained according to the TG results. Moreover, the ATC aerogels exhibited comparable photocatalytic activities for RhB and MO degradations with Degussa P25 under UV radiation, which might be served as novel green catalysts for water decontamination and organic pollutants decomposition.

Conflict of Interests

The authors declare that there is no conflict of interests regarding the publication of this paper.

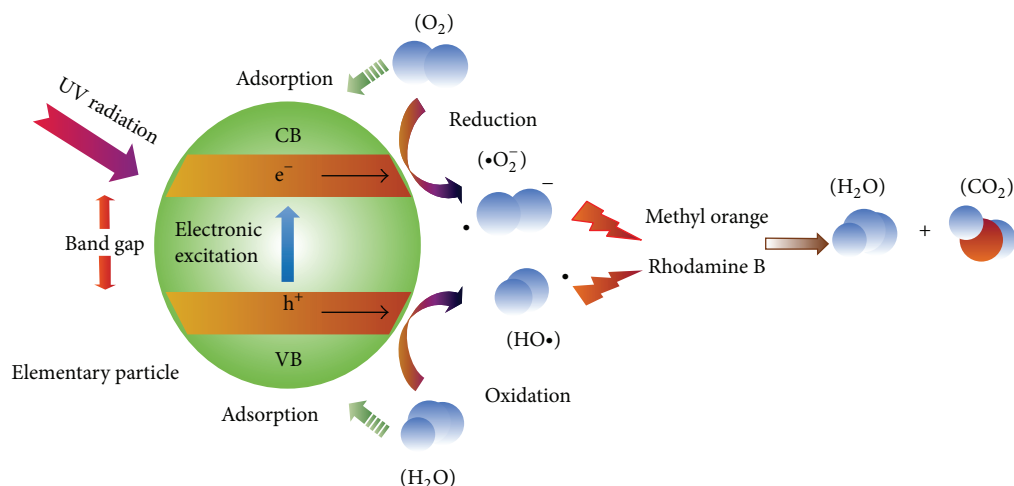


FIGURE 6: Schematic representation of the photocatalytic mechanism of ATC aerogels.

Acknowledgments

The authors appreciate the financial support of the China Postdoctoral Science Foundation (2013M540263), the National Natural Science Foundation of China (Grant no. 31270590), and the Doctoral Candidate Innovation Research Support Program of Science & Technology Review (kjdb2012006).

References

- [1] X. Chen and S. S. Mao, "Titanium dioxide nanomaterials: synthesis, properties, modifications and applications," *Chemical Reviews*, vol. 107, no. 7, pp. 2891–2959, 2007.
- [2] S. Gelover, P. Mondragón, and A. Jiménez, "Titanium dioxide sol-gel deposited over glass and its application as a photocatalyst for water decontamination," *Journal of Photochemistry and Photobiology A: Chemistry*, vol. 165, no. 1–3, pp. 241–246, 2004.
- [3] R. L. Pozzo, M. A. Baltanás, and A. E. Cassano, "Supported titanium oxide as photocatalyst in water decontamination: state of the art," *Catalysis Today*, vol. 39, no. 3, pp. 219–231, 1997.
- [4] Q. Sun, Y. Lu, H. Zhang et al., "Hydrothermal fabrication of rutile TiO₂ submicrospheres on wood surface: an efficient method to prepare UV-protective wood," *Materials Chemistry and Physics*, vol. 133, no. 1, pp. 253–258, 2012.
- [5] J. Sun, L. Gao, and Q. Zhang, "Synthesizing and comparing the photocatalytic properties of high surface area rutile and anatase titania nanoparticles," *Journal of the American Ceramic Society*, vol. 86, no. 10, pp. 1677–1682, 2003.
- [6] D. C. Hurum, A. G. Agrios, K. A. Gray, T. Rajh, and M. C. Thurnauer, "Explaining the enhanced photocatalytic activity of Degussa P25 mixed-phase TiO₂ using EPR," *The Journal of Physical Chemistry B*, vol. 107, no. 19, pp. 4545–4549, 2003.
- [7] X.-H. Xia, Z.-J. Jia, Y. Yu, Y. Liang, Z. Wang, and L.-L. Ma, "Preparation of multi-walled carbon nanotube supported TiO₂ and its photocatalytic activity in the reduction of CO₂ with H₂O," *Carbon*, vol. 45, no. 4, pp. 717–721, 2007.
- [8] Y. Yu, J. C. Yu, C.-Y. Chan et al., "Enhancement of adsorption and photocatalytic activity of TiO₂ by using carbon nanotubes for the treatment of azo dye," *Applied Catalysis B: Environmental*, vol. 61, no. 1–2, pp. 1–11, 2005.
- [9] Y. Yu, J. C. Yu, J.-G. Yu et al., "Enhancement of photocatalytic activity of mesoporous TiO₂ by using carbon nanotubes," *Applied Catalysis A: General*, vol. 289, no. 2, pp. 186–196, 2005.
- [10] Z.-S. Wu, W. Ren, L. Wen et al., "Graphene anchored with Co₃O₄ nanoparticles as anode of lithium ion batteries with enhanced reversible capacity and cyclic performance," *ACS Nano*, vol. 4, no. 6, pp. 3187–3194, 2010.
- [11] X. Zheng, D. Guo, Y. Shao et al., "Photochemical modification of an optical fiber tip with a silver nanoparticle film: a SERS chemical sensor," *Langmuir*, vol. 24, no. 8, pp. 4394–4398, 2008.
- [12] J. M. Miller, B. Dunn, T. D. Tran, and R. W. Pekala, "Deposition of ruthenium nanoparticles on carbon aerogels for high energy density supercapacitor electrodes," *Journal of the Electrochemical Society*, vol. 144, no. 12, pp. L309–L311, 1997.
- [13] C. D. Saquing, D. Kang, M. Aindow, and C. Erkey, "Investigation of the supercritical deposition of platinum nanoparticles into carbon aerogels," *Microporous and Mesoporous Materials*, vol. 80, no. 1, pp. 11–23, 2005.
- [14] J. Cai, S. Kimura, M. Wada, and S. Kuga, "Nanoporous cellulose as metal nanoparticles support," *Biomacromolecules*, vol. 10, no. 1, pp. 87–94, 2009.
- [15] R. J. Moon, A. Martini, J. Nairn, J. Simonsen, and J. Youngblood, "Cellulose nanomaterials review: structure, properties and nanocomposites," *Chemical Society Reviews*, vol. 40, no. 7, pp. 3941–3994, 2011.
- [16] P. Tingaut, T. Zimmermann, and G. Sèbe, "Cellulose nanocrystals and microfibrillated cellulose as building blocks for the design of hierarchical functional materials," *Journal of Materials Chemistry*, vol. 22, no. 38, pp. 20105–20111, 2012.
- [17] N. D. Luong, Y. Lee, and J.-D. Nam, "Highly-loaded silver nanoparticles in ultrafine cellulose acetate nanofibrillar aerogel," *European Polymer Journal*, vol. 44, no. 10, pp. 3116–3121, 2008.
- [18] Y. Lu, Q. Sun, J. Li, and Y. Liu, "Fabrication, characterization and photocatalytic activity of TiO₂/cellulose composite aerogel," *Key Engineering Materials*, vol. 609–610, pp. 542–546, 2014.
- [19] T. W. Hamann, A. B. F. Martinson, J. W. Elam, M. J. Pellin, and J. T. Hupp, "Atomic layer deposition of TiO₂ on aerogel templates: new photoanodes for dye-sensitized solar cells," *The Journal of Physical Chemistry C*, vol. 112, no. 27, pp. 10303–10307, 2008.

- [20] M. Kusabe, H. Kozuka, S. Abe, and H. Suzuki, "Sol-gel preparation and properties of hydroxypropylcellulose-titania hybrid thin films," *Journal of Sol-Gel Science and Technology*, vol. 44, no. 2, pp. 111–118, 2007.
- [21] H. Shin, D.-K. Jeong, J. Lee, M. M. Sung, and J. Kim, "Formation of TiO₂ and ZrO₂ nanotubes using atomic layer deposition with ultraprecise control of the wall thickness," *Advanced Materials*, vol. 16, no. 14, pp. 1197–1200, 2004.
- [22] L. Melone, L. Altomare, I. Alfieri, A. Lorenzi, L. de Nardo, and C. Punta, "Ceramic aerogels from TEMPO-oxidized cellulose nanofibre templates: synthesis, characterization, and photocatalytic properties," *Journal of Photochemistry and Photobiology A: Chemistry*, vol. 261, pp. 53–60, 2013.
- [23] N. S. Venkataramanan, K. Matsui, H. Kawanami, and Y. Ikushima, "Green synthesis of titania nanowire composites on natural cellulose fibers," *Green Chemistry*, vol. 9, no. 1, pp. 18–19, 2007.
- [24] K. Nelson and Y. Deng, "Enhanced light scattering from hollow polycrystalline TiO₂ particles in a cellulose matrix," *Langmuir*, vol. 24, no. 3, pp. 975–982, 2008.
- [25] J. Li, C. C. Wan, Y. Lu, and Q. F. Sun, "Fabrication of cellulose aerogel from wheat straw with strong absorptive capacity," *Frontiers of Agricultural Science and Engineering*, vol. 1, no. 1, pp. 46–52, 2014.
- [26] B. Wang, R. Karthikeyan, X.-Y. Lu, J. Xuan, and M. K. Leung, "High photocatalytic activity of immobilized TiO₂ nanorods on carbonized cotton fibers," *Journal of Hazardous Materials*, vol. 263, part 2, pp. 659–669, 2013.
- [27] B. Erdem, R. A. Hunsicker, G. W. Simmons, E. David Sudol, V. L. Dimonie, and M. S. El-Aasser, "XPS and FTIR surface characterization of TiO₂ particles used in polymer encapsulation," *Langmuir*, vol. 17, no. 9, pp. 2664–2669, 2001.
- [28] C. Hu, S. Duo, T. Liu, W. Li, and R. Zhang, "Low temperature facile synthesis of anatase TiO₂ coated multiwalled carbon nanotube nanocomposites," *Materials Letters*, vol. 64, no. 22, pp. 2472–2474, 2010.
- [29] W.-J. Gong, H.-W. Tao, G.-L. Zi et al., "Visible light photodegradation of dyes over mesoporous titania prepared by using chrome azurol S as template," *Research on Chemical Intermediates*, vol. 35, no. 6-7, pp. 751–760, 2009.
- [30] J. Ye, W. Liu, J. Cai et al., "Nanoporous anatase TiO₂ mesocrystals: additive-free synthesis, remarkable crystalline-phase stability, and improved lithium insertion behavior," *Journal of the American Chemical Society*, vol. 133, no. 4, pp. 933–940, 2011.
- [31] P. Mansikkamäki, M. Lahtinen, and K. Rissanen, "Structural changes of cellulose crystallites induced by mercerisation in different solvent systems; determined by powder X-ray diffraction method," *Cellulose*, vol. 12, no. 3, pp. 233–242, 2005.
- [32] T. J. Trentler, T. E. Denler, J. F. Bertone, A. Agrawal, and V. L. Colvin, "Synthesis of TiO₂ nanocrystals by nonhydrolytic solution-based reactions," *Journal of the American Chemical Society*, vol. 121, no. 7, pp. 1613–1614, 1999.
- [33] F. Shafizadeh and A. Bradbury, "Thermal degradation of cellulose in air and nitrogen at low temperatures," *Journal of Applied Polymer Science*, vol. 23, no. 5, pp. 1431–1442, 1979.
- [34] D. C. Schnitzler and A. J. Zarbin, "Organic/inorganic hybrid materials formed from TiO₂ nanoparticles and polyaniline," *Journal of the Brazilian Chemical Society*, vol. 15, no. 3, pp. 378–384, 2004.
- [35] H. Wang, W. Zhong, P. Xu, and Q. Du, "Polyimide/silica/titania nanohybrids via a novel non-hydrolytic sol-gel route," *Composites Part A: Applied Science and Manufacturing*, vol. 36, no. 7, pp. 909–914, 2005.
- [36] Q. Yu, P. Wu, P. Xu, L. Li, T. Liu, and L. Zhao, "Synthesis of cellulose/titanium dioxide hybrids in supercritical carbon dioxide," *Green Chemistry*, vol. 10, no. 10, pp. 1061–1067, 2008.
- [37] D. Sun, J. Yang, and X. Wang, "Bacterial cellulose/TiO₂ hybrid nanofibers prepared by the surface hydrolysis method with molecular precision," *Nanoscale*, vol. 2, no. 2, pp. 287–292, 2010.
- [38] W.-L. Guo, Z.-X. Yang, and X.-K. Wang, "Sonochemical deposition and characterization of nanophasic TiO₂ on silica particles," *Materials Research Innovations*, vol. 10, no. 1, pp. 11–13, 2006.
- [39] I. Moon, S. Vigneswaran, and R. Thiruvengkatachari, "A review on UV/TiO₂ photocatalytic oxidation process," 2008.
- [40] N. A. Laoufi, D. Tassalit, and F. Bentahar, "The degradation of phenol in water solution by TiO₂ photocatalysis in a helical reactor," *Global Nest Journal*, vol. 10, no. 3, pp. 404–418, 2008.
- [41] U. Sirimahachai, N. Ndiege, R. Chandrasekharan, S. Wongnawa, and M. A. Shannon, "Nanosized TiO₂ particles decorated on SiO₂ spheres (TiO₂/SiO₂): synthesis and photocatalytic activities," *Journal of Sol-Gel Science and Technology*, vol. 56, no. 1, pp. 53–60, 2010.
- [42] M. Rani, N. Gupta, and B. Pal, "Superior photodecomposition of pyrene by metal ion-loaded TiO₂ catalyst under UV light irradiation," *Environmental Science and Pollution Research*, vol. 19, no. 6, pp. 2305–2312, 2012.
- [43] M. Răileanu, M. Crișan, I. Nițoi et al., "TiO₂-based nanomaterials with photocatalytic properties for the advanced degradation of xenobiotic compounds from water. A literature survey," *Water, Air, and Soil Pollution*, vol. 224, no. 6, article 1548, 2013.

Research Article

Fabrication of Robust Superhydrophobic Bamboo Based on ZnO Nanosheet Networks with Improved Water-, UV-, and Fire-Resistant Properties

Jingpeng Li, Qingfeng Sun, Qiufang Yao, Jin Wang, Shenjie Han, and Chunde Jin

School of Engineering, Zhejiang Agricultural and Forestry University, Lin'an 311300, China

Correspondence should be addressed to Chunde Jin; zafujincd@163.com

Received 12 August 2014; Accepted 2 September 2014

Academic Editor: Ivan C. K. Tan

Copyright © 2015 Jingpeng Li et al. This is an open access article distributed under the Creative Commons Attribution License, which permits unrestricted use, distribution, and reproduction in any medium, provided the original work is properly cited.

Bamboo with water-resistant, UV-resistant, and fire-resistant properties was desirable in modern society. In this paper, the original bamboo was firstly treated with ZnO sol and then hydrothermally the ZnO nanosheet networks grow onto the bamboo surface and subsequently modified with fluoroalkyl silane (FAS-17). The FAS-17 treated bamboo substrate exhibited not only robust superhydrophobicity with a high contact angle of 161° but also stable repellency towards simulated acid rain (pH = 3) with a contact angle of 152° . Except for its robust superhydrophobicity, such a bamboo also presents superior water-resistant, UV-resistant, and fire-resistant properties.

1. Introduction

Bamboo is one of the most important nontimber forest products in the world [1, 2]. More than 1 billion people are living in bamboo houses, and the livelihoods of 2.5 billion people depend on this resource, making the bamboo increasingly be recognized as an environmental-friendly and cost-effective wood substitute [3]. As a fast-growing lignocelluloses material with high strength and surface hardness, easy machinability, and local availability, bamboo is widely used in the traditional applications, such as furniture, construction, pulping, and handicrafts [4–6]. However, when exposed in an outdoor environment, bamboo shows bad decay-resistance without protective treatment that would be attacked by fungi and insects and degraded caused by moisture, air, acid rain, and sunlight and thus shortens its service life and also reduces its value [7, 8]. To overcome this problem and enhance the economic value of bamboo products, it is necessary to develop a protective treatment for bamboo materials. In the previous studies, there were several approaches to improve water-repellency, fire-resistance, and UV-resistance of cellulose-based materials [9–14], for example, immersion-diffusion or vacuum-impregnation with

preservatives, heating, dipping, soaking, brushing paint, and surface modification.

Among these, surface modification has been used to improve the ultraviolet stability of bamboo, change the surface energy of bamboo (reduce wetting by water and/or improve compatibility with coatings or matrix materials), and improve the bonding between bamboo surfaces and inorganic materials. In the past decade, the modifications by using of inorganic materials, such as ZnO, SiO₂, TiO₂, and CaCO₃ through sol-gel or hydrothermal synthesis have been devoted to reach this goal [15, 16]. Nowadays, as one of the most interesting multifunctional material, ZnO has a promising application in various fields of solar cells [17], displays [18], gas sensors [19], varistors [20], piezoelectric devices [21], photodiodes [22], UV light emitting devices, and a photostabilizer [23]. Thus, after surface modification, the bamboo-inorganic composites could be attached with photostability and antibacterial properties [16], and the coating of inorganic materials may also impart new properties such as superhydrophobicity, UV-resistance, and antimicrobial properties to the bamboo. In recent years, many researchers have reported the role of ZnO nanoparticles in exterior coatings to improve photostability, as a component of UV

coatings for nanocomposites or modeling UV permeability of nano-ZnO filled coatings [24–26]. However, there are few reports on treating bamboo with nanomaterials or the effects of the nanomaterials on bamboo durability.

In the present study, the bamboo with multifunction of superhydrophobicity, UV-resistance, and fire-resistance was successfully fabricated by coating with ZnO nanosheet networks via a hydrothermal method and subsequent modification with FAS-17. The morphologies and chemical compositions were examined by scanning electron microscopy (SEM), energy dispersive spectroscopy (EDS), X-ray diffraction (XRD), and thermogravimetric and differential thermal analysis (TG-DTA). Water contact angle (WCA) was employed to measure superhydrophobicity of the prepared bamboo surface and the repellency towards simulated acid rain. Meanwhile, the fire-resistance was also illustrated in the paper.

2. Experimental Section

2.1. Materials. All the chemicals were purchased from Shanghai Boyle Chemical Company Limited and were all of analytical reagent grade. Bamboo samples of 10 (Length) × 10 (Width) × 4 (Height) mm³ were cleaned with deionized water and ethanol before drying for use.

2.2. Preparation of ZnO Sol. The ZnO sol was prepared based on the method of Jung et al. [27] with some modifications. Zinc acetate dehydrate (0.75 M) was dissolved in ethanol at 60°C under vigorous stirring. Then the resulting solution was added slowly to a solution of monoethanolamine (MEA) with volume ratio of 1 : 1 and subsequently stirred at 60°C for 0.5 h. The ZnO sol was thus obtained.

2.3. Growth of ZnO Nanosheet Networks on the Bamboo Surface. Bamboo samples with ZnO seed layers were fabricated through a simple dip-coating process. Then the samples were dried at 80°C for 5 h. This process was repeated 5 times. The growth of ZnO nanosheet networks on the bamboo substrate was performed as follows: Equimolar aqueous solutions (0.05 M) of zinc nitrate hexahydrate (Zn(NO₃)₂·6H₂O) and hexamethylenetetramine (C₆H₁₂N₄, HMTA) were prepared in a vessel under constant stirring, and, then, 0.04 M urea was added. The mixed solution was vigorously stirred for 30 minutes until it became clear and then the clear solution was transferred into a Teflon-lined autoclave. The treated bamboo substrates were then immersed in the above solution for 3 h at 90°C. Finally, the samples were rinsed with deionized water and dried at 80°C for 24 h. For comparative studies, the blank bamboo samples were also selected and the original bamboo was abbreviated as OB.

2.4. Surface Modification. The surface modification carried out by chemical vapor deposition of FAS-17 was illustrated in Figure 1. The ZnO nanosheet networks treated bamboo (hereafter abbreviated as ZNB) was placed in a sealed vessel with a smaller unsealed vessel within a small amount of FAS-17 on its bottom. The sealed vessel was then put in an oven

and heated at 130°C to enable the silane groups of FAS-17 vapor to react with the hydroxide groups from ZNB. After 3 h, the bamboo substrate was removed to another clean sealed vessel and heated at 140°C for 1 h to volatilize the residual FAS-17 molecules onto the bamboo substrate. The original bamboo sample modified with FAS-17 was abbreviated as FB. The FAS-17/ZnO nanosheet networks treated bamboo sample was abbreviated as FZNB.

2.5. Characterizations. Surface morphologies of the samples were characterized by scanning electron microscopy (SEM, FEI, Quanta 200). The surface chemical compositions of the samples were determined via energy-dispersive X-ray analysis (EDS, Genesis, EDAX) connected with SEM. Crystalline structures of the samples were identified by X-ray diffraction technique (XRD, Rigaku, D/MAX 2200) operating with Cu K α radiation ($\lambda = 1.5418 \text{ \AA}$) at a scan rate (2θ) of 4 min^{-1} , 40 Kv, 40 mA ranging from 5° to 80°. Water contact angle (WCA) was measured on an OCA40 contact angle system (Dataphysics, Germany) at room temperature. The final value of the WCA was obtained as an average of five measurements. Thermogravimetric and differential thermal analysis (TG-DTA) were performed using a PE-TGA7 thermogravimetric analyzer (Perkin Elmer Company) and a DTA/9050311 high temperature differential analyzer. 10 mg of the samples were taken and measured in air and then treated in 150 mL/min of dry pure N₂ with temperatures at the rate of 10°C/min ranging from 20°C to 700°C.

2.6. Accelerated Aging Test. The weathering was performed with an Accelerated Weathering Tester (Q-Panel, Cleveland, OH, USA), which allowed water spray and condensation. The samples were fixed in stainless steel holders and then rotated under irradiation of fluorescent UV light at 60°C for 0.5 h, followed by water spraying for 0.5 h and condensation at 45°C for 3 h. The irradiation energy was 35 W/m² and the spray temperature 25°C. The exposure time ranged from 0 h to 120 h. The color of all samples was determined before and after UV irradiation at regular intervals with a portable spectrophotometer (NF-333, Nippon Denshoku Company, Japan) equipped with a CIE-LAB system. Here, the parameters represent L^* , a^* , and b^* lightness, which varies from 100 (white) to 0 (black) and chromaticity indices ($+a^*$ red, $-a^*$ green, $+b^*$ yellow, and $-b^*$ blue).

The changes in L^* , a^* , and b^* were calculated according to (1), as follows:

$$\begin{aligned}\Delta a^* &= a_2 - a_1, \\ \Delta b^* &= b_2 - b_1, \\ \Delta L^* &= L_2 - L_1,\end{aligned}\quad (1)$$

where Δ means the difference between the indicated initial and final parameters after UV irradiation. The overall color changes (ΔE^*) were used to evaluate the total color change using (2). Consider

$$\Delta E^* = \left((L_2^* - L_1^*)^2 + (a_2^* - a_1^*)^2 + (b_2^* - b_1^*)^2 \right)^{1/2}. \quad (2)$$

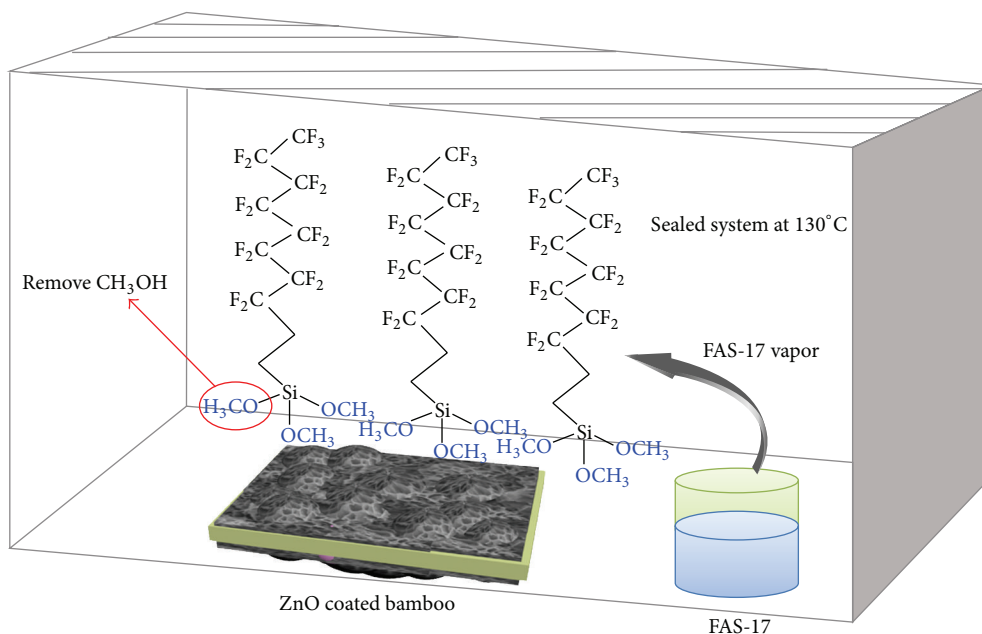


FIGURE 1: Schematic illustration of the surface modification on ZnO-coated bamboo surface.

A lower ΔE^* value corresponds to a smaller color difference and indicates strong resistance to UV radiation. CIE- L^* , a^* , b^* , and ΔE were measured at five locations on each sample, and the average values were calculated.

3. Results and Discussion

3.1. Characterization of ZnO Nanosheet Networks. SEM images were used to illustrate the morphology of OB and ZNB. As shown in Figure 2(a), the SEM image of OB showed smooth and clean surface. In Figure 2(b), the ZnO nanosheet networks appeared on the bamboo substrate and the bamboo surface became rougher in a result of coating with a dense film of ZnO nanostructured materials. In the magnified SEM image (Figure 2(c)), the ZnO nanosheet networks were slightly curved and the surface seemed to be uneven on a large scale. The average width and height for observation of the ZnO nanosheets was about 80 nm and 3 μm , respectively. The surface chemical elemental compositions of the ZNB were determined via EDS, and the results are presented as an insertion in Figure 2(b). Only carbon, oxygen, zinc, and gold elements could be detected from the EDS spectrum. Gold element was from the coating layer used for the EDS measurement and carbon element was originated from the bamboo substrates. No other elements were detected, confirming that the pure ZnO nanosheet networks were effectively formed on the bamboo surface. In Figure 2(d), the diffraction peaks at 16° and 22° represented the characteristic diffraction peaks of the cellulose from bamboo substrate [28, 29]. All others diffraction peaks could be indexed to the wurtzite ZnO (JCPDS card No. 36-1451). No other characteristic peaks were observed, indicating that pure wurtzite ZnO were formed on the bamboo surface after the hydrothermal process.

3.2. WCAs Test. With hydroxyl groups covering the surface, the OB was intrinsically hydrophilic and the water would fastly wet the surface, so WCAs were measured as soon as the water droplets contacted the samples surface. However, for the FB and FZNB, WCAs were achieved after contacted with the surfaces for 5 min. As shown in Figure 3, the WCA of OB was 12° for 5 μL water droplet, after modification with FAS-17, the FB became hydrophobicity with the WCA of 126° , and the FZNB was superhydrophobic with the WCA of 161° . As the results showed, both the surface energy and surface roughness deeply affected the degree of hydrophobicity of the surface, which was represented as water contact angle. The sliding angle of the FZNB was lower than 3° , indicating the water droplets could roll off the surface easily. Besides the excellent superhydrophobicity, FZNB exhibited stable repellency towards simulated acid rain (pH = 3) with a contact angle of 152° (Figure 3(d)). Thus, such an as-prepared surface would have the anticorrosion property against acid rain in the atmosphere environment.

A further understanding of the hydrophobicity of as-prepared samples could be obtained from the Cassie-Baxter equation, $\cos \theta_r = f_1 \cos \theta - f_2$. θ_r was the apparent contact angle measured on the interested bamboo surface; θ (100°) was the water contact angle on fluoridated smooth surface [30]; f_1 and f_2 were the fractional areas estimated for the solid and air on the surface, respectively; that is, $f_1 + f_2 = 1$. Here, the CA value of FB was 126° (θ_r) and the f_1 calculated using Cassie-Baxter equation was 0.49, which indicated that 51% of the surface was occupied by air. However, for FZNB ($\theta_r = 161^\circ$), the f_1 was 0.05, which indicated that about 95% of the surface was occupied by air. The surface allowed air to be trapped more easily underneath the water droplets,

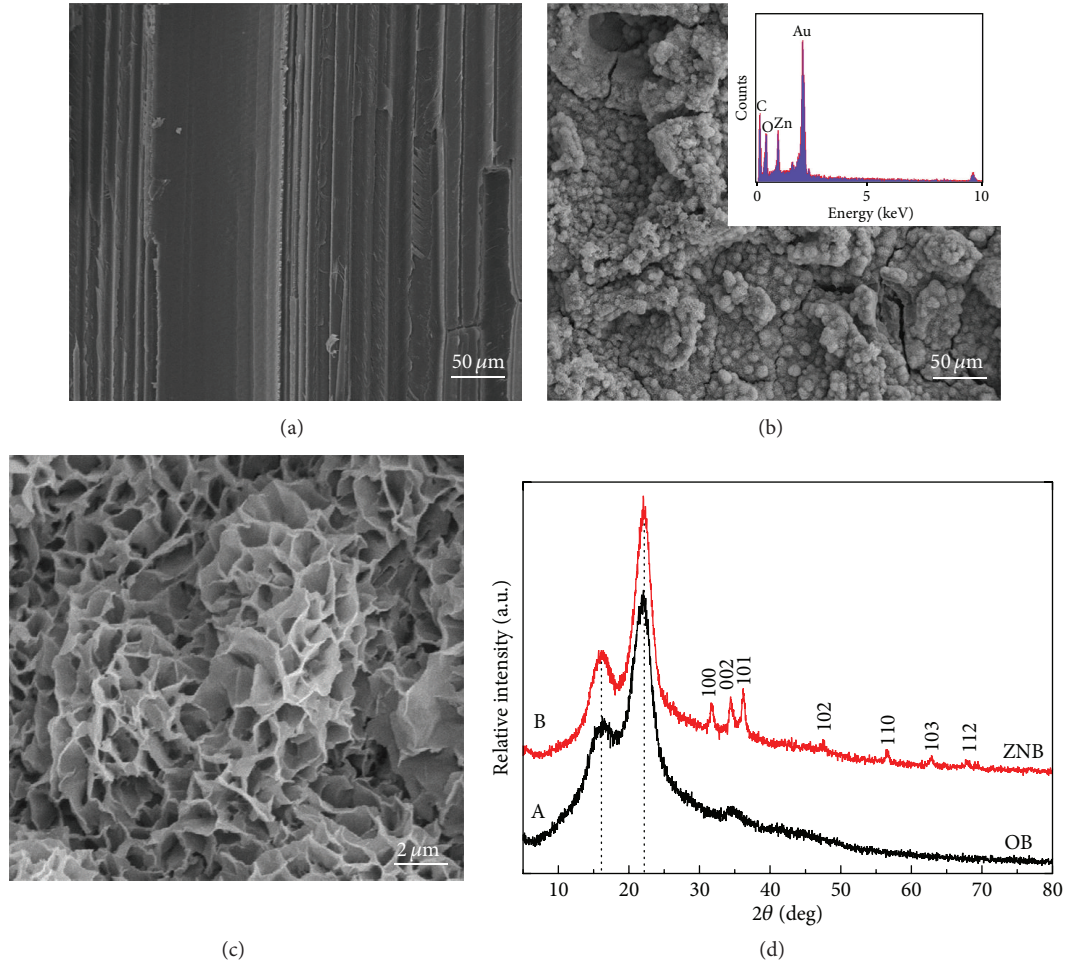


FIGURE 2: SEM images of (a) OB and ZNB at low (b) and high (c) magnification. The inset of (b) was EDS spectrum of ZNB. (d) XRD patterns of OB and ZNB, respectively.

so that the water droplets essentially rested on a layer of air. Therefore, WCAs of the FZNB increased significantly.

Except for superhydrophobicity, the FZNB showed a low adhesion to water. The water droplet could hardly stick to the bamboo surface, allowing water droplets to roll off from one side of the surface freely (Figure 4(a)). As the descent height of the water droplet increased, it could bounce up from the bamboo surface without any deformation (Figure 4(b)). In addition, the WCA values of the as-prepared surfaces were constant after storage for more than six months under ambient conditions. These performances confirmed the stable superhydrophobicity of FZNB under ambient conditions.

3.3. Water Absorption Properties. Water absorption is one of the most important characteristics of bamboo exposed to environmental conditions that determines their ultimate applications. In this study, the water resistance of the OB, FB, and FZNB was investigated. The experiments were carried out by immersing as-prepared specimens in water for 130 h at room temperature, followed by measuring the moisture content (%) and WCA (°) of the as-prepared specimens.

The moisture content of specimen was calculated by the following equation:

$$\text{moisture content (\%)} = \frac{\text{weight of specimen} - \text{weight of dry specimen}}{\text{weight of dry specimen}} \quad (3)$$

where the weight of dry specimen was obtained by drying bamboo specimen at 105°C until a constant weight was obtained.

As shown in Figure 5, it was found that the moisture content of the FZNB increased to 80% after the specimen was fully immersing in water for 24 h. After the specimen was fully immersing in water for 130 h, the moisture content of the FZNB was still around 80%, whereas the OB specimen and the FB specimen could absorb up to 180% and 200% water, respectively. After 24 h immersion, the moisture content of the FB was higher than that of the OB, which might due to the FAS-17 coated on the surface of OB be further hydrolyzed in water following the increasing time of immersion. It was also found that WCA of the FZNB maintained 152° after immersing in water for 130 h (Figure 5, inset), which

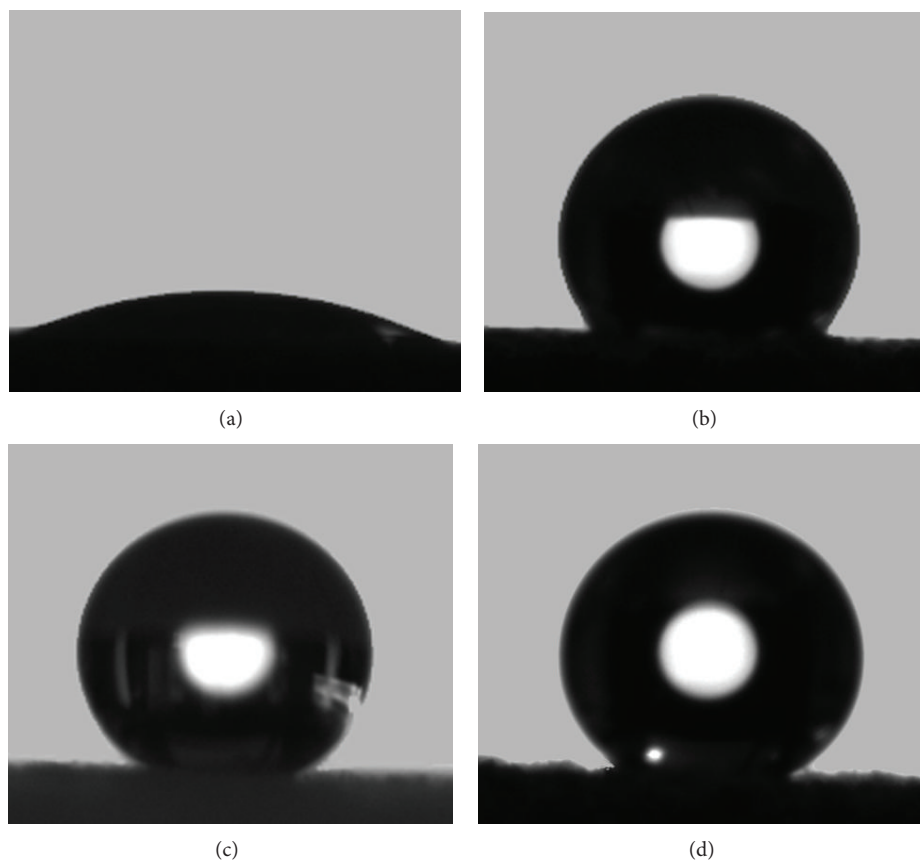


FIGURE 3: Shapes of water droplet on (a) OB, (b) FB, and (c) FZNB, respectively. (d) Shape of simulated acid rain (pH = 3) on FZNB.

demonstrated that the extremely high water resistance of the FZNB was obtained. The performance of the water resistance verified the FZNB would be a great potential for the applications in the environment with higher moist.

3.4. UV Resistance Study. The experimental results of color change upon UV irradiation were presented in Figure 6. Compared to OB, the ΔL^* value of the FZNB sample became positive, indicating that the light-colored bamboo turned white (Figure 6(a)). On the other hand, the ΔL^* value of the OB became negative, indicating that the light-colored bamboo turned black. The Δb^* value of the OB and FZNB specimens indicated that the surfaces colors turned dark yellow and slight yellow, respectively, with prolonged UV irradiation time (Figure 6(b)). More importantly, the Δa^* value of the OB under UV irradiation indicated that the surface color turned a deeper shade of red with increasing UV irradiation. The Δa^* of the FZNB sample showed a similar trend; however, the change in the FZNB Δa^* was much smaller than that of OB (Figure 6(c)). The total color change (ΔE^*) of OB was significant (Figure 6(d)), whereas for the FZNB was very slight. These results showed that FZNB exhibited an excellent UV resistance and prevented bamboo surface from damage.

3.5. Thermal Stability. The results of the TG-DTA analysis were shown in Figure 7. According to the TG curve

(Figure 7(a)), there was a small weight loss at about 50–80°C due to the loss of physically adsorbed water, which come from the ambient environment [31]. The three stages of the thermal degradation of the OB were clearly visible. At stage one (190–250°C), the pyrolysis rate was low with the weight loss of approximately 13%, which is mainly due to the partial degradation of hemicellulose [32]. Stage two (250–400°C) was mainly caused by cellulose degradation, accompanied with continuous degradation of lignin, whose maximum pyrolysis rate occurred at 375°C and the weight loss reached 68% [33]. At stage three (400–700°C), all the components of bamboo degraded gradually leading to aromatization and carbonization. Lignin was the most difficult one to decompose. Its decomposition happened slowly and kept on along the whole calcining process [34, 35]. At last, carbon residues with the weight of 8.9% were left, as observed from the TG curve (Figure 7(a)). For the ZNB and FZNB specimens, the TG curve exhibited the weight losses at about 170–240°C, which were caused by the decomposition of the residual organics and MEA [36, 37]. And the DTA curve (Figure 7(b)) presented strong and sharp endothermic peaks at a minimum of 356°C for ZNB and 347°C for CZNB, respectively, corresponding to the weight losses shown in the TG curve (Figure 7(a)). Due to the decomposition of cellulose and lignin, the maximum degradation rates of the ZNB and FZNB became lower than of the OB. This might be due to the catalysis of ZnO, which generated an accelerated pyrolysis

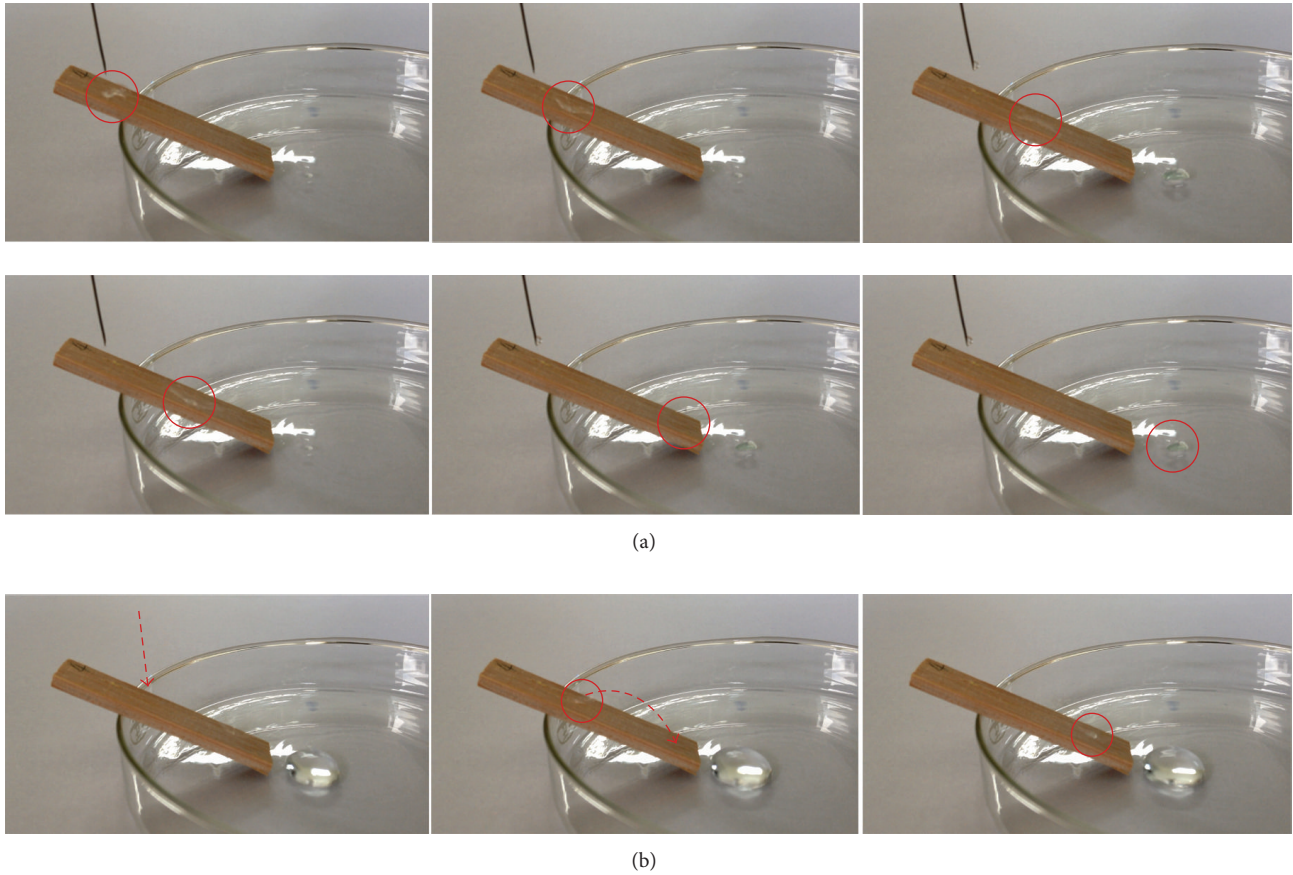


FIGURE 4: The rolling process of a water droplet on the superhydrophobic bamboo surface.

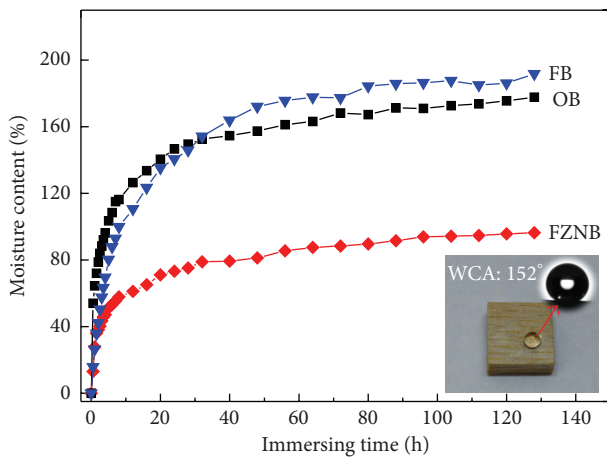


FIGURE 5: Moisture content of OB, FB, and FZNB, respectively. The inset was the WCA of FZNB after immersing in water to 130 h.

action on bamboo components. Moreover, the maximum degradation rate of the FZNB was the lowest (Figure 7(b)), which might be due to the decomposition of FAS-17 (a barrier effectively protected for the ZNB). Computable weight loss along the whole process was about 91.1% for OB, 78.3% for ZNB, and 73.2% for FZNB, respectively.

3.6. Fire-Resistant Properties. In order to describe a realistic fire scenario, it was important to test the ignitability of the OB and FZNB samples in the presence of a flame spread. Interestingly, the as-prepared FZNB sample exhibited excellent fire-resistance when exposed to the flame of the alcohol burner. A significant difference could be observed in Figure 8 where some typical pictures of the specimens after the flammability test were collected. When heated with the alcohol burner, the OB caught on fire at 3 s and was incinerated to ash in 101 s. Being burned for 24 s, the OB sample had a massive blaze. In the following 34 s, the strong flames gradually diminished, but the fire was still spreading. By contrast, the FZNB caught on fire at 16 s, implying that the FAS-17/ZnO films were capable of protecting the bamboo from the flame. Being burned for 46 s, there were no flames standing on the treated bamboo sample. Furthermore, the flames gradually quenched by itself in the following 2 s. After burning out, black char was left. Apparently, the treated bamboo samples were more suitable for functional materials and building materials.

4. Conclusions

In this paper, bamboo with multifunction involved in water-resistant, UV-resistant, and fire-resistant properties was

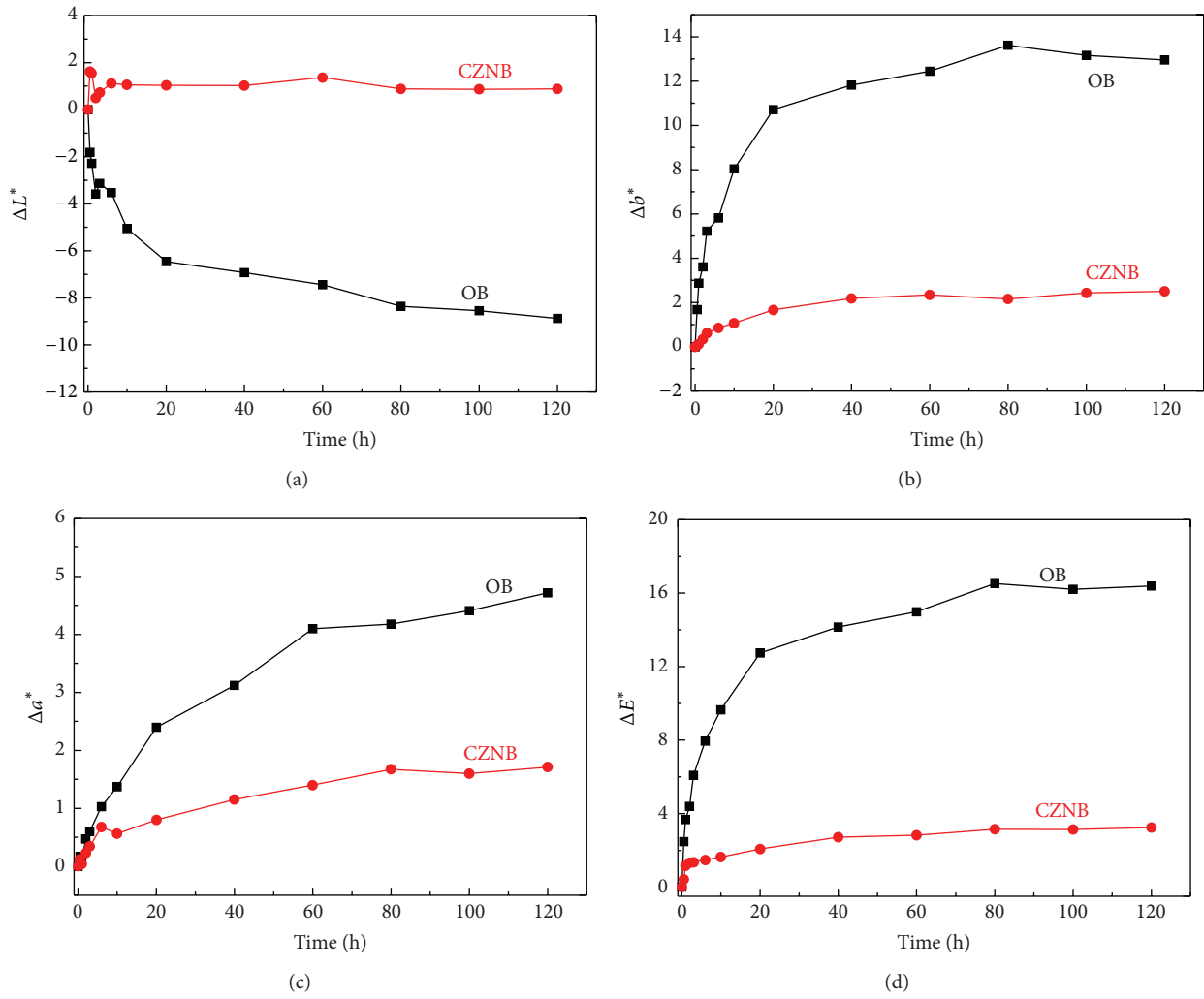


FIGURE 6: Color data of CIE- L^* , a^* , and b^* and ΔE^* measurements of OB and CZNB samples, respectively.

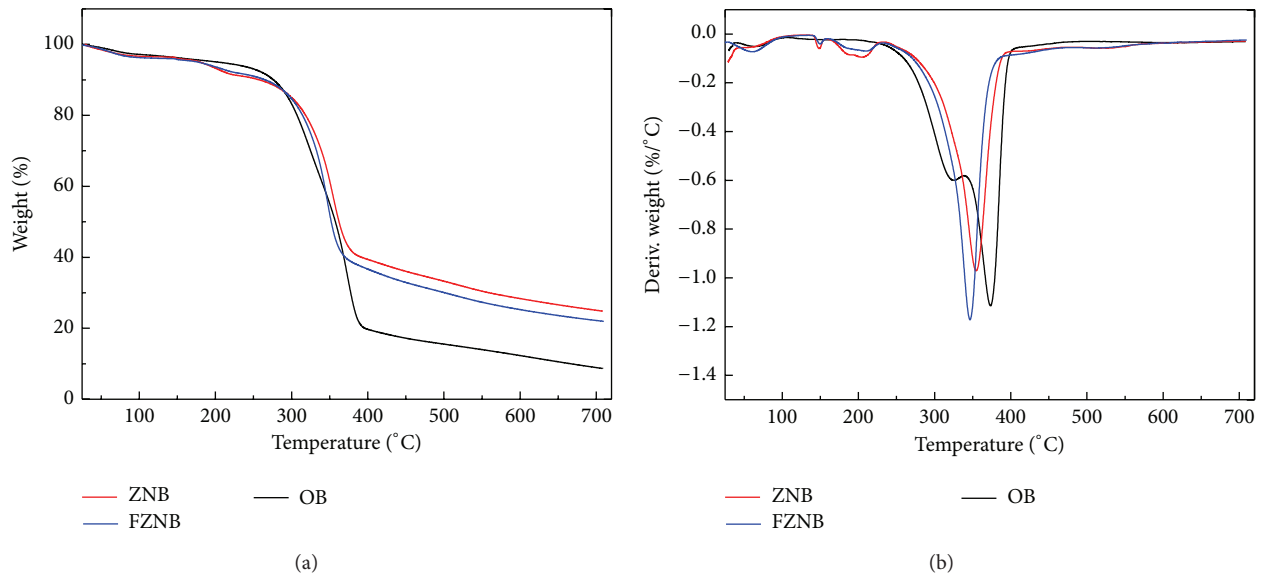


FIGURE 7: TG-DTA curves of OB, ZNB, and FZNB, respectively.

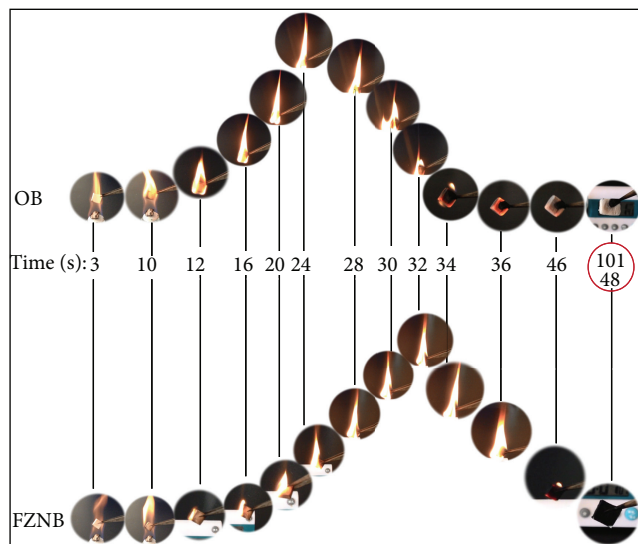


FIGURE 8: Digital photos of OB and FZNB burned at different times, respectively (the as-prepared samples firstly were all heated in an alcohol burner for 12 s).

successfully fabricated by ZnO nanosheet networks deposition, followed by a fluorination treatment. The treated bamboo substrate exhibited not only robust superhydrophobicity but also stable repellency towards simulated acid rain (pH = 3). Furthermore, the treated bamboo presented excellent water-resistant and UV-resistant properties and also exhibited superior fire-resistant property.

Conflict of Interests

The authors declare that there is no conflict of interests regarding the publication of this paper.

Acknowledgments

The work was financially supported by the National Natural Science Foundation of China (31470586) and Pre-research Project of Research Center of Biomass Resource Utilization, Zhejiang A & F University (2013SWZ01-03).

References

- [1] Z. Peng, Y. Lu, L. Li et al., "The draft genome of the fast-growing non-timber forest species moso bamboo (*Phyllostachys heterocycla*)," *Nature Genetics*, vol. 45, no. 4, pp. 456–461, 2013.
- [2] M.-J. Chung, S.-S. Cheng, C.-J. Lee, and S.-T. Chang, "Novel environmentally-benign methods for green-colour protection of bamboo culms and leaves," *Polymer Degradation and Stability*, vol. 96, no. 4, pp. 541–546, 2011.
- [3] Y. Onozawa, M. Chiwa, H. Komatsu, and K. Otsuki, "Rainfall interception in a moso bamboo (*Phyllostachys pubescens*) forest," *Journal of Forest Research*, vol. 14, no. 2, pp. 111–116, 2009.
- [4] X.-Q. Wang and H.-Q. Ren, "Surface deterioration of moso bamboo (*Phyllostachys pubescens*) induced by exposure to artificial sunlight," *Journal of Wood Science*, vol. 55, no. 1, pp. 47–52, 2009.
- [5] X. Wang and H. Ren, "Comparative study of the photo-discoloration of moso bamboo (*Phyllostachys pubescens* Mazel) and two wood species," *Applied Surface Science*, vol. 254, no. 21, pp. 7029–7034, 2008.
- [6] K.-C. Hung, Y.-L. Chen, and J.-H. Wu, "Natural weathering properties of acetylated bamboo plastic composites," *Polymer Degradation and Stability*, vol. 97, no. 9, pp. 1680–1685, 2012.
- [7] K.-T. Lu, "Effects of hydrogen peroxide treatment on the surface properties and adhesion of ma bamboo (*Dendrocalamus latiflorus*)," *Journal of Wood Science*, vol. 52, no. 2, pp. 173–178, 2006.
- [8] S.-T. Chang, T.-F. Yeh, and J.-H. Wu, "Mechanisms for the surface colour protection of bamboo treated with chromated phosphate," *Polymer Degradation and Stability*, vol. 74, no. 3, pp. 551–557, 2001.
- [9] M. Dunlap, "Protection wood from moisture," *Industrial & Engineering Chemistry*, vol. 18, no. 12, pp. 1230–1232, 1926.
- [10] Y. Lu, S. Xiao, R. Gao, J. Li, and Q. Sun, "Improved weathering performance and wettability of wood protected by CeO₂ coating deposited onto the surface," *Holzforschung*, vol. 68, no. 3, pp. 345–351, 2014.
- [11] Q. Sun, H. Yu, Y. Liu, J. Li, Y. Cui, and Y. Lu, "Prolonging the combustion duration of wood by TiO₂ coating synthesized using cosolvent-controlled hydrothermal method," *Journal of Materials Science*, vol. 45, no. 24, pp. 6661–6667, 2010.
- [12] J. R. Loferski, "Technologies for wood preservation in historic preservation," *Archives and Museum Informatics*, vol. 13, no. 3–4, pp. 273–290, 1999.
- [13] Q. Sun, H. Yu, Y. Liu, J. Li, Y. Lu, and J. F. Hunt, "Improvement of water resistance and dimensional stability of wood through titanium dioxide coating," *Holzforschung*, vol. 64, no. 6, pp. 757–761, 2010.
- [14] L. Wang, X. Zhang, B. Li et al., "Superhydrophobic and ultraviolet-blocking cotton textiles," *ACS Applied Materials & Interfaces*, vol. 3, no. 4, pp. 1277–1281, 2011.
- [15] O. Starkova, S. Chandrasekaran, L. A. S. A. Prado, F. Tölle, R. Mühlaupt, and K. Schulte, "Hydrothermally resistant thermally reduced graphene oxide and multi-wall carbon nanotube based epoxy nanocomposites," *Polymer Degradation and Stability*, vol. 98, no. 2, pp. 519–526, 2013.
- [16] Y. Yu, Z. Jiang, G. Wang, G. Tian, H. Wang, and Y. Song, "Surface functionalization of bamboo with nanostructured ZnO," *Wood Science and Technology*, vol. 46, no. 4, pp. 781–790, 2012.
- [17] T. Kuwabara, Y. Kawahara, T. Yamaguchi, and K. Takahashi, "Characterization of inverted-type organic solar cells with a ZnO layer as the electron collection electrode by ac impedance spectroscopy," *ACS Applied Materials and Interfaces*, vol. 1, no. 10, pp. 2107–2110, 2009.
- [18] B.-Y. Oh, M.-C. Jeong, T.-H. Moon et al., "Transparent conductive Al-doped ZnO films for liquid crystal displays," *Journal of Applied Physics*, vol. 99, no. 12, Article ID 124505, 2006.
- [19] X. Wang, W. Liu, J. Liu et al., "Synthesis of nestlike ZnO hierarchically porous structures and analysis of their gas sensing properties," *ACS Applied Materials and Interfaces*, vol. 4, no. 2, pp. 817–825, 2012.
- [20] K. Mukae, K. Tsuda, and I. Nagasawa, "Capacitance-vs-voltage characteristics of ZnO varistors," *Journal of Applied Physics*, vol. 50, no. 6, pp. 4475–4476, 1979.
- [21] B. J. M. Velazquez, S. Baskaran, A. V. Gaikwad et al., "Effective piezoelectric response of substrate-integrated ZnO nanowire

- array devices on galvanized steel," *ACS Applied Materials & Interfaces*, vol. 5, no. 21, pp. 10650–10657, 2013.
- [22] L. Luo, Y. Zhang, S. S. Mao, and L. Lin, "Fabrication and characterization of ZnO nanowires based UV photodiodes," *Sensors and Actuators A: Physical*, vol. 127, no. 2, pp. 201–206, 2006.
- [23] O. Lupan, T. Pauporté, B. Viana, I. M. Tiginyanu, V. V. Ursaki, and R. Cortès, "Epitaxial electrodeposition of ZnO nanowire arrays on p-GaN for efficient UV-light-emitting diode fabrication," *ACS Applied Materials and Interfaces*, vol. 2, no. 7, pp. 2083–2090, 2010.
- [24] M. Beyer, F. Weichelt, R. Emmeler, R. Flyunt, E. Beyer, and M. R. Buchmeiser, "ZnO-based UV nanocomposites for wood coatings in outdoor applications," *Macromolecular Materials and Engineering*, vol. 295, no. 2, pp. 130–136, 2010.
- [25] R. R. Devi and T. K. Maji, "Effect of Nano-ZnO on thermal, mechanical, UV stability, and other physical properties of wood polymer composites," *Industrial and Engineering Chemistry Research*, vol. 51, no. 10, pp. 3870–3880, 2012.
- [26] C. Hegedus, F. Pepe, D. Lindenmuth, and D. Burgard, "Zinc oxide nanoparticle dispersion as unique additives for coatings," *JCT CoatingsTech*, vol. 5, no. 4, pp. 42–52, 2008.
- [27] H. J. Jung, S. Lee, Y. Yu, S. M. Hong, H. C. Choi, and M. Y. Choi, "Low-temperature hydrothermal growth of ZnO nanorods on sol-gel prepared ZnO seed layers: optimal growth conditions," *Thin Solid Films*, vol. 524, pp. 144–150, 2012.
- [28] J. Li, Y. Lu, D. Yang, Q. Sun, Y. Liu, and H. Zhao, "Lignocellulose aerogel from wood-ionic liquid solution (1-allyl-3-methylimidazolium chloride) under freezing and thawing conditions," *Biomacromolecules*, vol. 12, no. 5, pp. 1860–1867, 2011.
- [29] Y. Lu, Q. Sun, D. Yang et al., "Fabrication of mesoporous lignocellulose aerogels from wood via cyclic liquid nitrogen freezing-thawing in ionic liquid solution," *Journal of Materials Chemistry*, vol. 22, no. 27, pp. 13548–13557, 2012.
- [30] H. Yang and Y. Deng, "Preparation and physical properties of superhydrophobic papers," *Journal of Colloid and Interface Science*, vol. 325, no. 2, pp. 588–593, 2008.
- [31] E. Ahmad and A. Luyt, "Effects of organic peroxide and polymer chain structure on morphology and thermal properties of sisal fibre reinforced polyethylene composites," *Composites Part A: Applied Science and Manufacturing*, vol. 43, no. 4, pp. 703–710, 2012.
- [32] X. Li, B. Lei, Z. Lin, L. Huang, S. Tan, and X. Cai, "The utilization of bamboo charcoal enhances wood plastic composites with excellent mechanical and thermal properties," *Materials and Design*, vol. 53, pp. 419–424, 2014.
- [33] H. Essabir, E. Hilali, A. Elgharad et al., "Mechanical and thermal properties of bio-composites based on polypropylene reinforced with Nut-shells of Argan particles," *Materials and Design*, vol. 49, pp. 442–448, 2013.
- [34] H. Yang, R. Yan, H. Chen, D. H. Lee, and C. Zheng, "Characteristics of hemicellulose, cellulose and lignin pyrolysis," *Fuel*, vol. 86, no. 12–13, pp. 1781–1788, 2007.
- [35] H. Yang, R. Yan, H. Chen, C. Zheng, D. H. Lee, and D. T. Liang, "In-depth investigation of biomass pyrolysis based on three major components: hemicellulose, cellulose and lignin," *Energy and Fuels*, vol. 20, no. 1, pp. 388–393, 2006.
- [36] D. Raoufi and T. Raoufi, "The effect of heat treatment on the physical properties of sol-gel derived ZnO thin films," *Applied Surface Science*, vol. 255, no. 11, pp. 5812–5817, 2009.
- [37] J.-H. Lee, K.-H. Ko, and B.-O. Park, "Electrical and optical properties of ZnO transparent conducting films by the sol-gel method," *Journal of Crystal Growth*, vol. 247, no. 1–2, pp. 119–125, 2003.

Research Article

Synthesis, Characterization, and Photocatalytic Activity of g-C₃N₄/KTaO₃ Composites under Visible Light Irradiation

Zhiqing Yong,^{1,2} Jian Ren,^{1,2} Huilin Hu,¹ Peng Li,³ Shuxin Ouyang,^{1,2}
Hua Xu,^{1,2} and Defa Wang^{1,2}

¹TU-NIMS Joint Research Center and Tianjin Key Laboratory of Composite and Functional Materials, School of Materials Science and Engineering, Tianjin University, 92 Weijin Road, Nankai District, Tianjin 300072, China

²Collaborative Innovation Center of Chemical Science and Engineering (Tianjin), 92 Weijin Road, Nankai District, Tianjin 300072, China

³Environmental Remediation Materials Unit, National Institute for Materials Science (NIMS), 1-1 Namiki, Tsukuba, Ibaraki 305-0044, Japan

Correspondence should be addressed to Defa Wang; defawang@tju.edu.cn

Received 2 October 2014; Accepted 3 December 2014

Academic Editor: Chee Kiang Ivan Tan

Copyright © 2015 Zhiqing Yong et al. This is an open access article distributed under the Creative Commons Attribution License, which permits unrestricted use, distribution, and reproduction in any medium, provided the original work is properly cited.

Novel graphitic carbon nitride/KTaO₃ (g-C₃N₄/KTaO₃) nanocomposite photocatalysts have been successfully synthesized via a facile and simple ultrasonic dispersion method. Compared to either g-C₃N₄ or KTaO₃, the composite photocatalysts show significantly increased photocatalytic activity for degradation of Rhodamine B (RhB) under visible light irradiation. The increased photocatalytic performance of the composite could be attributed to the enhanced photogenerated charge carrier separation capacity. Moreover, it is observed that •O₂⁻ is the main active species in the photocatalytic degradation of RhB using the g-C₃N₄/KTaO₃ composite photocatalysts.

1. Introduction

Semiconductor photocatalysis has been regarded as an ideal green chemistry technology in dealing with the globally concerned energy shortage and environment pollution issues. In view of practical application, developing highly active photocatalysts has drawn great attention in recent years. Among the various photocatalytic materials, KTaO₃ has been reported as a unique photocatalyst for hydrogen generation as well as organic pollutant degradation [1, 2]. However, its large band gap (3.6 eV) limits the photoactivity only to the UV light, which covers less than 4% of the solar spectrum.

Recently, Wang and coworkers discovered that the graphitic carbon nitride (g-C₃N₄), a conjugative π structure material, is a metal-free visible-light-driven semiconductor [3]. Due to its narrow band gap (2.7 eV) and high thermal and chemical stability, g-C₃N₄ has attracted extensive interest. However, the photocatalytic efficiency of bare g-C₃N₄ is

greatly limited by the high recombination of photogenerated electron-hole pairs. It has been proved that the composite can promote the generation and separation of photoinduced electron-holes pairs. So far Bi₂WO₆/g-C₃N₄ [4], CdS/g-C₃N₄ [5, 6], DyVO₄/g-C₃N₄ [7], WO₃/g-C₃N₄ [8], TaON/g-C₃N₄ [9], SrTiO₃/g-C₃N₄ [10], C₆₀/g-C₃N₄ [11], Ag₂O/g-C₃N₄ [12], NiS/g-C₃N₄ [13], and rGO/g-C₃N₄ [14] have been demonstrated to exhibit better photocatalytic performance compared with pure g-C₃N₄.

Since the conduction band bottom of g-C₃N₄ (-1.13 eV) [15] is more negative than that of KTaO₃ (-0.96 eV) [1, 2, 16]; g-C₃N₄ (CN) and KTaO₃ (KTO) might be suitable candidates to form an ideal composite photocatalyst to show a high visible light activity. In this paper, we report for the first time that the g-C₃N₄/KTaO₃ composite photocatalyst synthesized by a facile ultrasonic dispersion method has demonstrated a significantly improved photocatalytic performance for Rhodamine B degradation.

2. Experiment Section

2.1. Sample Preparation. The $g\text{-C}_3\text{N}_4$ powder sample was synthesized by directly heating melamine under 550°C according to the previously reported procedure [17]. KTaO_3 (KTO) was prepared by an improved polymerized complex (PC) method [15]. In a typical run, 1 g TaCl_5 was added into 15 mL 2-methoxyethanol and the solution was stirred for 30 min. Then, 0.20 g K_2CO_3 , 12.0 g critic acid, 30 mL 2-methoxyethanol, and 2.0 mL of ethylene glycol were added. After it was stirred for 30 min, the mixture was heated to 120°C for 20 h in air and, finally, the polymer was oxidized in air at 600°C for 2 h.

The typical process for preparation of $g\text{-C}_3\text{N}_4/\text{KTO}$ (CN/KTO) composites was as follows: an appropriate amount of $g\text{-C}_3\text{N}_4$ was added into methanol and then ultrasonically treated in an ultrasonic bath for 30 min. After KTaO_3 powder was added, the solution was stirred in the fume hood for 24 h. Finally the mixture was dried at 100°C overnight and then heated to 300°C for 2 h. The CN/KTO composites with different ratios of $g\text{-C}_3\text{N}_4$ to KTO were prepared and denoted as gcn30, gcn50, and gcn70, respectively, in which the number indicates percentage (mass%) of $g\text{-C}_3\text{N}_4$ in the composite.

2.2. Characterization. Crystal structures of the synthesized samples were examined by a powder X-ray diffractometer (XRD, Rigaku D/MAX 2500 with $\text{Cu K}\alpha 1$ radiation, $\lambda = 0.154$ nm). UV-Vis diffuse reflectance spectra (DRS) of the samples were measured in the range of 200–800 nm using a spectrophotometer (UV-2700, Shimadzu). Transmission electron microscopy (TEM) images were recorded on a Tecnai G2 F20 with an accelerating voltage of 200 kV. The photoluminescence (PL) emission spectra were measured on a spectrofluorometer (Fluorolog-3 system, Horiba Jobin Yvon) using the Xenon lamp with a 325 nm as a source of excitation.

2.3. Photocatalytic Activity Evaluation. Photocatalytic activities of CN/KTO samples were evaluated by Rhodamine B (RhB) degradation in aqueous solution under visible light irradiation. 100 mL aqueous solution of RhB (4 mg/L) was put in a glass beaker, and 0.1 g photocatalyst was then added. In order to establish the adsorption-desorption equilibrium, the suspension was ultrasonically treated and stirred in the dark for 60 min, respectively. Photocatalytic activity was evaluated under irradiation from a 300 W Xenon lamp with a UV cutoff filter, which provides the visible light ranging from 420 to 700 nm. At each given irradiation time interval, 3 mL of the mixture was collected and then the slurry sample was centrifuged to separate the photocatalyst particles. The concentration of RhB was analyzed by measuring the maximum absorption at 553 nm using Shimadzu UV2700 spectrophotometer.

3. Results and Discussion

3.1. Characterization of the CN/KTO. The XRD patterns of KTO, $g\text{-C}_3\text{N}_4$, and their composites are shown in Figure 1.

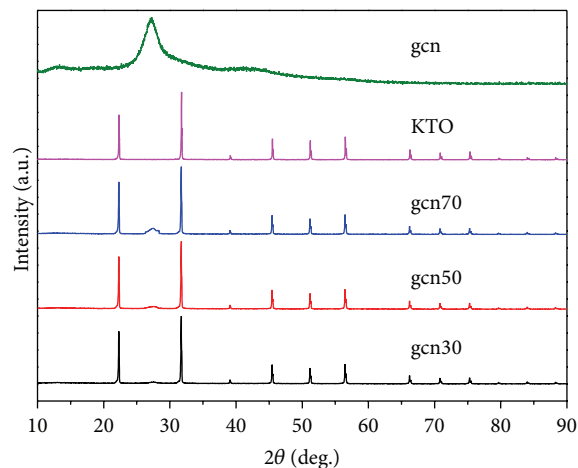


FIGURE 1: XRD patterns of KTO, $g\text{-C}_3\text{N}_4$, and their composites.

We can see that the pattern of KTO matches the standard data for a cubic structure (JCPDS Card number 38-1470). The formation of $g\text{-C}_3\text{N}_4$ can be confirmed by the strong characteristic peak at $2\theta = 27.4^\circ$ in its XRD pattern. For the composites, the XRD patterns can be indexed by two corresponding phases, that is, KTO and $g\text{-C}_3\text{N}_4$ (featured by the peak at $2\theta = 27.4^\circ$), respectively.

From the UV-Vis diffuse reflectance spectra of KTO, $g\text{-C}_3\text{N}_4$, and their composites as shown in Figure 2, we can see clearly that KTO and $g\text{-C}_3\text{N}_4$ show absorption edges of 360 nm and 460 nm, respectively. For the composites, two absorption edges corresponding to KTO and $g\text{-C}_3\text{N}_4$ are observed. With the increase of $g\text{-C}_3\text{N}_4$ amount, the absorbance of the composite to visible light also increases.

The microstructures of KTO, $g\text{-C}_3\text{N}_4$, and their composites were observed on a transmission electron microscope (TEM). As shown in Figure 3(a), KTO is like small and irregular cube and the mean size is about 30 nm. The TEM image of $g\text{-C}_3\text{N}_4$ (Figure 3(b)) shows typical layered platelet-like morphology. From Figure 3(c) we can see clearly that the KTO nanoparticles are deposited on the surface of $g\text{-C}_3\text{N}_4$. In other words, KTO nanoparticles are wrapped well by $g\text{-C}_3\text{N}_4$.

3.2. Photocatalytic Activity. As shown in Figure 4, no noticeable degradation of RhB was observed with pure KTO photocatalyst or without photocatalyst. Pure $g\text{-C}_3\text{N}_4$ photocatalyst could degrade RhB by 65% in 90 min. All of the CN/KTO composites exhibit photocatalytic activities under visible light irradiation, indicating the success of hybrid. When the $g\text{-C}_3\text{N}_4$ amount was less than 50% of the total catalyst weight (such as gcn30, gcn50), the photocatalytic activities of gcn30 and gcn50 are inferior compared with $g\text{-C}_3\text{N}_4$. When the $g\text{-C}_3\text{N}_4$ amount was 70% of the total catalyst weight, the CN/KTO composite exhibited the best activity and nearly 90% RhB was photodegraded. The reason why gcn70 sample showed the best performance could be a result of competition between the following two facts, that is, the absorbance of CN/KTO composite to incident visible light and the effectiveness of photoexcited charge transfer from CN to

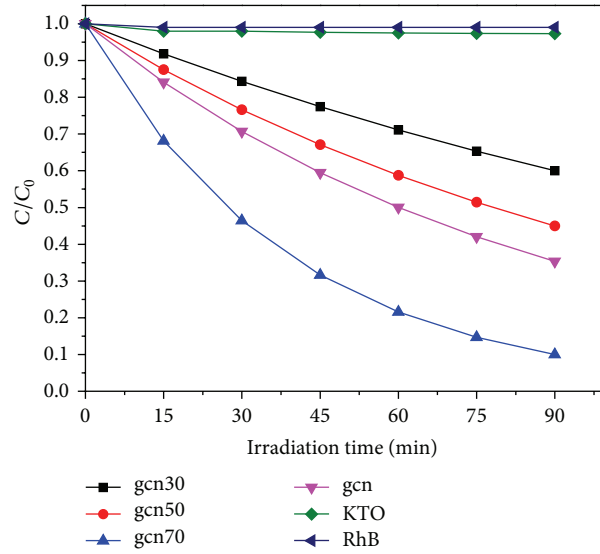


FIGURE 4: Photocatalytic degradation of RhB over $g\text{-C}_3\text{N}_4$, KTO, and their composites under visible light irradiation.

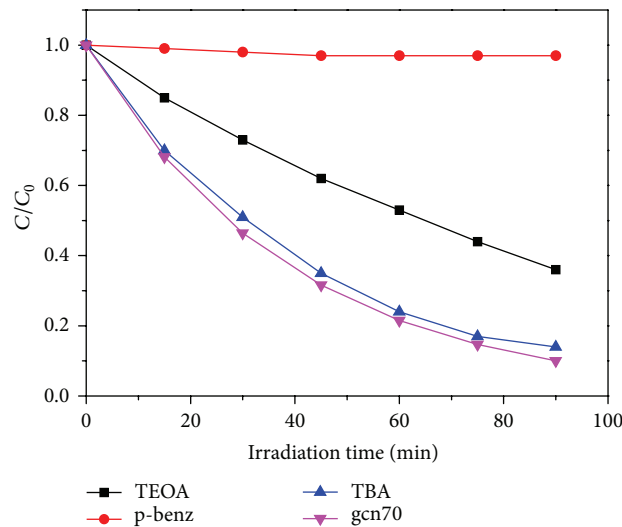


FIGURE 5: Photocatalytic degradation of RhB with different scavengers under visible light irradiation.

As an effective electron donor, triethanolamine (TEOA) can supply electrons to combine with photogenerated holes [20]. As for p-benzoquinone (p-benz), it can react with $\bullet\text{O}_2^-$ and possibly form phenol, implying that p-benz is an effective $\bullet\text{O}_2^-$ trapper [21, 22]. Considering the above-mentioned facts, TBA, TEOA, and p-benz could be employed as the scavengers for hydroxyl radicals ($\text{OH}\bullet$), photogenerated holes (h^+), and superoxide radicals ($\bullet\text{O}_2^-$), respectively. Corresponding control reactions were carried out with the purpose of clarifying the main active species in the photocatalytic process of RhB degradation.

As shown in Figure 5, when TBA was added, the photocatalytic degradation of RhB was decreased slightly. With the introduction of TEOA, the photocatalytic activity also decreased with the addition of hole-scavenger. At last, the introduction of scavenger for $\bullet\text{O}_2^-$ (p-benz, 0.5 mM) resulted

in a remarkable deactivation. These results clearly indicate that superoxide radical $\bullet\text{O}_2^-$ plays the main role in the photocatalytic performance.

Repeatability of the photocatalytic activity was tested by running several cycles of photocatalytic degradation for RhB over gcn70. Each cycle ran for the same time of 90 min, and the photocatalyst was filtered to use for next cycle. As shown in Figure 6(a), gcn70 could still degrade RhB by nearly 90% after running 5 cycles, indicating quite good stability for photocatalytic degradation for RhB. Moreover, the XRD patterns spectra (Figure 6(b)) of gcn70 sample are almost the same before and after running for 5 cycles of photocatalytic degradation for RhB, which further proved the stability of the composite photocatalyst.

Figure 7 presents the PL spectra of the samples. Obviously, a KTO modification leads to a significant fluorescence

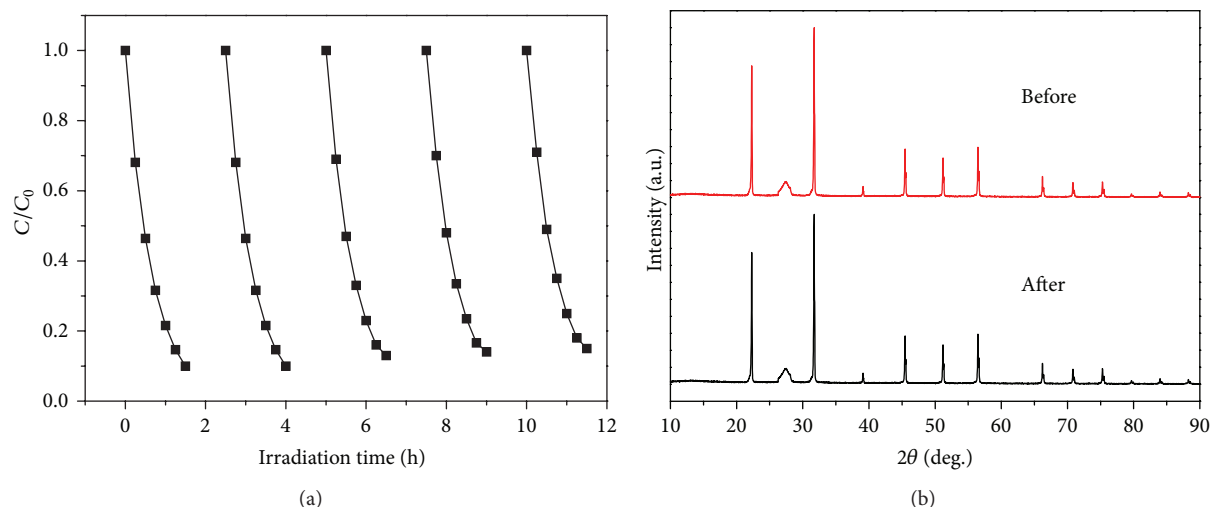


FIGURE 6: (a) Cycling test for the degradation of RhB by gcn70 sample and (b) XRD patterns of gcn70 before and after the cycling test.

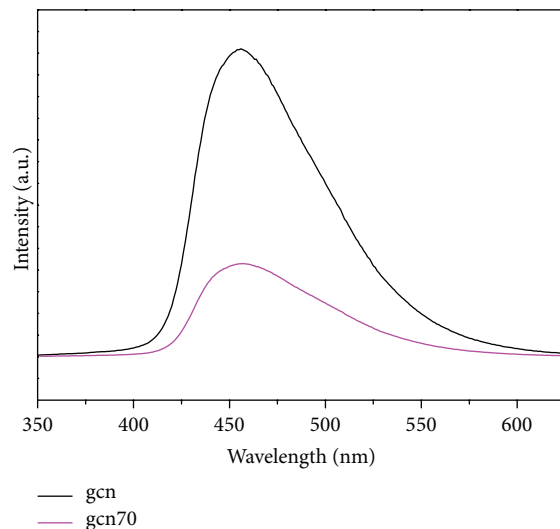


FIGURE 7: Photoluminescence (PL) spectra of g-C₃N₄ and gcn70.

quenching of the gcn70 composite because it prevents the recombination of photogenerated charge pairs. In order to rule out the possibility that the PL intensity decreased when the g-C₃N₄ was diluted with KTO in the composite, the intensity was normalized to the mass of g-C₃N₄.

As mentioned above, the composites CN/KTO have shown much better photocatalytic activity than either KTO or g-C₃N₄ under visible light irradiation. It is known that under visible light irradiation, g-C₃N₄ can be excited due to the appropriate band gap (2.7 eV), whereas KTO is inert owing to its wide band gap. Since the conduction band bottom of g-C₃N₄ (-1.13 eV) [15] is more negative than that of KTO (-0.96 eV) [1, 2, 16], the photoexcited electrons on g-C₃N₄ could be directly injected into the CB of KTO through the well-developed interfaces. The charge transfer from g-C₃N₄ to KTO was also confirmed by the significantly decreased photoluminescence intensity of gcn70 in comparison with

that of g-C₃N₄ (see Figure 7). It is believed that the effective charge transfer can inhibit the recombination of photogenerated electrons and holes and thus enhance the photocatalytic activity. The photoinduced electrons diffuse to the surface and reacted with the oxygen molecule (electron acceptor), generating superoxide radicals $\bullet\text{O}_2^-$. The active superoxide radicals are highly oxidative to decompose RhB effectively. On the basis of experimental results and theoretical analysis, a possible synergistic mechanism for the charge transfer between g-C₃N₄ and KTO and for the enhanced photocatalytic activity of RhB degradation was proposed as illustrated in Figure 8.

4. Conclusions

The novel g-C₃N₄/KTaO₃ composites were successfully prepared by a facile and simple ultrasonic dispersion

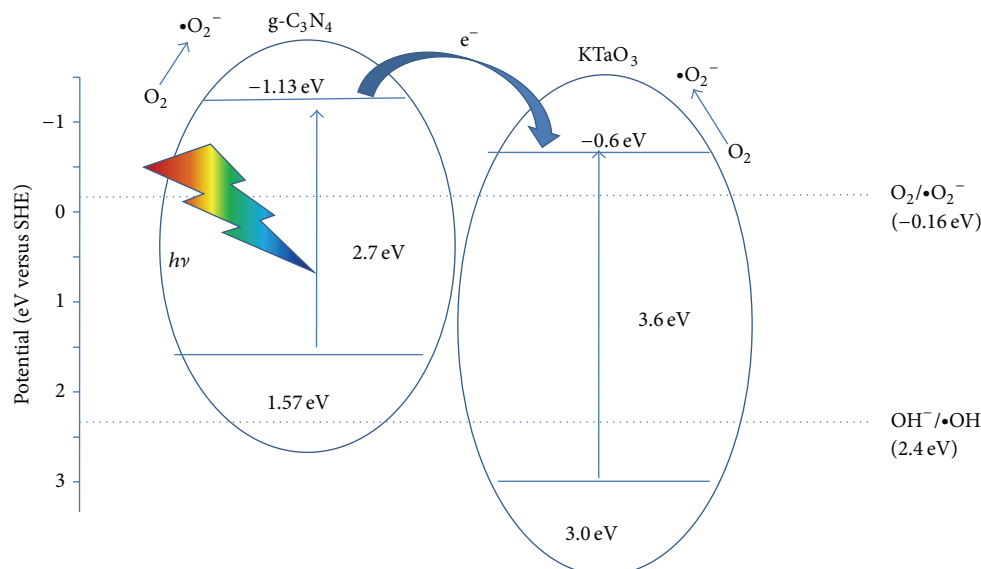


FIGURE 8: Proposed mechanism for the photodegradation of RhB on CN/KTO composite.

method. The resulting $g\text{-C}_3\text{N}_4/\text{KTaO}_3$ composites showed an enhanced photocatalytic activity for degradation of RhB under visible light irradiation, and the optimal mass ratio of $g\text{-C}_3\text{N}_4/\text{KTaO}_3$ was 70/30. Owing to the well-aligned energy band edges and interface between $g\text{-C}_3\text{N}_4$ and KTaO_3 , effective photogenerated charge carrier transfer and separation was evidenced by photoluminescence, which suppressed the recombination of electrons and holes. As a consequence, the photocatalytic activity of the $g\text{-C}_3\text{N}_4/\text{KTaO}_3$ composite was significantly improved.

Conflict of Interests

The authors declare that there is no conflict of interests regarding the publication of this paper.

Acknowledgments

This work was supported by the National Basic Research Program of China (973 Program, Contract no. 2014CB239301). Zhiqing Yong is grateful to Dr. Naoto Umezawa and Professor Jinhua Ye (NIMS) for hosting his internship visit to NIMS. Dr. Hua Tong, Dr. Haiying Jiang (NIMS), and Dr. Xianguang Meng (NIMS) are appreciated for their valuable discussion and/or assistance in photocatalytic evaluation.

References

- [1] H. Kato and A. Kudo, "New tantalate photocatalysts for water decomposition into H_2 and O_2 ," *Chemical Physics Letters*, vol. 295, no. 5-6, pp. 487-492, 1998.
- [2] H. Kato and A. Kudo, "Water splitting into H_2 and O_2 on alkali tantalate photocatalysts ATaO_3 ($A = \text{Li, Na, and K}$)," *The Journal of Physical Chemistry B*, vol. 105, no. 19, pp. 4285-4292, 2001.
- [3] X. Wang, K. Maeda, A. Thomas et al., "A metal-free polymeric photocatalyst for hydrogen production from water under visible light," *Nature Materials*, vol. 8, no. 1, pp. 76-80, 2009.
- [4] Y. Tian, B. Chang, J. Lu, J. Fu, F. Xi, and X. Dong, "Hydrothermal synthesis of graphitic carbon nitride- Bi_2WO_6 heterojunctions with enhanced visible light photocatalytic activities," *ACS Applied Materials and Interfaces*, vol. 5, no. 15, pp. 7079-7085, 2013.
- [5] J. Zhang, Y. Wang, J. Jin, Z. Lin, F. Huang, and J. Yu, "Efficient visible-light photocatalytic hydrogen evolution and enhanced photostability of core/shell $\text{CdS}/g\text{-C}_3\text{N}_4$ nanowires," *ACS Applied Materials and Interfaces*, vol. 5, no. 20, pp. 10317-10324, 2013.
- [6] J. Fu, B. Chang, Y. Tian, F. Xi, and X. Dong, "Novel $\text{C}_3\text{N}_4\text{-CdS}$ composite photocatalysts with organic-inorganic heterojunctions: in situ synthesis, exceptional activity, high stability and photocatalytic mechanism," *Journal of Materials Chemistry A*, vol. 1, no. 9, pp. 3083-3090, 2013.
- [7] Y. He, J. Cai, T. Li et al., "Synthesis, characterization, and activity evaluation of $\text{DyVO}_4/g\text{-C}_3\text{N}_4$ composites under visible-light irradiation," *Industrial & Engineering Chemistry Research*, vol. 51, no. 45, pp. 14729-14737, 2012.
- [8] L. Huang, H. Xu, Y. Li et al., "Visible-light-induced $\text{WO}_3/g\text{-C}_3\text{N}_4$ composites with enhanced photocatalytic activity," *Dalton Transactions*, vol. 42, no. 24, pp. 8606-8616, 2013.
- [9] S. C. Yan, S. B. Lv, Z. S. Li, and Z. G. Zou, "Organic-inorganic composite photocatalyst of $g\text{-C}_3\text{N}_4$ and TaON with improved visible light photocatalytic activities," *Dalton Transactions*, vol. 39, no. 6, pp. 1488-1491, 2010.
- [10] X. Xu, G. Liu, C. Randorn, and J. T. S. Irvine, " $G\text{-C}_3\text{N}_4$ coated SrTiO_3 as an efficient photocatalyst for H_2 production in aqueous solution under visible light irradiation," *International Journal of Hydrogen Energy*, vol. 36, no. 21, pp. 13501-13507, 2011.
- [11] B. Chai, X. Liao, F. Song, and H. Zhou, "Fullerene modified C_3N_4 composites with enhanced photocatalytic activity under visible light irradiation," *Dalton Transactions*, vol. 43, no. 3, pp. 982-989, 2014.

- [12] M. Xu, L. Han, and S. Dong, "Facile fabrication of highly efficient g-C₃N₄/Ag₂O heterostructured photocatalysts with enhanced visible-light photocatalytic activity," *ACS Applied Materials and Interfaces*, vol. 5, no. 23, pp. 12533–12540, 2013.
- [13] J. Hong, Y. Wang, W. Zhang, and R. Xu, "Noble-metal-free NiS/C₃N₄ for efficient photocatalytic hydrogen evolution from water," *ChemSusChem*, vol. 6, no. 12, pp. 2263–2268, 2013.
- [14] Y. Zhang, T. Mori, L. Niu, and J. Ye, "Non-covalent doping of graphitic carbon nitride polymer with graphene: controlled electronic structure and enhanced optoelectronic conversion," *Energy & Environmental Science*, vol. 4, no. 11, pp. 4517–4521, 2011.
- [15] X. Wang, K. Maeda, X. Chen et al., "Polymer semiconductors for artificial photosynthesis: hydrogen evolution by mesoporous graphitic carbon nitride with visible light," *Journal of the American Chemical Society*, vol. 131, no. 5, pp. 1680–1681, 2009.
- [16] J. W. Liu, G. Chen, Z. H. Li, and Z. G. Zhang, "Hydrothermal synthesis and photocatalytic properties of ATaO₃ and ANbO₃ (A = Na and K)," *International Journal of Hydrogen Energy*, vol. 32, no. 13, pp. 2269–2272, 2007.
- [17] S. C. Yan, Z. S. Li, and Z. G. Zou, "Photodegradation performance of g-C₃N₄ fabricated by directly heating melamine," *Langmuir*, vol. 25, no. 17, pp. 10397–10401, 2009.
- [18] R. Flyunt, A. Leitzke, G. Mark et al., "Determination of •OH, O₂^{•-}, and hydroperoxide yields in ozone reactions in aqueous solution," *The Journal of Physical Chemistry B*, vol. 107, no. 30, pp. 7242–7253, 2003.
- [19] J. Peller, O. Wiest, and P. Kamat, "Sonolysis of 2, 4-dichlorophenoxyacetic acid in aqueous solutions. Evidence for OH-radical-mediated degradation," *The Journal of Physical Chemistry A*, vol. 105, no. 13, pp. 3176–3181, 2001.
- [20] S. C. Yan, Z. S. Li, and Z. G. Zou, "Photodegradation of rhodamine B and methyl orange over boron-doped g-C₃N₄ under visible light irradiation," *Langmuir*, vol. 26, no. 6, pp. 3894–3901, 2010.
- [21] M. Styliidi, D. I. Kondarides, and X. E. Verykios, "Visible light-induced photocatalytic degradation of Acid Orange 7 in aqueous TiO₂ suspensions," *Applied Catalysis B: Environmental*, vol. 47, no. 3, pp. 189–201, 2004.
- [22] E. Baciocchi, T. Del Giacco, F. Elisei et al., "Electron transfer and singlet oxygen mechanisms in the photooxygenation of dibutyl sulfide and thioanisole in MeCN sensitized by N-methylquinolinium tetrafluoroborate and 9,10-dicyanoanthracene. The probable involvement of a thiadioxirane intermediate in electron transfer photooxygenations," *Journal of the American Chemical Society*, vol. 125, no. 52, pp. 16444–16454, 2003.

Research Article

Enhanced Light Output of Dipole Source in GaN-Based Nanorod Light-Emitting Diodes by Silver Localized Surface Plasmon

Huamao Huang,¹ Haiying Hu,² Hong Wang,¹ and Kuiwei Geng³

¹ Engineering Research Center for Optoelectronics of Guangdong Province, School of Physics and Optoelectronics, South China University of Technology, Guangzhou, Guangdong 510640, China

² School of Civil and Transportation Engineering, South China University of Technology, Guangzhou, Guangdong 510640, China

³ School of Electronics and Information Engineering, South China University of Technology, Guangzhou, Guangdong 510640, China

Correspondence should be addressed to Hong Wang; pnhwang@scut.edu.cn

Received 20 July 2014; Accepted 6 August 2014; Published 20 August 2014

Academic Editor: Xijin Xu

Copyright © 2014 Huamao Huang et al. This is an open access article distributed under the Creative Commons Attribution License, which permits unrestricted use, distribution, and reproduction in any medium, provided the original work is properly cited.

The light output of dipole source in three types of light-emitting diodes (LEDs), including the conventional planar LED, the nanorod LED, and the localized surface plasmon (LSP) assisted LED by inserting silver nanoparticles in the gaps between nanorods, was studied by use of two-dimensional finite difference time domain method. The height of nanorod and the size of silver nanoparticles were variables for discussion. Simulation results show that a large height of nanorod induces strong wavelength selectivity, which can be significantly enhanced by LSP. On condition that the height of nanorod is 400 nm, the diameter of silver nanoparticle is 100 nm, and the wavelength is 402.7 nm, the light-output efficiency for LSP assisted LED is enhanced by 190% or 541% as compared to the nanorod counterpart or the planar counterpart, respectively. The space distribution of Poynting vector was present to demonstrate the significant enhancement of light output at the resonant wavelength of LSP.

1. Introduction

High-efficiency GaN-based light-emitting diode (LED) has tremendous potential for general lighting. However, in conventional planar epilayers, the InGaN/GaN multiple quantum well (MQW) contains large strain, which would induce a high dislocation density and piezoelectric field, due to the mismatches in lattice constant and thermal expansion between heteroepitaxial layers. To mitigate the strain in MQWs, nanorod LEDs were proposed [1]. The active layer is composed of nanoscale rod array in nanorod LEDs instead of planar thin-film in conventional counterparts. A straightforward fabrication method for nanorod LEDs is to etch the planar epilayers with nanoscale patterned mask [2–10]. In these published literatures, most researchers focused on the strain relaxation processes, and few studies were involved in light-output enhancement. To improve the light output, the nanorod LED was annealed in a mixture of N₂ and NH₃ gases [2]. Moreover, the size of the nanorods [6] and

the spatial occupation factor of the nanorod sidewall [7], which was defined by the sidewall length over the unetched area of planar epilayer, should be carefully selected. As for the light extraction efficiency, after the alumina powders were spin-coated on the p-GaN layer as mask for etching of nanorod array, the residual alumina particles on the top of nanorods benefit the light extraction efficiency [10].

Localized surface plasmon (LSP) has attracted much attention for the enhancement of light output in LEDs [11–20]. The LSP provides a fast energy transfer channel by coupling the excited dipole energy of MQWs into surface plasmon modes of noble metal particles and consequently enhances the spontaneous emission rate of MQWs, thereby improving the light output of LEDs. However, due to the exponential decay of the LSP evanescent field, the penetration depth of the LSP field into the GaN material is limited to be several tens of nanometers [21]. On the other hand, the p-GaN is generally thicker than 100 nm to maintain p-n junction. In order to place the metal particles within

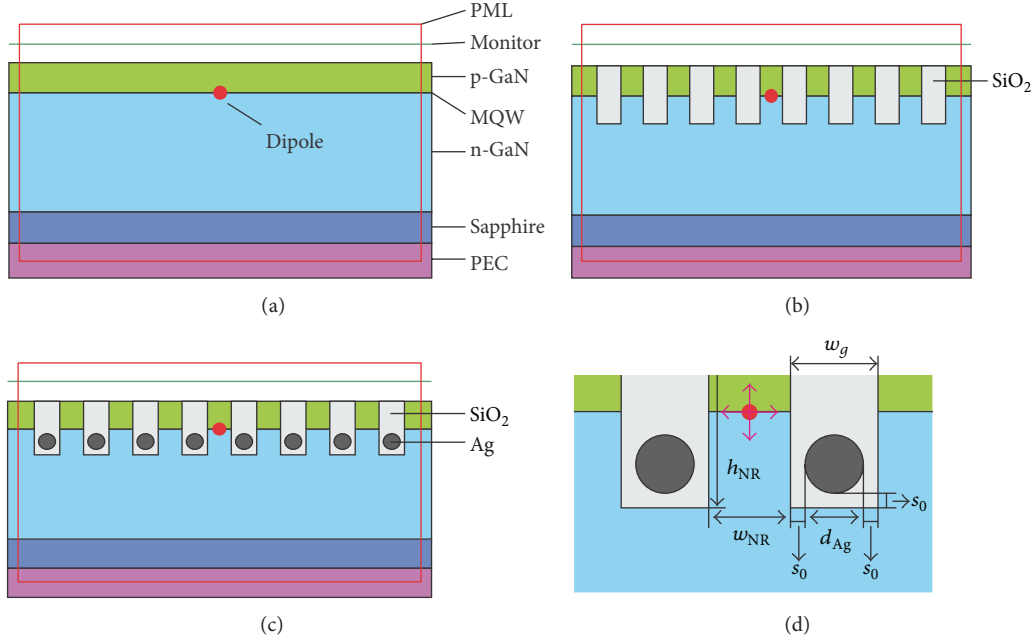


FIGURE 1: Schematic structure of (a) planar LED, (b) nanorod LED, and (c) LSP assisted LED. (d) is an enlarged view of the vicinity of dipole source in (c). The red circle is the dipole source.

the fringing field of MQWs for effective MQW-LSP coupling, the metal particles were embedded into the n-GaN [11–13] or p-GaN [14–17] layers. However, the epitaxial growth process must be interrupted for the fabrication of metal particles and the epilayers following the metal particles may exhibit poor crystal quality. Alternately, after the epitaxial wafer was completely finished, the p-GaN layer was partially etched; if the etching part is thinner enough, the LSP assisted light emission was significantly enhanced [18–20]. For the case of nanorod LEDs, the noble metal particles can be placed in the gaps between the nanorods without additional etching process.

In this paper, the nanorod LEDs with the assistance of silver LSP are proposed, and the light output of dipole source in the planar LED, the nanorod LED, and the LSP assisted LED is studied by two-dimensional finite difference time domain (2D FDTD) method.

2. Materials and Methods

In order to clarify the effects of the nanorod array and the LSP, three types of LED chips shown in Figure 1 were simulated by 2D FDTD method. The first type is the conventional planar LED. The second type is the nanorod LED, in which the nanorod array was achieved by etching part of planar epilayers and filling SiO₂ in the gaps for passivation. The third one is the LSP assisted LED by inserting silver (Ag) nanoparticles in the gaps between nanorods. The width of the nanorods was set to be $w_{NR} = 100$ nm and the height, h_{NR} , was chosen as a variable. The spacing between the Ag nanoparticle and the surrounding SiO₂ sidewall was set to

be $s_0 = 10$ nm, as shown in Figure 1(d). This can be realized by employing core-shell Ag/SiO₂ nanoparticles. The widths of gaps were set to be $w_g = d_{Ag} + 2 \times s_0$, where d_{Ag} is the diameter of Ag nanoparticles. In order to reduce the computation resource [22], our model is only composed of four layers, including a $0.2 \mu\text{m}$ thick p-GaN layer, a $2 \mu\text{m}$ thick n-GaN layer, a $1 \mu\text{m}$ thick sapphire substrate, and a perfect electrical conductor (PEC) layer. The MQW layer was simplified as the interface between the two types of GaN layers, and the electric point dipole was chosen as the source for spontaneous emission. The dipole source was placed at the middle of the horizontal axis of the chip, of which the width was set to be $w_{chip} = 5.22 \mu\text{m}$ and the nanorods were in symmetric distribution with regard to the dipole source. Due to the isotropic emission feature, two orthogonal orientations of dipole source shown in Figure 1(d) were considered [22]. The mesh grids in the vicinity of the dipole source and the Ag nanoparticles were set to be 1 nm. The power monitor was placed at $0.45 \mu\text{m}$ distance from the top surface of p-GaN layer. The perfect matched layer (PML) boundaries were used and the maximum simulation time was set to be a large value of 2000 fs, while the simulation would automatically shut off early when the total energy within the simulation domain drops to 1×10^{-8} of the maximum energy injected.

The material parameters used in our simulation were from experimental data [23, 24]. However, the discrete experimental data should be represented by a continuous function in FDTD simulation. Using the multicoefficient fitting algorithm [25], the refractive indices of Ag [23] and GaN [24] in the wavelength range from 300 nm to 800 nm can be described by an analytic model, and the fitting curves are

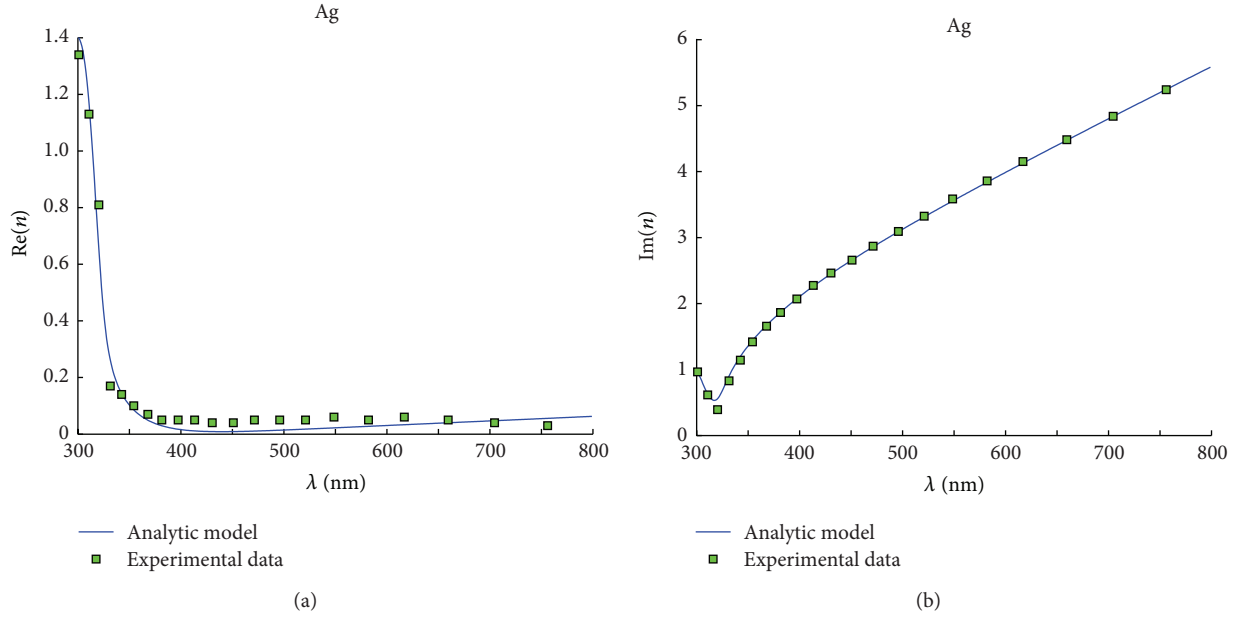


FIGURE 2: The experimental data and fitting curves of (a) the real part and (b) the imaginary part of refractive index, n , of Ag.

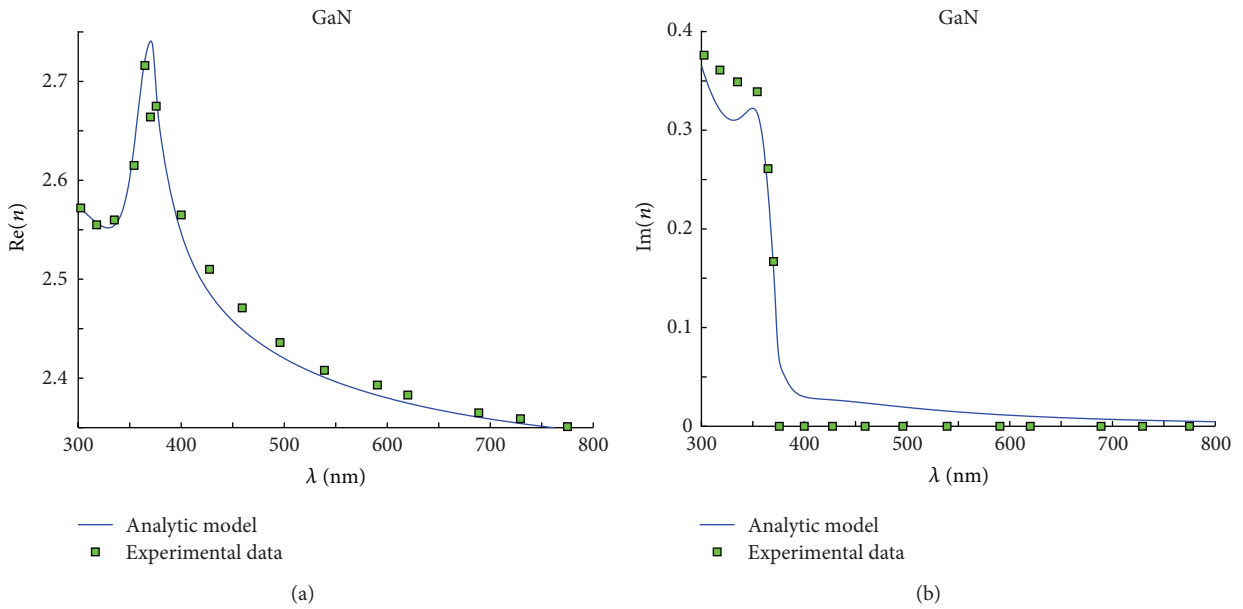


FIGURE 3: The experimental data and fitting curves of (a) the real part and (b) the imaginary part of refractive index, n , of GaN.

shown in Figures 2 and 3. On the other hand, the refractive indices of sapphire and SiO_2 were constants of 1.78084 and 1.46665, respectively.

Since the dipole-LSP coupling is strongly depending on the distance and the particle size, the h_{NR} varied from 100 nm to 500 nm with the interval of 100 nm, and the d_{Ag} varied from 20 nm to 200 nm with the interval of 20 nm. Because the w_{chip} was fixed while d_{Ag} varied, the number of nanorods, $m_{\text{NR}} = 2 \times \text{floor}\{(1/2)w_{\text{chip}}/(\omega_{\text{NR}} + d_{\text{Ag}} + 2s_0)\}$, in each serial of simulation was also a variable, where $\text{floor}\{x\}$ was the arithmetic operation to find the closest integer less than x .

The minimal value of m_{NR} was calculated as 16 for $d_{\text{Ag}} = 200$ nm, while the maximum was 36 for $d_{\text{Ag}} = 20$ nm.

3. Results and Discussion

Figure 4 shows the light-output efficiency, η , which was defined by light-output power normalized to the source power. It is shown from the left column of figures, Figure 4(a), that the η for planar LEDs are always less than 17%. A high degree of coincidence of $\eta(\lambda)$ curves for various h_{NR} and d_{Ag}

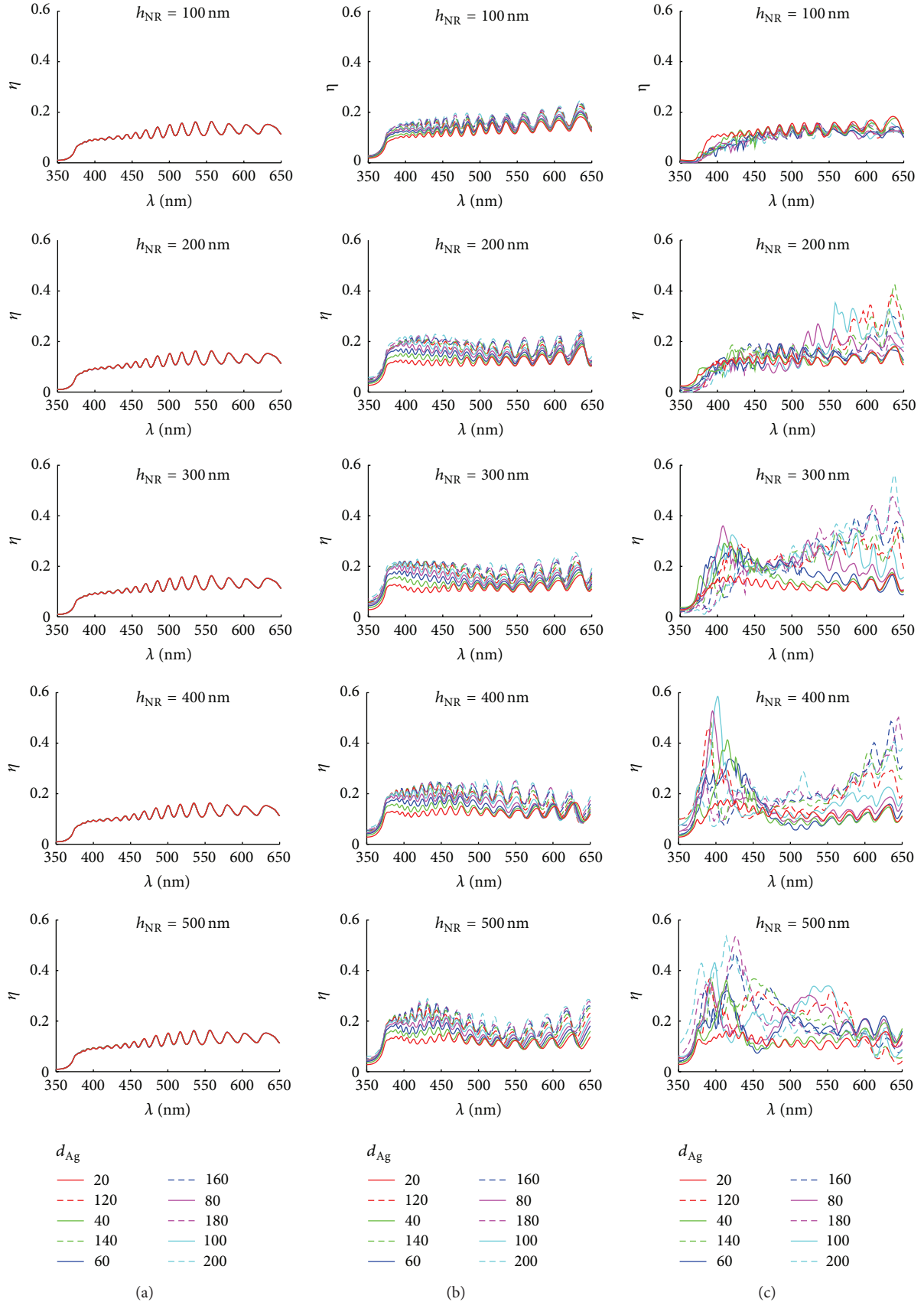


FIGURE 4: The light-output efficiency of dipole source, η , in (a) planar LED, (b) nanorod LED, and (c) LSP assisted LED, where $h_{NR} = [100, 200, 300, 400, 500]$ nm and $d_{Ag} = [20, 40, 60, \dots, 200]$ nm.

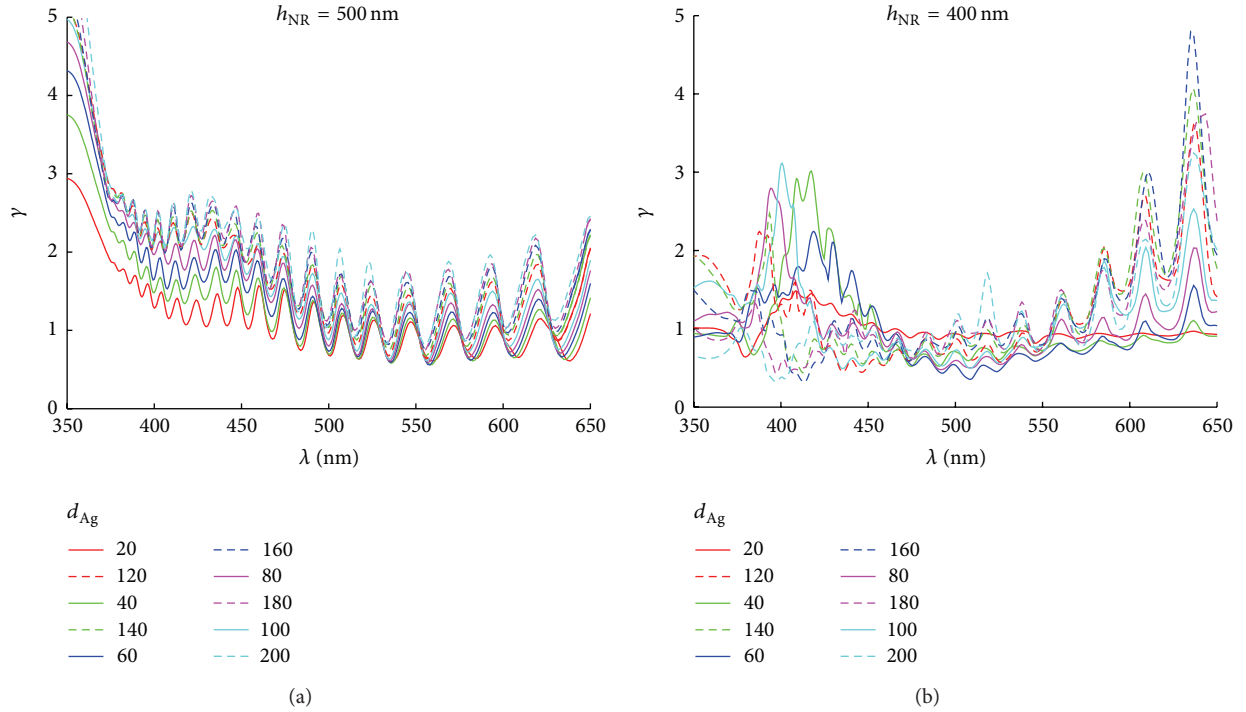


FIGURE 5: The enhancement of the light-output efficiency, γ , for (a) nanorod LEDs as compared to planar LEDs at $h_{NR} = 500 \text{ nm}$ and (b) LSP assisted LEDs as compared to nanorod LEDs at $h_{NR} = 400 \text{ nm}$, where $d_{Ag} = [20, 40, 60, \dots, 200] \text{ nm}$. Note that $\gamma > 1$ means the enhancement while $\gamma < 1$ is the degradation.

shows that the calculation errors coming from the different mesh grids can be ignored.

Figure 4(b) shown in the middle column are the results for nanorod LEDs. Generally, the η increases as the d_{Ag} increases because of the larger surface area and reduced absorption of GaN material. On the condition of $h_{NR} = 100 \text{ nm}$, all η over the whole wavelength range for nanorod LEDs are higher than that for planar counterparts, which imply that the short nanorod does not induce strong resonance oscillation at specific wavelength and mainly provides scattering centers. However, if h_{NR} increases, the strong wavelength selectivity occurs. The η fluctuates intensively and the fluctuation is expanded with the increasing of h_{NR} , d_{Ag} , and λ . The η in the short wavelength range, e.x. from 400 nm to 470 nm, exhibits significant enhancement, especially in the case of d_{Ag} being 500 nm. The maximal value of η for nanorod LED is 28.9%, which is enhanced by 108% compared to the planar counterpart, in the case of $h_{NR} = 500 \text{ nm}$, $d_{Ag} = 200 \text{ nm}$, and $\lambda = 431.65 \text{ nm}$, as shown in Figure 5(a). However, in specific domain of longer wavelength range, the η is reduced as compared to the planar LED. For example, as shown in Figure 5(a), in the case of $h_{NR} = 500 \text{ nm}$ and $d_{Ag} = 20 \text{ nm}$, the η for nanorod LED is less than that for planar LED in the wavelength range from 550.5 nm to 568.5 nm.

The results for LSP assisted LED are shown in Figure 4(c) in the right column. On the condition of $h_{NR} = 100 \text{ nm}$, the η for LSP assisted LED are always lower than nanorod counterparts, except the case of $d_{Ag} = 20 \text{ nm}$. This can be ascribed to the competition of the absorption loss from

Ag material and the scattering effect from Ag metal mirror. The absorption loss is always the dominant effect unless the particle size is small enough. If h_{NR} increases, the LSP takes effect and provides significant wavelength selectivity. With the increasing of h_{NR} from 200 nm to 500 nm, the significant enhancement of η appears firstly in the long wavelength, e.x. nearby 610 nm, then in short wavelength, e.x. nearby 400 nm, and later in middle wavelength range, e.x. nearby 535 nm. The maximal value of η for LSP assisted LED is 58.5%, which is enhanced by 190% compared to the nanorod counterpart, in the case of $h_{NR} = 400 \text{ nm}$, $d_{Ag} = 100 \text{ nm}$, and $\lambda = 402.7 \text{ nm}$, as shown in Figure 5(b). As compared to the planar counterpart, this η is enhanced by 541%. Note that the maximum of η shown in Figure 4(c) and the maximal value of γ , which is the enhancement of η , shown in Figure 5(b) do not coincide. On the other hand, the suppressing of η still exists. For example, as shown in Figure 5(b), in the case of $h_{NR} = 400 \text{ nm}$ and d_{Ag} less than 120 nm, the η for LSP assisted LED is less than that for planar LED in the wavelength range from 460 nm to 555 nm.

The η was estimated by the average value of independent simulation results for each orientation of the dipole source shown in Figure 1(d). To further understand the effects of LSP on different polarization of dipole source, the magnitude of Poynting vector at the wavelength of 402.7 nm and 460 nm is shown in Figures 6 and 7 in the case of $h_{NR} = 400 \text{ nm}$ and $d_{Ag} = 100 \text{ nm}$. As shown in Figure 4, for LSP assisted LED, the η reached maximum at $\lambda = 402.7 \text{ nm}$, while the η at $\lambda = 460 \text{ nm}$ is a relative small value.

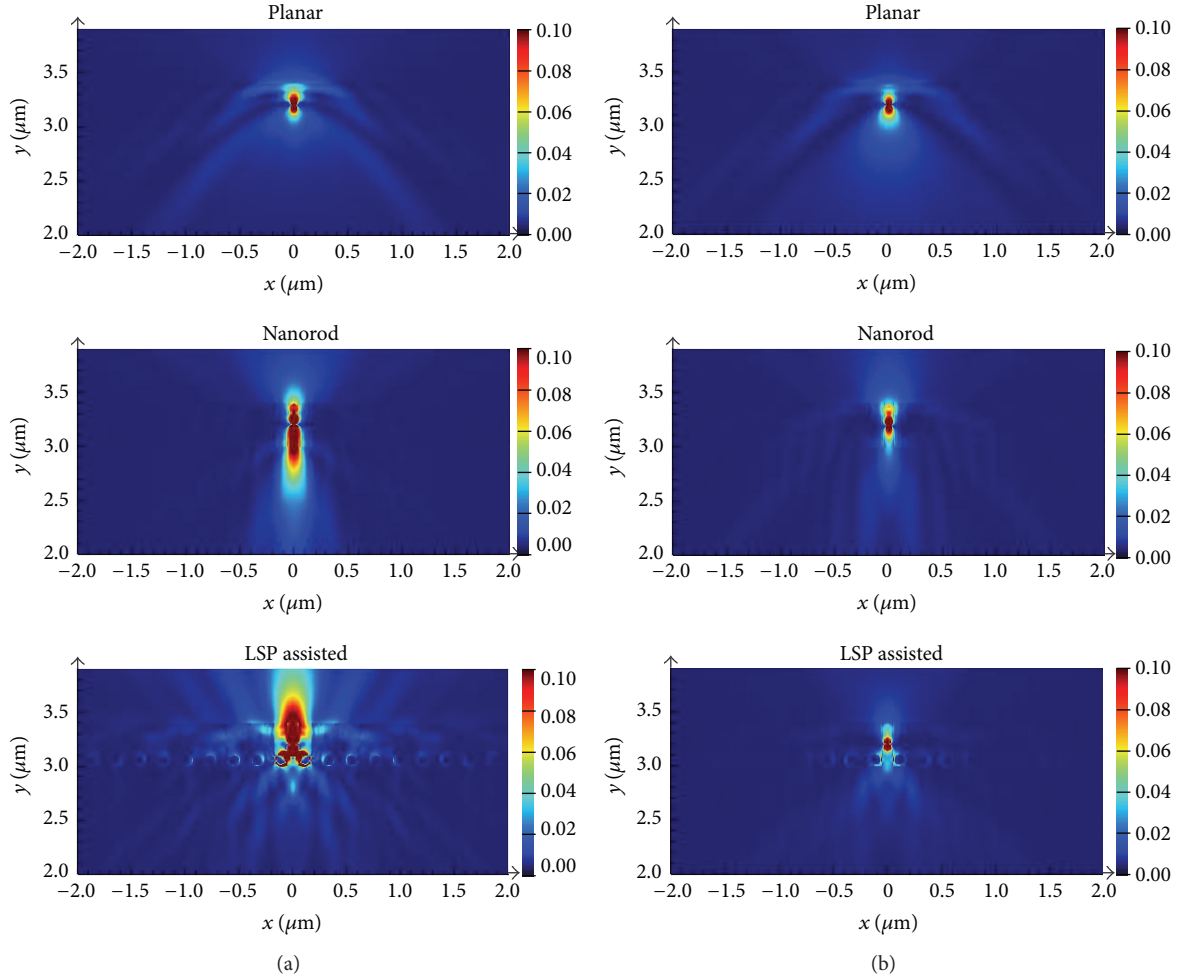


FIGURE 6: As the polarization of dipole source is along the horizontal direction, the magnitude of Poynting vector at the wavelength of (a) 402.7 nm and (b) 460 nm, where $h_{\text{NR}} = 400$ nm and $d_{\text{Ag}} = 100$ nm.

Figure 6 shows the magnitude of Poynting vector as the polarization of dipole source is along the horizontal direction. It is shown that the light energy is confined well in the planar LEDs at the two wavelengths. Two diffraction orders can be observed due to the planar structure. For the nanorod LEDs, most of the light energy is restricted in the nanorod. Due to the strong resonance oscillation at the wavelength of 402.7 nm, the light energy is much higher than that at the wavelength of 460 nm. In addition, lots of light energy leaks out of the nanorod downward to the n-GaN layer, but the light energy which escaped from the top surface is still limited. In the case of LSP assisted LEDs, the significant enhancement of light output is achieved at the resonant wavelength of 402.7 nm. Since the dipole source is placed above the Ag nanoparticles, the LSP is mainly located on the top surface of nanoparticles, and thus the lights generated from the LSP escape from the chip via the top surface; thereby the downward-leaking light energy is suppressed. For the detuning wavelength of 460 nm, the Ag nanoparticles do not produce the LSP but provide the reflective effects and suffer absorption loss; therefore, the light output at 460 nm for LSP assisted LED is less than that for nanorod LED.

As shown in Figure 7, on condition that the polarization of dipole source is along the perpendicular direction, the results are similar to the horizontal-polarization case shown in Figure 6. The light energy from the dipole source with perpendicular polarization expands widely toward left side and right side, and thus the confinement effects from the nanorod and the dipole-LSP coupling from the Ag nanoparticles are reduced. Consequently, the light output from the dipole source with perpendicular polarization is less than that with horizontal polarization.

4. Conclusion

In summary, the light output of dipole source which escaped from planar LED, nanorod LED, and LSP assisted LED is studied by use of 2D FDTD method. The maximal value of light-output efficiency for LSP assisted LED is enhanced by 190% or 541% as compared to the nanorod counterpart or the planar counterpart, respectively. The significant enhancement of light output at the resonant wavelength of LSP was demonstrated by the space distribution of

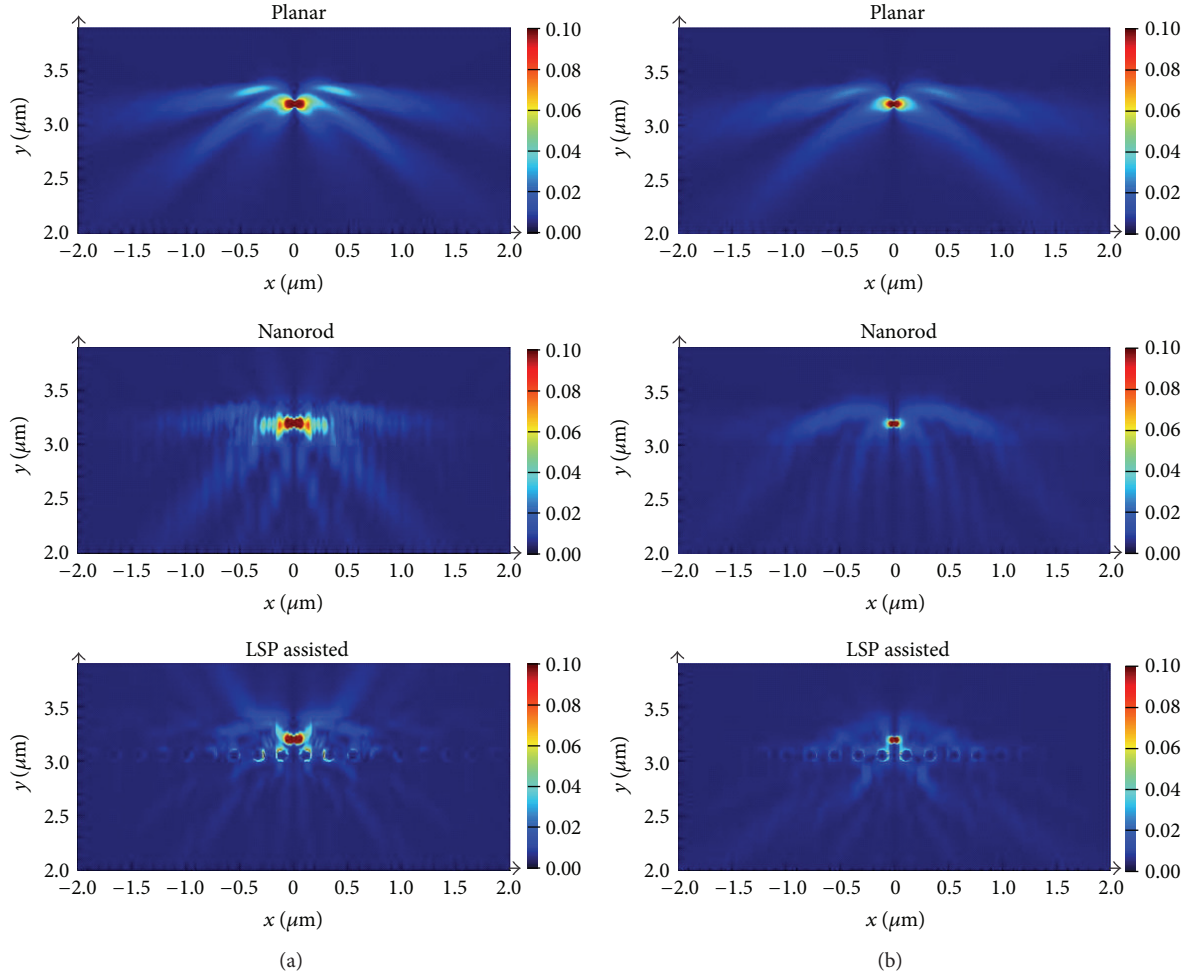


FIGURE 7: As the polarization of dipole source is along the perpendicular direction, the magnitude of Poynting vector at the wavelength of (a) 402.7 nm and (b) 460 nm, where $h_{\text{NR}} = 400$ nm and $d_{\text{Ag}} = 100$ nm.

the Poynting vector. Although only the dipole-LSP coupling was considered in this paper, these results can be extended to the MQW-LSP coupling, since the MQW can be modeled by multiple electric dipole sources located in specific positions with orthogonal polarizations.

Conflict of Interests

The authors declare that there is no conflict of interests regarding the publication of this paper.

Acknowledgments

This work was supported by the National High Technology Research and Development Program of China (863 Program) (no. 2014AA032609), the Strategic Emerging Industry Special Funds of Guangdong Province (no. 2011A081301004, no. 2012A080302003, and no. 2012A080304015), the Key Technologies R&D Program of Guangzhou City (no. 2011Y5-00006), and the Fundamental Research Funds for the Central Universities (no. 2013ZM093 and no. 2013ZP0017).

References

- [1] S. Li and A. Waag, "GaN based nanorods for solid state lighting," *Journal of Applied Physics*, vol. 111, no. 7, Article ID 071101, 2012.
- [2] S. Keller, C. Schaake, N. A. Fichtenbaum et al., "Optical and structural properties of GaN nanopillar and nanostripe arrays with embedded InGaN/GaN multi-quantum wells," *Journal of Applied Physics*, vol. 100, no. 5, Article ID 054314, 2006.
- [3] C. H. Chiu, T. C. Lu, H. W. Huang et al., "Fabrication of InGaN/GaN nanorod light-emitting diodes with self-assembled Ni metal islands," *Nanotechnology*, vol. 18, no. 44, Article ID 445201, 2007.
- [4] C.-Y. Wang, L.-Y. Chen, G.-P. Chen et al., "GaN nanorod light emitting diode arrays with a nearly constant electroluminescent peak wavelength," *Optics Express*, vol. 16, no. 14, pp. 10549–10556, 2008.
- [5] H. Ono, Y. Ono, K. Kasahara, J. Mizuno, and S. Shoji, "Fabrication of high-intensity light-emitting diodes using nanostructures by ultraviolet nanoimprint lithography and electrodeposition," *Japanese Journal of Applied Physics*, vol. 47, no. 2, pp. 933–935, 2008.
- [6] Y.-R. Wu, C. Chiu, C.-Y. Chang, P. Yu, and H.-C. Kuo, "Size-dependent strain relaxation and optical characteristics of

- InGaN/GaN nanorod LEDs,” *IEEE Journal of Selected Topics in Quantum Electronics*, vol. 15, no. 4, pp. 1226–1233, 2009.
- [7] V. Ramesh, A. Kikuchi, K. Kishino, M. Funato, and Y. Kawakami, “Strain relaxation effect by nanotexturing InGaN/GaN multiple quantum well,” *Journal of Applied Physics*, vol. 107, no. 11, Article ID 114303, 2010.
 - [8] Q. Li, K. R. Westlake, M. H. Crawford et al., “Optical performance of top-down fabricated InGaN/GaN nanorod light emitting diode arrays,” *Optics Express*, vol. 19, no. 25, pp. 25528–25534, 2011.
 - [9] Q. Wang, J. Bai, Y. P. Gong, and T. Wang, “Influence of strain relaxation on the optical properties of InGaN/GaN multiple quantum well nanorods,” *Journal of Physics D: Applied Physics*, vol. 44, no. 39, Article ID 395102, 2011.
 - [10] S. H. Kim, H. H. Park, Y. H. Song et al., “An improvement of light extraction efficiency for GaN-based light emitting diodes by selective etched nanorods in periodic microholes,” *Optics Express*, vol. 21, no. 6, pp. 7125–7130, 2013.
 - [11] M.-K. Kwon, J.-Y. Kim, B.-H. Kim et al., “Surface-plasmon-enhanced light-emitting diodes,” *Advanced Materials*, vol. 20, no. 7, pp. 1253–1257, 2008.
 - [12] L.-W. Jang, J.-W. Ju, D.-W. Jeon et al., “Enhanced light output of InGaN/GaN blue light emitting diodes with Ag nano-particles embedded in nano-needle layer,” *Optics Express*, vol. 20, no. 6, pp. 6036–6041, 2012.
 - [13] M. K. Kwon, J. Y. Kim, and S. J. Park, “Enhanced emission efficiency of green InGaN/GaN multiple quantum wells by surface plasmon of Au nanoparticles,” *Journal of Crystal Growth*, vol. 370, pp. 124–127, 2013.
 - [14] C.-Y. Cho, M.-K. Kwon, S.-J. Lee et al., “Surface plasmon-enhanced light-emitting diodes using silver nanoparticles embedded in p-GaN,” *Nanotechnology*, vol. 21, no. 20, Article ID 205201, 2010.
 - [15] C.-Y. Cho, K. S. Kim, S.-J. Lee et al., “Surface plasmon-enhanced light-emitting diodes with silver nanoparticles and SiO₂ nanodisks embedded in p-GaN,” *Applied Physics Letters*, vol. 99, no. 4, Article ID 041107, 2011.
 - [16] C. Cho, S. Lee, J. Song et al., “Enhanced optical output power of green light-emitting diodes by surface plasmon of gold nanoparticles,” *Applied Physics Letters*, vol. 98, no. 5, Article ID 051106, 2011.
 - [17] S. Hong, C. Cho, S. Lee et al., “Localized surface plasmon-enhanced nearultraviolet emission from InGaN/GaN lightemitting diodes using silver and platinum nanoparticles,” *Optics Express*, vol. 21, no. 3, pp. 3138–3144, 2013.
 - [18] C. C. Kao, Y. K. Su, C. L. Lin, and J. J. Chen, “Localized surface plasmon-enhanced nitride-based light-emitting diode with Ag nanotriangle array by nanosphere lithography,” *IEEE Photonics Technology Letters*, vol. 22, no. 13, pp. 984–986, 2010.
 - [19] C. Lu, C. Lan, Y. Lai, Y. Li, and C. Liu, “Enhancement of green emission from InGaN/GaN multiple quantum wells via coupling to surface plasmons in a two-dimensional silver array,” *Advanced Functional Materials*, vol. 21, no. 24, pp. 4719–4723, 2011.
 - [20] C.-H. Lu, S.-E. Wu, Y.-L. Lai, Y.-L. Li, and C.-P. Liu, “Improved light emission of GaN-based light-emitting diodes by efficient localized surface plasmon coupling with silver nanoparticles,” *Journal of Alloys and Compounds*, vol. 585, pp. 460–464, 2014.
 - [21] K. Okamoto, I. Niki, A. Shvartser, Y. Narukawa, T. Mukai, and A. Scherer, “Surface-plasmon-enhanced light emitters based on InGaN quantum wells,” *Nature Materials*, vol. 3, no. 9, pp. 601–605, 2004.
 - [22] J.-W. Pan, P.-J. Tsai, K.-D. Chang, and Y.-Y. Chang, “Light extraction efficiency analysis of GaN-based light-emitting diodes with nanopatterned sapphire substrates,” *Applied Optics*, vol. 52, no. 7, pp. 1358–1367, 2013.
 - [23] P. B. Johnson and R. W. Christy, “Optical constants of the noble metals,” *Physical Review B*, vol. 6, no. 12, pp. 4370–4379, 1972.
 - [24] Filmetrics, “Refractive index database,” 2014, <http://www.filmetrics.com/refractive-index-database>.
 - [25] A. E. Khalifa and M. A. Swillam, “Cheap and efficient plasmonic solar cell,” in *Physics, Simulation, and Photonic Engineering of Photovoltaic Devices III, 8981IR*, vol. 8981 of *Proceedings of SPIE*, San Francisco, Calif, USA, March 2014.

Research Article

Synthesis of Hierarchical CoO Nano/Microstructures as Anode Materials for Lithium-Ion Batteries

Dan Qin, Peng Yan, Guangzhong Li, Yunchuang Wang, Yukuan An, and Juan Xing

Binzhou Medical University, Guanhai Road 346, Yantai 264003, China

Correspondence should be addressed to Peng Yan; yp_ok@163.com

Received 25 June 2014; Accepted 16 July 2014; Published 6 August 2014

Academic Editor: Xijin Xu

Copyright © 2014 Dan Qin et al. This is an open access article distributed under the Creative Commons Attribution License, which permits unrestricted use, distribution, and reproduction in any medium, provided the original work is properly cited.

Hierarchical CoO nano/microstructures are synthesized via a hydrothermal method and a subsequent annealed process. When evaluated for use in lithium-ion batteries, hierarchical CoO nano/microstructures show a high initial discharge capacity of 1370 mAh/g and a high reversible capacity of 1148 mAh/g over 20 cycles at a current density of 100 mA/g. Superior rate performance with coulombic efficiency of about 100% upon galvanostatic cycling is also revealed. The excellent electrochemical properties of hierarchical CoO nano/microstructures make it a promising alternative anode material for high power lithium-ion batteries applications.

1. Introduction

The ever-increasing demands for the high power rechargeable lithium-ion batteries (LIBs) have been propelling the researches on the high performance electrode materials [1, 2]. The commercialized graphite-based anode materials exhibit excellent charge and discharge cycling performance, but their low specific capacities are far from the requirement of the high energy LIBs [3]. Recently, transition metal oxides (MO, where M refers to Co, Fe, Ti, or Ni) have aroused intense interests in the field of LIBs since their high electrochemical capacities were first reported by Poizot et al. [4]. Different from the classical intercalation reaction, the conversion reaction mechanism is adopted in transition metal oxides for the lithium-ion storage [5]. Theoretical and experimental investigations further demonstrate the occurrence of the multiple redox reaction between the transition metal oxides and lithium, which will lead to the high capacities in the transition metal oxides based LIBs [6–10].

Cobalt monoxide (CoO) with a relatively high theoretical capacity of 715 mAh/g is one of the potential candidate anode materials for rechargeable LIBs [11]. However, similar to other transition metal oxides anode materials, the poor cycle stability and rate capability of CoO anode materials hamper their large scale practical applications in LIBs [12–14]. Previous studies show that the poor electrochemical performance of

CoO anode materials is mainly due to the low conductivity and drastic volume change during lithiation/delithiation cycles [15, 16]. In recent years, considerable efforts have been devoted to overcome this drawback and an intuitively straightforward route is to decrease the size of the CoO anode materials to nanoscale [17–19]. Nanosized electrode materials with high specific surface may increase the contact area between the electrolyte and electrode materials and shorten the path length for Li ion transport during electrochemical reaction, which would do favor to the improvement of the discharge capacities [20–22].

In this paper, we report the synthesis of hierarchical CoO nano/microstructures via a hydrothermal method followed by a subsequent thermal annealing process. Hierarchical CoO nano/microstructures with the size of 5–7 μm are consisting of many nanoparticles chains. The as-synthesized hierarchical CoO nano/microstructures exhibit a high initial capacity of about 1370 mAh/g and superior cycle stability. Good rate capability is also obtained in CoO nano/microstructures as anode materials for LIBs.

2. Experimental

The detailed synthesis process of hierarchical CoO nano/microstructures is described as follows. To begin, 1.50 g

(25 mmol) of urea and 0.05 g of cetyltrimethylammonium bromide (CTAB) are dissolved in 30 mL of deionized water under magnetic stirring. After the solution becomes transparent, 10 mL 0.5 M of $\text{CoSO}_4 \cdot 7\text{H}_2\text{O}$ is added and stirred for another 10 minutes. Finally, the whole mixture is transferred into a Teflon-lined autoclave and maintained at 120°C for 12 h. When the autoclave is cooled to room temperature naturally, the rosy products are collected by filtration, rinsed several times with deionized water and absolute ethyl alcohol, and dried at 60°C . Finally, black CoO materials are obtained by thermal decomposition of the rosy precursor at 500°C for 2 h in a vacuum of 10^{-5} torr.

The samples are characterized by X-ray powder diffraction (XRD, Philips X'pert PRO diffractometer, $\text{Cu K}\alpha$ radiation), field emission scanning electron microscopy (FESEM, Hitachi S-4800, Japan), and high-resolution transmission electron microscopy (HRTEM, JEOL, 2010, 200 kV). To investigate the electrochemical properties of the as-prepared CoO hierarchical nano/microstructures, two-electrode coin-type cells are assembled with lithium metal as counter and reference electrodes. The working electrode was fabricated by spreading the mixture of CoO, acetylene black (ATB), and polyvinylidene fluoride (PVDF) in a weight ratio of 7:2:1 onto the copper foil. The electrode was then dried at 120°C for 2 h and cut into a disk. The electrolyte solution was 1 M LiPF_6 dissolved in a mixture of ethylene carbonate (EC) and diethyl carbonate (DEC) with the volume ratio of EC/DEC = 1:1. Cyclic voltammograms (CVs) test is conducted at room temperature, using the electrochemical workstation (CHI 660C) at a scan rate of 0.2 mV/s in a range of 0.01–3.0 V versus Li/Li^+ . The rate capacity and the cycle performance are measured by a galvanostatic discharge-charge method at current densities of 100 mA/g, 200 mA/g, 300 mA/g, and 500 mA/g, respectively, in the range of 0.01–3.0 V with a multichannel battery test system (Land CT 2001A).

3. Results and Discussion

The crystalline phase of the as-prepared products was analyzed by XRD. Figure 1(a) shows the diffraction patterns for the products. All the characteristic diffraction peaks can be assigned to cubic CoO (JCPDS 78-0341, $a = 4.2602 \text{ \AA}$). In addition, no additional diffraction peaks were detected, indicating the high purity of the CoO products. FESEM image (Figure 1(b)) illustrates the typical morphologies of the obtained CoO products. These CoO products are of hierarchical structures with diameters in the range of 5–7 μm . Figure 1(c) represents the TEM image of a single CoO hierarchical structure, which is assembled from many nanosized branches radiating from a center. The HRTEM image (Figure 1(d)) further demonstrates that these radial nanosized branches are composed of numerous nanoparticles with the size of several nanometers. The measured lattice spacing of 0.216 nm corresponds to the (200) planes of cubic CoO.

Cyclic voltammogram (CV) measurements were carried out to investigate the electrochemical properties of the hierarchical CoO nano/microstructures as anode materials for

the LIBs. Figure 2 shows the first three CV curves at a scan rate of 0.2 mV/s in the range of 0.01–3.0 V. In the first cycle, a wide and irreversible reduction peak at about 0.20 V is observed, corresponding to the electrochemical lithiation reaction of the CoO and the formation of the solid electrolyte interface (SEI) layer. Previous studies reveal that the SEI layer might be formed on the surface of the transition metal oxides and results in the irreversible peak in the first CV curve [23, 24]. In the anodic scan process, a broad anodic peak is recorded at about 2.3 V, which is ascribed to the complex oxidation of metallic cobalt to cobalt oxide. The total chemical reaction can be expressed as $\text{CoO} + 2\text{Li} \leftrightarrow \text{Li}_2\text{O} + \text{Co}$ [11]. The CV curve of the second cycle nearly overlaps with the curve for the third cycle, indicating the good cyclic stability of the CoO.

To investigate the lithium storage capacity, the galvanostatic discharge-charge performances were measured in the voltage window of 0.01–3.0 V at a current density of 100 mA/g. Figure 3 displays the 1st, 2nd, and 20th galvanostatic discharge-charge curves for the hierarchical CoO nano/microstructures. A long potential plateau at about 1.0 V, followed by a sloping curve down to the cutoff voltage of 0.01 V, is clearly observed from the first discharge curve. The long potential plateau could be ascribed to the conversion reaction between CoO and Li, while the sloping curve corresponds to the formation of the SEI layer [25]. The initial specific discharge capacity goes up to as much as 1370 mAh/g, which is much higher than its theoretical value of 715 mAh/g. The extra capacity could be ascribed to the formation of a polymer-gel-like film during the reduction process of CoO to Co and the formation of a $\text{Co/Li}_2\text{O}$ interface in the course of the heterogeneous solid-state reaction process [26]. For the first charge, a voltage plateau at around 2.3 V is recorded, corresponding to the process of oxidation of metallic Co to CoO and the decomposition of the Li_2O , which is in accord with the CV measurement. The initial coulombic efficiency reaches 71.5% with the discharge and charge capacities of 1370 and 981 mAh/g, respectively. Compared to the initial discharge/charge curve, the discharge curves undergo a notable change in subsequent cycles, with shorter potential plateaus and longer sloping ranges. After the 20th cycle, the discharge and the charge capacities become 1148 and 1119 mAh/g, respectively, demonstrating the good capacity retention and cycle stability of the as-prepared hierarchical CoO nano/microstructures materials.

Figure 4 shows the discharge capacities of the as-prepared hierarchical CoO nano/microstructures as a function of the cycle number at different current densities. The CoO materials display a superior cyclic stability as well as high capacity. The initial discharge capacity is 1370 mAh/g at a current density of 100 mA/g. The discharge capacity of the 20th cycle is as high as 1144 mAh/g, which is 83.5% of the first discharge capacities. The rate performance of the hierarchical CoO nano/microstructures is also revealed, and the discharge capacities at 100 mA/g, 200 mA/g, 300 mA/g, and 500 mA/g are 1370 mAh/g, 1040 mAh/g, 822 mAh/g, and 593 mAh/g, respectively. Even under the high current density of 500 mA/g, the capacity of CoO is still higher than the theoretical capacity of commercial graphite anodes' materials

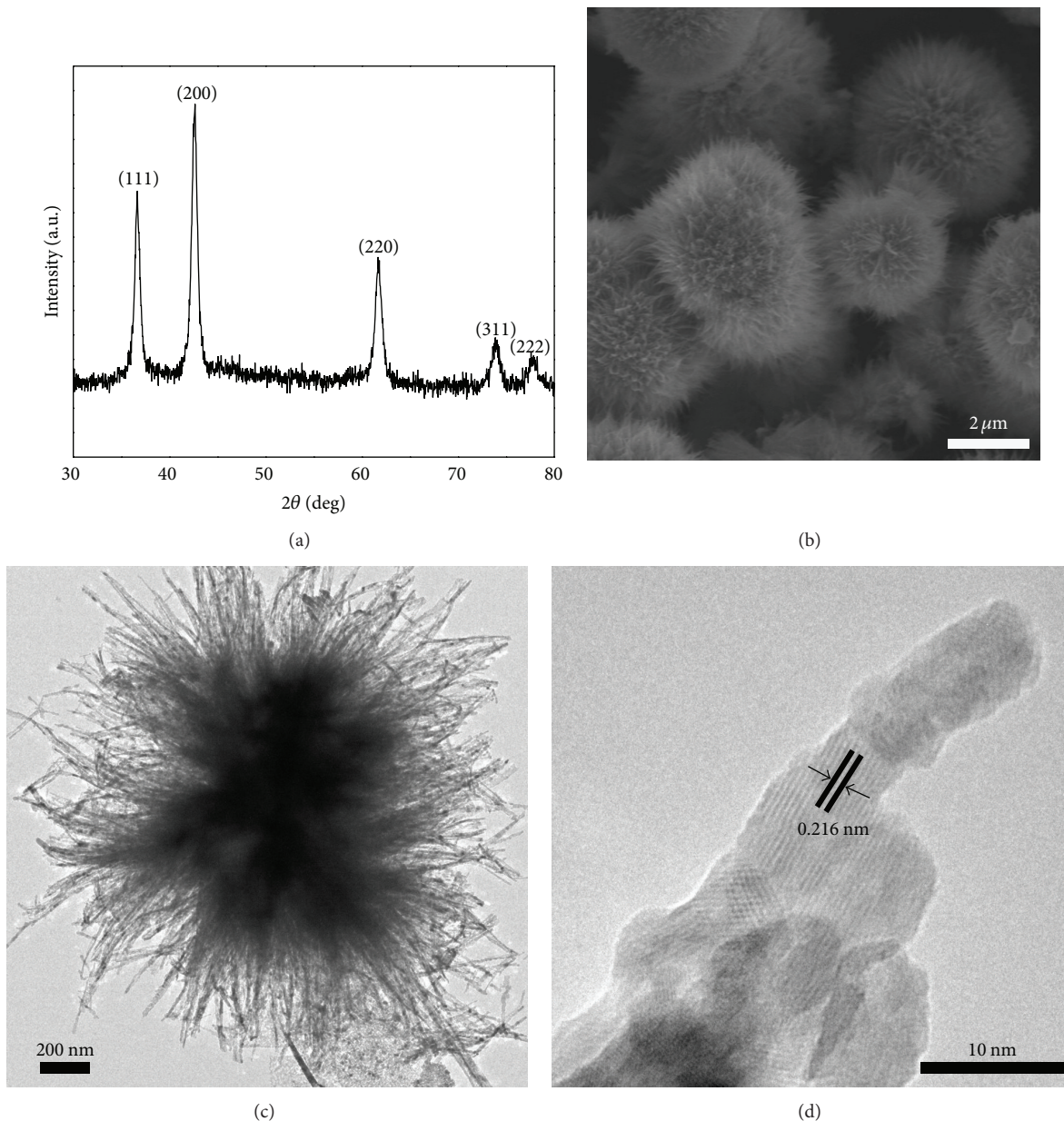


FIGURE 1: (a) XRD pattern of the as-prepared CoO products. ((b)–(d)) Characterization of hierarchical CoO nano/microstructures: (b) FESEM image, (c) TEM image, and (d) HRTEM image.

of 372 mAh/g. Moreover, when the current density reduces to 100 mA/g again, the capacity reaches back to 1054 mAh/g accordingly. The coulombic efficiency of the CoO is close to 100% during the cycles.

The superior electrochemical performance of the as-prepared hierarchical CoO nano/microstructures might originate from their unique nano/microstructures. The hierarchical CoO nano/microstructures with the size of several micrometers are composed of many CoO nanoparticles chains. The high specific surface of the CoO nanoparticles and the large porosity of the hierarchical nano/microstructures increase the contact area between the

electrolyte and CoO electroactive materials and shorten the path length for Li^+ transport, improving the discharge capacity and the cycle stability of the CoO as anode materials for LIBs. Furthermore, the good rate performance of the CoO can be attributed to the electrochemical milling effect [27, 28], which can be observed in various metal oxides systems, including Fe_3O_4 and $\text{Cu}_2\text{O-Li}_2\text{O}$ composite electrodes.

4. Conclusion

Hierarchical CoO nano/microstructures have been successfully synthesized by using a hydrothermal method and

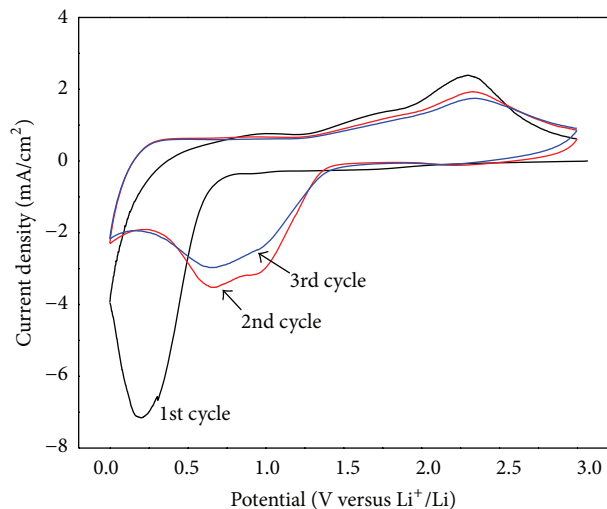


FIGURE 2: First three cyclic CV curves of the hierarchical CoO nano/microstructures at a scan rate of 0.2 mV/s.

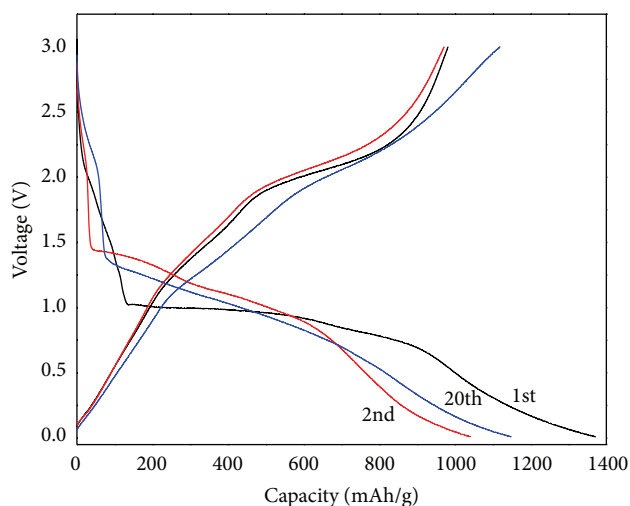


FIGURE 3: The galvanostatic discharge-charge profiles of the CoO electrode at a current density of 100 mA/g between 0.01 V and 3.0 V.

an annealing procedure. The as-prepared hierarchical CoO nano/microstructures exhibit superior electrochemical performance as anode materials for LIBs. A high discharge capacity of 1370 mAh/g and the retained discharge capacity of about 1144 mAh/g over 20 cycles are achieved at a current density of 100 mA/g. The excellent electrochemical performance might originate from these unique CoO nano/microstructures. Our works shed light on the extending applications of CoO as anode materials for high power LIBs.

Conflict of Interests

The authors declare that there is no conflict of interests regarding the publication of this paper.

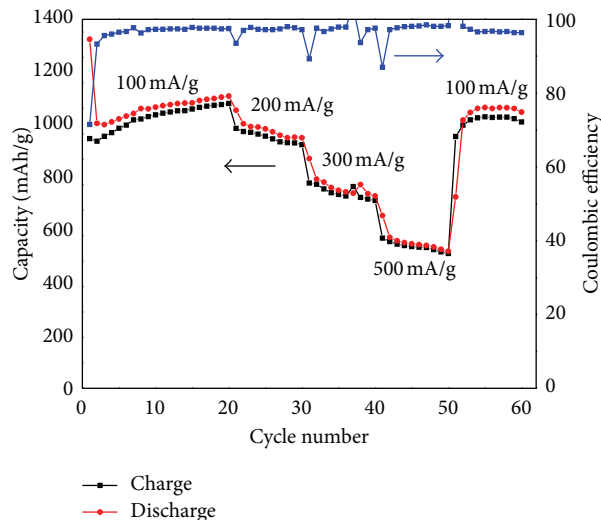


FIGURE 4: The specific capacity and the coulombic efficiency of CoO electrode under different current densities (100–500 mA/g).

Acknowledgments

This work was supported by the National Natural Science Foundation of China (no. 11074254 and no. 51171176) and the Visiting Scholar Project for the Young Core Instructor of Higher Institutions in Shandong Province.

References

- [1] A. S. Aricò, P. Bruce, B. Scrosati, J.-M. Tarascon, and W. van Schalkwijk, "Nanostructured materials for advanced energy conversion and storage devices," *Nature Materials*, vol. 4, no. 5, pp. 366–377, 2005.
- [2] K. S. Kang, Y. S. Meng, J. Bréger, C. P. Grey, and G. Ceder, "Electrodes with high power and high capacity for rechargeable lithium batteries," *Science*, vol. 311, no. 5763, pp. 977–980, 2006.
- [3] D. D. Li, L. X. Ding, S. Q. Wang, D. D. Cai, and H. H. Wang, "Ultrathin and highly-ordered CoO nanosheet arrays for lithium-ion batteries with high cycle stability and rate capability," *Journal of Materials Chemistry A*, vol. 2, no. 16, pp. 5625–5630, 2014.
- [4] P. Poizot, S. Laruelle, S. Grugeon, L. Dupont, and J. M. Tarascon, "Nano-sized transition-metal oxides as negative-electrode materials for lithium-ion batteries," *Nature*, vol. 407, no. 6803, pp. 496–499, 2000.
- [5] F. Li, Q. Q. Zou, and Y. Y. Xia, "CoO-loaded graphitizable carbon hollow spheres as anode materials for lithium-ion battery," *Journal of Power Sources*, vol. 177, no. 2, pp. 546–552, 2008.
- [6] X. W. Lou, D. Deng, J. Y. Lee, J. Feng, and L. A. Archer, "Self-supported formation of needlelike Co₃O₄ nanotubes and their application as lithium-ion battery electrodes," *Advanced Materials*, vol. 20, no. 2, pp. 258–262, 2008.
- [7] A. Hu, C. Curran, C. Tran, A. Kaplani, and V. Kalra, "Fabrication of transition metal oxide-carbon nanofibers with novel hierarchical architectures," *Journal of Nanoscience and Nanotechnology*, vol. 14, no. 7, pp. 5501–5507, 2014.
- [8] H. Iddir and R. Benedek, "First-principles analysis of phase stability in layered-layered composite cathodes for lithium-ion

- batteries," *Chemistry Materials*, vol. 26, no. 7, pp. 2407–2413, 2014.
- [9] P. Tammawat and N. Meethong, "Synthesis and characterization of stable and binder-free electrodes of TiO₂ nanofibers for li-ion batteries," *Journal of Nanomaterials*, vol. 2013, Article ID 413692, 8 pages, 2013.
- [10] Z. P. Wang, G. W. Xie, and L. J. Gao, "Electrochemical characterization of Li₄ Ti₅ O₁₂/C anode material prepared by starch-sol-assisted rheological phase method for Li-ion battery," *Journal of Nanomaterials*, vol. 2012, Article ID 876197, 7 pages, 2012.
- [11] F. D. Wu and Y. Wang, "Self-assembled echinus-like nanostructures of mesoporous CoO nanorod@CNT for lithium-ion batteries," *Journal of Materials Chemistry*, vol. 21, no. 18, pp. 6636–6641, 2011.
- [12] A. Yu, H. W. Park, A. Davies, D. C. Higgins, Z. Chen, and X. Xiao, "Free-standing layer-by-layer hybrid thin film of graphene-MnO₂ nanotube as anode for lithium ion batteries," *Journal of Physical Chemistry Letters*, vol. 2, no. 15, pp. 1855–1860, 2011.
- [13] C. C. Li, Q. H. Li, L. B. Chen, and T. H. Wang, "Self-assembled echinus-like nanostructures of mesoporous CoO nanorod@CNT for lithium-ion batteries," *Journal of Materials Chemistry*, vol. 21, no. 18, pp. 11867–11872, 2011.
- [14] W. L. Yao, J. Yang, J. L. Wang, and L. A. Tao, "Synthesis and electrochemical performance of carbon nanofiber-cobalt oxide composites," *Electrochimica Acta*, vol. 53, no. 24, pp. 7326–7330, 2008.
- [15] Y. M. Sun, X. L. Hu, W. Luo, and Y. H. Huang, "Self-assembled mesoporous CoO nanodisks as a long-life anode material for lithium-ion batteries," *Journal of Materials Chemistry*, vol. 22, no. 27, pp. 13826–13831, 2012.
- [16] X. L. Huang, R. Z. Wang, D. Xu et al., "Homogeneous CoO on graphene for binder-free and ultralong-life lithium ion batteries," *Advanced Functional Materials*, vol. 23, no. 35, pp. 4345–4353, 2013.
- [17] W. Yao, J. Chen, and H. Cheng, "Platelike CoO/carbon nanofiber composite electrode with improved electrochemical performance for lithium ion batteries," *Journal of Solid State Electrochemistry*, vol. 15, no. 1, pp. 183–188, 2011.
- [18] H. Guan, X. Wang, H. Li et al., "CoO octahedral nanocages for high-performance lithium ion batteries," *Chemical Communications*, vol. 48, no. 40, pp. 4878–4880, 2012.
- [19] B. D. Chen, C. X. Peng, and Z. Cui, "Ultrasonic synthesis of CoO/graphene nanohybrids as high performance anode materials for lithium-ion batteries," *Transactions of Nonferrous Metals Society of China*, vol. 22, no. 10, pp. 2517–2522, 2012.
- [20] W. W. Yuan, J. Zhang, D. Xie, Z. Donga, Q. M. Su, and G. H. Du, "Porous CoO/C polyhedra as anode material for Li-ion batteries," *Electrochimica Acta*, vol. 108, pp. 506–511, 2013.
- [21] M. Zhang, F. L. Yan, X. Tang, Q. H. Li, T. H. Wang, and G. Z. Cao, "Flexible CoO-graphene-carbon nanofiber mats as binder-free anodes for lithium-ion batteries with superior rate capacity and cyclic stability," *Journal of Materials Chemistry A*, vol. 2, no. 16, pp. 5890–5897, 2014.
- [22] F. Wang, C. C. Lu, Y. F. Qin et al., "Solid state coalescence growth and electrochemical performance of plate-like Co₃O₄ mesocrystals as anode materials for lithium-ion batteries," *Journal of Power Sources*, vol. 235, pp. 67–73, 2013.
- [23] J. Cao, H. Liu, J. Xie, G. Cao, and X. Zhao, "Effect of K-doping on the electrochemical performance of Ca₃Co₄O₉ anode for Li-ion batteries," *Journal of Materials Science & Technology*, vol. 26, no. 7, pp. 669–672, 2010.
- [24] M. M. Rahman, J. Z. Wang, X. L. Deng, Y. Li, and H. K. Liu, "Hydrothermal synthesis of nanostructured Co₃O₄ materials under pulsed magnetic field and with an aging technique, and their electrochemical performance as anode for lithium-ion battery," *Electrochimica Acta*, vol. 55, no. 2, pp. 504–510, 2009.
- [25] C. H. Chen, B. J. Hwang, J. S. Do et al., "An understanding of anomalous capacity of nano-sized CoO anode materials for advanced Li-ion battery," *Electrochemistry Communications*, vol. 12, no. 3, pp. 496–498, 2010.
- [26] W. Yao, J. Yang, J. Wang, and Y. Nuli, "Multilayered cobalt oxide platelets for negative electrode material of a lithium-ion battery," *Journal of the Electrochemical Society*, vol. 155, no. 12, pp. A903–A908, 2008.
- [27] S. Wang, J. Zhang, and C. Chen, "Fe₃O₄ submicron spheroids as anode materials for lithium-ion batteries with stable and high electrochemical performance," *Journal of Power Sources*, vol. 195, no. 16, pp. 5379–5381, 2010.
- [28] Y. Yu, Y. Shi, and C. H. Chen, "Nanoporous cuprous oxide/lithia composite anode with capacity increasing characteristic and high rate capability," *Nanotechnology*, vol. 18, no. 5, Article ID 055706, 2007.

Research Article

Cross-Linked ZnO Nanowalls Immobilized onto Bamboo Surface and Their Use as Recyclable Photocatalysts

Chunde Jin, Jingpeng Li, Jin Wang, Shenjie Han, Zhe Wang, and Qingfeng Sun

School of Engineering, Zhejiang Agricultural and Forestry University, Lin'an 311300, China

Correspondence should be addressed to Qingfeng Sun; qfsun@nefu.edu.cn

Received 14 May 2014; Accepted 22 June 2014; Published 10 July 2014

Academic Editor: Chuanfei Guo

Copyright © 2014 Chunde Jin et al. This is an open access article distributed under the Creative Commons Attribution License, which permits unrestricted use, distribution, and reproduction in any medium, provided the original work is properly cited.

A novel recyclable photocatalyst was fabricated by hydrothermal method to immobilize the cross-linked ZnO nanowalls on the bamboo surface. The resultant samples were characterized by using scanning electron microscopy (SEM), X-ray diffraction (XRD), energy dispersive spectroscopy (EDS), and Fourier transformation infrared (FTIR) techniques. FTIR spectra demonstrated that the cross-linked wurtzite ZnO nanowalls and bamboo surface were interconnected with each other by hydrogen bonds. Meanwhile, the cross-linked ZnO nanowalls modified bamboo (CZNB) presented a superior photocatalytic ability and could be recycled at least 3 times with a photocatalytic efficiency up to 70%. The current research provides a new opportunity for the development of a portable and recycled biomass-based photocatalysts which can be an efficiently degraded pollutant solution and reused several times.

1. Introduction

In recent years, environmental problems such as air and water pollution had provided the impetus for sustained fundamental and applied research in the area of environmental remediation [1–3]. The wastewater from textile, paper, plastics, rubber, cosmetics, and other drying industries contains residual dyes, which are not readily biodegradable [4]. These dyes were invariably left in the industrial waste and consequently discharged mostly to surface water resources, which were greatly harmful to the environment, hazardous to human health, and difficult to degrade by traditional techniques [5]. Recently, nanosized semiconductor materials like TiO_2 [6, 7], ZnO [8, 9], and SnO_2 [10], which mediate photocatalytic decomposition of organic molecules, are paid tremendous attention for the treatment of the organic pollutants of wastewater [11, 12]. One of the most important semiconductor photocatalysts, especially for ZnO, has been greatly focused on the photodegradation of the environmental pollutants due to its high catalytic activity, low cost, and environmental friendliness [13]. In the previous research, the structure or morphology of the photocatalysts is considered to have a strong relationship with their photocatalytic performance. For instance, Guo et al. [14, 15] have demonstrated that

morphology of materials can be well controlled in some important photocatalytic materials like BiOCl and Bi_2S_3 . Also, the interconnected nanostructures can greatly improve their mechanical strength [16]. Many organic pollutants, such as rhodamine B, methyl orange, phenols, dye, and carboxylic acids, can be photodegraded by nanosized ZnO materials under UV or visible light irradiation [8, 17–19]. The development of an efficient, green, and low-cost method for the removal of organic pollutant compounds is essential for the protection of the environment [20]. Wood, bamboo, and cellulose are usually considered good candidates as host materials of nanomaterials because they can improve the stability, retain the special morphology, and control the growth of nanoparticles. Meanwhile, these cellulose-based materials have always been environmentally friendly, easily biocompatible, easily designed, and feasibly biodegraded [21, 22]. Therefore, the inorganic nanomaterials/polymer composite materials can be considered as a portable catalyst.

Our previous research has confirmed that hydrothermal method is a facile method for the growth of inorganic nanomaterials on the surface of cellulose-based materials such as wood [23–27]. Moreover, the porous wood substrate rich in abundant hydroxyl groups provides a chance for the deposition of inorganic nanomaterials in the hydrothermal

process [28]. The porous structure in the surface and hydroxyl groups have been shown to be very useful for the creation of an inorganic nanoparticle/polymer catalyst. Bamboo surface with similar chemical constituents of wood can also provide a suitable template to prepare ZnO nanomaterial through strong hydrogen bond and electronic interactions under hydrothermal conditions. Herein, in our present work, a portable catalyst of cross-linked ZnO nanowalls/bamboo composites was prepared for the photocatalytic application under UV light irradiation. Compared with those powder photocatalysts, the as-prepared photocatalyst was very easily separated from the dye aqueous solution and cyclically used. We hope to provide a novel method for easy creation of ZnO nanomaterial bound with cellulose-based materials. The paper may provide a new and “green” pathway for the design and fabrication of photocatalytic materials to solve the problem of organic pollution.

2. Experimental

2.1. Raw Materials. All the chemicals were supplied by Shanghai Boyle Chemical Co., Ltd., and used as received. The moso bamboo was cut into slices with a size of 50 mm (tangential) × 20 mm (radial) × 2 mm (longitudinal). The bamboo slices were ultrasonically rinsed in deionized water and ethanol for 30 min and vacuum-dried at 60°C for 48 h. The original bamboo sample was abbreviated as OB.

2.2. Immobilization of the Cross-Linked ZnO Nanowalls on the Bamboo Surface. In a typical preparation method, zinc acetate dihydrate (0.75 M) was dissolved in methanol at 60°C under vigorous magnetic stirring. Then, the above solution was added dropwise to a solution of monoethanolamine with volume ratio of 1:1 at room temperature. The resulting mixture solutions were then stirred at 60°C for 30 min. The ZnO sol solution was thus obtained. Immobilization of the cross-linked ZnO nanowalls on the bamboo surface was employed by the following process. Firstly, bamboo slices were coated by ZnO sol through a repeated dip-coating process. The obtained bamboo slices were immersed into the ZnO sol solution for 5 min. After that, these bamboo slices were dried at 80°C for 5 hours using a drying oven. The procedures from dip-coating to drying were repeated 5 times to obtain multilayer films. The bamboo sample coated by ZnO sol was abbreviated as ZSB. Then, the cross-linked ZnO nanowalls were grown via an aqueous solution route with a mixture solution consisting of zinc nitrate hexahydrate (0.05 M), hexamethylenetetramine (0.05 M), polyvinyl alcohol (0.06 M), and deionized water (250 mL). The main growth of the cross-linked ZnO nanowalls was carried out at 95°C for 1 h. The samples were collected and rinsed with distilled water several times. Finally, the samples were dried at 50°C for 48 h. The cross-linked ZnO nanowalls that treated the bamboo were abbreviated as CZNB.

2.3. Characterizations. Surface morphology of samples was characterized by scanning electron microscopy (SEM, FEI, Quanta 200). The chemical compositions of the untreated and treated bamboo were measured by energy dispersive spectroscopy (EDS) in connection with SEM. Crystalline

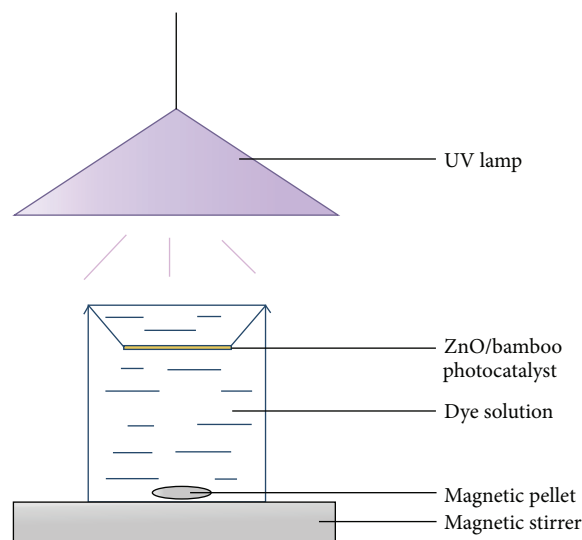


FIGURE 1: Experimental setup of photocatalytic degradation.

structures of the samples were identified by X-ray diffraction technique (XRD, Rigaku, D/MAX 2200) operating with Cu K α radiation ($\lambda = 1.5418 \text{ \AA}$) at a scan rate (2θ) of 4° min^{-1} , 40 Kv, and 40 mA, ranging from 5° to 80° . Surface chemical compositions of the samples were characterized by Fourier transformation infrared (FTIR) spectroscopy using a Thermo Magna-IR 560 E.S.P FTIR spectrometer (Nicolet).

2.4. Measurement of Photocatalytic Activity. The photocatalytic activities of the as-prepared samples were assessed by monitoring the degradation of rhodamine B (Rh B) solutions at ambient temperature. A 35 W mercury lamp (Hg lamp) (Shanghai Rongbo Co., China) with main wavelength of 254 nm was used as ultraviolet light source. The degradation experiments were carried out in a 100 mL beaker, opening to air, and the distance between the lamp and the solution was about 10 cm. Magnetic stirring at a speed of 100 rpm was applied to the solution. For a comparative study of photocatalytic activity, blank experiments using similar conditions without the addition of photocatalysts were performed. The bamboo slices with ZnO were added to 100 mL of the Rh B solution (50 mg L^{-1}) with ultrasonic treatment for 30 min. Before the photocatalytic degradation, the solution was magnetically stirred in dark environment for 60 min to reach the adsorption equilibrium. The change of solution concentration in every 30 min was measured to judge the absorbability of catalysts in the dark. At every interval during the process of 3 h, a series of aqueous solutions in a certain volume were collected and were then analyzed on a TU-1901 UV-vis spectrophotometer (TU-1901, Beijing Purkinje, China), and its maximum absorption wavelength of Rh B was 554.5 nm.

The efficiency was calculated by the following equation:

$$Y = 100 \times \left(\frac{C - C_0}{C_0} \right), \quad (1)$$

where C_0 and C are the initial dye concentration and the concentration at time t , respectively. The schematic diagram of the photocatalytic reactor was shown in Figure 1.

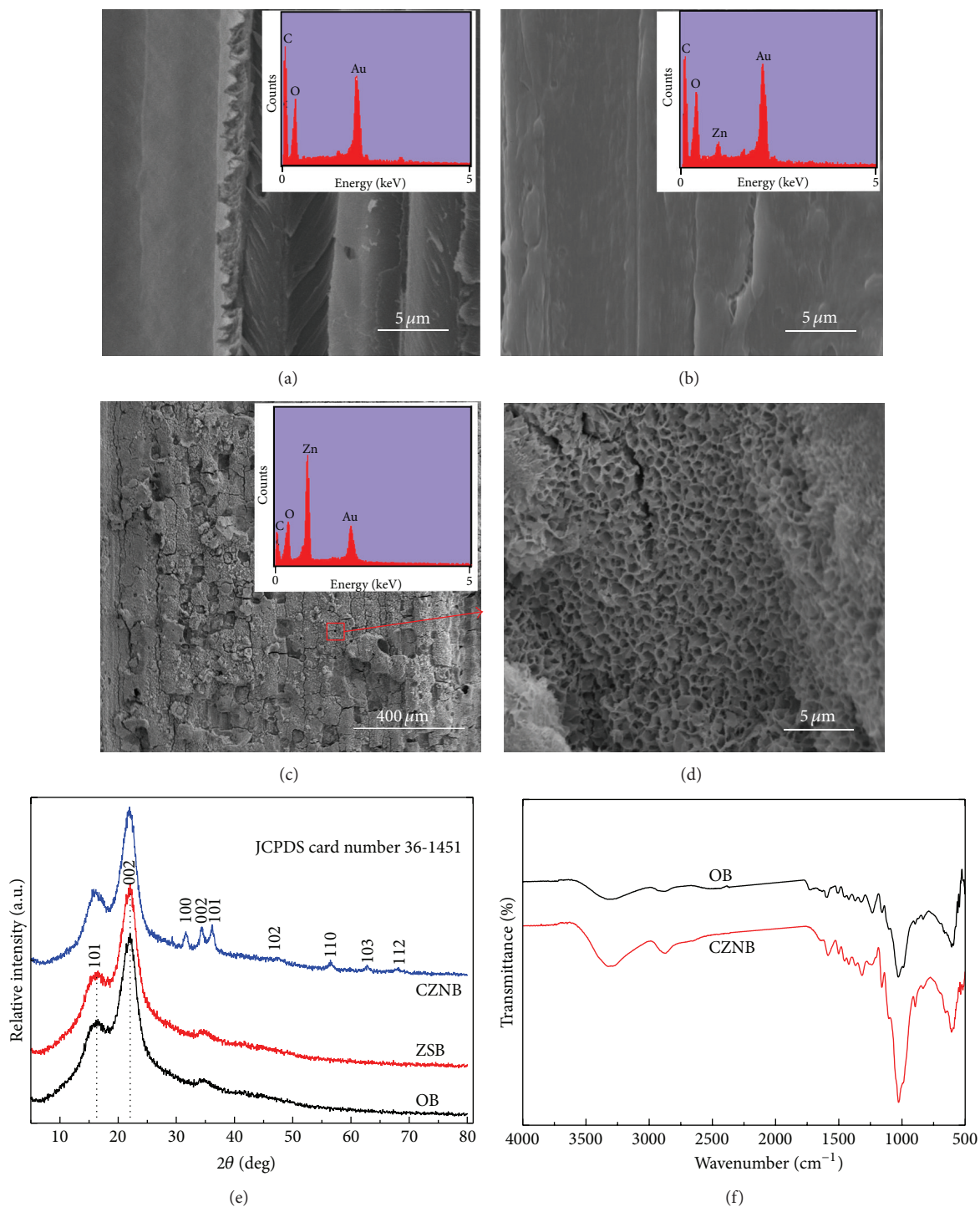


FIGURE 2: SEM images of the surface of (a) OB. The inset was its corresponding EDS spectrum. (b) ZSB. The inset was its corresponding EDS spectrum. CZNB at (c) low and (d) high magnification, respectively. The inset in (d) was its corresponding EDS spectrum. (e) XRD spectra of OB, ZSB, and CZNB. (f) FTIR spectra of OB and CZNB.

3. Results and Discussion

Figure 2(a) showed SEM image of the surface of OB. The microstructures of OB could be clearly observed, which displayed a kind of nonsmooth morphological surface. The

inset in Figure 2(a) gave a typical EDS spectrum of the chemical compositions for OB. Only C, Au, and O elements could be detected from the spectrum. The element of Au came from the coating layer used for SEM observation and C and O elements were from the bamboo substrate. After

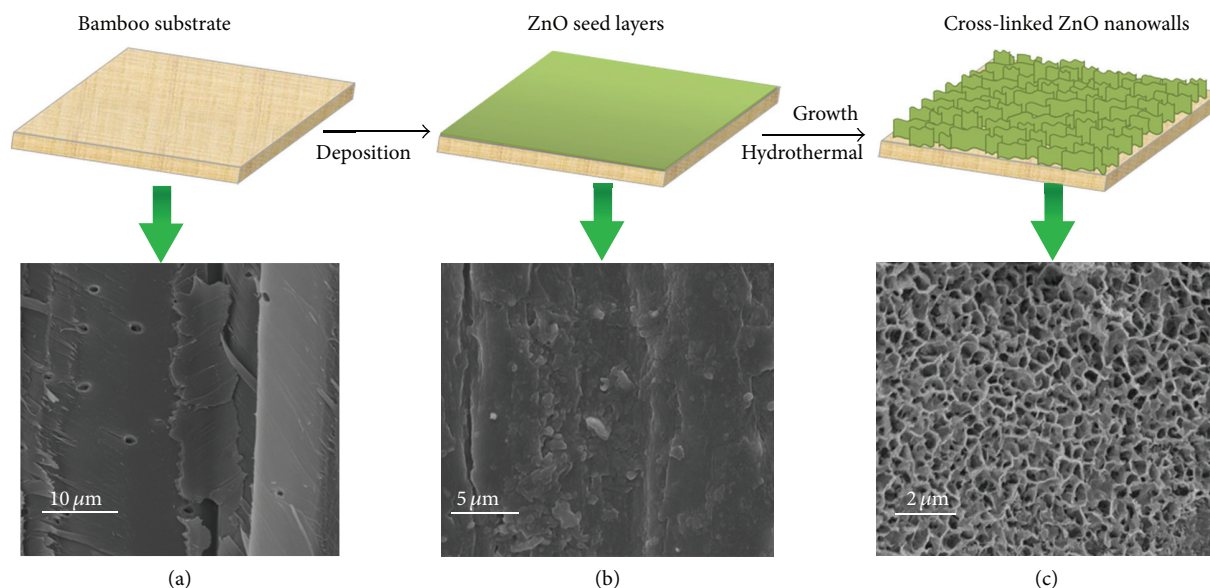


FIGURE 3: Schematic illustration of the formation process of CZNB.

the dip-coating process by ZnO sol, the microstructures of OB were disappeared, which presented a smooth and clean surface as shown in Figure 2(b). From the inset of this figure, besides the signal of carbon and oxygen elements, weak peaks corresponding to zinc element were also observed in the spectrum of ZnO sol coated bamboo substrate, indicating the formation of ZnO sol on the bamboo surface. Figure 2(c) showed a SEM image of CZNB at low magnification. From the SEM image, it could be clearly seen that thickly ZnO nanostructured materials had been immobilized onto the bamboo surface after the hydrothermal reaction. In the magnified SEM image (Figure 2(d)), the morphology of CZNB could be clearly observed. These cross-linked ZnO nanowalls were randomly oriented due to the unevenness of the bamboo surface, leading to the cross-linked ZnO nanowalls observed most frequently. Moreover, the ZnO nanosheets were interconnected with each other and had an uneven surface morphology on a large scale with diameters of about $0.5\sim 1\ \mu\text{m}$. In the corresponding EDS spectrum of the inset in Figure 2(c), Zn element with a strong peak could be detected, indicating that ZnO had been grown on the bamboo surface.

Figure 2(e) displayed the XRD patterns of OB, ZSB, and CZNB. The diffraction peaks at about 16° and 22° were assigned to OB [29]. But, for ZSB, no other new diffraction peaks were detected from the XRD patterns except for the cellulose diffraction peaks from bamboo, which might be due to the fact that the crystal phase of ZnO sol consisted of amorphous ZnO. After hydrothermal reaction, some new strong diffraction peaks were observed and all diffraction peaks could be assigned to the wurtzite-type ZnO (JCPDS, 36-1451). No excess peaks were detected, implying that only high purity ZnO nanostructure was formed following the hydrothermal reaction. Figure 2(f) presented the FTIR absorption spectra of OB and CZNB. The absorption peaks at $3321\ \text{cm}^{-1}$ became increasingly stronger, which was attributed to the stretching

vibrations of hydroxyl groups indicating that more hydroxyl groups were assembled on the bamboo surface. The self-assembly of the cross-linked ZnO nanowalls was achieved by the hydrothermal reaction due to the interaction between the O-H groups of bamboo surface and the deposited ZnO [23, 27]. The absorption peaks at $2881\ \text{cm}^{-1}$ were assigned to the C-H stretching vibrations [30]. As we all know, the peaks around $500\ \text{cm}^{-1}$ were due to the vibration of metal-oxygen (M-O) bonds as reported in the literature [31]. The wide band observed in the $400\text{--}600\ \text{cm}^{-1}$ frequency range was characteristic of ZnO as previously reported [32].

Based on the results mentioned above, a schematic diagram of the formation of CZNB using a hydrothermal method was proposed, which could be helpful in understanding the growth mechanism of wurtzite ZnO on the bamboo surface. The porous bamboo substrate with abundant hydroxyl groups provided a chance for the deposition of ZnO nanomaterials on the bamboo surface under hydrothermal conditions (Figure 3(a)). When the bamboo substrate was immersed in ZnO sol solution, the zinc alkoxides from ZnO sol solution could adsorb onto the micronanoporous structure through strong hydrogen bond and electronic interactions (Figure 3(b)). With hydrothermal reaction, the zinc alkoxides continuously hydrolyzed to form ZnO seeds for the growth of CZNB (Figure 3(c)). Thus, the ZnO nanomaterials were covered and immobilized well in the bamboo surface.

Rh B was adopted as a representative organic pollutant to evaluate the photocatalytic performance of CZNB as photocatalysts. In this experiment, the commercially available TiO_2 P25 (Degussa, Germany) was used as a photocatalytic reference to help understand the photocatalytic activity of CZNB. The photocatalytic activities of the as-prepared samples and P25 were shown in Figure 4(a). The CZNB as photocatalysts showed the highest photocatalytic activity. The OB had a little photocatalytic activity of about 5.6% on Rh B during the whole process, which was mainly due to the

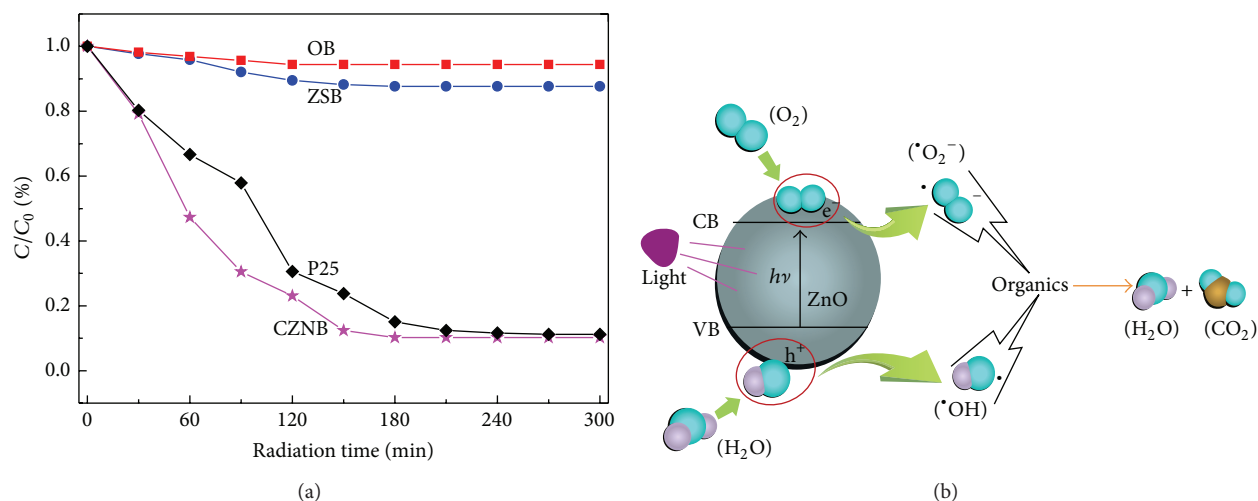


FIGURE 4: (a) Photocatalytic activity of OB, ZSB, P25, and CZNB, respectively. (b) Schematic photocatalytic mechanism of ZnO.

physical absorption effect of bamboo. In Figure 4(a), the Rh B degradation efficiency was about 12.3% for ZSB. However, the required time for an entire decolorization of Rh B over CZNB as photocatalysts was about 180 min, which was much shorter than P25. The photocatalytic efficiency of CZNB was greatly enhanced, which was probably because the photocatalytic activity of ZnO particles strongly depends on some specific exposed crystal faces [33, 34]. This result would contribute to the potential application of our ZnO/bamboo composite materials to the treatment of dye wastewater.

Based on the above results, the photocatalytic activities of CZNB under UV irradiation could be illuminated by Figure 4(b). When the bamboo-based photocatalysts were irradiated by UV light at 254 nm, which was with photon energy higher than or equal to the band gap of ZnO nanocrystals, holes could react with water adhering to the surfaces of ZnO nanowalls to form highly reactive hydroxyl radicals ($\cdot OH$). Meanwhile, on the surfaces of ZnO nanowalls, oxygen was reduced as an electron captor to superoxide radical anions ($\cdot O_2^-$). The radical anions were further combined with H^+ to form $\cdot OOH$ and $\cdot OOH$ radicals and the trapped electrons combined to produce H_2O_2 and this led to production of hydroxyl radicals ($\cdot OH$). The formed radicals had a powerful oxidation ability to degrade Rh B dye [35, 36].

Regeneration of ZnO photocatalyst was one of the key steps to make heterogeneous photocatalysis technology for practical applications. It was important to investigate the stability and repeatability of the as-synthesized CZNB as a photocatalyst in photocatalytic degradation of aqueous Rh B. So, in our work, CZNB was recycled for three times in the same photocatalytic reactions under ultraviolet irradiation. After each cycle, which lasted for 180 min, the photocatalyst was separated from the suspension by tweezers, washed with deionized water, dried, and used for a new cycle. Figure 5 presented the degradation evolution of Rh B for CZNB as a photocatalyst at 180 min illumination for the first three cycles. Obviously, the photocatalytic activity of CZNB exhibited a

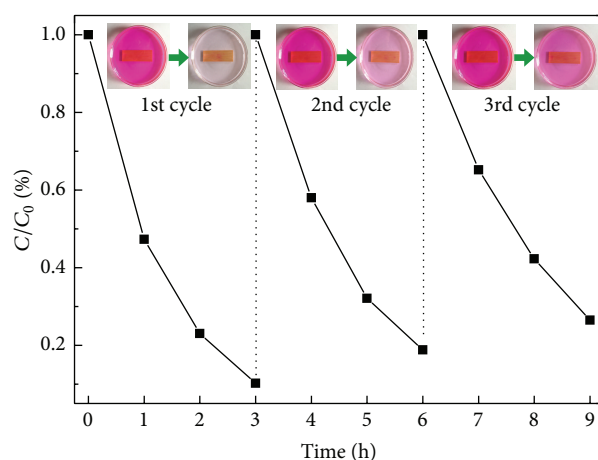


FIGURE 5: Photocatalytic activity of CZNB as a photocatalyst at 180 min illumination for the first three cycles. The insets were its corresponding macrographs, respectively.

little decline after three cycles, and the degradation ratio was still higher than 77%. It was obvious that the Rh B solutions were degraded by CZNB under ultraviolet irradiation, resulting in the faded solution (Figure 5, insets).

4. Conclusions

The cross-linked ZnO nanowalls had been successfully immobilized onto the bamboo surface using the hydrothermal method. The wurtzite cross-linked ZnO nanowalls were attached to the bamboo surface through the hydroxyl group interactions. The cross-linked ZnO nanowalls on the bamboo surface showed a superior photocatalytic ability and could be used as recyclable photocatalysts. This study also provided a recycled green photocatalyst of the ZnO/bamboo composite materials.

Conflict of Interests

The authors declare that there is no conflict of interests regarding the publication of this paper.

Acknowledgment

The work was financially supported by the Pre-Research Project of Research Center of Biomass Resource Utilization, Zhejiang A & F University (2013SWZ01-03).

References

- [1] Y. Zheng, L. Zheng, Y. Zhan, X. Lin, Q. Zheng, and K. Wei, "Ag/ZnO heterostructure nanocrystals: synthesis, characterization, and photocatalysis," *Inorganic Chemistry*, vol. 46, no. 17, pp. 6980–6986, 2007.
- [2] Y. Zheng, Y. Cheng, Y. Wang et al., "Quasicubic α -Fe₂O₃ nanoparticles with excellent catalytic performance," *Journal of Physical Chemistry B*, vol. 110, no. 7, pp. 3093–3097, 2006.
- [3] C. T. Williams and D. A. Beattie, "Probing buried interfaces with non-linear optical spectroscopy," *Surface Science*, vol. 500, no. 1–3, pp. 545–576, 2002.
- [4] R. Gong, Y. Ding, M. Li, C. Yang, H. Liu, and Y. Sun, "Utilization of powdered peanut hull as biosorbent for removal of anionic dyes from aqueous solution," *Dyes and Pigments*, vol. 64, no. 3, pp. 187–192, 2005.
- [5] I. Kanu and O. Achi, "Industrial effluents and their impact on water quality of receiving rivers in Nigeria," *Journal of Applied Technology in Environmental Sanitation*, vol. 1, no. 1, pp. 75–86, 2011.
- [6] J. Yu, M. Jaroniec, H. Yu, and W. Fan, "Synthesis, characterization, properties, and applications of nanosized photocatalytic materials," *Journal of Nanomaterials*, vol. 2012, Article ID 783686, 17 pages, 2012.
- [7] W. Asghar, I. A. Qazi, H. Ilyas, A. A. Khan, M. A. Awan, and M. Rizwan Aslam, "Comparative solid phase photocatalytic degradation of polythene films with doped and undoped TiO₂ nanoparticles," *Journal of Nanomaterials*, vol. 2011, Article ID 461930, 12 pages, 2011.
- [8] M. H. Habibi and M. K. Sardashti, "Preparation of glass plate-supported nanostructure ZnO thin film deposited by sol-gel spin-coating technique and its photocatalytic degradation to monoazo textile dye," *Journal of Nanomaterials*, vol. 2008, Article ID 356765, 5 pages, 2008.
- [9] S.-M. Lee, G. Grass, G.-M. Kim et al., "Low-temperature ZnO atomic layer deposition on biotemplates: flexible photocatalytic ZnO structures from eggshell membranes," *Physical Chemistry Chemical Physics*, vol. 11, no. 19, pp. 3608–3614, 2009.
- [10] L. Wang, L. Shen, L. Zhu, H. Jin, and N. Bing, "Preparation and photocatalytic properties of SnO₂ coated on nitrogen-doped carbon nanotubes," *Journal of Nanomaterials*, vol. 2012, Article ID 794625, 6 pages, 2012.
- [11] I. Poullos and I. Aetopoulou, "Photocatalytic degradation of the textile dye reactive orange 16 in the presence of TiO₂ suspensions," *Environmental Technology*, vol. 20, no. 5, pp. 479–487, 1999.
- [12] K. Onda, B. Li, J. Zhao, and H. Petek, "The electronic structure of methanol covered TiO₂(110) surfaces," *Surface Science*, vol. 593, no. 1–3, pp. 32–37, 2005.
- [13] Y. Zheng, C. Chen, Y. Zhan et al., "Photocatalytic activity of Ag/ZnO heterostructure nanocatalyst: correlation between structure and property," *Journal of Physical Chemistry C*, vol. 112, no. 29, pp. 10773–10777, 2008.
- [14] C. F. Guo, S. Cao, J. Zhang et al., "Topotactic transformations of superstructures: from thin films to two-dimensional networks to nested two-dimensional networks," *Journal of the American Chemical Society*, vol. 133, no. 21, pp. 8211–8215, 2011.
- [15] C. F. Guo, J. Zhang, M. Wang, Y. Tian, and Q. Liu, "A strategy to prepare wafer scale bismuth compound superstructures," *Small*, vol. 9, no. 14, pp. 2394–2398, 2013.
- [16] C. Guo, T. Sun, Q. Liu, Z. Suo, and Z. Ren, "Highly stretchable and transparent nanomesh electrodes made by grain boundary lithography," *Nature Communications*, vol. 5, article 3121, 2014.
- [17] A. Phuruangrat, O. Yayapao, T. Thongtem, and S. Thongtem, "Synthesis and characterization of europium-doped zinc oxide photocatalyst," *Journal of Nanomaterials*, vol. 2014, Article ID 367529, 9 pages, 2014.
- [18] S. L. Wang, H. W. Zhu, W. H. Tang, and P. G. Li, "Propeller-shaped ZnO nanostructures obtained by chemical vapor deposition: photoluminescence and photocatalytic properties," *Journal of Nanomaterials*, vol. 2012, Article ID 594290, 5 pages, 2012.
- [19] E. S. Jang, J. H. Won, S. J. Hwang, and J. H. Choy, "Fine tuning of the face orientation of ZnO crystals to optimize their photocatalytic activity," *Advanced Materials*, vol. 18, no. 24, pp. 3309–3312, 2006.
- [20] J. Zeng, S. Liu, J. Cai, and L. Zhang, "TiO₂ immobilized in cellulose matrix for photocatalytic degradation of phenol under weak UV light irradiation," *Journal of Physical Chemistry C*, vol. 114, no. 17, pp. 7806–7811, 2010.
- [21] S. H. Imam, S. H. Gordon, L. Mao, and L. Chen, "Environmentally friendly wood adhesive from a renewable plant polymer: characteristics and optimization," *Polymer Degradation and Stability*, vol. 73, no. 3, pp. 529–533, 2001.
- [22] M. Singh, J. Martínez-Fernández, and A. R. de Arellano-López, "Environmentally conscious ceramics (ecoceramics) from natural wood precursors," *Current Opinion in Solid State and Materials Science*, vol. 7, no. 3, pp. 247–254, 2003.
- [23] Q. Sun, H. Yu, Y. Liu, J. Li, Y. Lu, and J. F. Hunt, "Improvement of water resistance and dimensional stability of wood through titanium dioxide coating," *Holzforschung*, vol. 64, no. 6, pp. 757–761, 2010.
- [24] Y. Lu, S. Xiao, R. Gao, J. Li, and Q. Sun, "Improved weathering performance and wettability of wood protected by CeO₂ coating deposited onto the surface," *Holzforschung*, vol. 68, no. 3, pp. 345–351, 2013.
- [25] Q. Sun, Y. Lu, and Y. Liu, "Growth of hydrophobic TiO₂ on wood surface using a hydrothermal method," *Journal of Materials Science*, vol. 46, no. 24, pp. 7706–7712, 2011.
- [26] Q. Sun, Y. Lu, D. Yang, J. Li, and Y. Liu, "Preliminary observations of hydrothermal growth of nanomaterials on wood surfaces," *Wood Science and Technology*, vol. 48, no. 1, pp. 51–58, 2014.
- [27] Q. Sun, Y. Lu, H. Zhang et al., "Improved UV resistance in wood through the hydrothermal growth of highly ordered ZnO nanorod arrays," *Journal of Materials Science*, vol. 47, no. 10, pp. 4457–4462, 2012.
- [28] Q. Sun, Y. Lu, H. Zhang et al., "Hydrothermal fabrication of rutile TiO₂ submicrospheres on wood surface: an efficient method to prepare UV-protective wood," *Materials Chemistry and Physics*, vol. 133, no. 1, pp. 253–258, 2012.

- [29] Y. Yu, Z. Jiang, G. Wang, G. Tian, H. Wang, and Y. Song, "Surface functionalization of bamboo with nanostructured ZnO," *Wood Science and Technology*, vol. 46, no. 4, pp. 781–790, 2012.
- [30] K. K. Pandey, "A study of chemical structure of soft and hardwood and wood polymers by FTIR spectroscopy," *Journal of Applied Polymer Science*, vol. 71, no. 12, pp. 1969–1975, 1999.
- [31] S. K. Dhoke, T. J. M. Sinha, P. Dutta, and A. S. Khanna, "Formulation and performance study of low molecular weight, alkyd-based waterborne anticorrosive coating on mild steel," *Progress in Organic Coatings*, vol. 62, no. 2, pp. 183–192, 2008.
- [32] G. Xiong, U. Pal, J. G. Serrano, K. B. Ucer, and R. T. Williams, "Photoluminescence and FTIR study of ZnO nanoparticles: the impurity and defect perspective," *Physica Status Solidi C*, vol. 3, no. 10, pp. 3577–3581, 2006.
- [33] Y. Yamaguchi, M. Yamazaki, S. Yoshihara, and T. Shirakashi, "Photocatalytic ZnO films prepared by anodizing," *Journal of Electroanalytical Chemistry*, vol. 442, no. 1-2, pp. 1–3, 1998.
- [34] L. Jing, Z. Xu, X. Sun, J. Shang, and W. Cai, "The surface properties and photocatalytic activities of ZnO ultrafine particles," *Applied Surface Science*, vol. 180, no. 3-4, pp. 308–314, 2001.
- [35] S. Chakrabarti and B. K. Dutta, "Photocatalytic degradation of model textile dyes in wastewater using ZnO as semiconductor catalyst," *Journal of Hazardous Materials*, vol. 112, no. 3, pp. 269–278, 2004.
- [36] J. Yu and X. Yu, "Hydrothermal synthesis and photocatalytic activity of zinc oxide hollow spheres," *Environmental Science and Technology*, vol. 42, no. 13, pp. 4902–4907, 2008.

Research Article

Facile Synthesis of Carbon-Coated Zn_2SnO_4 Nanomaterials as Anode Materials for Lithium-Ion Batteries

Xiaoxu Ji, Xintang Huang, Qinghuai Zhao, Aihua Wang, and Xuyan Liu

School of Physics and Electronic Engineering, Nanyang Normal University, Nanyang 473061, China

Correspondence should be addressed to Xiaoxu Ji; xxji@nynu.edu.cn

Received 5 May 2014; Accepted 22 May 2014; Published 8 July 2014

Academic Editor: Xiang Wu

Copyright © 2014 Xiaoxu Ji et al. This is an open access article distributed under the Creative Commons Attribution License, which permits unrestricted use, distribution, and reproduction in any medium, provided the original work is properly cited.

Carbon-coated Zn_2SnO_4 nanomaterials have been synthesized by a facile hydrothermal method in which as-prepared Zn_2SnO_4 was used as the precursor and glucose as the carbon source. The structural, morphological, and electrochemical properties were investigated by means of X-ray (XRD), scanning electron microscopy (SEM), transmission electron microscopy (TEM), and electrochemical measurement. The first discharge/charge capacity of carbon-coated Zn_2SnO_4 was about 1248.8 mAh/g and 873.2 mAh/g at a current density of 200 mA/g in the voltage range of 0.05 V–3.0 V, respectively, corresponding to Coulombic efficiency of 69.92%. After 40 cycles, the capacity retained 400 mAh/g, which is much better than bare Zn_2SnO_4 .

1. Introduction

Tin-based oxide materials have been considered as promising anode materials in lithium-ion batteries (LIBs) due to their large lithium-ion capacities (over 600 mAh/g [1]) at low potentials and high densities [2–5], which is greater than that of commercialized graphite anodes (372 mAh/g) [6]. However, the practical usage of these anodes is hindered by their poor capacity retention during cycling as well as the large irreversible capacity during the first discharge/charge cycle [7–10]. This is mainly caused by a large volume change during the lithium insertion and extraction, which is leading to the pulverization of electrodes and rapid capacity fading [11–14]. To overcome the large volume change, numerous efforts have been made to develop anode materials with high energy density and excellent cycling performance, one of which is to synthesize nanosized materials with different shapes and structures. It was also found that nanosized tin-based oxides exhibit especially good electrochemical performance on account of the large specific area and high Li-ion conductivity [15–18]. Another is to prepare carbonaceous materials because carbon materials have high electronic conductivity and favorable electrochemical performance, which not only provides greatly improved electric conductivity, but also helps buffer the severe volume change [19–21].

As an important semiconductor material, Zn_2SnO_4 ($E_g = 3.6$ eV) has attracted much more attention owing to its applications in gas sensors [22, 23], photocatalysts [24, 25], and solar cells [26, 27]. Recently, nanosized Zn_2SnO_4 has been successfully synthesized by various methods and applied in lithium-ion batteries with good electrochemical properties. For instance, Zhu et al. [28] synthesized inverse-spinel by hydrothermal method. After 20 cycles, the reversible capacity decayed to 664.7 mAh/g at a current density of 50 mA/g, with an average capacity fade rate of 3.3% per cycle. Feng et al. [29] synthesized single crystal Zn_2SnO_4 cubes with reversible capacity of 775 mAh/g after 20 cycles at a current density of 50 mA/g. Rong et al. [30] synthesized cube-shaped particles with the reversible capacity of 580 mAh/g and a slowly fading capacity after 50 cycles at a current density of 50 mA/g. To the best of our knowledge, little attention has been paid to carbon-coated Zn_2SnO_4 as anode materials for lithium-ion batteries at a bigger current density. In this study, carbon-coated Zn_2SnO_4 materials were made by a facile hydrothermal method using the Zn_2SnO_4 octahedron as the precursor and glucose as the carbon source. The electrochemical properties were investigated, and the electrochemical tests showed that the carbon-coated Zn_2SnO_4 exhibits high rate capability and long cycle life compared with bare Zn_2SnO_4 , indicating its promising application as anode for lithium-ion batteries.

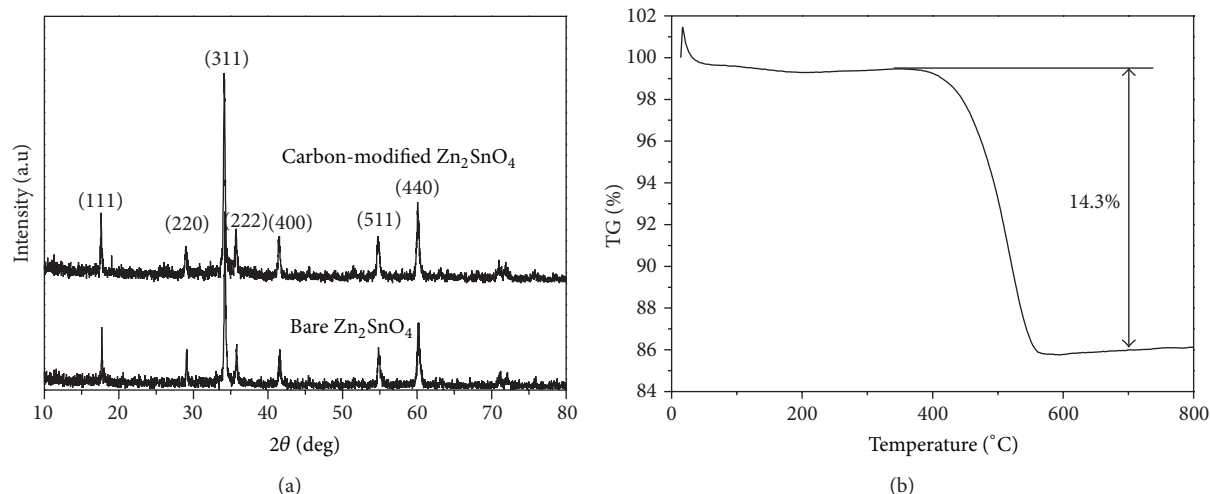


FIGURE 1: (a) XRD result of bare and carbon-coated Zn_2SnO_4 and (b) TGA of the as-obtained carbon-coated Zn_2SnO_4 .

2. Experimental

2.1. Preparation of Bare and Carbon-Coated Zn_2SnO_4 . In a typical synthesis, 0.025 M $\text{SnCl}_4 \cdot 5\text{H}_2\text{O}$ and 0.05 M $\text{ZnSO}_4 \cdot 7\text{H}_2\text{O}$ were dissolved in 60 mL distilled water, and then 1 M NaOH was added dropwise to the mixture under magnetic stirring. After 20 min, the slurry was transferred to a 100 mL Teflon autoclave, heated at 200°C in an electric oven for 24 h, and then cooled down to room temperature naturally. After the reaction, the precipitate was centrifuged and washed with distilled water and ethanol and then dried at 60°C for 3 h. The bare Zn_2SnO_4 was obtained by carbonizing precursor at 450°C for 3 h under air.

Then, 0.2 g obtained-bare Zn_2SnO_4 was dispersed in mixed solution of distilled and ethanol by ultrasonication, and then 1 g glucose was dissolved in the mixed solution by magnetic stirring for 30 min. The mixed solution was placed in a Teflon autoclave, and then it was placed in an electric oven at 180°C for 16 h. After cooling down in air, the carbon precursor-coated Zn_2SnO_4 was obtained by washing with distilled water and ethanol and dried in a vacuum oven at 60°C for 3 h. Hereafter, the as-prepared product was carbonized at 450°C for 3 h under nitrogen flow to obtain carbon-coated Zn_2SnO_4 .

2.2. Sample Characterizations. The morphology of the as-prepared product was characterized by field-emission scanning electron microscopy (FESEM, JEOL, and JSM-6700F). The crystalline structure of the product was analyzed by an X-ray diffractometer (XRD, Y-2000) with $\text{Cu K}\alpha$ radiation ($\lambda = 1.5418 \text{ \AA}$) at a scan rate of $0.04^\circ \text{ s}^{-1}$. Transmission electron microscopy (TEM) and high-resolution transmission electron microscopy (HRTEM) observations were carried out on a JEOL JEM-2010 instrument in bright field.

2.3. Electrochemical Test. Electrochemical performance evaluations were performed with coin cells using Li foil as

counter electrode. The working electrodes were prepared by mixing the bare Zn_2SnO_4 or carbon-coated Zn_2SnO_4 , carbon black and polyvinylidene fluoride (PVDF) at a weight ratio of 70:15:15. The mixture was dissolved in 1-methyl-2-pyrrolidinone (NMP) forming a slurry and was uniformly cast on a thick copper foil. The electrolyte consists of 1 M solution of LiPF₆ in ethylene carbonate (EC) and diethyl carbonate (DEC) (1:1 by volume). Electrochemical cells were assembled in an argon-filled glovebox. The charge-discharge cycling was performed by using a multichannel battery tester (model SCN, Bitrode, USA). Discharge/charge measurements were performed in the voltage range 0.05 V–3.00 V at a current density of 200 mA/g.

3. Results and Discussion

As reported in the literatures, glucose-derived carbon precursor (PS) can be readily integrated onto nanostructure in solution and furthermore carbonized at a temperature as low as 400°C [31]. In this work, throughout a complex polymerization of glucose at 180°C in the autoclave, the color of sample turned from white to puce, indicating that organic carbonaceous layers exist. After heat treatment at 450°C for 3 h under nitrogen atmosphere, the sample became black, indicating existing carbon layer.

All the diffraction peaks of the two samples were consistent with the data of pure reverse spinel Zn_2SnO_4 (JPCDS No. 74-2184), indicating that the glucose did not affect the configuration of sample in the process of hydrothermal synthesis. From the XRD patterns, no other peaks are detected, accounting for the low carbon content or forming amorphous carbon. Figure 1(b) shows the TGA curve of carbon-coated Zn_2SnO_4 in air between 30°C and 800°C. The weight loss before 100°C is due to the loss of water. The continuous weight loss between 400°C and 600°C signifies the removal of the combustion of the carbon layers into carbon oxides. The carbon content in carbon-coated Zn_2SnO_4 is estimated to be 14.3% based on the TGA analysis.

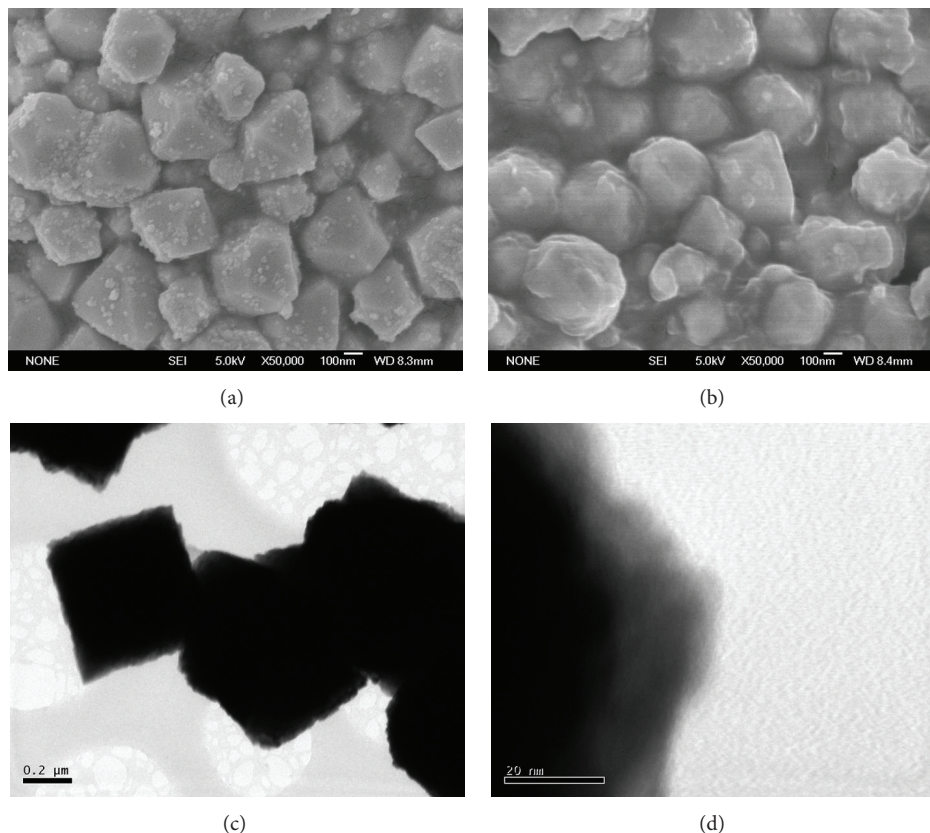
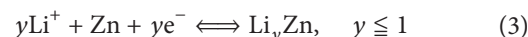
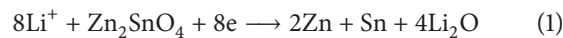


FIGURE 2: SEM images of (a) bare and (b) carbon-coated Zn_2SnO_4 . (c) Low-magnification and (d) high-magnification TEM image of the as-obtained carbon-coated Zn_2SnO_4 .

Representative SEM images of as-obtained products are observed in Figure 2. Figures 2(a) and 2(b) show a typical image of the bare Zn_2SnO_4 and carbon-coated Zn_2SnO_4 , respectively. As can be seen, the sample of bare Zn_2SnO_4 is dispersive quasi-octahedron shape with an average diameter of about 300 nm and nanoparticles on its surface. From Figure 2(b), it can be seen that the nanoparticles on the surface disappear and the morphology of carbon-coated Zn_2SnO_4 shows quasisphere. All of the quasi-octahedron Zn_2SnO_4 is uniformly coated by amorphous carbon layer and the sample is well dispersive as before after coating. The decoration of carbon on the surface of Zn_2SnO_4 is further investigated by TEM in Figures 2(c) and 2(d), from which carbon layer coated on the surface of quasi-octahedron samples is markedly observed. It is noteworthy that introducing the amorphous carbon layer does not affect the other features of Zn_2SnO_4 . From HRTEM image in Figure 2(d), it can be confirmed that the average thickness of carbon layer is about 35 nm and the carbon layer closely sticks to the Zn_2SnO_4 surface without vacant space between the carbon “shell” and Zn_2SnO_4 “core.” It is expected to provide good electric conductivity and help buffer the volume change of anode materials.

Recently, different morphology and structures of Zn_2SnO_4 electrodes have been demonstrated to improve the cycling capability, but the electrochemical performance of dispersive carbon-coated Zn_2SnO_4 nanomaterials at higher

current density was rarely investigated. To demonstrate the potential use of the carbon-coated Zn_2SnO_4 as an anode for LIBs, we carried out a comparison of the electrochemical performance of the bare Zn_2SnO_4 and carbon-coated Zn_2SnO_4 . Galvanostatic charge-discharge test was carried out at a current density of 200 mA/g between 0.05 and 3.00 V. The bare Zn_2SnO_4 and carbon-coated Zn_2SnO_4 electrodes show similar voltage profiles which agree well with that previously reported Zn_2SnO_4 materials. As reported, the electrochemical reaction mechanism of Li with Zn_2SnO_4 can be described in (1)–(3). The theoretical maximum capacity of Zn_2SnO_4 is about 547 mAh/g based on (2) and (3) according to the reaction mechanism proposed by Rong et al. [30]:



Figures 3(a) and 3(b) show the first, second, and twentieth charge-discharge curves of the two different samples. As can be seen, there is a wide steady discharging plateau around 0.5–1.0 V (versus Li^+/Li) for the lithium reaction with Zn_2SnO_4 and subsequent metallic Sn or Zn between 0.05–0.5 V. From the second cycle afterward, the potential plateaus shift upward to 1.0 V gradually and display more inclined shape. The initial charge and discharge capacity

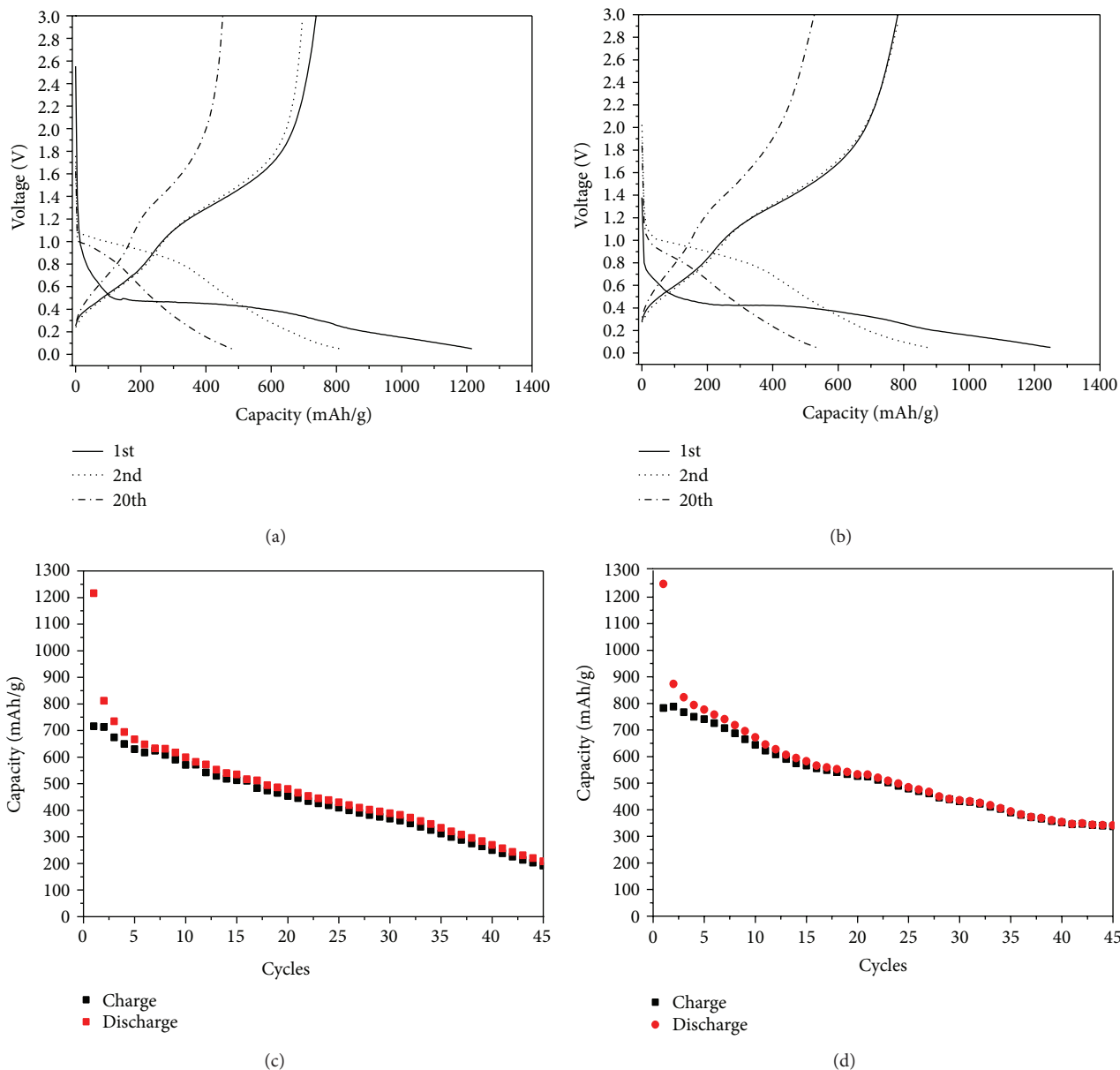


FIGURE 3: The discharge-charge profiles of (a) bare and (b) carbon-coated Zn₂SnO₄. The cycling performance of (c) bare and (d) carbon-coated Zn₂SnO₄ electrodes in a voltage range of 0.05–3.0 versus Li⁺/Li at current density of 200 mA/g.

is 1215.9 mAh/g and 812.1 mAh/g for bare Zn₂SnO₄ and 1248.8 mAh/g and 873.2 mAh/g for carbon-coated Zn₂SnO₄, respectively. The extra capacity resulted from the formation of solid electrolyte interphase film and possibly interfacial lithium storage during the first discharging process [32]. The initial Coulombic efficiency for the first cycle is 66.79% and 66.92%, which is higher than many corresponding reports. However, for both materials a large first irreversible capacity is observed, due to the decomposition of the electrolyte and the formation of the solid electrolyte interphase (SEI) [30].

The comparison of cycling stability between bare Zn₂SnO₄ and carbon-coated Zn₂SnO₄ is shown in Figures 3(c) and 3(d). It can be seen that the capacity retain rate of carbon-coated Zn₂SnO₄ is obviously better than that of

bare Zn₂SnO₄. The charge capacity of bare Zn₂SnO₄ and carbon-coated Zn₂SnO₄ retains 479.7 and 533.2 mAh/g after 20 cycles at 200 mA/g, which is higher than the theoretical capacity of graphite. However, the charge capacity of bare Zn₂SnO₄ drops rapidly after 30 cycles. For carbon-coated Zn₂SnO₄, the charge capacity fades slowly and a charge capacity of 341 mAh/g can still be retained after 45 cycles at 200 mA/g. The better electrochemical properties of carbon-coated Zn₂SnO₄ can be ascribed to the carbon shell. First, carbon has enough mechanical strength to buffer volume expansion [33]. Thus, the presence of carbon shell on the Zn₂SnO₄ surface would effectively alleviate the strains caused by the volume variation of Zn₂SnO₄ and prevent the disintegration. For carbon-coated Zn₂SnO₄, the

preservation of structure during the Li^+ insertion/extraction processes helps to keep physical contact between the anode materials and the current collector, leading to better cycling stability. Second, carbon itself is an electronic conductor [34], which ensures good electrical contact of Zn_2SnO_4 with the current collector and ensures the charge transfer/ Li^+ transport. Because of uniform and full coating of carbon, electrons can easily reach all the positions where Li^+ ion intercalation takes place [35]. Thirdly, carbon is a very stable electroactive anode material for LIBs. The solid electrolyte interphase (SEI) film on carbon surface was reported to be relatively stable compared with that on bare transition metal oxides [36]. The stable SEI film will also be useful for the maintenance of inner Zn_2SnO_4 structure. Therefore, all of these advantages contribute to the improved battery performance for carbon-coated Zn_2SnO_4 .

4. Conclusions

In summary, dispersive carbon-coated Zn_2SnO_4 was synthesized by a hydrothermal method using bare Zn_2SnO_4 as the precursor and glucose as the carbon source. The as-made electrodes of carbon-coated Zn_2SnO_4 have shown high reversible capacity, good cycle stability, and enhanced rate capability as anode material in LIBs. The carbon introducing can help prevent crack and pulverization, maintain the integrity of electrodes, and provide good electric conductivity, eventually leading to better electrochemical performance than bare Zn_2SnO_4 . The good electrochemical performance of carbon-coated Zn_2SnO_4 makes it a promising anode material for LIBs.

Conflict of Interests

The authors declare that there is no conflict of interests regarding the publication of this paper.

Acknowledgments

This work was supported by the Natural Science Foundation of Henan Province (nos. 122300410214 and 132102210048) and the Natural Science Foundation of China (no. 61306007). The authors would like to thank Professor X. T. Huang for his guide and help at the Central China Normal University.

References

- [1] Y. Idota, T. Kubota, A. Matsufuji, Y. Maekawa, and T. Miyasaka, "Tin-based amorphous oxide: a high-capacity lithium-ion-storage material," *Science*, vol. 276, no. 5317, pp. 1395–1397, 1997.
- [2] S. Machill, T. Shodai, Y. Sakurai, and J. Yamaki, "Electrochemical characterization of tin based composite oxides as negative electrodes for lithium batteries," *Journal of Power Sources*, vol. 73, no. 2, pp. 216–223, 1998.
- [3] N. Li and C. R. Martin, "A high-rate, high-capacity, nanostructured sn-based anode prepared using sol-gel template synthesis," *Journal of the Electrochemical Society*, vol. 148, no. 2, pp. A164–A170, 2001.
- [4] Q. Q. Xiong, Y. Lu, X. L. Wang, C. D. Gu, Y. Q. Qiao, and J. P. Tu, "Improved electrochemical performance of porous Fe_3O_4 /carbon core/shell nanorods as an anode for lithium-ion batteries," *Journal of Alloys and Compounds*, vol. 536, pp. 219–225, 2012.
- [5] M. Mohamedi, S. Lee, D. Takahashi, M. Nishizawa, T. Itoh, and I. Uchida, "Amorphous tin oxide films: preparation and characterization as an anode active material for lithium ion batteries," *Electrochimica Acta*, vol. 46, no. 8, pp. 1161–1168, 2001.
- [6] Y. P. Wu, E. Rahm, and R. Holze, "Carbon anode materials for lithium ion batteries," *Journal of Power Sources*, vol. 114, no. 2, pp. 228–236, 2003.
- [7] J.-. Tarascon and M. Armand, "Issues and challenges facing rechargeable lithium batteries," *Nature*, vol. 414, no. 6861, pp. 359–367, 2001.
- [8] M. Winter, J. O. Besenhard, M. E. Spahr, and P. Novák, "Insertion electrode materials for rechargeable lithium batteries," *Advanced Materials*, vol. 10, no. 10, pp. 725–763, 1998.
- [9] J. Y. Lee, R. Zhang, and Z. Liu, "Dispersion of Sn and SnO on carbon anodes," *Journal of Power Sources*, vol. 90, no. 1, pp. 70–75, 2000.
- [10] L. G. Xue, G. J. Xu, Y. Li et al., "Carbon-coated Si nanoparticles dispersed in carbon nanotube networks as anode material for lithium-ion batteries," *ACS Applied Materials & Interfaces*, vol. 5, no. 1, pp. 21–25, 2013.
- [11] H. X. Yang, J. F. Qian, Z. X. Chen, X. P. Ai, and Y. L. Cao, "Multi-layered nanocrystalline SnO_2 hollow microspheres synthesized by chemically induced self-assembly in the hydrothermal environment," *Journal of Physical Chemistry C*, vol. 111, no. 38, pp. 14067–14071, 2007.
- [12] X. W. Lou, C. M. Li, and L. A. Archer, "Designed synthesis of coaxial SnO_2 @carbon hollow nanospheres for highly reversible lithium storage," *Advanced Materials*, vol. 21, no. 24, pp. 2536–2539, 2009.
- [13] R. A. Huggins, "Lithium alloy negative electrodes," *Journal of Power Sources*, vol. 81–82, pp. 13–19, 1999.
- [14] I. A. Courtney and J. R. Dahn, "Key factors controlling the reversibility of the reaction of lithium with SnO_2 and Sn_2BPO_6 glass," *Journal of the Electrochemical Society*, vol. 144, no. 9, pp. 2943–2948, 1997.
- [15] L. Gao, F. Y. Qu, and X. Wu, "Hierarchical WO_3 @ SnO_2 coreshell nanowire arrays on carbon cloth: a new class of anode for high-performance lithium-ion batteries," *Journal of Materials Chemistry A*, vol. 2, pp. 7367–7372, 2014.
- [16] Y. Liu, Y. Jiao, Z. L. Zhang, F. Y. Qu, A. Umar, and X. Wu, "Hierarchical SnO_2 nanostructures made of intermingled ultrathin nanosheets for environmental remediation, smart gas sensor, and supercapacitor applications," *ACS Applied Materials & Interfaces*, vol. 6, pp. 2174–2184, 2014.
- [17] J. Zhu, Z. Lu, S. T. Aruna, D. Aurbach, and A. Gedanken, "Sonochemical synthesis of SnO_2 nanoparticles and their preliminary study as Li insertion electrodes," *Chemistry of Materials*, vol. 12, no. 9, pp. 2557–2566, 2000.
- [18] Y. Wang and J. Y. Lee, "Molten salt synthesis of tin oxide nanorods: morphological and electrochemical features," *Journal of Physical Chemistry B*, vol. 108, no. 46, pp. 17832–17837, 2004.
- [19] P. Wu, N. Du, H. Zhang, C. X. Zhai, and D. R. Yang, "Self-templating synthesis of SnO_2 -carbon hybrid hollow spheres for superior reversible lithium ion storage," *ACS Applied Materials & Interfaces*, vol. 3, no. 6, pp. 1946–1952, 2011.

- [20] S. Lee, H. S. Kim, and T. Seong, "Electrochemical properties of the carbon-coated lithium vanadium oxide anode for lithium ion batteries," *Journal of Alloys and Compounds*, vol. 509, no. 6, pp. 3136–3140, 2011.
- [21] S.-H. Ng, J. Wang, D. Wexler, K. Konstantinov, Z.-P. Guo, and H. Liu, "Highly reversible lithium storage in spheroidal carbon-coated silicon nanocomposites as anodes for lithium-ion batteries," *Angewandte Chemie*, vol. 45, no. 41, pp. 6896–6899, 2006.
- [22] S. Park, S. An, H. Ko, C. Jin, and C. Lee, "Enhanced NO₂ sensing properties of Zn₂SnO₄-core/ZnO-shell nanorod sensors," *Ceramics International*, vol. 39, no. 4, pp. 3539–3545, 2013.
- [23] Y. Jiang, X. Chen, R. Sun, Z. Xiong, and L. Zheng, "Hydrothermal syntheses and gas sensing properties of cubic and quasi-cubic Zn₂SnO₄," *Materials Chemistry and Physics*, vol. 129, no. 1-2, pp. 53–61, 2011.
- [24] Y. Lin, S. Lin, M. Luo, and J. Liu, "Enhanced visible light photocatalytic activity of Zn₂SnO₄ via sulfur anion-doping," *Materials Letters*, vol. 63, no. 13-14, pp. 1169–1171, 2009.
- [25] X. L. Fu, X. X. Wang, J. L. Long et al., "Hydrothermal synthesis, characterization, and photocatalytic properties of Zn₂SnO₄," *Journal of Solid State Chemistry*, vol. 182, no. 3, pp. 517–524, 2009.
- [26] L. Huang, L. Jiang, and M. Wei, "Metal-free indoline dye sensitized solar cells based on nanocrystalline Zn₂SnO₄," *Electrochemistry Communications*, vol. 12, no. 2, pp. 319–322, 2010.
- [27] Y. F. Li, X. Z. Zheng, H. X. Zhang, B. B. Guo, A. Y. Pang, and M. D. Wei, "Improving the efficiency of dye-sensitized Zn₂SnO₄ solar cells: the role of Al³⁺ ions," *Electrochimica Acta*, vol. 56, no. 25, pp. 9257–9261, 2011.
- [28] X. J. Zhu, L. M. Geng, F. Q. Zhang, Y. X. Liu, and L. B. Cheng, "Synthesis and performance of Zn₂SnO₄ as anode materials for lithium ion batteries by hydrothermal method," *Journal of Power Sources*, vol. 189, no. 1, pp. 828–831, 2009.
- [29] N. Feng, S. Peng, X. Sun et al., "Synthesis of monodisperse single crystal Zn₂SnO₄ cubes with high lithium storage capacity," *Materials Letters*, vol. 76, pp. 66–68, 2012.
- [30] A. Rong, X. P. Gao, G. R. Li et al., "Hydrothermal synthesis of Zn₂SnO₄ as anode materials for Li-Ion battery," *Journal of Physical Chemistry B*, vol. 110, no. 30, pp. 14754–14760, 2006.
- [31] X. Sun, J. Liu, and Y. Li, "Oxides@C core-shell nanostructures: One-pot synthesis, rational conversion, and Li storage property," *Chemistry of Materials*, vol. 18, no. 15, pp. 3486–3494, 2006.
- [32] A. Débart, L. Dupont, P. Poizot, J.-B. Leriche, and J. M. Tarascon, "A transmission electron microscopy study of the reactivity mechanism of tailor-made CuO particles toward lithium," *Journal of the Electrochemical Society*, vol. 148, no. 11, pp. A1266–A1274, 2001.
- [33] G. Cui, Y. Hu, L. Zhi et al., "A one-step approach towards carbon-encapsulated hollow tin nanoparticles and their application in lithium batteries," *Small*, vol. 3, no. 12, pp. 2066–2069, 2007.
- [34] N. Dimov, S. Kugino, and M. Yoshio, "Carbon-coated silicon as anode material for lithium ion batteries: advantages and limitations," *Electrochimica Acta*, vol. 48, no. 11, pp. 1579–1587, 2003.
- [35] S.-H. Ng, J. Wang, D. Wexler, K. Konstantinov, Z.-P. Guo, and H.-K. Liu, "Highly reversible lithium storage in spheroidal carbon-coated silicon nanocomposites as anodes for lithium-ion batteries," *Angewandte Chemie*, vol. 45, no. 41, pp. 6896–6899, 2006.
- [36] W. M. Zhang, X. L. Wu, J. S. Hu, Y. G. Guo, and L. J. Wan, "Carbon coated Fe₃O₄ nanospindles as a superior anode material for lithium-ion batteries," *Advanced Functional Materials*, vol. 18, no. 24, pp. 3941–3946, 2008.

Research Article

Optical and Magnetic Properties of Fe Doped ZnO Nanoparticles Obtained by Hydrothermal Synthesis

Xiaojuan Wu,^{1,2} Zhiqiang Wei,^{1,2} Lingling Zhang,² Xuan Wang,²
Hua Yang,^{1,2} and Jinlong Jiang²

¹ State Key Laboratory of Advanced Processing and Recycling Nonferrous Metals, Lanzhou University of Technology, Lanzhou 730050, China

² School of Science, Lanzhou University of Technology, Lanzhou 730050, China

Correspondence should be addressed to Zhiqiang Wei; zqwei7411@163.com

Received 25 May 2014; Revised 13 June 2014; Accepted 16 June 2014; Published 3 July 2014

Academic Editor: Chee Kiang Ivan Tan

Copyright © 2014 Xiaojuan Wu et al. This is an open access article distributed under the Creative Commons Attribution License, which permits unrestricted use, distribution, and reproduction in any medium, provided the original work is properly cited.

Diluted magnetic semiconductors $\text{Zn}_{1-x}\text{Fe}_x\text{O}$ nanoparticles with different doping concentration ($x = 0, 0.01, 0.05, 0.10, \text{ and } 0.20$) were successfully synthesized by hydrothermal method. The crystal structure, morphology, and optical and magnetic properties of the samples were characterized by X-ray diffraction (XRD), energy dispersive spectrometer (EDS), high-resolution transmission electron microscopy (HRTEM), Raman scattering spectra (Raman), photoluminescence spectra (PL), and the vibrating sample magnetometer (VSM). The experiment results show that all samples synthesized by this method possess hexagonal wurtzite crystal structure with good crystallization, no other impurity phases are observed, and the morphology of the sample shows the presence of ellipsoidal nanoparticles. All the Fe^{3+} successfully substituted for the lattice site of Zn^{2+} and generates single-phase $\text{Zn}_{1-x}\text{Fe}_x\text{O}$. Raman spectra shows that the peak shifts to higher frequency. PL spectra exhibit a slight blue shift and the UV emission is annihilated with the increase of Fe^{3+} concentration. Magnetic measurements indicated that Fe-doped ZnO samples exhibit ferromagnetic behavior at room temperature and the saturation magnetization is enhanced with the increase of iron doping content.

1. Introduction

Diluted magnetic semiconductors (DMSs) are referred to as nonmagnetic semiconductors in which a small fraction of host cations are replaced by transition metal or rare-earth ions, with both spin and charge degrees of freedom in a single material [1, 2]. In recent years, DMSs have been under intense research due to their potential applications in spin-based multifunctional electronic devices, such as ultraviolet absorbers, optoelectronics, spin field-effect transistors, field-emission devices, gas sensors, nonvolatile memory devices, and quantum computer [3–8]. Of all the oxide diluted magnetic semiconductors, the transition metal (TM) doped ZnO has been identified as a promising one, because the host material ZnO is a chemically and thermally stable n -type II–VI compound semiconductor with a wide band gap energy (3.37 eV) and a large exciton binding energy (60 meV) [9–11]. During the past years, transition metal doped ZnO has been

doped into the ZnO lattice to modulate the local electronic structure and cause dramatic changes in their optical and electromagnetic properties [12–15]. Various methods have been used to synthesize TM doped ZnO nanoparticles: some experimental results observed the room temperature ferromagnetism in ZnO:Fe system, but the experimental results were contradictory, and the theoretical explanation about the origin of the magnetism is still not mature [16–20]. However, there are very few reports on the magnetic behavior of transition metal doped ZnO synthesized using hydrothermal method. Thus, in this paper, our aim is to synthesize $\text{Zn}_{1-x}\text{Fe}_x\text{O}$ nanoparticles with different concentration using hydrothermal method and to study their structural, optical, and magnetic properties.

In this paper, diluted magnetic semiconductors $\text{Zn}_{1-x}\text{Fe}_x\text{O}$ nanoparticles with different doping consistency ($x = 0, 0.01, 0.05, 0.10, \text{ and } 0.20$) were synthesized by hydrothermal method. And the crystal structure,

morphology, and optical and magnetic properties of the samples were characterized by X-ray diffraction (XRD), energy dispersive spectrometer (EDS), high-resolution transmission electron microscopy (HRTEM), Raman scattering spectra (Raman), photoluminescence spectra (PL), and the vibrating sample magnetometer (VSM).

2. Experimental

$\text{Zn}_{1-x}\text{Fe}_x\text{O}$ ($x = 0, 0.01, 0.05, 0.10,$ and 0.20) nanoparticles were prepared by hydrothermal method. All materials were of analytical grade and used without further purification in this study. In a typical experiment, zinc acetate ($\text{Zn}(\text{CH}_3\text{COO})_2 \cdot 2\text{H}_2\text{O}$, 99.0%, AR) and ferric nitrate ($\text{Fe}(\text{NO}_3)_3 \cdot 9\text{H}_2\text{O}$, $\geq 99.0\%$, AR) were mixed together according to the required amounts of the corresponding chemical reagents and dissolved into absolute alcohol under magnetic stirring at room temperature. Then cetyltrimethylammonium bromide (CTAB, $\geq 99.0\%$, AR) was added to the above solution; meanwhile, sodium hydroxide (NaOH , $\geq 96.0\%$, AR) was dissolved into absolute ethanol and introduced into the above solution. After being stirred for 30 min, the mixture was transferred into a 45 mL Teflon lined stainless steel autoclave. The hydrothermal synthesis was heated to 180°C and maintained for 24 h in an oven and then cooled down to the room temperature naturally. The obtained products were washed with distilled water and absolute ethanol several times and dried at 60°C for 24 h. Finally, the samples were obtained.

The crystalline structures of the samples were examined by a rotating-target X-ray diffractometer (Japan Rigaku D/Max-2400) equipped with graphite monochromatized $\text{CuK}\alpha$ radiation ($\lambda = 1.54056 \text{ \AA}$, 40 kV, 100 mA). The samples were scanned in the angular range from 10 to 90° (2θ) with scanning rate $0.005^\circ/\text{s}$ and step size 0.02° . The morphology and microstructure of the samples were observed through transmission electron microscopy (TEM, Japan JEOL JEM 1200EX), the corresponding selected-area electron diffraction (SAED), and high-resolution transmission electron microscopy (HRTEM, JEM-2010). The chemical composition of the products was verified by energy dispersive spectroscopy (EDS) at an acceleration voltage of 200 keV in TEM. Raman spectral measurements at room temperature in the energy region between 100 and 1500 cm^{-1} were carried out using a micro-Raman spectrometer (HR800) with 525 nm line of He-Ne ion laser as exciting light source. Photoluminescence (PL) spectra were performed at 266 nm wavelength using a PerkinElmer spectrophotometer with a He-Cd laser as excitation source. Magnetic hysteresis loops were investigated at room temperature using a vibrating sample magnetometer (VSM, Lakeshore 7304) with an applied field from -12000 Oe to 12000 Oe.

3. Results and Discussion

The phase purity and crystal structure of the $\text{Zn}_{1-x}\text{Fe}_x\text{O}$ samples were examined by XRD. Figure 1 shows the typical XRD patterns of $\text{Zn}_{1-x}\text{Fe}_x\text{O}$ ($x = 0, 0.01, 0.05, 0.10,$ and

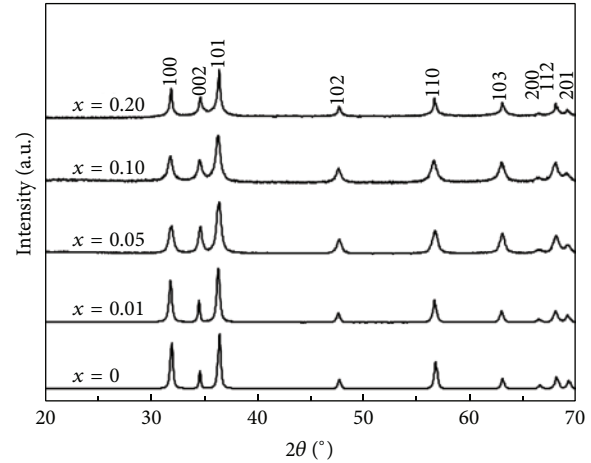


FIGURE 1: XRD patterns of $\text{Zn}_{1-x}\text{Fe}_x\text{O}$ nanoparticles.

0.20) nanoparticles. It is clearly observed from the pattern that all the diffraction peaks can be well corresponding to the diffractions of (100), (002), (101), (102), (110), (103), (200), (112), (201), and (202) planes of single-phase hexagonal wurtzite structure with the space group 6_3mc , respectively. All the diffraction peaks are in good agreement with the values of the standard spectrum (JCPDS 01-079-2205). In addition, there are no traces of impurity or secondary phases within the detection limit of XRD and there are no obvious diffraction patterns of Fe species such as Fe, Fe_2O_3 , and Fe_3O_4 in the samples where the doping atomic percentage is from 1% to 20%. These results indicate that all Fe ions were incorporated in the lattice of the host crystals, the products consist of pure phase, and no characteristic peaks can be found from other impurities.

For Fe-doped ZnO dilute magnetic semiconductors, the peak position of the doped ZnO samples shifts to lower angles compared with pure ZnO, and also there is a decrease in the intensity of peaks with the Fe doping concentration. This shifting as well as decrease in intensity of the characteristic peak clearly indicates the successful incorporation of Fe in the ZnO matrix, which can be attributed to the difference of ion radius of Zn^{2+} (0.74 \AA) comparing with that of Fe^{3+} (0.64 \AA). It is indicated that Fe ions occupy the Zn ions sites in the hexagonal wurtzite structure and no impurity phase appears.

The morphology and microstructure of the samples were observed through HRTEM. The images of all samples reveal the presence of randomly distributed ellipsoidal shape nanoparticles. Figure 2(a) shows the HRTEM image of the $\text{Zn}_{0.95}\text{Fe}_{0.05}\text{O}$; it can be seen that the sample consists of ellipsoidal shape particles, and well dispersed with smooth surface and uniform size, the diameter of the nanoparticles ranges from 10 to 40 nm, with an average diameter approximately 25 nm. The crystalline quality improves since CTAB promotes the establishment of a net surface charge onto the nanocrystals preventing their aggregation. Figure 2(b) shows a typical HRTEM image of $\text{Zn}_{0.95}\text{Fe}_{0.05}\text{O}$ nanoparticles. The resolved lattice plane extending through the image confirms that the particle is crystallized. Figure 2(b) displays the clear lattice fringes; the interplanar distance is about 0.263 nm,

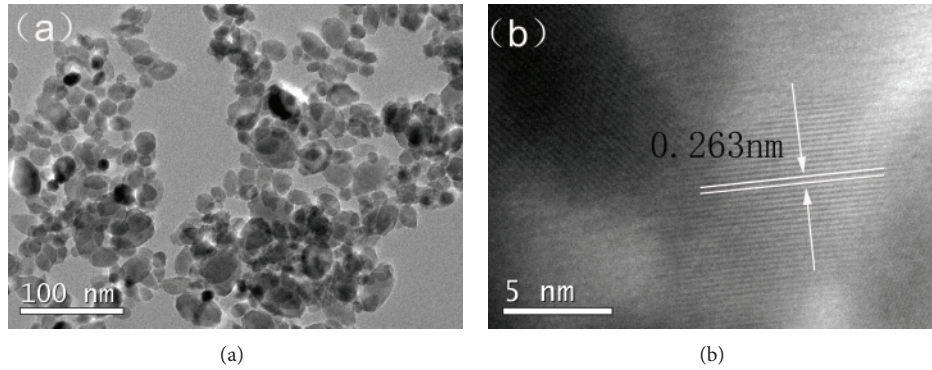


FIGURE 2: HRTEM images of the $\text{Zn}_{0.95}\text{Fe}_{0.05}\text{O}$ nanoparticles.

which is in good agreement with the d -spacing of (002) planes of hexagonal wurtzite ZnO structure. The value of lattice spacing is greater than that of pure ZnO (0.26 nm). The HRTEM analysis is consistent with the XRD results, which further indicates that all the Fe ions successfully substituted for the lattice site of Zn^{2+} in the hexagonal wurtzite structure and no impurity phase appeared.

In order to determine the elements of the prepared samples, EDS analysis was performed. Figure 3 shows the EDS patterns of $\text{Zn}_{0.95}\text{Fe}_{0.05}\text{O}$ sample. The EDS spectrum indicates that the as-prepared nanoparticles mainly contain Fe, Zn, and O three elements. The characteristic peaks of O appeared at 0.5 keV and the characteristic peaks of Zn appeared at 1 and 8.7 keV. The characteristic peaks of Cu appeared at 0.9, 8 and 8.9 keV. The Fe signal at 0.7, 6.4, and 7.1 keV was observed in the Fe-doped ZnO nanoparticles. Apart from that, the Cu and C peaks in the EDS originate from the TEM micromesh grid. The EDS results further verify XRD conclusion; this indicates that Fe-doped ZnO diluted magnetic semiconductor was successfully synthesized by hydrothermal method and Fe^{3+} in the sample occupied the place of Zn^{2+} .

Raman spectra are a versatile technique for detecting the incorporation of dopants and the resulted defects and lattice disorder in the host lattice. In order to further confirm the phase transition and the defect chemistry variation after Fe-doped ZnO, Raman spectra of the as-prepared products were measured with an excitation wavelength of 532 nm at room temperature. Wurtzite structure ZnO as a n -type II-VI semiconductor with the space group 6_3mc , has zone center optical phonon modes: $\Gamma_{\text{opt}} = A_1 + 2B_1 + E_1 + 2E_2$ [21], where A_1 , E_1 , and E_2 are Raman active and B_1 is Raman forbidden. A_1 and E_1 modes are polar and split into the transverse optical (TO) and longitudinal optical (LO) phonons, and E_2 mode consists of two modes: E_2 high which is associated with the vibration of oxygen atoms and E_2 low attributed to the Zn sublattices.

Room temperature Raman spectrum of all the synthesized samples is presented in Figure 4. The spectra reveal that all the major peaks which are the characteristics of vibrational modes in ZnO exist in all samples. For all the samples, Raman

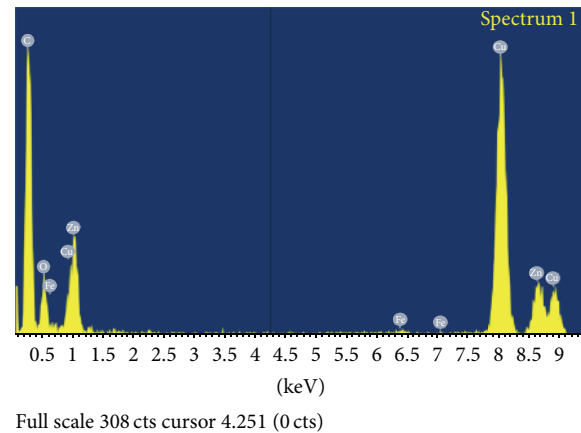


FIGURE 3: EDS patterns of the $\text{Zn}_{0.95}\text{Fe}_{0.05}\text{O}$ nanoparticles.

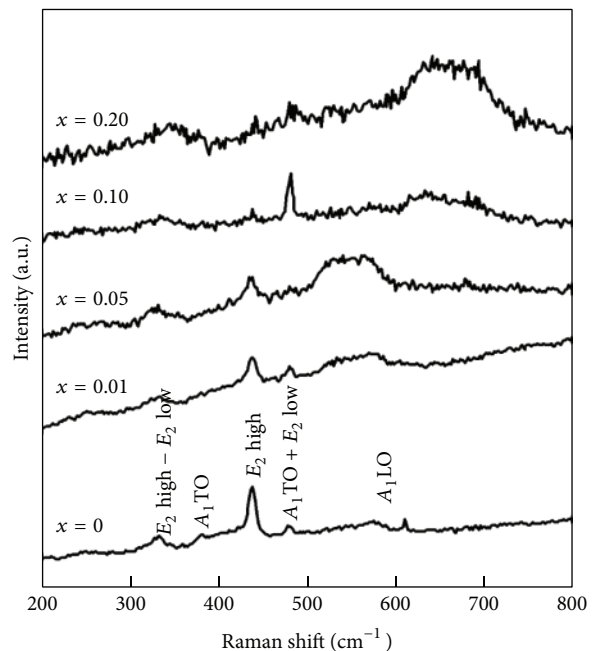


FIGURE 4: Raman patterns of the $\text{Zn}_{1-x}\text{Fe}_x\text{O}$ nanoparticles.

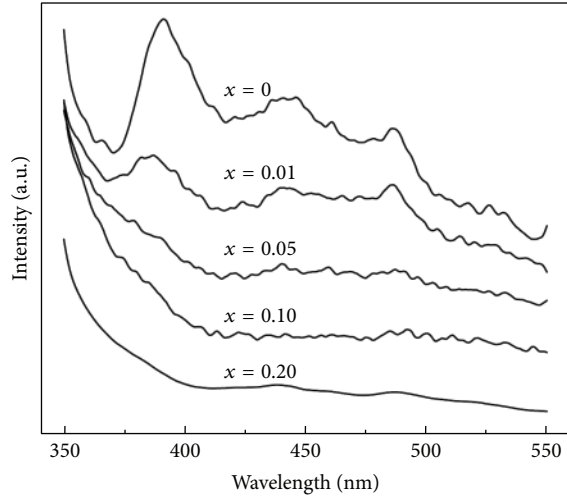


FIGURE 5: Photoluminescence spectra of the $\text{Zn}_{1-x}\text{Fe}_x\text{O}$ nanoparticles.

peak at 332 cm^{-1} is attributed to the second order Raman mode arising from zone boundary phonons E_2 high- E_2 low, the peak at 381 cm^{-1} is assigned to the fundamental optical mode $A_1\text{TO}$, and the peak at 444 cm^{-1} is the E_2 high mode, whereas peak at about 478 cm^{-1} is thought as originated from two phonon process, which correspond to $A_1\text{TO} + E_2$ low mode. Moreover, for the $\text{Zn}_{0.99}\text{Fe}_{0.01}\text{O}$ and $\text{Zn}_{0.95}\text{Fe}_{0.05}\text{O}$ samples, a broad hump at 574 cm^{-1} is $A_1\text{LO}$ symmetry modes [11, 22, 23]. And for the $\text{Zn}_{0.90}\text{Fe}_{0.10}\text{O}$ and $\text{Zn}_{0.80}\text{Fe}_{0.20}\text{O}$ samples, a broad peak centered at 640 cm^{-1} is related to intrinsic host-lattice defects after doping and it is also a powerful evidence to prove Fe^{3+} occupation at Zn^{2+} sites in the ZnO lattice [24, 25]. Besides, with increasing the content of Fe^{3+} doping in the samples, there is shift in all peaks towards higher frequency region, broaden asymmetrically and weakened peak intensity. This shift can be due to strain, phonon confinement by boundaries, and the force constant changes caused by the less defects or impurities.

In these modes, the E_2 high peak in all the samples is attributed to the standard mode in wurtzite structure, which indicates that Fe-doped ZnO nanoparticles keep a good hexagonal ZnO structure. Moreover, E_2 high mode is very sensitive to the stress in the crystal [24]. From Figure 4, the peaks at 444 cm^{-1} of E_2 high mode are lowered in the intensity with the more Fe content, which due to the radius of Fe^{3+} (0.063 nm) smaller than radius of Zn^{2+} (0.074 nm), and after being doped with Fe^{3+} , it can cause the lattice expansion, defects, and the stress increase [26].

Figure 5 depicts PL spectra of Fe-doped ZnO nanoparticles at room temperature. For comparison, PL spectrum of undoped ZnO sample is also given. The pure ZnO sample contains six main emission peaks, including three obvious broad bands centered at 390, 440, and 490 nm and three comparatively weak emission peaks at 420, 460, and 525 nm, respectively. The 1% sample exhibits similar emission to pure ZnO. This illustrates that the $\text{Zn}_{0.99}\text{Fe}_{0.01}\text{O}$ sample displays nearly the same structure of pure ZnO. But the emission peak position of doped sample exhibits a slight blue shift with the

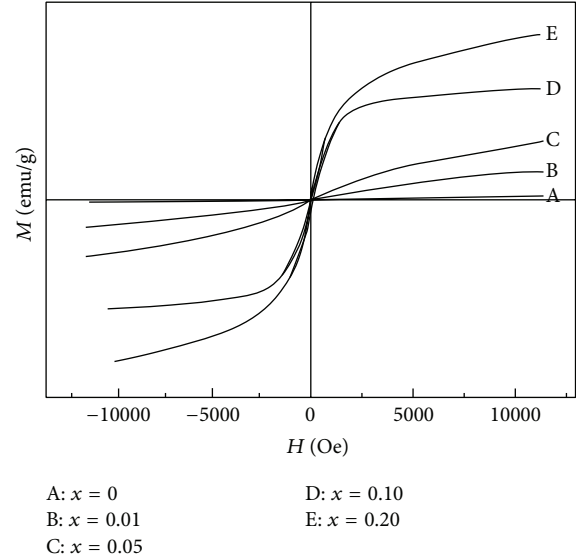


FIGURE 6: The magnetic hysteresis loops of the $\text{Zn}_{1-x}\text{Fe}_x\text{O}$ nanoparticles.

increase of Fe^{3+} concentration, and this is attributed to defects or the oxygen vacancies in ZnO induced by Fe^{3+} doping. In addition, the visible light (VL) emission band is also suppressed with the increase of the Fe^{3+} concentration. The strong ultraviolet (UV) emission band at 390 nm (3.18 eV) and the weak violet emission peak located at 420 nm (2.95 eV) originate from excitonic recombination corresponding to the near-band-edge emission (NBE) of wide band gap of ZnO, because of the quantum confinement effect [27]. The strong blue emission bands centered at 440 nm (2.8 eV) and the weak blue emission peak at 460 nm (2.69 eV) are attributed to the transitions between the shallow donor levels of the interstitial Zn to the top of the valence band [14] or the transitions between shallow acceptor levels of oxygen vacancies and shallow donor levels of zinc vacancy [28]. The blue-green bands centered at 490 nm (2.55 eV) for samples are ascribed to the transition between the deep donor level of oxygen vacancy, which is close to the bottom of the conduction band of about 0.8~0.9 eV, to the valence band [28, 29]. The weak green emission peak at 525 nm (2.36 eV) is possibly assigned to positively charged electron transition and surface traps mediated by defects in the band gap [30]. PL spectrum analysis further illustrates that Fe ions are probably incorporated into the ZnO host matrix in the doped ZnO sample.

The related PL intensity of doped sample decreases rapidly with the increase of Fe doping concentration compared with undoped ZnO, and the emission peak position intensity of 20% Fe-doped ZnO sample was annihilated; this is because the photogenerated electrons preferentially occupy the Fe ion induced trap centers, resulting in the quenching of luminescence [14].

Figure 6 shows the magnetic hysteresis (M-H) loops of the $\text{Zn}_{1-x}\text{Fe}_x\text{O}$ nanoparticles with different doping consistency ($x = 0, 0.01, 0.05, 0.10,$ and 0.20) measured at room temperature. The magnetic hysteresis loops of ZnO

and lower doped ZnO ($x = 0.01$ and 0.05) samples pass origin of coordinates, and the remanent magnetization (M_r), and coercivity (H_c) are zero. It suggests that these samples show paramagnetic behaviors at room temperature. While the higher doped ZnO ($x = 0.10$ and 0.20) samples exhibit obvious ferromagnetic behaviors. The saturation magnetization values are 0.74 emu/g and 1.74 emu/g and the coercive force values are 90 Oe and 78 Oe, respectively, for ZnO ($x = 0.10$ and 0.20). It is evident from Figure 6 that a transition from the paramagnetic state to the ferromagnetism state occurs. The saturation magnetization of $Zn_{1-x}Fe_xO$ nanoparticles increases with the increasing of Fe doping concentration compared with pure ZnO.

The room temperature ferromagnetism of the $Zn_{1-x}Fe_xO$ nanoparticles could arise from two possible sources. One is extrinsic magnetism and the other is intrinsic magnetism. Extrinsic source includes the formation of clusters of transition elements or secondary phase. Exchange interactions come under intrinsic source of magnetism. But the XRD results of the $Zn_{1-x}Fe_xO$ nanoparticles suggest no traces of impurity or secondary phases (these parasitic phases include the Fe clusters and any other phases like Fe_2O_3 , Fe_3O_4 , etc.). Thus, the possibility of ferromagnetism due to the clusters of transition elements or secondary phases in the samples could be ruled out. Hence, the obtained ferromagnetism is an intrinsic magnetic property of the $Zn_{1-x}Fe_xO$ nanoparticles. It is evident from the XRD analysis that Fe is incorporated into the ZnO lattice. In view of the Fe^{3+} ions substituted into ZnO lattice, the origin of magnetism in the samples is due to the exchange interaction between local spin-polarized electrons (such as the electrons of Fe^{3+} ions) and the conductive electrons. Such interaction can lead to the spin polarization of conductive electrons. Consequently, the spin-polarized conductive electrons undergo an exchange interaction with local spin-polarized electrons of Fe^{3+} ions. Thus, after a successive long-range exchange interaction, almost all Fe^{3+} ions exhibit the same spin direction, resulting in the ferromagnetism of the material [31].

4. Conclusions

- (1) Diluted magnetic semiconductors $Zn_{1-x}Fe_xO$ nanoparticles with different concentration ($x = 0, 0.01, 0.05, 0.10,$ and 0.20) have been synthesized by hydrothermal method. The samples possess hexagonal wurtzite crystal structure with good crystallization, no other impurity phase appeared, and the morphology of samples is ellipsoidal shape nanoparticles with good dispersion.
- (2) All the Fe^{3+} successfully substituted for the lattice site of Zn^{2+} and generates single-phase $Zn_{1-x}Fe_xO$. The Raman spectra of the $Zn_{1-x}Fe_xO$ nanoparticles occurs red shift, and the UV emission of photoluminescence spectra is annihilated with the increase of Fe^{3+} concentration. The ferromagnetic behaviors are found for all doped samples at room temperature.

Conflict of Interests

The authors declare that there is no conflict of interests regarding the publication of this paper.

Acknowledgments

This work was supported by the National Natural Science Foundation of China (no. 51261015) and the Natural Science Foundation of Gansu Province, China (no. 1308RJZA238).

References

- [1] H. Ohno, "Making nonmagnetic semiconductors ferromagnetic," *Science*, vol. 281, no. 5379, pp. 951–956, 1998.
- [2] S. J. Pearton, D. P. Norton, M. P. Ivill et al., "ZnO doped with transition metal ions," *IEEE Transactions on Electron Devices*, vol. 54, no. 5, pp. 1040–1048, 2007.
- [3] A. Moezzi, A. M. McDonagh, and M. B. Cortie, "Zinc oxide particles: synthesis, properties and applications," *Chemical Engineering Journal*, vol. 185–186, pp. 1–22, 2012.
- [4] D. Chu, Y. Masuda, T. Ohji, and K. Kato, "Formation and photocatalytic application of ZnO nanotubes using aqueous solution," *Langmuir*, vol. 26, no. 4, pp. 2811–2815, 2010.
- [5] J. Zhang, S. Wang, M. Xu et al., "Hierarchically porous ZnO architectures for gas sensor application," *Crystal Growth and Design*, vol. 9, no. 8, pp. 3532–3537, 2009.
- [6] X. J. Liu, X. Y. Zhu, C. Song, F. Zeng, and F. Pan, "Intrinsic and extrinsic origins of room temperature ferromagnetism in Ni-doped ZnO films," *Journal of Physics D: Applied Physics*, vol. 42, no. 3, Article ID 035004, 2009.
- [7] J. R. Neal, A. J. Behan, R. M. Ibrahim et al., "Room-temperature magneto-optics of ferromagnetic transition-metal-doped ZnO thin films," *Physical Review Letters*, vol. 96, no. 19, Article ID 197208, pp. 1–4, 2006.
- [8] X. H. Huang, G. H. Li, B. Q. Cao, M. Wang, and C. Hao, "Morphology evolution and CL property of Ni-doped zinc oxide nanostructures with room-temperature ferromagnetism," *Journal of Physical Chemistry C*, vol. 113, no. 11, pp. 4381–4385, 2009.
- [9] S. J. Pearton, D. P. Norton, K. Ip, Y. W. Heo, and T. Steiner, "Recent progress in processing and properties of ZnO," *Progress in Materials Science*, vol. 50, no. 3, pp. 293–340, 2005.
- [10] A. B. Djurišić, X. Chen, Y. H. Leung, and A. Man Ching Ng, "ZnO nanostructures: growth, properties and applications," *Journal of Materials Chemistry*, vol. 22, no. 14, pp. 6526–6535, 2012.
- [11] F. Decremps, J. Pellicer-Porres, A. M. Saitta, J. Chervin, and A. Polian, "High-pressure Raman spectroscopy study of wurtzite ZnO," *Physical Review B: Condensed Matter and Materials Physics*, vol. 65, no. 9, pp. 092101–092105, 2002.
- [12] A. Alsaad, "Structural, electronic and magnetic properties of Fe, Co, Mn-doped GaN and ZnO diluted magnetic semiconductors," *Physica B: Condensed Matter*, vol. 440, pp. 1–9, 2014.
- [13] C. Yilmaz and U. Unal, "Electrochemical deposition of Mn:ZnO films under hydrothermal conditions," *Journal of the Electrochemical Society*, vol. 160, no. 4, pp. D163–D167, 2013.
- [14] M. V. Limaye, S. B. Singh, R. Das, P. Poddar, and S. K. Kulkarni, "Room temperature ferromagnetism in undoped and Fe doped ZnO nanorods: microwave-assisted synthesis," *Journal of Solid State Chemistry*, vol. 184, no. 2, pp. 391–400, 2011.

- [15] G. Lawes, A. S. Risbud, A. P. Ramirez, and R. Seshadri, "Absence of ferromagnetism in Co and Mn substituted polycrystalline ZnO," *Physical Review B: Condensed Matter and Materials Physics*, vol. 71, no. 4, Article ID 045201, 2005.
- [16] Y. T. Prabhu, V. Kumar, and K. V. Rao, "Effect of Fe doping on structural, optical and magnetic properties of ZnO nanoparticles derived by surfactant assisted combustion synthesis," *Advanced Science, Engineering and Medicine*, vol. 5, no. 3, pp. 198–205, 2013.
- [17] F. Ahmed, S. Kumar, N. Arshi, M. S. Anwar, and B. Heun Koo, "Morphological evolution between nanorods to nanosheets and room temperature ferromagnetism of Fe-doped ZnO nanostructures," *CrystEngComm*, vol. 14, no. 11, pp. 4016–4026, 2012.
- [18] V. K. Sharma and G. D. Varma, "Fe clusters as origin of ferromagnetism in hydrogenated $Zn_{1-x}Fe_xO$ ($x=0.02$ & 0.05) samples," *Advanced Materials Letters*, vol. 3, no. 2, pp. 126–129, 2012.
- [19] J. J. Beltrán, J. A. Osoriol, C. A. Barrero1, C. B. Hanna, and A. Punnoose, "Magnetic properties of Fe doped, Co doped, and Fe+Co co-doped ZnO," *Journal of Applied Physics*, vol. 113, no. 17, Article ID 17C308, 2013.
- [20] A. Baranowska-Korczyk, A. Reszka, K. Sobczak et al., "Magnetic Fe doped ZnO nanofibers obtained by electrospinning," *Journal of Sol-Gel Science and Technology*, vol. 61, no. 3, pp. 494–500, 2012.
- [21] T. C. Damen, S. P. S. Porto, and B. Tell, "Raman effect in zinc oxide," *Physical Review*, vol. 142, no. 2, pp. 570–574, 1966.
- [22] A. Singhal, S. N. Achary, J. Manjanna, S. Chatterjee, P. Ayyub, and A. K. Tyagi, "Chemical synthesis and structural and magnetic properties of dispersible cobalt- and nickel-doped ZnO nanocrystals," *The Journal of Physical Chemistry C*, vol. 114, no. 8, pp. 3422–3430, 2010.
- [23] B. N. Mavrin, L. N. Demyanets, and R. M. Zakalukin, "Raman spectroscopy and Fermi resonance in Mn-doped ZnO bulk single crystal," *Physics Letters A: General, Atomic and Solid State Physics*, vol. 374, no. 39, pp. 4054–4056, 2010.
- [24] B. Zhang, S. Zhou, H. Wang, and Z. Du, "Raman scattering and photoluminescence of Fe-doped ZnO nanocantilever arrays," *Chinese Science Bulletin*, vol. 53, no. 11, pp. 1639–1643, 2008.
- [25] C. Bundesmann, N. Ashkenov, M. Schubert et al., "Raman scattering in ZnO thin films doped with Fe, Sb, Al, Ga, and Li," *Applied Physics Letters*, vol. 83, no. 10, pp. 1974–1976, 2003.
- [26] D. Shuang, X. X. Zhu, J. B. Wang, X. L. Zhong, G. J. Huang, and C. He, "The influence of Mn content on luminescence properties in Mn-doped ZnO films deposited by ultrasonic spray assisted chemical vapor deposition," *Applied Surface Science*, vol. 257, no. 14, pp. 6085–6088, 2011.
- [27] K. Vanheusden, W. L. Warren, C. H. Seager, D. R. Tallant, J. A. Voigt, and B. E. Gnade, "Mechanisms behind green photoluminescence in ZnO phosphor powders," *Journal of Applied Physics*, vol. 79, no. 10, pp. 7983–7990, 1996.
- [28] G. Song, X. Fang, and H. Liang, "Effect of O_2/Ar ratio on blue photoluminescence spectrum of nanocrystalline ZnO films," *Spectroscopy and Spectral Analysis*, vol. 30, no. 3, pp. 591–594, 2010.
- [29] H. Chen, J. Ding, and S. Ma, "Violet and blue-green luminescence from Ti-doped ZnO films deposited by RF reactive magnetron sputtering," *Superlattices and Microstructures*, vol. 49, no. 2, pp. 176–182, 2011.
- [30] J. Wang and L. Gao, "Hydrothermal synthesis and photoluminescence properties of ZnO nanowires," *Solid State Communications*, vol. 132, no. 3-4, pp. 269–271, 2004.
- [31] R. Elilarassi and G. Chandrasekaran, "Synthesis and characterization of ball milled Fe-doped ZnO diluted magnetic semiconductor," *Optoelectronics Letters*, vol. 8, no. 2, pp. 109–112, 2012.

Research Article

Direct Growth of Copper Oxide Films on Ti Substrate for Nonenzymatic Glucose Sensors

Xiaoxu Ji, Aihua Wang, and Qinghui Zhao

School of Physics and Electronic Engineering, Nanyang Normal University, Nanyang 473061, China

Correspondence should be addressed to Xiaoxu Ji; xxji@nynu.edu.cn

Received 8 June 2014; Accepted 9 June 2014; Published 25 June 2014

Academic Editor: Xiang Wu

Copyright © 2014 Xiaoxu Ji et al. This is an open access article distributed under the Creative Commons Attribution License, which permits unrestricted use, distribution, and reproduction in any medium, provided the original work is properly cited.

Copper oxide (CuO) films directly grown on Ti substrate have been successfully prepared via a hydrothermal method and used to construct an amperometric nonenzymatic glucose sensor. XRD and SEM were used to characterize the samples. The electrochemical performances of the electrode for detection of glucose were investigated by cyclic voltammetry and chronoamperometry. The CuO films based glucose sensors exhibit enhanced electrocatalytic properties which show very high sensitivity ($726.9 \mu\text{A mM}^{-1} \text{cm}^{-2}$), low detection limit ($2 \mu\text{M}$), and fast response (2 s). In addition, reproducibility and long-term stability have been observed. Low cost, convenience, and biocompatibility make the CuO films directly grown on Ti substrate electrodes a promising platform for amperometric nonenzymatic glucose sensor.

1. Introduction

Reliable and fast determination of glucose is important in areas such as clinical diagnostics [1], biotechnology [2], and environmental and food chemistry [3], so the development of electrochemical glucose sensors has received continuous interest. Glucose oxidase (GO_x) has been widely used to construct various amperometric biosensors for glucose detection due to its high sensitivity and selectivity to glucose [4]. However, GO_x -based biosensors suffer from problems because of the disadvantages of the enzyme-modified electrodes, such as instability, high cost, complicated immobilization process, the requirement of low temperature storage, and their PH and toxic environment [5–8]. To resolve this problem, many attempts have been made to develop nonenzymatic glucose sensors in recent years. For example, the direct electrocatalytic oxidation of glucose on electrodes modified with metal nanoparticles has been explored in the development of nonenzymatic glucose sensors because it shows good performances through increasing the surface area and enhancing the mass transport and catalysis [9–14]. However, metallic nanoparticles based electrodes usually suffer from the stable problems [15] or high cost [16], which hinders their practical applications. Hence, it is important

to develop a fast, sensitive, highly selective, stable, and inexpensive nonenzymatic glucose sensor. In contrast, metal oxides based glucose sensors have been widely investigated for nonenzymatic detecting due to their good stability and low cost.

CuO, as a *p*-type semiconductor with a narrow band gap of 1.2 eV, has been widely studied because of its numerous applications in catalysis, gas sensors, lithium-ion battery, and field transistors [17–20]. Meanwhile, nanostructured CuO is a very economic functional material which is promising in the development of nonenzymatic glucose sensors because of its highly specific surface area, good electrochemical activity, and the possibility of promoting electron transfer reactions at a lower overpotential [21]. It is well known that the microstructures (crystal size, aspect ratio, density, etc.) and morphologies of metal oxide nanoparticles play a determining role for the activity, selectivity, and stability in a catalytic process. Thus, a variety of CuO nanomaterials with different morphologies including nanowires [22], nanospheres [23], nanosheets [24], and flower-like nanostructures [25] have been synthesized in order to achieve enhanced performance for the monitoring and detection of glucose. In comparison to nanostructures, structured CuO films could avoid the drawbacks of complex fabrication processed, harsh modification

conditions for electrodes, expensive glassy carbon electrode, and possible decline of electron transfer rate between isolated nanostructures and electrodes. Recently, CuO nanostructures (nanosheets [26], nanobelts [27], and nanowalls [28]) on Cu foils directly applied for glucose sensing have been explored. To the best of our knowledge, CuO grown directly on electric and biocompatible substrate, which acts as electrode for detection of glucose have been rarely reported. Here, we design a new CuO film on Ti substrate (CuO/Ti) electrode by effectively taking advantage of the conductivity and biocompatibility of the substrate. The CuO/Ti electrode, fabricated simply by a template-free hydrothermal method, can be an inexpensive and high-performance alternative to conventional CuO electrodes for use in biosensors. There is no need to use extra binders or other classical electrodes such as glassy carbon and Au electrode. We investigated the application of this new electrode for glucose determination. In addition, we demonstrated that the fabricated glucose biosensor exhibited high sensitivity, fast response, an appropriate linear range, and good stability. The good analytical performance, low cost, and one-step preparation method make this electrode material promising for the development of a nonenzymatic glucose sensor.

2. Experimental Details

2.1. Reagents and Materials. $\text{Cu}(\text{NO}_3)_2 \cdot 3\text{H}_2\text{O}$, NaOH, urea, and glucose are purchased from Shanghai Chemical Co. (China). All chemicals used are analytical grade and are used as received without further purification. The titanium foil is of 99% purity. Glucose solution containing various concentrations is freshly prepared daily. All aqueous solutions are prepared in distilled water.

2.2. Preparation of CuO Films on Ti Substrate Electrodes. In a typical process, 1 mmol $\text{Cu}(\text{NO}_3)_2 \cdot 3\text{H}_2\text{O}$ and 10 mmol urea were dissolved in 80 mL distilled water to form a blue transparent solution. Then, the solution was transferred into a Teflon-lined autoclave (a piece of Ti substrate washed by hydrofluoric acid/water was placed upright in the autoclave). After that, the autoclave was placed in an electric oven at 120°C for 12 h. Lastly, the substrate was washed with distilled water and dried at room temperature. In this way, CuO films could be fabricated on the Ti substrate by a simple method with low cost. This opened up the possibility of large-scale preparation of the novel probe which can be applied as the electrode for a glucose sensor.

2.3. Sample Characterizations and Electrochemical Test. The film was characterized using powder X-ray diffraction (XRD, Y-2000) with Cu $K\alpha$ radiation ($\lambda = 1.5418 \text{ \AA}$) and scanning electron microscopy (SEM, JSM-6700F). All electrochemical measurements were performed on a CHI 660C electrochemical workstation (Shanghai, China) with a conventional three-electrode system composed of a platinum auxiliary, a saturated calomel electrode (SCE) reference, and CuO films grown on Ti substrate as working electrodes. All electrochemical experiments were performed in 0.1 M NaOH

solutions under continuous stirring at room temperature. Glucose concentration was controlled by addition as desired.

3. Results and Discussion

3.1. Morphology and Structure of Obtained Sample. XRD pattern of the as-obtained sample is displayed in Figure 1(a). Except for the peaks originating from the Ti substrate, others are the peaks of monoclinic phase of CuO (JCPDS number 89-5899) with lattice constants of $a = 0.469 \text{ nm}$, $b = 0.342 \text{ nm}$, and $c = 0.513 \text{ nm}$. The major sharp peaks at 35.5° and 38.7° are attributable to the (002) and (200) plane, respectively, indicating pure phase monoclinic crystallites. Figure 1(b) illustrates a typical optical image of CuO film grown on Ti substrate. As it is obvious from the image, the prepared CuO film is uniform on Ti substrate on a large scale. The typical morphology of the as-obtained CuO film, as observed by SEM, is illustrated in Figures 1(c) and 1(d) at different magnifications. Figure 1(c) is the low-magnification SEM image. It can be seen that the substrate is absolutely covered by uniform maize cob-like CuO nanostructures. From Figure 1(d), it is displayed that maize cob-like nanostructure is composed of many small nanoparticles, which has the potential to provide large surface area and high surface energy for catalytic reaction. The mechanism for the direct growth of CuO film on Ti substrate could be ascribed to the uniform roughness of etched Ti substrate surface. Roughness of substrate surface is especially valuable to the reduction of binding energy between seeds and substrate [29]. Therefore, it is more convenient for the nucleation and adhesion of seeds to be done on rough surface than on smooth surface.

3.2. Electrochemical Activities. The electrocatalytic activity of the CuO/Ti electrode towards the oxidation of glucose in alkaline solution was demonstrated by voltammograms (CV_s). The CV_s of the CuO/Ti electrode were conducted in 0.1 M NaOH solution in the presence and absence of glucose, respectively, at a scan rate of 100 mV/s.

As shown in Figure 2, only small background current and no peak are observed for the pure Ti electrode, while a dramatic increase of current signal with a wave potential of about +0.58 V is observed when the CuO/Ti electrode is used, which should correspond to a Cu(II)/Cu(III) redox couple. This result is similar to precious reports [30, 31]. This indicates that CuO nanostructures have greatly improved the performance of the electrode and increased the electrocatalytic ability towards glucose oxidation, which may be attributed to their large surface, high surface energy, and enhanced electron transfer ability [23]. The good electrochemical ability and easy fabrication method make the as-obtained CuO/Ti electrode an excellent electrochemical sensing platform for glucose detection. Figure 3(a) displays a typical amperometric response curve of the CuO/Ti electrode to the successive addition of glucose at an applied potential of +0.58 V in 0.1 M NaOH recorded at an interval of 50 s. A well-defined, stable, and fast amperometric response could be observed with successive addition of glucose to NaOH. As the

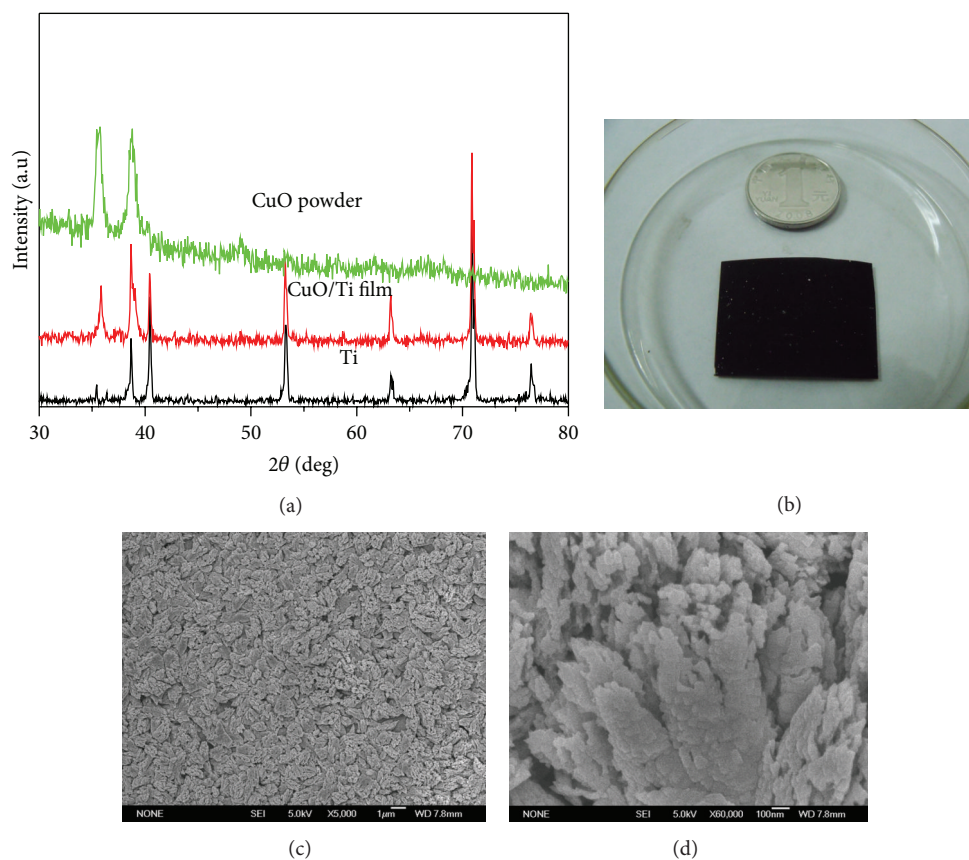


FIGURE 1: (a) XRD pattern of Ti substrate, CuO film on Ti substrate, and CuO powder, (b) optical image, (c) low-magnification, and (d) high-magnification SEM images of as-prepared CuO film on Ti substrate.

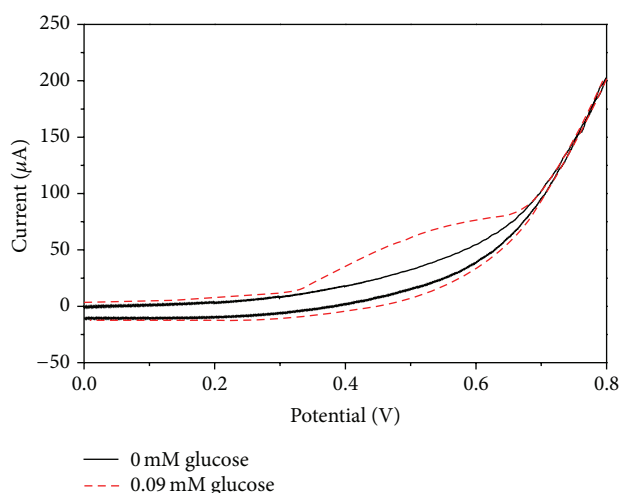


FIGURE 2: Cyclic voltammograms of CuO film electrode in absence and presence of glucose in 0.1M NaOH solution at a scan rate of 100 mV/s.

glucose was injected, the biosensor yields a typical steady-state amperometric response. The average time required to reach the stable response is less than 2 s, demonstrating a fast

current response to glucose. Meanwhile, as can be seen from Figure 3(b), the CuO/Ti electrode gives a linear dependence range from 5 μM to 1.6 mM of glucose, a remarkably high sensitivity of 726.9 $\mu\text{A mM}^{-1} \text{cm}^{-2}$, and a low detection limit of 2 μM .

Although the direct electrocatalytic oxidation of glucose at copper-based electrode remains ambiguous till now, the $\text{Cu}^{2+}/\text{Cu}^{3+}$ redox couple is considered to be playing an important role for carbohydrate oxidation because it has been reported to be strongly dependent upon the hydroxide concentration. Hydroxyl radicals are probably formed in the OH oxidation at Cu(III) catalytic centre during the potential window, which react with the organic molecules through the abstraction of a hydrogen atom from the carbon in a position with respect to $-\text{OH}$ group [32]. Large surface area and strong electron transfer rate from electrode to glucose are two commonly important issues responsible for the excellent sensing properties of nonenzymatic glucose sensors. As for as-obtained CuO/Ti electrode, more accessible reaction sites provided by the high-density nanoscale “maize cob-like” CuO building units may generate more Cu(III) species for the adsorption and reaction of glucose molecules, while abundant spacing among the maize-like building units may facilitate the fast diffusion of glucose molecules. In addition, more electron transfer passages and lower charge transfer

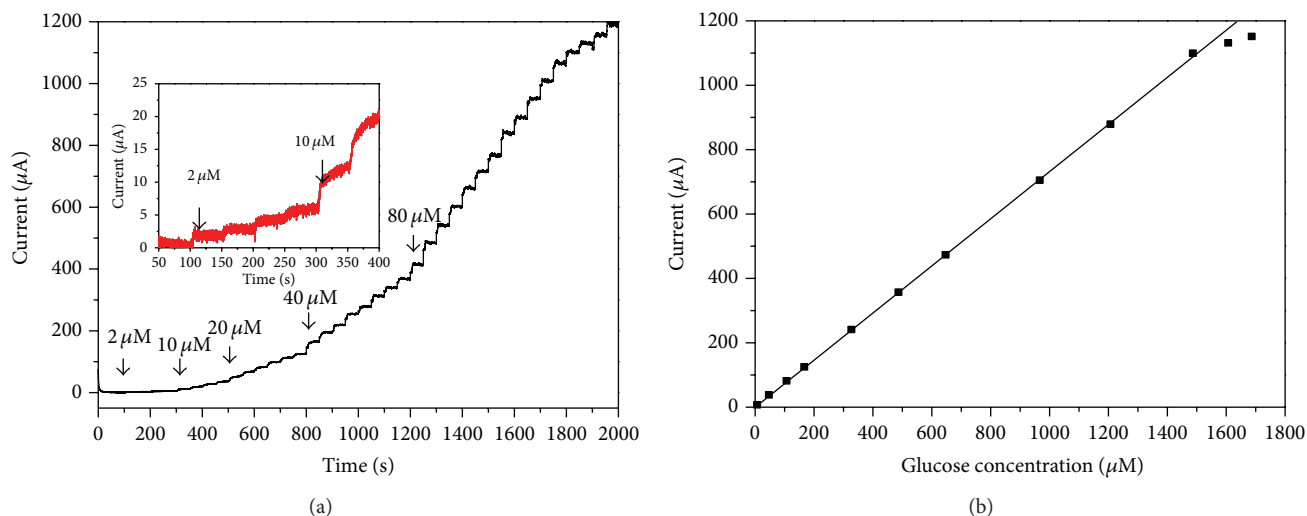


FIGURE 3: (a) Amperometric responses of the CuO film electrode to successive addition of glucose at applied potential of +0.58 V in 0.1M NaOH; (b) the calibration curve for the amperometric responses of CuO film electrode. Inset of (a) displays the response to 2 μM and 10 μM glucose of the CuO film electrode.

resistance for hierarchical CuO micro/nanostructures can promote the shuttle of electron between glucose and the working electrode. In a way, in situ fabrication of maize cob-like CuO on Ti substrate may further ensure the direct and fast electron transfer between electrode and electrolyte.

The long-term stability of glucose sensor is a critical factor in practical detection application. The reproducibility and stability of the as-obtained sensor were evaluated by the comparison of the sensitivity of different electrodes. Six different electrodes were made under the same fabrication condition and their current responses to glucose at +0.58 V were investigated. The relative standard deviation (RSD) is 3.5%, which shows highly reproducible. Thirty successive measurements of glucose on one electrode yield an RSD of 4.1%, demonstrating that the sensor is stable. It indicates that the glucose sensor based on CuO/Ti electrode has good reproductivity and long-term stability. The excellent long-term storage stability of the electrode can be attributed to the strong adhesion of CuO/Ti substrate, as well as the chemical stability of CuO in basic solution.

4. Conclusion

We have successfully synthesized CuO films on the Ti substrate by a simple, rapid, and reproducible method. For the first time, we used CuO/Ti as working electrode to detect glucose which is inexpensive and convenient. The novel amperometric glucose sensor based on the CuO/Ti electrode shows high sensitivity, low detection limit, good stability, reproducibility, and fast response time. The CuO/Ti electrode is easily fabricated and afforded an excellent platform for glucose sensor.

Conflict of Interests

The authors declare that there is no conflict of interests regarding the publication of this paper.

Acknowledgments

This work was supported by the Natural Science Foundation of Henan Province (nos. 122300410214; 132102210048). The authors would like to thank Professor X. T. Huang for his guidance and help at Central China Normal University.

References

- [1] A. Safavi, N. Maleki, and E. Farjami, "Fabrication of a glucose sensor based on a novel nanocomposite electrode," *Biosensors and Bioelectronics*, vol. 24, no. 6, pp. 1655–1660, 2009.
- [2] E. Ohashi and I. Karube, "Development of a thin membrane glucose sensor using β -type crystalline chitin for implantable biosensor," *Journal of Biotechnology*, vol. 40, no. 1, pp. 13–19, 1995.
- [3] D. R. Shankaran, K. V. Gobi, and N. Miura, "Recent advancements in surface plasmon resonance immunosensors for detection of small molecules of biomedical, food and environmental interest," *Sensors and Actuators, B: Chemical*, vol. 121, no. 1, pp. 158–177, 2007.
- [4] B. J. White and H. J. Harmon, "Novel optical solid-state glucose sensor using immobilized glucose oxidase," *Biochemical and Biophysical Research Communications*, vol. 296, no. 5, pp. 1069–1071, 2002.
- [5] S. Cherevko and C. Chung, "Gold nanowire array electrode for non-enzymatic voltammetric and amperometric glucose detection," *Sensors and Actuators, B: Chemical*, vol. 142, no. 1, pp. 216–223, 2009.

- [6] K. M. El Khatib and R. M. Abdel Hameed, "Development of Cu₂O/Carbon Vulcan XC-72 as non-enzymatic sensor for glucose determination," *Biosensors and Bioelectronics*, vol. 26, no. 8, pp. 3542–3548, 2011.
- [7] T. Watanabe and Y. Einaga, "Design and fabrication of nickel microdisk-arrayed diamond electrodes for a non-enzymatic glucose sensor based on control of diffusion profiles," *Biosensors and Bioelectronics*, vol. 24, no. 8, pp. 2684–2689, 2009.
- [8] C. Xia and W. Ning, "A novel non-enzymatic electrochemical glucose sensor modified with FeOOH nanowire," *Electrochemistry Communications*, vol. 12, no. 11, pp. 1581–1584, 2010.
- [9] M. Q. Guo, H. S. Hong, X. N. Tang, H. D. Fang, and X. H. Xu, "Ultrasonic electrodeposition of platinum nanoflowers and their application in nonenzymatic glucose sensors," *Electrochimica Acta*, vol. 63, pp. 1–8, 2012.
- [10] L.-M. Lu, L. Zhang, F.-L. Qu et al., "A nano-Ni based ultrasensitive nonenzymatic electrochemical sensor for glucose: enhancing sensitivity through a nanowire array strategy," *Biosensors and Bioelectronics*, vol. 25, no. 1, pp. 218–223, 2009.
- [11] J. Wang, D. F. Thomas, and A. Chen, "Nonenzymatic electrochemical glucose sensor based on nanoporous Pt/Pb networks," *Analytical Chemistry*, vol. 80, no. 4, pp. 997–1004, 2008.
- [12] H. B. Noh, K. S. Lee, P. Chandra, M. S. Won, and Y. B. Shim, "Application of a Cu-Co alloy dendrite on glucose and hydrogen peroxide sensors," *Electrochimica Acta*, vol. 61, pp. 36–43, 2012.
- [13] Y. Zhao, J. Z. Zhao, D. C. Ma et al., "Synthesis, growth mechanism of different Cu nanostructures and their application for non-enzymatic glucose sensing," *Colloids and Surfaces A: Physicochemical and Engineering Aspects*, vol. 409, pp. 105–111, 2012.
- [14] Y. Mu, D. Jia, Y. He, Y. Miao, and H. L. Wu, "Nano nickel oxide modified non-enzymatic glucose sensors with enhanced sensitivity through an electrochemical process strategy at high potential," *Biosensors and Bioelectronics*, vol. 26, no. 6, pp. 2948–2952, 2011.
- [15] X. Kang, Z. Mai, X. Zou, P. Cai, and J. Mo, "A sensitive nonenzymatic glucose sensor in alkaline media with a copper nanocluster/multiwall carbon nanotube-modified glassy carbon electrode," *Analytical Biochemistry*, vol. 363, no. 1, pp. 143–150, 2007.
- [16] J. S. Ye, Y. Wen, W. D. Zhang, L. M. Gan, G. Q. Xu, and F. Sheu, "Nonenzymatic glucose detection using multi-walled carbon nanotube electrodes," *Electrochemistry Communications*, vol. 6, no. 1, pp. 66–70, 2004.
- [17] J. B. Reitz and E. I. Solomon, "Propylene oxidation on copper oxide surfaces: Electronic and geometric contributions to reactivity and selectivity," *Journal of the American Chemical Society*, vol. 120, no. 44, pp. 11467–11478, 1998.
- [18] A. Chowdhuri, V. Gupta, K. Sreenivas, R. Kumar, S. Mozumdar, and P. K. Patanjali, "Response speed of SnO₂-based H₂S gas sensors with CuO nanoparticles," *Applied Physics Letters*, vol. 84, no. 7, pp. 1180–1182, 2004.
- [19] C.-T. Hsieh, J.-M. Chen, H.-H. Lin, and H.-C. Shih, "Field emission from various CuO nanostructures," *Applied Physics Letters*, vol. 83, no. 16, pp. 3383–3385, 2003.
- [20] X. P. Gao, J. L. Bao, G. L. Pan et al., "Preparation and electrochemical performance of polycrystalline and single crystalline CuO nanorods as anode materials for Li ion battery," *Journal of Physical Chemistry B*, vol. 108, no. 18, pp. 5547–5551, 2004.
- [21] M. U. Anu Prathap, B. Kaur, and R. Srivastava, "Hydrothermal synthesis of CuO micro-/nanostructures and their applications in the oxidative degradation of methylene blue and non-enzymatic sensing of glucose/H₂O₂," *Journal of Colloid and Interface Science*, vol. 370, no. 1, pp. 144–154, 2012.
- [22] P. Zhang, L. Zhang, G. C. Zhao, and F. Feng, "A highly sensitive nonenzymatic glucose sensor based on CuO nanowires," *Microchimica Acta*, vol. 176, no. 3–4, pp. 411–417, 2012.
- [23] E. Reitz, W. Z. Jia, M. Gentile, Y. Wang, and Y. Lei, "CuO nanospheres based nonenzymatic glucose sensor," *Electroanalysis*, vol. 20, no. 22, pp. 2482–2486, 2008.
- [24] Z. H. Ibupoto, K. Khun, V. Beni, X. J. Liu, and M. Willander, "Synthesis of novel CuO nanosheets and their non-enzymatic glucose sensing applications," *Sensors*, vol. 13, no. 6, pp. 7926–7938, 2013.
- [25] X. Wang, C. G. Hu, H. Liu, G. J. Du, X. S. He, and Y. Xi, "Synthesis of CuO nanostructures and their application for non-enzymatic glucose sensing," *Sensors and Actuators, B: Chemical*, vol. 144, no. 1, pp. 220–225, 2010.
- [26] L.-L. Tian and B.-T. Liu, "Fabrication of CuO nanosheets modified Cu electrode and its excellent electrocatalytic performance towards glucose," *Applied Surface Science*, vol. 283, pp. 947–953, 2013.
- [27] T. K. Huang, K. W. Lin, S. P. Tung et al., "Glucose sensing by electrochemically grown copper nanobelt electrode," *Journal of Electroanalytical Chemistry*, vol. 636, no. 1–2, pp. 123–127, 2009.
- [28] X. Zhang, A. X. Gu, G. F. Wang et al., "Fabrication of CuO nanowalls on Cu substrate for a high performance enzyme-free glucose sensor," *CrystEngComm*, vol. 12, no. 4, pp. 1120–1126, 2010.
- [29] X. Li, J. Liu, X. Ji et al., "Ni/Al layered double hydroxide nanosheet film grown directly on Ti substrate and its application for a nonenzymatic glucose sensor," *Sensors and Actuators B: Chemical*, vol. 147, no. 1, pp. 241–247, 2010.
- [30] G. Y. Liu, B. Z. Zheng, Y. S. Jiang et al., "Improvement of sensitive CuO NFs-ITO nonenzymatic glucose sensor based on in situ electrospun fiber," *Talanta*, vol. 101, pp. 24–31, 2012.
- [31] D. Ye, G. Liang, H. Li et al., "A novel nonenzymatic sensor based on CuO nanoneedle/graphene/carbon nanofiber modified electrode for probing glucose in saliva," *Talanta*, vol. 116, pp. 223–230, 2013.
- [32] I. G. Casella, T. R. I. Cataldi, A. Guerrieri, and E. Desimoni, "Copper dispersed into polyaniline films as an amperometric sensor in alkaline solutions of amino acids and polyhydric compounds," *Analytica Chimica Acta*, vol. 335, no. 3, pp. 217–225, 1996.